The role of small-scale cloud, aerosol, and radiation processes for Earth's climate

Thesis by
Clare E. Singer

In Partial Fulfillment of the Requirements for the
Degree of
Ph.D. in Environmental Science and Engineering

CALIFORNIA INSTITUTE OF TECHNOLOGY
Pasadena, California

2024
Defended July 20, 2023

Clare E. Singer
ORCID: 0000-0002-1708-0997

ACKNOWLEDGEMENTS

There are many people I need to thank for both supporting me in my pursuit of the Ph.D. and for distracting me enough along the way to make sure I had a good time.

To my partner, my biggest supporter, and my soon-to-be husband, Dan. Thank you for waking up at weird hours to call me on the other side of the world when I was away doing science. Thank you for your huge sacrifice of taking on a remote graduate study to live with me in Pasadena and moving with me to New York. Thank you for all the home-cooked dinners and lunches that made my office mates jealous.

To my parents, your support goes back to the very beginning. I had the immense privilege to learn the joys and perils of academic science from a young age. Thank you for always bringing me along to conferences, and taking off time to explore the cool places we were able to travel as a result. Thank you for fiercely protecting my love of learning and never pushing me more than I pushed myself as a child, which was probably already too much. Mom, thank you for leading by example and showing me that there's no better time than right now to have a big adventure.

To my friends, in Pasadena and far beyond. Thank you for your support and immense curiosity. Thank you for letting me teach you about the weather on every one of our hikes. Sherry, thank you for always asking what I'm studying so you can give my elevator pitch to your family. Thank you to my friends at Caltech who have cheered me on and cheered me up throughout the past five years. Lily and Sara, I wouldn't have made it this far, this happily, without the two of you.

To my research group. The CliMA House has been an incredibly special place to do a Ph.D., and mostly because of the wonderful people who sit inside it everyday. Thank you for teaching me everything I know about climate and coding. Thank you for celebrating every birthday with cake and every Friday with a BBQ. Thank you for indulging my passions for baking and organizing. Thanks especially to Zhaoyi Shen and Anna Jaruga for teaching me so much and being amazing role models.

To my advisor, Tapio Schneider. Thank you for your support, guidance, and trust. I am so glad I ended up at Caltech working with you, and that you accepted me into the group despite an unconventional start. Often along the way I felt lost or confused, but you never doubted I could figure my own way out. Your willingness to let me succeed has brought me so much confidence, thank you.

And finally, a bizarre thank you to the COVID-19 pandemic lock-downs. Thank you for upending life as we knew it, but providing a small silver lining of a chance to unplug from the daily grind and reconnect in new ways with friends and family. Thank you for providing the impetus for Dan to move to California and for giving us the freedom to spend three months in Steamboat skiing with friends and family. Thank you for inspiring two road trips from Chicago to D.C. and extending my visits home from days to weeks. And thank you for pushing me to start reading novels again and sending snail mail to loved ones on the East Coast.

ABSTRACT

What makes clouds ethereal and beautiful also makes them complex and challenging to understand and to model. The important (thermo)dynamical processes of clouds occur at scales from microns (cloud-aerosol interactions), to meters (turbulence), to thousands of kilometers (synoptic weather patterns), and every scale in between. In this thesis, I explore several facets of how clouds interact with, respond to, and shape Earth's climate. I focus on small-scale processes, using high-resolution models and theory, to understand phenomena that can have large-scale impacts.

In the first three chapters of this thesis, I explore the idea of stratocumulus-cumulus transitions. Chapters 1 and 2 develop and demonstrate a conceptual model of a cloud-topped atmospheric boundary layer, which is rooted in mixed-layer theory. This model is able to concisely explain both the spatial stratocumulus-cumulus transition observed in the historical period, as well as a transition that has only been hypothesized by models, which may occur in the future as the direct effect of extreme concentrations of atmospheric CO_2, or which may have occurred in the past. I use this conceptual model to show the importance of sea surface temperature variations for driving the climatological transition, and on sea surface warming as a positive feedback for the CO_2-induced transition. Chapter 3 extends this work to understand the global response to CO_2-induced stratocumulus-cumulus transitions and the role for spatial teleconnections by embedding this conceptual model of the boundary layer into a global climate model (GCM). In the GCM we see both a fast adjustment in low cloud cover to CO_2, as well as a slower surface temperature-mediated feedback. Under CO_2 quadrupling, the stratocumulus cloud regions shrink in extent as the cloud-top longwave cooling is inhibited by CO_2 and surface temperatures also increase.

The final two chapters diverge from the previous theme to present two studies using very high-resolution models to explore how clouds interact with i) aerosols and ii) radiation. In Chapter 4, using a particle-based cloud microphysics model, I find that aerosol hygroscopicity, determined by the chemical composition of the particles, can alter stratocumulus cloud macrophysical properties, like liquid water path by up to 25% (in the regime of small aerosol sizes). I compare these results to a more standard moment-based microphysics model and find that this model is overly sensitive to aerosol hygroscopicity in the regime of small aerosol sizes, but realistically represents the negative sensitivity for large aerosol sizes. Finally, in

Chapter 5, I use a Monte Carlo 3D radiative transfer solver to estimate the global albedo bias introduced in models which make the standard assumption that photon fluxes in the horizontal are zero (the so-called Independent Column Approximation). I extrapolate globally from a set of resolved tropical cloud fields, using a learned empirical relation between top-of-atmosphere flux bias and cloud water path. I conclude that in a global model that resolves clouds at small-enough spatial scales, the tropical-mean, annual-mean bias may be on the order of 3 W m^{-2}.

PUBLISHED CONTENT AND CONTRIBUTIONS

[1] C. E. Singer et al. “Top-of-Atmosphere Albedo Bias from Neglecting Three-Dimensional Cloud Radiative Effects”. In: *Journal of the Atmospheric Sciences* 78.12 (2021), pp. 4053–4069. DOI: 10.1175/JAS-D-21-0032.1.
C.E.S. participated in the design of the project and led the radiative transfer modeling, analysis of the simulation data, and writing and editing of the manuscript.
Used for Chapter 5.
Published content used with permission from the American Meteorological Society.

TABLE OF CONTENTS

Chapter 0

INTRODUCTION

The overarching theme of the works presented in this thesis will be examining the role that clouds play in Earth's climate system. To this end, the chapters that follow will focus on two aspects: how the background meteorological and aerosol conditions determine the properties of the clouds that form, and how clouds in turn affect the climate system they exist within via radiative feedbacks. Specifically, I will present results using a range of models, from highly idealized conceptual frameworks, to very high-resolution small-scale simulations, to full complexity climate models.

0.1 Background

Contrary to the popular nickname for Earth as the "blue marble," the Earth often appears mostly white from space due to the clouds. Clouds cover 70% of Earth's surface on average, reflecting around 15% of all incoming shortwave radiation back to space (Cesana et al., 2019). In total, the Earth reflects 29% of the incoming radiation (i.e. the albedo is 0.29), and the clouds account for about half of this, thus exerting a strong cooling effect (Stephens et al., 2015). Clouds regulate the Earth's temperature, both through this shortwave reflection, but also through their greenhouse effect by trapping outgoing longwave radiation (OLR). Clouds generally fall into three categories, illustrated in Figure 0.1:

1. Low clouds (stratocumulus and cumulus), which have a strong cooling effect due to their optical thickness and weak warming effect due to their warm cloud-top temperatures.

2. High clouds (cirrus), which typically are optically thin at visible wavelengths and thus have a weak cooling effect, but are still quite opaque in the infrared and thus still have a strong warming effect since they emit at similarly cold temperatures.

3. Deep clouds (cumulonimbus), which also have a strong cooling due to their large albedo, but also a strong warming due to their cold cloud-tops that emit at very cold temperatures and reduce OLR.

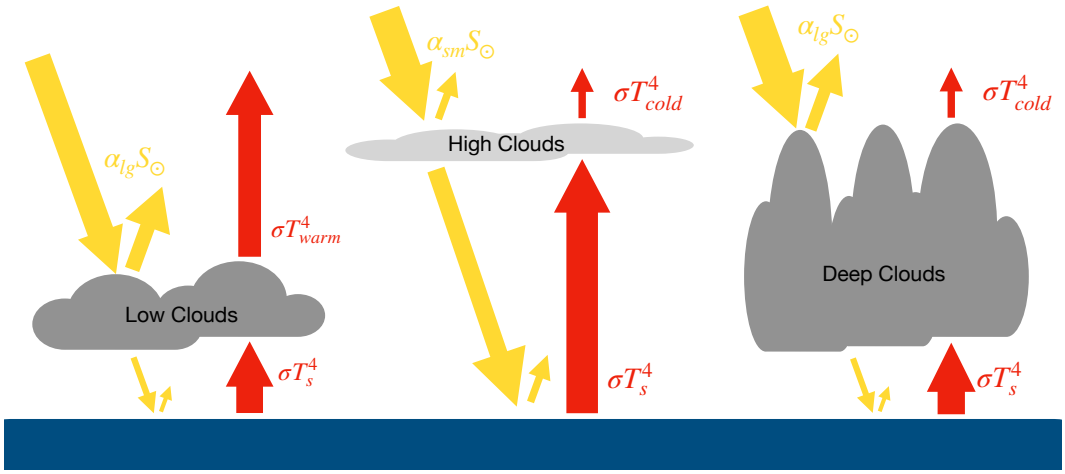

Figure 0.1: Schematic illustration of shortwave and longwave cloud radiative effects from low, high, or deep clouds. Low clouds have a large albedo α_{lg} and weak greenhouse effect $T_{warm} \sim T_s$, which results in a net cooling. High clouds have a small albedo α_{sm} and strong greenhouse effect $T_{cold} \ll T_s$, which results in net warming. Deep clouds combine both, because they have a large albedo and strong greenhouse effect, and thus result in near zero net radiative effect.

Chapters 1 through 4 of this thesis will focus on low clouds, particularly subtropical marine stratocumulus clouds. Chapter 5 is more expansive, including both shallow and deep clouds.

Low clouds, or specifically subtropical marine boundary layer (MBL) clouds, are a main focus in this thesis primarily because of their outsized role in the climate system (Stevens and Brenguier, 2009), but also because of the difficulties we have simulating them which lead to large errors in current generation global climate models (GCMs) (Bony and Dufresne, 2005). MBL clouds fall into two main categories: stratocumulus (Sc) and cumulus (Cu). Sc clouds occur over eastern subtropical ocean basins (e.g. off the coast here near Pasadena) where there is strong subsidence and relatively cool sea surface temperatures (SST). The Sc-topped boundary layer is shallow (approx. 1 km) and well-mixed, due to an upside-down overturning circulation driven by longwave cloud-top radiative cooling. The cloud layer itself is usually quite geometrically thin (approx. 200 m), but optically thick, with nearly 100% cloud cover. Cu clouds in contrast occur further west where the SSTs are warmer and the subsidence is weaker. They penetrate deeper into the atmosphere (approx. 2 km) with the cloud layer decoupled from the sea surface. Cu clouds are scattered, with typical cloud cover of 10–20%, but the albedo of each cloud is still fairly high. Observations along transects from the east to west across

subtropical ocean basins show a climatological transition from Sc to Cu that is termed the "stratocumulus-cumulus transition" or SCT (Bretherton, McCoy, et al., 2019) and this has been replicated in numerical experiments as well (Roode et al., 2016; Tan et al., 2016).

In addition to the background meteorology, the formation of a cloud is predicated on the existence of aerosol particles that can serve as cloud condensation nuclei (CCN). The efficacy of a CCN depends on its size and composition, which can be parameterized by the hygroscopicity using κ-Köhler theory (Petters and Kreidenweis, 2007). Aerosol-cloud interactions (ACI) contribute substantially to the overall uncertainty of climate prediction, partly because of the difficulty both simulating and measuring the important processes of condensation and coalescence that take place at the microscale (Myhre et al., 2013; Fan et al., 2016; Gettelman et al., 2019).

Finally, the coupling goes both ways: not only are the properties of the clouds that form strongly controlled by the atmospheric conditions within which they occur, but the climate system is also strongly controlled by clouds. Clouds control the climate state through their radiative effects, e.g. how they scatter shortwave and absorb longwave radiation. This controls the heating and cooling within the atmosphere and of the Earth's surface. The precise amount of heating and cooling from clouds — their radiative effects — depends on the detailed structure of the clouds. In climate models, and higher resolution simulations, we make approximations to the radiative transfer to make it computationally tractable. The most important of these is called the independent column approximation, or ICA, wherein we assume that horizontal fluxes of photons between atmospheric columns are negligible (Cahalan et al., 1994; Schäfer et al., 2016; Hogan and Bozzo, 2018; Hogan, Fielding, et al., 2019). Without the ICA, the distributed computation in a global model becomes impossible, because all vertical columns must now exchange information at a rate that makes it impossible to scale the computation across multiple processing units. However, this approximation necessarily neglects three-dimensional effects of clouds which can be important, especially for clouds with larger aspect ratios.

0.2 Thesis Outline

The works presented in this thesis use a variety of tools and methods ranging from idealized, conceptual models, to very high-resolution limited-domain models, to coarse-resolution global models. The first three chapters explore the theme of stratocumulus-cumulus transitions (SCT). Chapter 1, develops a conceptual model

of a cloud-topped atmospheric boundary layer. This model builds on the foundation of mixed-layer models for stratocumulus clouds (e.g., Lilly, 1968; Bretherton and Wyant, 1997; Stevens, 2006), but extends the framework to explicitly include decoupling of the cloud-topped boundary layer, breakup of the stratocumulus deck, and existence of cumulus clouds (Bretherton and Wyant, 1997; Schneider et al., 2019). In Chapter 1, I show how this model applies to the climatological SCT observed across the North East Pacific transect between California and Hawaii. I use the model to quantify the importance of different meteorological factors in driving this transition.

In Chapter 2, I extend the bulk boundary layer model by coupling it to a slab ocean with interactive surface temperatures and an idealized representation of radiative transfer. This extended model is therefore able to capture important feedbacks between cloud-thinning and surface warming that is ignored when sea surface temperatures (SSTs) are fixed (Tan et al., 2016). With this setup, I demonstrate the direct effect of CO_2 on stratocumulus clouds by running experiments with increasing CO_2, analogous to the large-eddy simulations (LES) from Schneider et al., 2019. I show that this conceptual model also has a critical concentration of CO_2 that leads to stratocumulus cloud breakup and exhibits hysteresis behavior, with the clouds not reforming until CO_2 concentrations are lowered much past the tipping point.

Chapter 3 takes another step forward, delving into one of the key limitations of the work in Chapter 2, which is the idealized representation of how a single location with climatological stratocumulus cloud cover is coupled with the rest of the tropics. In this chapter, I apply the key idea of decoupling induced cloud breakup from the bulk boundary layer model to the Community Earth System Model (CESM). CESM has a very complex representation of boundary layer turbulence and clouds, called the Cloud Layers Unified By Binormals (CLUBB) scheme, which I replace with a simple diagnostic cloud fraction based on the degree of decoupling of the boundary layer, as calculated in the theory from Chapters 1 and 2. I explore how including feedbacks between local cloud cover and large-scale changes in circulation and thermodynamics modifies the prediction of a stratocumulus tipping point with CO_2 predicted in Chapter 2 and Schneider et al., 2019.

The last two chapters diverge from this main theme to explore two detailed aspects of clouds and their interactions with aerosols and radiation. In these chapters I use two different high-resolution large eddy models, coupled to first, a high-resolution microphysics scheme, and second to a high-resolution radiative transfer scheme.

In Chapter 4, I use a Lagrangian cloud model with particle-based microphysics to explore how aerosol properties influence the macroscopic cloud. This relatively new type of microphysics scheme contrasts to traditional bulk (moment) representations of aerosols, cloud droplets, and rain drops — where the distributions of these particles are characterized by a finite number of (usually 1 or 2) moments of the distribution — by instead tracking a random statistical sample of these particles explicitly throughout the domain (Shima et al., 2009; Arabas et al., 2015; Dziekan et al., 2019; Grabowski et al., 2019). These particle-based schemes often go by the name superdroplet methods, where the particles that are tracked are called "superdroplets," and can be used in a range of dynamical models from 0D boxes, to 1D parcels, to fully 3D LES. Chapter 4 examines the role of aerosol hygroscopicity on cloud formation and in which regimes hygroscopicity may be an important factor to consider. In particular, these superdroplet schemes are well-suited for studying the role of aerosol composition because they can introduce additional properties to the particles (e.g., aerosol chemical composition, ice crystal density or shape) with little additional computational cost. Studies of aerosol-cloud-interactions historically have only looked at hygroscopicity effects in parcel models where the microphysical effects do not feedback on the cloud dynamics (Reutter et al., 2009; Chen et al., 2016; Pöhlker et al., 2021).

Chapter 5 ties together themes from throughout the thesis, asking the question: "how do the smallest scales influence the largest?". I look at the 3D radiative effects of clouds, and present an estimate of the global albedo bias introduced by neglecting these effects in models. I use LES to simulate clouds in various dynamical regimes and then uses a 3D radiative transfer model to track the trajectories of individual photons as they scatter through the cloudy domain (Mayer and Kylling, 2005; Emde et al., 2016). By doing so, I am able to calculate the bias introduced by typical radiative transfer schemes that neglect these 3D effects (Pincus et al., 2003; Shonk and Hogan, 2008), and extrapolate from these few LES cases up to a global estimate (Barker, Kato, et al., 2012; Barker, Cole, Li, Yi, et al., 2015; Barker, Cole, Li, and Salzen, 2016).

Finally, this thesis concludes with an appendix discussion on the topic of the "climate" of the geoscience community at Caltech (not the physical climate of Earth). I present data collected during my Ph.D. on the Caltech GPS Division's Qualifying Exam and results I found of disparity in exam outcome by gender.

References

[1] G. Cesana et al. "The Cumulus And Stratocumulus CloudSat-CALIPSO Dataset (CASCCAD)". In: *Earth System Science Data* 11.4 (2019), pp. 1745–1764. DOI: 10.5194/essd-11-1745-2019.

[2] G. L. Stephens et al. "The albedo of Earth". In: *Reviews of Geophysics* 53.1 (2015), pp. 141–163. DOI: 10.1002/2014RG000449.

[3] B. Stevens and J.-l. Brenguier. "Cloud-controlling Factors: Low Clouds". In: *Clouds Perturbed Clim. Syst. Their Relatsh. to Energy Balanc. Atmos. Dyn. Precip.* 1802. 2009.

[4] S. Bony and J.-L. Dufresne. "Marine boundary layer clouds at the heart of tropical cloud feedback uncertainties in climate models". In: *Geophys. Res. Lett.* 32.20 (2005), p. L20806. DOI: 10.1029/2005GL023851.

[5] C. S. Bretherton, I. L. McCoy, et al. "Cloud, Aerosol, and Boundary Layer Structure across the Northeast Pacific Stratocumulus–Cumulus Transition as Observed during CSET". In: *Mon. Weather Rev.* 147.6 (2019), pp. 2083–2103. DOI: 10.1175/MWR-D-18-0281.1.

[6] S. R. de Roode et al. "Large-Eddy Simulations of EUCLIPSE–GASS Lagrangian Stratocumulus-to-Cumulus Transitions: Mean State, Turbulence, and Decoupling". In: *J. Atmos. Sci.* 73.6 (2016), pp. 2485–2508. DOI: 10.1175/JAS-D-15-0215.1.

[7] Z. Tan et al. "Large-eddy simulation of subtropical cloud-topped boundary layers: 1. A forcing framework with closed surface energy balance". In: *J. Adv. Model. Earth Syst.* 8.4 (2016), pp. 1565–1585. DOI: 10.1002/2016MS000655.

[8] M. D. Petters and S. M. Kreidenweis. "A single parameter representation of hygroscopic growth and cloud condensation nucleus activity". In: *Atmos. Chem. Phys.* 7.8 (2007), pp. 1961–1971. DOI: 10.5194/acp-7-1961-2007.

[9] G. Myhre et al. "Anthropogenic and Natural Radiative Forcing". In: *Climate Change 2013: The Physical Science Basis. Contribution of Working Group I to the Fifth Assessment Report of the Intergovernmental Panel on Climate Change*. Ed. by T. Stocker et al. Cambridge, United Kingdom and New York, NY, USA: Cambridge University Press, 2013. Chap. 8, pp. 659–740.

[10] J. Fan et al. "Review of Aerosol–Cloud Interactions: Mechanisms, Significance, and Challenges". In: *Journal of the Atmospheric Sciences* 73.11 (2016), pp. 4221–4252. DOI: 10.1175/JAS-D-16-0037.1.

[11] A. Gettelman et al. "Cloud Microphysics Across Scales for Weather and Climate". In: *Current Trends in the Representation of Physical Processes in Weather and Climate Models*. Ed. by D. A. Randall et al. Singapore: Springer Singapore, 2019, pp. 71–94. DOI: 10.1007/978-981-13-3396-5_4.

[12] R. F. Cahalan et al. “Independent Pixel and Monte Carlo Estimates of Stratocumulus Albedo”. In: *Journal of the Atmospheric Sciences* 51.24 (1994), pp. 3776–3790. DOI: 10.1175/1520-0469(1994)051<3776:IPAMCE>2.0.CO;2.

[13] S. A. K. Schäfer et al. “Representing 3-D cloud radiation effects in two-stream schemes: 1. Longwave considerations and effective cloud edge length”. In: *Journal of Geophysical Research: Atmospheres* 121.14 (2016), pp. 8567–8582. DOI: 10.1002/2016JD024876.

[14] R. J. Hogan and A. Bozzo. “A Flexible and Efficient Radiation Scheme for the ECMWF Model”. In: *Journal of Advances in Modeling Earth Systems* 10 (8 2018). https://doi.org/10.1029/2018MS001364, pp. 1990–2008. DOI: https://doi.org/10.1029/2018MS001364.

[15] R. J. Hogan, M. D. Fielding, et al. “Entrapment: An Important Mechanism to Explain the Shortwave 3D Radiative Effect of Clouds”. In: *Journal of the Atmospheric Sciences* 2019 (1 2019), pp. 48–66. DOI: 10.1175/JAS-D-18-0366.1.

[16] D. K. Lilly. “Models of cloud-topped mixed layers under a strong inversion”. In: *Quart. J. Roy. Meteor. Soc.* 94 (1968), pp. 292–309. DOI: 10.1002/qj.49709440106.

[17] C. S. Bretherton and M. C. Wyant. “Moisture Transport, Lower-Tropospheric Stability, and Decoupling of Cloud-Topped Boundary Layers”. In: *J. Atmos. Sci.* 54 (1997), pp. 148–167. DOI: 10.1175/1520-0469(1997)054<0148:MTLTSA>2.0.CO;2.

[18] B. Stevens. “Bulk boundary-layer concepts for simplified models of tropical dynamics”. In: *Theor. Comput. Fluid Dyn.* 20.5-6 (2006), pp. 279–304. DOI: 10.1007/s00162-006-0032-z.

[19] T. Schneider et al. “Possible climate transitions from breakup of stratocumulus decks under greenhouse warming”. In: *Nat. Geosci.* 12.3 (2019), pp. 163–167. DOI: 10.1038/s41561-019-0310-1.

[20] S.-I. Shima et al. “The super-droplet method for the numerical simulation of clouds and precipitation: a particle-based and probabilistic microphysics model coupled with a non-hydrostatic model”. In: *Q. J. R. Meteorol. Soc.* 135.642 (2009), pp. 1307–1320. DOI: 10.1002/qj.441.

[21] S. Arabas et al. “libcloudph++ 1.0: a single-moment bulk, double-moment bulk, and particle-based warm-rain microphysics library in C++”. In: *Geosci. Model Dev.* 8 (2015), pp. 1677–1707. DOI: 10.5194/gmd-8-1677-2015.

[22] P. Dziekan et al. “University of Warsaw Lagrangian Cloud Model (UWLCM) 1.0: a modern large-eddy simulation tool for warm cloud modeling with Lagrangian microphysics”. In: *Geosci. Model Dev.* 12 (2019), pp. 2587–2606. DOI: 10.5194/gmd-12-2587-2019.

[23] W. W. Grabowski et al. “Modeling of Cloud Microphysics: Can We Do Better?” In: *Bulletin of the American Meteorological Society* 100.4 (2019), pp. 655–672. DOI: 10.1175/BAMS-D-18-0005.1.

[24] P. Reutter et al. “Aerosol-and updraft-limited regimes of cloud droplet formation: influence of particle number, size and hygroscopicity on the activation of cloud condensation nuclei (CCN)”. In: *Atmos. Chem. Phys.* 9 (2009), pp. 7067–7080. DOI: 10.5194/acp-9-7067-2009.

[25] J. Chen et al. “New understanding and quantification of the regime dependence of aerosol-cloud interaction for studying aerosol indirect effects”. In: *Geophys. Res. Lett.* 43.4 (2016), pp. 1780–1787. DOI: 10.1002/2016GL067683.

[26] M. L. Pöhlker et al. “Aitken mode particles as CCN in aerosol- and updraft-sensitive regimes of cloud droplet formation”. In: *Atmos. Chem. Phys.* 21.15 (2021), pp. 11723–11740. DOI: 10.5194/acp-21-11723-2021.

[27] B. Mayer and A. Kylling. “Technical note: The libRadtran software package for radiative transfer calculations - description and examples of use”. In: *Atmospheric Chemistry and Physics* 5.7 (2005), pp. 1855–1877. DOI: 10.5194/acp-5-1855-2005.

[28] C. Emde et al. “The libRadtran software package for radiative transfer calculations (version 2.0.1)”. In: *Geoscientific Model Development* 9.5 (2016), pp. 1647–1672. DOI: 10.5194/gmd-9-1647-2016.

[29] R. Pincus et al. “A fast, flexible, approximate technique for computing radiative transfer in inhomogeneous cloud fields”. In: *Journal of Geophysical Research: Atmospheres* 108.13 (2003), pp. 1–5. DOI: 10.1029/2002jd003322.

[30] J. K. Shonk and R. J. Hogan. “Tripleclouds: An efficient method for representing horizontal cloud inhomogeneity in 1D Radiation schemes by using three regions at each height”. In: *Journal of Climate* 21.11 (2008), pp. 2352–2370. DOI: 10.1175/2007JCLI1940.1.

[31] H. W. Barker, S. Kato, et al. “Computation of Solar Radiative Fluxes by 1D and 3D Methods Using Cloudy Atmospheres Inferred from A-train Satellite Data”. In: *Surveys in Geophysics* 33.3-4 (2012), pp. 657–676. DOI: 10.1007/s10712-011-9164-9.

[32] H. W. Barker, J. N. S. Cole, J. Li, B. Yi, et al. “Estimation of Errors in Two-Stream Approximations of the Solar Radiative Transfer Equation for Cloudy-Sky Conditions”. In: *Journal of the Atmospheric Sciences* 72.11 (2015), pp. 4053–4074. DOI: 10.1175/JAS-D-15-0033.1.

[33] H. W. Barker, J. N. S. Cole, J. Li, and K. von Salzen. “A parametrization of 3-D subgrid-scale clouds for conventional GCMs: Assessment using A-Train satellite data and solar radiative transfer characteristics”. In: *Journal of Advances in Modeling Earth Systems* 8.2 (2016), pp. 566–597. DOI: 10.1002/2015MS000601.

Chapter 1

STRATOCUMULUS-CUMULUS TRANSITION EXPLAINED BY BULK BOUNDARY LAYER THEORY

[1] C. E. Singer and T. Schneider. "Stratocumulus-cumulus transition explained by bulk boundary layer theory". In: *Journal of Climate* (2023). In revision.

Abstract. Stratocumulus clouds occurring over eastern subtropical ocean basins dominate climatological cloudiness at low latitudes and are important for Earth's global radiative energy budget. Further west, there is an observed transition to scattered cumulus cloud cover, the so-called stratocumulus-cumulus transition (SCT), which is controlled by changing large-scale meteorological conditions. To explore the mechanisms driving the SCT, we present an extension of the traditional bulk boundary layer model (bulk model) for stratocumulus-topped boundary layers that explicitly considers cloud decoupling from the surface and subsequent cloud fraction reduction. By forcing our bulk model with boundary conditions from ERA5 reanalysis, we are able to quantitatively capture the climatological SCT. We compare the modeled SCT to satellite observations across transects of the eastern Pacific and show good agreement. The bulk model highlights the importance of surface temperature variations across the transect for controlling the SCT. We also use the bulk model to explore the sensitivity of low clouds to changing meteorological factors and show how this sensitivity is nonlinear and depends on cloud regime.

Significance statement. The purpose of this study, and the companion paper Singer and Schneider, 2023, is to develop a simple model to explain mechanisms controlling stratocumulus-cumulus transitions. In this first work, we describe the bulk model in cases with prescribed boundary conditions. We demonstrate its relevance by showing how its predictions of stratocumulus-cumulus transitions across the subtropical eastern Pacific ocean basin compares to observations from satellites. We use the simple model to explore how boundary layer clouds are sensitive to different large-scale environmental factors and show how this sensitivity is nonlinear, depending on cloud regime.

1.1 Introduction

Stratocumulus clouds cover about 20% of tropical oceans in the annual-mean (Wood, 2012; Cesana et al., 2019). They are only a few hundred meters thick, yet because of their large areal coverage, are an important regulator of Earth's radiative energy balance: by scattering sunlight, stratocumulus cool Earth by about 8 K in the global mean (Randall et al., 1984; Schneider et al., 2019). Stratocumulus cloud decks are especially common over eastern subtropical ocean basins, off the west coasts of continents, for example, near California, Peru, and Namibia, where sea surface temperatures (SSTs) are low, subsidence is strong, and there exists a strong temperature inversion at the top of the boundary layer (Klein, Hartmann, et al., 1993; Zhang et al., 2009; Eastman et al., 2011; Chung and Teixeira, 2012; Myers and Norris, 2013; Bretherton and Blossey, 2014).

Uniquely among clouds, stratocumulus clouds are sustained by an upside-down convective circulation that is driven by cloud-top longwave radiative cooling rather than surface heating. The longwave cooling arises because stratocumulus clouds, despite their geometric thinness, are relatively opaque to longwave radiation (Lilly, 1968; Bretherton and Wyant, 1997; Stevens, 2006; Bellon and Geoffroy, 2016; Schneider et al., 2019). Radiative cooling at the cloud tops drives the turbulent convective circulations, which are also associated with turbulent entrainment of free-tropospheric warm and dry air across the cloud top. Stratocumulus clouds exist in a delicate balance between radiative cooling at the cloud tops and warming by turbulent entrainment, on the one hand, and evaporative moistening from the surface and drying by cloud-top entrainment, on the other hand. Additionally, subsidence above the clouds works against the deepening of the cloud layer that otherwise results from entrainment of free-tropospheric air into the cloudy boundary layer.

Meteorological factors on which cloud cover depends, commonly termed "cloud controlling factors" (CCFs) (Stevens and Brenguier, 2009; Siebesma et al., 2009; Bretherton, 2015), include SST, subsidence strength, the strength of the temperature inversion above the clouds (measured by either lower-tropospheric stability, LTS, or estimated inversion strength, EIS), horizontal temperature or moisture advection, wind speed, and more. A more appropriate term may be "cloud correlated factors" because the causality—whether the meteorological properties determine the clouds, or vice versa—is not always definitive. CCFs have been the focus of many previous studies (e.g., Klein, Hartmann, et al., 1993; Stevens and Brenguier, 2009; Qu et al., 2014; Klein, Hall, et al., 2017).

An important test of CCFs has been the observed stratocumulus-cumulus transition (SCT). SCT describes the observed phenomenon of stratocumulus clouds dominating subtropical cloud cover just off the west coasts of continents, and the cloud cover transitioning to a state that is dominated by scattered cumulus clouds farther west, over higher SSTs and under weaker subsidence. The accepted explanation is that as the subsidence weakens, the boundary layer deepens to the point where it becomes no longer well-mixed and the clouds decouple from their surface moisture source (Bretherton and Wyant, 1997). The SCT has been studied using theory (Wyant et al., 1997), high-resolution models (Roode et al., 2016; McGibbon and Bretherton, 2017; Yamaguchi et al., 2017; Neggers et al., 2017), satellite observations (Sandu, Stevens, and Pincus, 2010; Chung and Teixeira, 2012), and numerous field campaigns, such as ASTEX (Albrecht et al., 1995), GPCI (Teixeira et al., 2011), MAGIC (Kalmus et al., 2014), and CSET (Bretherton, McCoy, et al., 2019). However, it remains unclear to what extent correlations between cloud cover and CCFs in the present climate, for example, across the SCT, are informative about the climate response of clouds. For example, while a strengthened inversion in the present climate is associated with increased cloud cover (Klein, Hartmann, et al., 1993), the relation may be reversed when considering the response to global warming (Lauer et al., 2010).

In this paper, we present a new bulk boundary layer model (bulk model) for a stratocumulus-topped boundary layer. Building from standard bulk models for the atmospheric boundary layer, we add a prognostic equation for cloud fraction, which allows the model to make quantitative predictions of the state of the cloudy boundary layer after the point of decoupling, when the cloud fraction is less than 100%. The model is compared against satellite observations in this paper, and against high-resolution large-eddy simulations (LES) in a companion paper (Singer and Schneider, 2023).

The paper is organized as follows: Section 1.2 describes the bulk model. Section 1.3 introduces the data sources used as boundary conditions for the model and against which the results are compared. Section 1.4a explores sensitivities of the bulk model to idealized perturbations of boundary conditions. Section 1.4b compares results from the bulk model forced with reanalysis data to satellite observations of shallow clouds in the eastern Pacific. Section 1.5 has discussion of the assumptions in the model and key limitations. Section 1.6 summarizes the conclusions.

1.2 Bulk boundary layer model description

The general class of bulk boundary layer models describe the planetary boundary layer in terms of "bulk" or vertically-averaged quantities (Stevens, 2006). The boundary layer extends up to a level, coincident with a temperature inversion and the cloud top in stratocumulus regions, whose altitude we denote as z_i (Figure 1.1). After vertical integration, the continuity equation simplifies to an equation for this boundary layer depth, where z_i increases due to entrainment mixing and decreases from subsidence suppression.

We formulate the bulk model in terms of liquid water static energy $s = c_p T + gz - L_v q_\ell$ and total water specific humidity $q_t = q_v + q_\ell$. Subscript v stands for "vapor" and ℓ for "liquid." These two thermodynamic quantities (referred to with generality as ψ) are (approximately) conserved under adiabatic motions of a moist air parcel. Their temporal evolution is governed by budget equations that describe a balance between diabatic source terms (ΔF_ψ) and turbulent fluxes at the surface and across the inversion. The prognostic equations for the thermodynamic variables are derived by integrating from the surface to the top of the inversion layer $z = z_i$ to give the bulk value $\hat{\psi}$. They have the form

$$z_i \frac{d\hat{\psi}}{dt} = V\Delta_{0,\psi} + w_e \Delta_{+,\psi} - \Delta F_\psi, \tag{1.1}$$

where the Δ_i terms represent discontinuous jumps in the quantity ψ at the surface (0) and at the inversion (+). The exchange velocity at the surface V is the product of surface wind speed (U) and an effective drag coefficient (C_d). The drag coefficient is assumed to be the same for s and q_t. Across the inversion, the exchange velocity is given by the entrainment velocity w_e, the form of which must be assumed and is discussed in Section 1.2. To specify the surface and cross-inversion fluxes, a vertical structure of the boundary layer must be assumed so that the bulk quantity $\hat{\psi}$ can be related to the values just above the surface $\psi(z = +\epsilon)$ and just below the inversion $\psi(z = z_i - \epsilon)$. The most common path forward is to make a well-mixed assumption where $\psi(z) = \hat{\psi}$, which simplifies the equation to

$$z_i \frac{d\psi}{dt} = V(\psi_0 - \psi) + w_e(\psi_+ - \psi) - \Delta F_\psi. \tag{1.2}$$

where ψ without a subscript denotes the vertically-uniform value and the subscripts 0 and + denote the value at the surface and just above the inversion, respectively.

For the liquid static energy, there is a source term from radiation, namely the radiative cooling ΔR coming from the cloud-top emitting upward longwave radiation. For

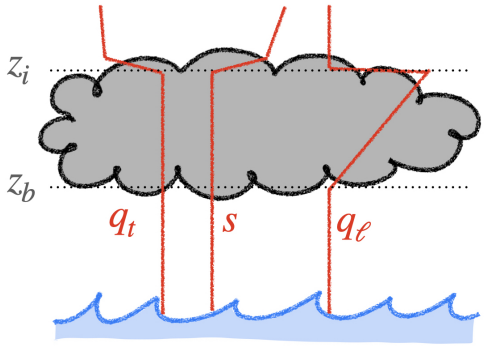

Figure 1.1: Schematic of stratocumulus-topped boundary layer with representative profiles of thermodynamic quantities shown. To determine $q_\ell(z)$ from the bulk model, a mixed-layer assumption is made, where the thermodynamic quantities s and q_t are assumed to be constant with height, as illustrated.

moisture, we choose to neglect the sink term that would come from precipitation. Under many conditions, stratocumulus clouds have no precipitation or only very light drizzle, which justifies this assumption. In terms of the thermodynamics, however, a precipitation sink would be easy to include in future work.

The bulk model predicts the boundary layer depth and bulk energy and moisture variables given prescribed surface and above-cloud boundary conditions. These are often given as: above-cloud horizontal divergence D (or subsidence velocity), above-cloud temperature and relative humidity, which are used to calculate $s_+ = c_p T_+ + g z_i$ and $q_{t,+} = \mathrm{RH}_+ q_{\mathrm{sat}}(T_+, z_i)$, cloud-top radiative cooling ΔR, and SST, which is used to calculate $s_0 = c_p \mathrm{SST}$ and $q_{t,0} = q_{\mathrm{sat}}(\mathrm{SST}, z = 0)$.

We extend this model to include a prognostic cloud fraction (CF). Cloud fraction is relaxed toward a diagnosed state, CF_d, which depends on the state of decoupling in the boundary layer and is explained in the following section.

In this form, with prescribed boundary conditions, our bulk model consists of a system of four coupled ordinary differential equations:

$$\frac{dz_i}{dt} = w_e - D z_i + w_{\mathrm{vent}} \tag{1.3a}$$

$$\frac{ds}{dt} = \frac{1}{z_i}\left[V(s_0 - s) + w_e(s_+ - s) - \Delta R\right] + s_{\mathrm{exp}} \tag{1.3b}$$

$$\frac{dq_t}{dt} = \frac{1}{z_i}\left[V(q_{t,0} - q_t) + w_e(q_{t,+} - q_t)\right] + q_{t,\mathrm{exp}} \tag{1.3c}$$

$$\frac{d\mathrm{CF}}{dt} = \frac{\mathrm{CF}_d - \mathrm{CF}}{\tau_{\mathrm{CF}}}. \tag{1.3d}$$

In Eq. (1.3a), D is assumed constant, so $-Dz_i$ is the subsidence velocity at the cloud-top, and w_{vent} is an additional additive entrainment term used to parameterize ventilation and mixing from overshooting cumulus convective thermals. Equations (1.3b) and (1.3c) are the prognostic equations for liquid water static energy and specific humidity following from (1.2). In (1.3b), the diabatic sink term is written as ΔR, which is the cloud-top radiative cooling per unit density (units of W m kg^{-1}). In (1.3c), no source term appears because precipitation is neglected. In (1.3b) and (1.3c), the export terms (subscript exp) are there to represent the effect of large-scale dynamics (synoptic eddies and Hadley circulation) transporting energy and moisture laterally out of the model domain into other regions. We use the same specification as in Schneider et al., 2019 with $s_{\text{exp}} = c_p(-1.2)$ J kg^{-1} day^{-1} and $q_{t,\text{exp}} = \left(-6 \times 10^{-4}\right) (q_{\text{sat}}(\text{SST})/q_{\text{sat}}(290\text{ K}))$ day^{-1}.

The cloud base, z_b, is diagnosed as the lifiting condensation level (as shown in Figure 1.1),

$$z_b = \min_z \left[q_\ell(z) > 0\right].$$

To calculate the cloud base, the subcloud layer is assumed to be well-mixed (s and q_t are constant). The liquid water specific humidity is diagnosed as the excess above saturation,

$$q_\ell(z) = q_t - \frac{R_d}{R_v}\left(\frac{p_{\text{sat}}(T(z))}{p(z) - p_{\text{sat}}(T(z))}\right),$$

with the saturation vapor pressure (Romps, 2008),

$$p_{\text{sat}}(z) = e_0 \exp\left(-\frac{L_0}{R_v}\left(\frac{1}{T(z)} - \frac{1}{T_0}\right)\right).$$

The constants $e_0 = 610.78$ Pa, $L_0 = 2.5 \times 10^6$ J kg^{-1}, and $T_0 = 273.16$ K are the saturation vapor pressure, latent heat of vaporization, and temperature at the triple point, respectively; $R_d = 287$ J kg^{-1} K^{-1} and $R_v = 461$ J kg^{-1} K^{-1} are the gas constants of dry air and water vapor, respectively. To calculate the liquid water content in the cloud, the cloud layer is also assumed to be well-mixed, but this is purely done for diagnostic purposes, because there are no feedbacks between q_ℓ and the prognostic variables in the model. This is discussed further in Section 1.5.

The in-cloud liquid water path, LWP_{cld}, is calculated as the integral of q_ℓ from z_b to z_i, which assumes an adiabatic cloud, with no mixing:

$$\text{LWP}_{\text{cld}} = \int_{z_b}^{z_i} \rho(z) q_\ell(z) dz.$$

The all-sky LWP is $\text{LWP} = \text{CF} \cdot \text{LWP}_{\text{cld}}$.

Predicted cloud fraction

Cloud fraction is relaxed to a diagnosed state CF_d, which depends on the degree of decoupling of the boundary layer. When topped with stratocumulus clouds, we take the boundary layer to remain well-mixed and coupled to the ocean surface by an overturning circulation that is driven by cloud-top longwave radiative cooling. In contrast to other cloud regimes, where clouds are formed from buoyant thermals driven by surface heating, the circulation in stratocumulus clouds is upside-down (Randall, 1980). In order for the radiative cooling to keep the boundary layer well-mixed, the buoyancy anomalies created must be large enough for parcels to travel through the stably stratified cloud layer. The subcloud layer is neutrally stratified, but the cloud layer, due to latent heat release during condensation, acts as a barrier to parcels from above as they sink toward the surface. In the event where the stratification is too large compared to the radiative cooling, parcels sinking from the cloud-top will not reach the surface, and the cloud effectively becomes disconnected from its moisture supply at the ocean surface. This behavior is termed "decoupling" (Bretherton and Wyant, 1997). We can diagnose boundary layer decoupling by considering the competition between cloud-top radiative cooling and surface latent heat fluxes. We introduce the decoupling parameter $\mathscr{D}$ from Bretherton and Wyant, 1997,

$$\mathscr{D} = \left(\frac{\mathrm{LHF}}{\rho \Delta R}\right)\left(\frac{z_i - z_b}{z_i}\right), \tag{1.4}$$

where z_b is the cloud base altitude. When $\mathscr{D} < 1$, the boundary layer remains coupled; when $\mathscr{D} > 1$, the boundary layer is decoupled.

We parameterize the cloud fraction, based on ideas from Sandu, Stevens, and Pincus (2010) and Chung and Teixeira (2012) and observations of monthly mean climatological cloudiness, as a logistic function with a maximum of $\mathrm{CF}_{\max} = 80\%$ cloud cover and minimum of $\mathrm{CF}_{\min} = 10\%$,

$$\mathrm{CF}_d = \mathrm{CF}_{\max} - \frac{\mathrm{CF}_{\max} - \mathrm{CF}_{\min}}{1 + \frac{1}{9}\exp(-m(\mathscr{D} - \mathscr{D}_c))}, \tag{1.5}$$

with cloud fraction smoothly varying on the nondimensional scale m. The maximum and minimum cloud fraction values, $\mathrm{CF}_{\max}$ and $\mathrm{CF}_{\min}$, are dependent on the spatiotemporal resolution (maximum cloud fraction will necessarily be smaller when averaged over larger spatial scales and longer timescales); the values chosen here are based on monthly mean observations at $2.5° \times 2.5°$ resolution (Cesana et al., 2019). The cloud fraction is 90% depleted when the critical decoupling threshold $\mathscr{D}_c = 1$ is reached. The scale m determines the strength of the nonlinearity, but

results are not strongly sensitive to m. We choose $m = 8$, which agrees well with monthly-mean observations of cloud cover (Figure 1.2).

The prognostic equation for cloud fraction, Eq. (1.3d), is a linear relaxation of the state CF_d, on a timescale $\tau_{\mathrm{CF}} = 2$ days. The timescale for the relaxation here is arbitrary, since this model is used only to predict steady-state solutions; timescales are discussed further in Section 1.4.

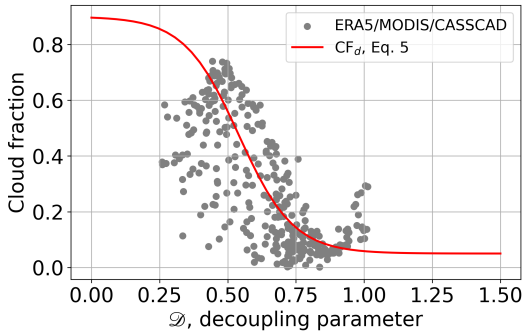

Figure 1.2: Scatter plot of observations of monthly-mean cloud fraction from CASCCAD (Cesana et al., 2019) against decoupling parameter $\mathscr{D}$. LHF is taken from ERA5 reanalysis, and observations of cloud-top radiative cooling from Zheng, Zhu, et al., 2021. We assumed a fixed $(z_i - z_b)/z_i = 0.4$. The red line shows the analytical form of cloud fraction predicted from Eq. 1.5 with $m = 8$.

One aspect that is neglected here, due to our previous assumption not to include precipitation in the moisture budget, is that we do not consider the possibility of drizzle-induced stratocumulus breakup (Yamaguchi et al., 2017; Uchida et al., 2010; Stevens, Vali, et al., 2005; Geoffroy et al., 2008; Prabhakaran et al., 2023). Precipitation can deplete the cloud layer of moisture through a different mechanism than the cloud-top cooling route captured by decoupling parameter, and lead to cloud fraction reduction while $\mathscr{D} < 1$. This could be explored in future work.

Entrainment closure

To close the system of equations, we must specify the entrainment velocity. We parameterize it here such that entrainment mixing balances radiative cooling in the steady state: an "energy-balance entrainment" closure (Bretherton and Wyant, 1997). The entrainment velocity is proportional to the radiative cooling and inversely proportional to the buoyancy jump across the inversion

$$w_e = \frac{\Delta R}{s_{vir_+} - s_{vir}}. \tag{1.6}$$

We write this with the virtual liquid static energy $s_{vir} = c_p T_{vir} + gz - L_v q_\ell$ which accounts for the buoyancy effects of water vapor through the virtual temperature $T_{vir} = (R_m/R_d)T$.

An additional additive entrainment term, w_{vent}, is introduced which depends on the cloud fraction. The physical idea is that in a cumulus state, buoyant plumes will overshoot z_i and lead to additional entrainment or ventilation and growth of the boundary layer. This is modeled as

$$w_{\text{vent}} = \alpha_{\text{vent}} \left(\frac{\text{CF}_{\text{max}} - \text{CF}}{\text{CF}_{\text{max}} - \text{CF}_{\text{min}}} \right) \tag{1.7}$$

where $\alpha_{\text{vent}} = 1.69$ mm s^{-1}. This parameter value was selected as described in Singer and Schneider, 2023 to best fit the LES results from Schneider et al., 2019.

Cloud-top cooling closure

Rather than specifying the cloud-top cooling directly as an independent boundary condition, we parameterize the radiative cooling as a function of the longwave absorbers in the free-troposphere above the cloud (CO_2 and H_2O). Conceptually, higher concentrations of absorbers will decrease the cloud-top cooling because the atmosphere will be optically thicker in the infrared, and the downwelling longwave radiation hitting the cloud-top will be coming from closer levels, or higher temperatures, reducing the net upward longwave flux. Mathematically, we can write the cloud-top radiative cooling term as the difference between the upwelling radiation emitted from the cloud top and the downwelling radiation emitted back from the atmosphere. The upwelling radiation is emitted at the cloud top temperature $T_{ct} = T(z_i)$, while the downwelling radiation comes from a temperature $T_{ct} + \Delta T_{em}$. The cloud-top radiative cooling then is

$$\Delta R = \text{CF} \cdot \epsilon_c \sigma \left(T_{ct}^4 - (T_{ct} + \Delta T_{em})^4 \right), \tag{1.8}$$

where $\epsilon_c = 0.9$ is the cloud emissivity. The cloud emissivity is assumed constant, which is reasonable given large enough liquid water paths as the longwave emission tends to saturate around 20 g m^{-2} (Petters et al., 2012). We then parameterize ΔT_{em}, which depends on the optical thickness of the atmosphere above the cloud top, or the concentrations of CO_2 and H_2O as,

$$\Delta T_{em} = a_0 + a_1 \ln(\text{CO}_2) + a_2 \ln(q_{t,+}). \tag{1.9}$$

We fit the parameters $a_0 = -10.1$ K, $a_1 = 3.1$ K, and $a_2 = 5.3$ K based on the radiative transfer model (RRTMG) in the LES simulations presented in Schneider et al., 2019 (see Fig. 1.3).

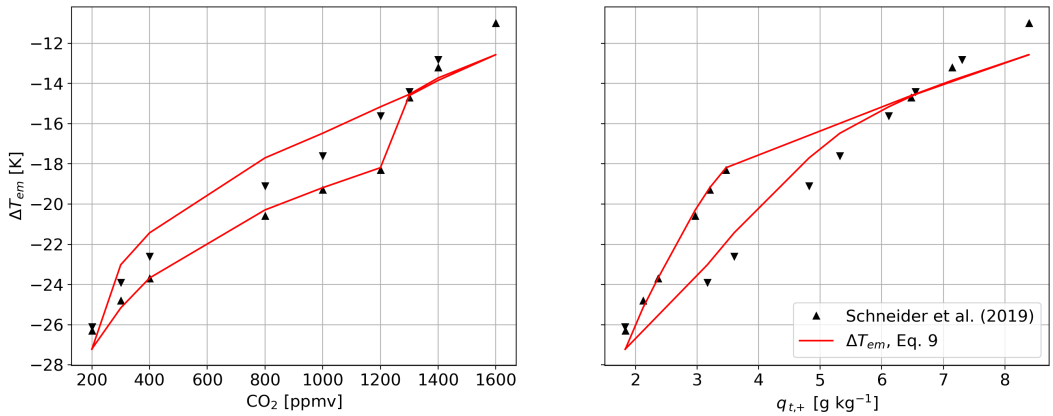

Figure 1.3: Difference between cloud-top temperature and effective downwelling emission temperature (ΔT_{em}) fit to LES from Schneider et al., 2019. Shown with ΔT_{em} plotted against (a) the CO_2 concentration and (b) the above-cloud specific humidity $q_{t,+}$. Upward (downward) pointing triangle markers are LES experiments with increasing (decreasing) CO_2.

1.3 Observational data for model comparison and evaluation

We use monthly observations of low-cloud cover (CF) from the CASCCAD dataset, which is a combined product using Cloudsat and CALIPSO (Cesana et al., 2019). The CASSCAD algorithm separates observed clouds by cloud type, but here we use the total "low" cloud cover product. The CASSCAD product has monthly mean cloud fraction observations from January 2007 to December 2016.

The monthly climatological observations of cloud-top radiative fluxes come from Zheng, Rosenfeld, et al., 2019; Zheng, Zhu, et al., 2021. This is a combined product using observations from MODIS, NCEP reanalysis, and the Santa Barbara DISORT Atmospheric RTM.

All other "observations" are from ERA5 reanalysis (Hersbach et al., 2020); we use the same 10-year period of the CASSCAD observations. To obtain the fields used as boundary conditions to the bulk model (shown in Figure 1.4), the following daily ERA5 fields are used: sea surface temperature (SST), 10-m horizontal winds, vertical velocity at 500 hPa, relative humidity at 500 hPa (RH_{500}), surface pressure, 2-m temperature, temperature at 700 hPa, and temperature at 850 hPa. Estimated inversion strength (EIS) is calculated according to Wood and Bretherton, 2006 (their Eq. 4) from T_{850}, T_{700}, T_{2m}, and p_s. The above-cloud liquid water static energy is calculated as $s_+ = c_p(T(z_i) + \text{EIS}) + gz_i$. Above cloud relative humidity, RH_+ is taken directly as RH_{500}, implicitly assuming that relative humidity is vertically

uniform in the free-troposphere. Divergence at 500 hPa (D_{500}) is calculated from vertical velocity as in Tan et al. (2016), with an assumed quadratic profile in pressure. Surface wind speed U is calculated from 10-m horizontal velocity components as $U = \sqrt{u^2 + v^2}$.

We use daily reanalysis data for NH summer (JJA). Observations are filtered to only include days with mean subsidence across the North East Pacific (NEP) transect because the bulk model can only be applied to regions of subsidence. The results are insensitive to exactly how this filtering is done. See the appendix for more detail.

The monthly mean fields of SST, U, EIS, D_{500}, RH_{500}, and CF are shown in Figure 1.4. These fields, the canonical CCFs, are the boundary conditions given as input to the bulk model, along with the resulting cloud fraction, which is the output of the model. The red dotted line shows the transect from the coast of California to near Hawaii analyzed throughout this study. Below each map in Figure 1.4, the subplots show the climatological mean values of the CCFs along this transect in summer (JJA) as well as their year-to-year standard deviations (shading).

1.4 Results

The bulk model predicts the evolution of the cloudy boundary layer in addition to the steady-state result. The timescale for convergence to the steady-state is set by the slowest timescale in the problem. The thermodynamic variables ψ evolve on a timescale $\tau_\psi = z_i/(V + w_e)$, and the boundary layer depth evolves on a timescale $\tau_{z_i} = D^{-1}$ (Bretherton, Uchida, et al., 2010; Jones et al., 2014). Numerically, these timescales are on the order $\tau_\psi = 20$ hours and $\tau_{z_i} = 46$ hours. We introduce here a fourth equation for cloud fraction with a specified timescale $\tau_{\mathrm{CF}} = 2$ days, which is longer than these others, such that cloud fraction responds to changes in the boundary layer properties, without introducing large positive feedbacks that lead to oscillations in the system. The model is designed to examine steady-state responses of the boundary layer to forcing. Short-timescale variability, such as a diurnal cycle, synoptic variability, and Lagrangian advection, are not included in the forcing. Therefore, the model should not be expected to compare realistically to observations of transient behavior that includes these short-timescale forcing. However, as has been demonstrated in the literature numerous times, the Lagrangian and climatological stratocumulus-cumulus transitions are quite comparable (e.g., Sandu, Stevens, and Pincus, 2010; Sandu and Stevens, 2011; Blossey et al., 2013). In summary, the steady-state behavior gives useful insight into mechanisms controlling

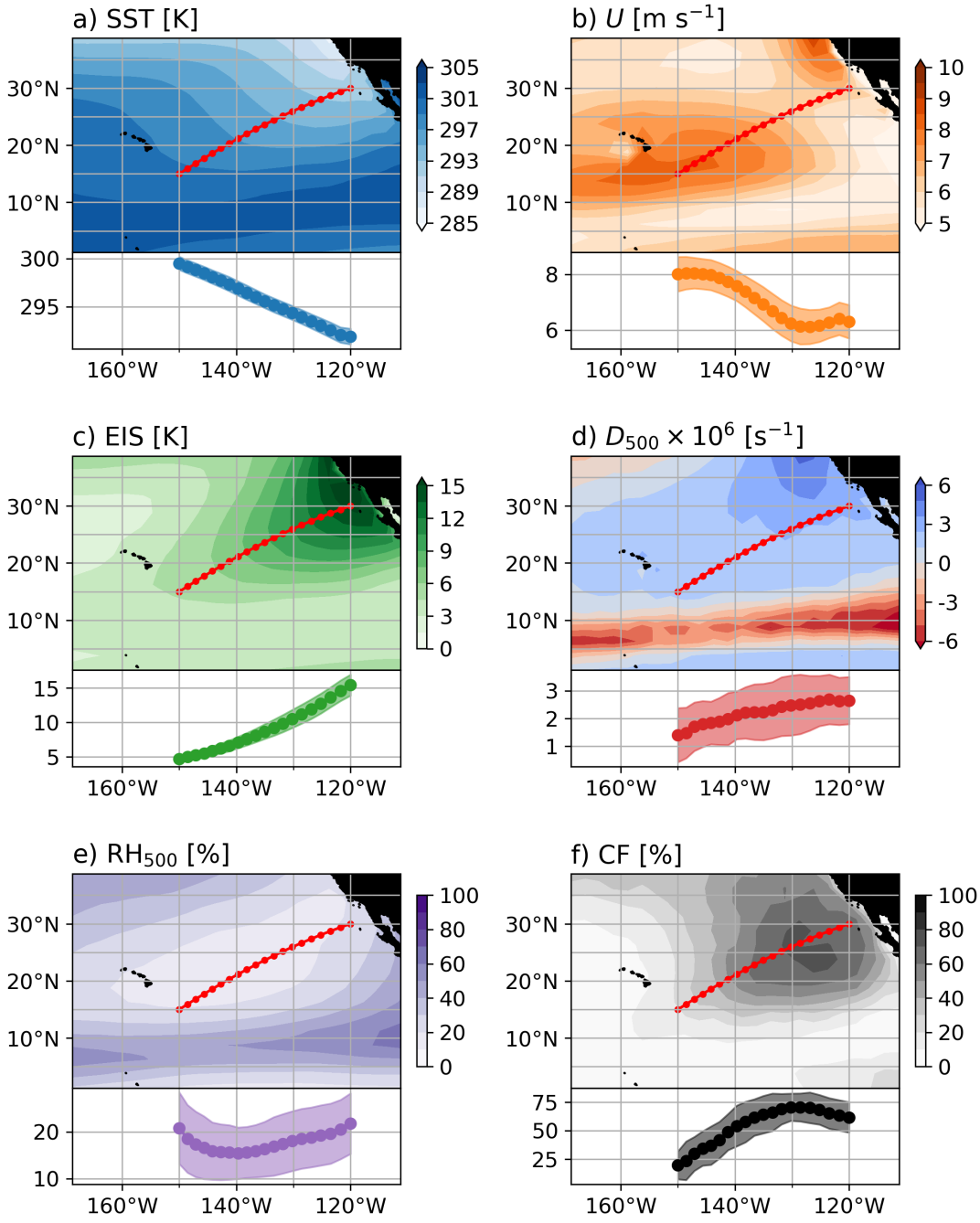

Figure 1.4: Boundary conditions from reanalysis in JJA for the North East Pacific (NEP) SCT region. Shown are: (a) SST, (b) surface wind speed, (c) estimated inversion strength, (d) large-scale horizontal divergence, (e) above-cloud relative humidity, and (f) cloud fraction. The transect is shown in the red line. Mean and standard deviations from the JJA climatology (2007-2016) are plotted in the insets below each map.

climatological cloudiness, but it does not provide realistic predictions of individual trajectories.

Idealized linear response to perturbations

The bulk model solution is dependent on all boundary conditions, or CCFs, though to some more strongly than to others. Figure 1.5 shows the steady-state results of cloud fraction and in-cloud liquid water path (LWP_{cld}) predicted by the bulk model for a variety of conditions. Each subplot shows perturbations of just one boundary condition while the rest remain fixed; included are the five meteorological boundary conditions from Figure 1.4 and CO_2. Perturbations are applied to two idealized states: a high-cloud fraction stratocumulus (Sc) state (solid lines), and a low-cloud fraction cumulus (Cu) state (dotted lines). The two regimes are distinguished by the references values of SST (290 vs. 295 K) and inversion strength (IS) (12 vs. 6 K), shown by filled and unfilled circles in Figure 1.5, respectively. The goal of this figure is to demonstrate the sensitivity of the model to perturbations of each boundary condition *within* regimes, not exploring transitions between the regimes.

For perturbations about the stratocumulus state (solid lines), cloud fraction is relatively fixed at the maximum value (80%), except at the warmest SSTs when cloud fraction starts to drop off (Fig. 1.5a). By designation of the regimes, the cloud fraction is of course larger in the Sc than Cu case. Additionally, the in-cloud liquid water path (LWP_{cld}) is larger in the Cu regime, because the clouds are deeper; while the all-sky liquid water paths tend to be smaller because the cloud cover is much lower. The response of LWP_{cld} is positive for SST, wind speed, above-cloud humidity, and inversion strength and negative for subsidence and CO_2. While the boundary layer remains in the coupled state, higher SSTs and stronger winds lead to greater LHFs which increase cloud moisture (Fig. 1.5a,b); a more humid free-troposphere and stronger inversion reduce entrainment drying and increase LWP_{cld} (Fig. 1.5e,c). On the other hand, stronger subsidence shoals the boundary layer and reduces cloud thickness and LWP_{cld} (Fig. 1.5d), and increased CO_2 decreases cloud-top cooling and reduces LWP_{cld} (Fig. 1.5f). However, higher SSTs and hence stronger LHFs also increase decoupling and ultimately lead to reduced CF, which is seen in Fig. 1.5a; hence increasing SST has opposite sign effects on CF and LWP_{cld}.

For perturbations about the cumulus state (dotted lines), cloud fraction is pinned to its minimum value (10%). The sign of the LWP_{cld} response to each CCF is the same, though the magnitude varies compared to the perturbations around the stratocumulus

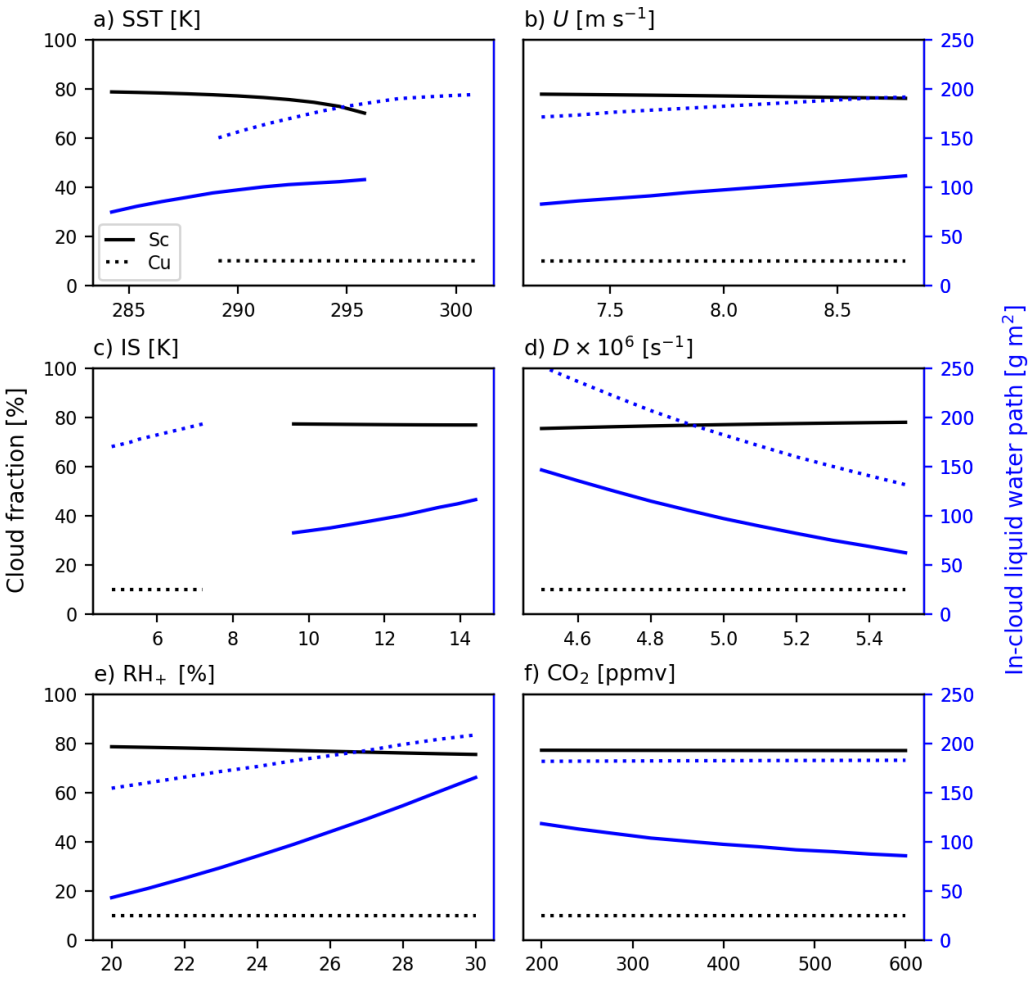

Figure 1.5: CF and $\mathrm{LWP_{cld}}$ when varying individual boundary condition parameters around some reference values typical of stratocumulus conditions (solid lines) and cumulus state (dotted lines). Reference values are indicated by filled and unfilled circles for Sc and Cu states, respectively. Boundary conditions varied are: (a) SST, (b) surface wind speed U, (c) inversion strength (IS, the actual inversion prescribed in the bulk model), (d) large-scale horizontal divergence D, (e) above-cloud relative humidity $\mathrm{RH_+}$, and (f) $\mathrm{CO_2}$ alone (no surface warming or water vapor feedbacks).

state. Most notable are the nonlinear responses (evident by the different slopes of the solid and dotted lines) to above-cloud humidity (Fig. 1.5e) and $\mathrm{CO_2}$ (Fig. 1.5f). The $\mathrm{LWP_{cld}}$ response from the Cu state is weaker than from the Sc state, and the response to $\mathrm{CO_2}$ is nearly nonexistent here. The sensitivity of Cu to subsidence is slightly stronger compared to Sc (Fig. 1.5d).

Stratocumulus-cumulus transition across North East Pacific

To evaluate the bulk model, we predict the cloud fraction given the observed large-scale conditions and compare it to the observed cloud fraction across the NEP SCT transect. The result is shown in Figure 1.6a. We predict the cloud cover in two ways: 1) by forcing the bulk model to steady-state with the climatological mean boundary conditions over the observed 10-year period (pink dashed line, single simulation), and 2) by forcing the bulk model to steady-state with 100 randomly chosen days from the same period (pink solid line, average of 100 simulations). Because the cloudiness of the boundary layer is a nonlinear process, and the bulk model exhibits strongly nonlinear behavior, the cloud fraction predicted from the monthly mean boundary conditions is different from the mean of the cloud fraction predicted from daily conditions.

The nonlinearity in the bulk model from the strong positive feedback between cloud cover and cloud-top radiative cooling results in sharp transitions day to day. Over long-time averages, this results in a smooth curve. However, when the bulk model is forced with the mean of the reanalysis-derived boundary conditions, a sharp transition is predicted.

Further, we investigate which CCFs most strongly control the transition by varying only one at a time in the simulations (Figure 1.6b). We observe that SST alone is sufficient to create a SCT, but the other CCFs are not. The other factors do contribute and create variability in cloud thickness and decoupling strength, but each in itself is insufficient to induce a full transition to a low cloud fraction, Cu-like, state.

Moving beyond our analysis of a one-dimensional transect, we compare the observed cloud fraction to the predicted cloud fraction in the entire NEP region. Figure 1.7 compares the observed cloud fraction to that predicted by the bulk model. The bulk model cloud fraction is the mean predicted value from the model averaged over approximately 100 randomly chosen days from the 10-year CASCCAD record. A total of 200 individual days were randomly selected, but since the bulk model was only applied in places with mean daily subsidence, the number of days included in the average varies by location (from 74 to 181).

Extending the analysis of the response of the cloud to perturbations from idealized mean states (Figure 1.5), Figure 1.8 shows the dependence of all-sky liquid water path (LWP) on each boundary condition for observed states across the NEP region. In the steady-state, both the cloud fraction (CF) and in-cloud liquid water path (LWP_{cld}) respond to perturbations in boundary conditions. LWP combines changes

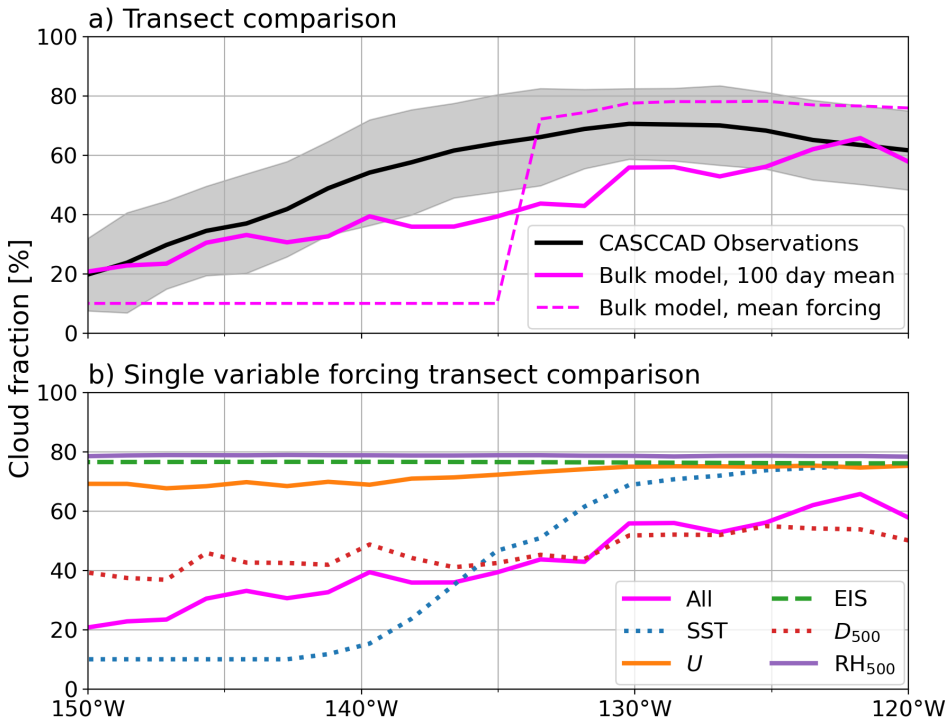

Figure 1.6: Cloud fraction along North East Pacific (NEP) stratocumulus-cumulus transect. (a) Mean JJA climatology (2007-2016) and standard deviation from CASCCAD observations (black), mean of bulk model forced by ERA5 boundary conditions from 100 randomly chosen days from the subsidence-only reanalysis record over the same time period (pink, solid), and bulk model prediction forced by climatological boundary conditions (pink, dashed). (b) Cloud fraction predicted by bulk model with single-variable forcing, again averaged over 100 randomly chosen days: SST (blue), U (orange), EIS (green), D (red), and RH_+ (purple); all variable forcing duplicated for comparison (pink). Only variations in SSTs alone produce a transition along the transect, through other factors also contribute to the total.

in CF and $\mathrm{LWP}_{\mathrm{cld}}$. The goal of this analysis is to illustrate how the sensitivity to changes in the various boundary conditions depends on the mean state from which we are perturbing.

Changes in LWP are shown normalized by the observed year-to-year variability for each boundary condition parameter (shown in Fig. 1.4), except for CO_2 where changes are shown relative to a $\sigma_{x_i} = 100$ ppmv perturbation. Specifically, the difference in steady-state LWP for a forcing of $x_i \pm \sigma_{x_i}/2$ is plotted for each factor x_i, where σ_{x_i} is the year-to-year variability during JJA in the 10-year record (2006-2017). This normalization is important to put the magnitude of perturbations of each boundary condition into context; for example, a 5 K change in SST is not

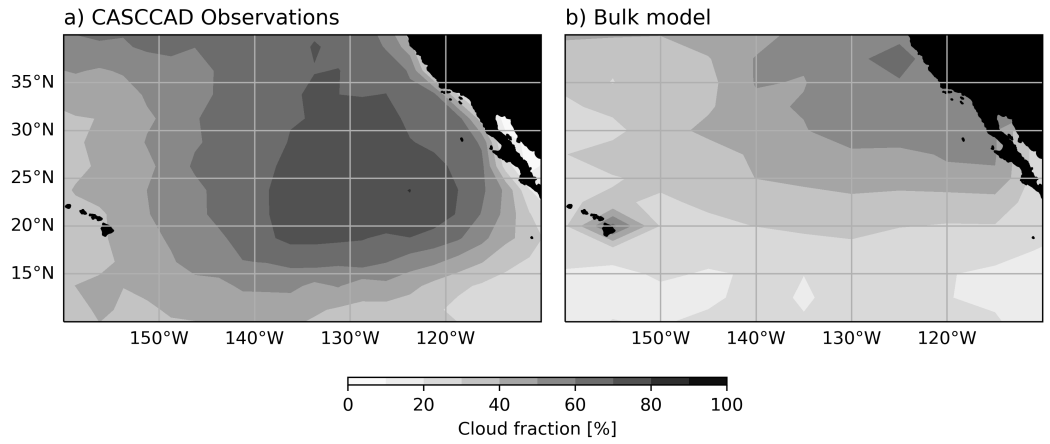

Figure 1.7: (a) Observed and (b) predicted cloud fraction climatology across the North East Pacific region during JJA. Prediction from bulk model is the average over approximately 100 randomly chosen days from the 10-year period 2006-2017. For each day, the bulk model is driven with climatological boundary conditions of SST, U, EIS, D_{500}, and RH_{500} from ERA5 reanalysis and run to steady-state. The resulting cloud fraction is averaged to produce this mean climatology plot.

easily comparable to a 10% change in above-cloud relative humidity. Because the normalization is based on the temporal variability of each boundary condition parameter, not the spatial variability, the results do not correspond directly to the sensitivities along the transect shown in Figure 1.6b.

In general, the results agree very well with Figure 1.5. The all-sky LWP is mostly reflecting $\mathrm{LWP}_{\mathrm{cld}}$ changes, except at the edges of the region where transitions between cloud states may occur. We saw from the perturbation analysis before that LWP is most sensitive to changes in subsidence and above-cloud humidity (Figure 1.5). Stronger subsidence thins the boundary layer and reduces LWP, while a more humid free-troposphere suppresses entrainment drying and increases LWP. Sensitivity to SST, EIS, and CO_2 is quite weak, but positive for SST and EIS and negative for CO_2, agreeing with Fig. 1.5. The sensitivity of all-sky LWP to surface wind speeds has the most complex spatial structure. In the center of the stratocumulus region, there is almost no sensitivity to wind speed, but toward the edges, stronger wind speeds result in more LWP due to increase LHF, until the LHF becomes too large and results in decoupling, which then dramatically reduces all-sky LWP (seen by sharp transition from red to blue colors at the edges).

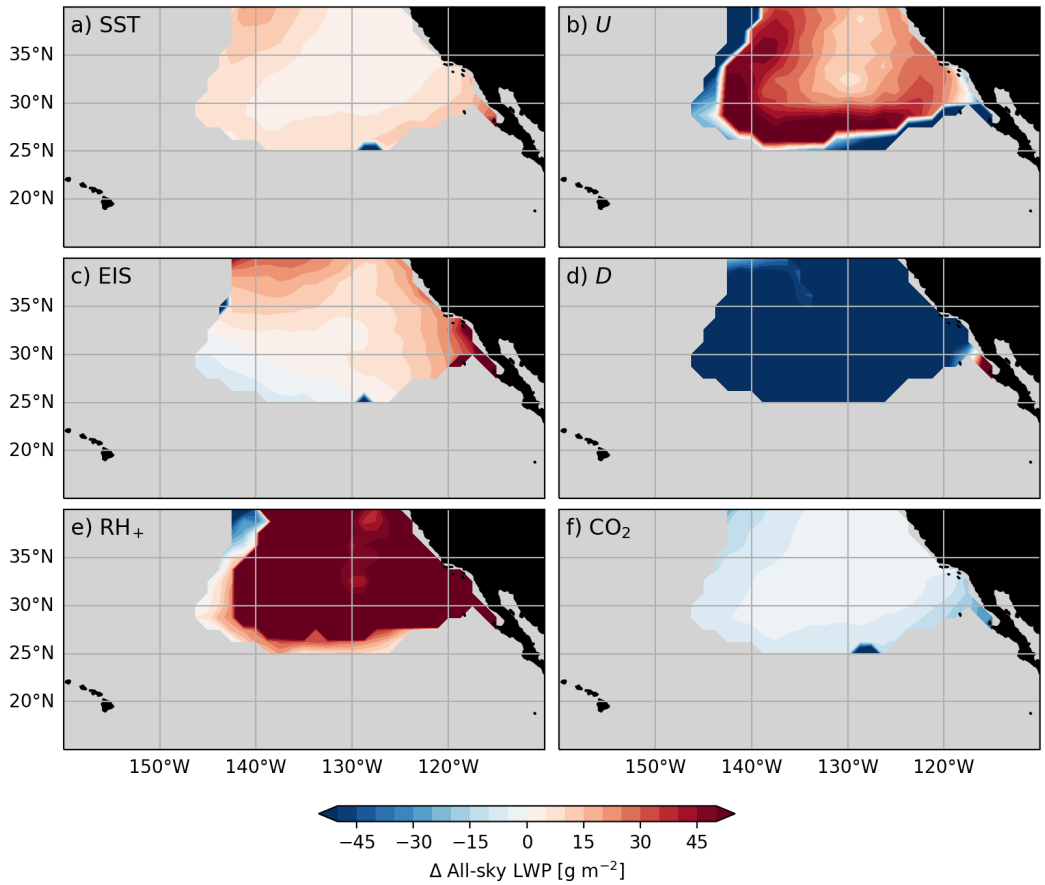

Figure 1.8: Change in all-sky LWP given a normalized perturbation of each CCF at each location across the NEP region (in JJA). Regions with mean CF < 0.5 are shaded in grey. The sensitivities to each CCF vary in space depending on the initial state of the cloud, highlighting the nonlinear response. LWP increases with SST and above-cloud humidity everywhere, decreases with subsidence and CO_2 everywhere, while the sign of response to surface wind speed and EIS varies in space.

1.5 Discussion

Our bulk model is able to capture key features of the stratocumulus-cumulus transition (SCT) and highlights the key mechanisms that drive the breakup of stratocumulus clouds along these westward transects. However, the model makes many assumptions that cannot represent the full complexity of the atmospheric boundary layer. Here we present a short discussion of some key limitations and imperfections of this model, some of which may be interesting avenues of future research.

First, the model has a limited representation of the effect of decoupling on the vertical structure of the boundary layer. In the derivation in Section 1.2, we introduce our bulk model in the more general form, not as a mixed-layer model, highlighting the

flexibility of this approach to include more nuanced representations of the vertical structure. However, in the end we did make the well-mixed assumption in how we specified the form of the surface fluxes. And we included a somewhat artificial ventilation term, w_{vent}, which represents extra mixing by positively buoyant thermals that overshoot the inversion. Future work could look into extending this model by including a non-well-mixed vertical structure throughout, or only after decoupling, along the lines of what was done by Schalkwijk et al., 2013 or Salazar and Tziperman, 2023.

Second, this bulk model represents a single column of the atmosphere and neglects advection, or the Lagrangian history of the air parcels, which is known to be important (Sandu, Stevens, and Pincus, 2010). Previous work has found that temperature advection can be an important cloud controlling factor (e.g., Scott et al., 2020), but based on Figure 1.6, in the monthly-mean sense, we are able to reproduce the salient features of the observed SCT without this. Including temperature advection into the bulk model can be done trivially by including an additional source term on Equation 1.3b, and could be explored in future work.

Third, the bulk model assumes that cloud emissivity (in Equation 1.8) is independent of LWP. We explored making the emissivity dependent on LWP following Stephens, 1978 as

$$\epsilon_c = 1 - e^{-\text{LWP}/\text{LWP}_0},$$

where $\text{LWP}_0 = 7$ g m^{-2}. We chose not to use this option for this study as it proved not to be critical for the qualitative results, and it introduced an additional positive feedback in the system that made interpretations more difficult. As with most choices made while developing this model, the goal was a minimal representation of the important physics, while retaining as simple a model as possible.

In this vein, the fourth major limitation is the lack of temporal variability. The bulk model is used to make steady-state predictions, and given the timescales of the problem, the system takes $O(10$ days$)$ to equilibrate. However, the model neglects the diurnal cycle, synoptic variability, and seasonal variability when solving for these equilibrium solutions. Again, this is done to retain simplicity by keeping the boundary conditions fixed, but it could be relaxed in future work if desired.

1.6 Conclusions

Stratocumulus clouds are a radiatively important feature of Earth's climate because they contribute to shortwave reflectance without compensating greenhouse warming.

They appear in specific locations on Earth, predominantly over eastern subtropical ocean basins due to their sensitive dependence on large-scale meteorological factors (CCFs). These CCFs have been used many times previously as a basis for constraining stratocumulus response to climate change. However, these models rely only on linear, statistical correlations between CCFs and cloudiness. In this work we presented a nonlinear and physical, but still simple, bulk boundary layer model for low cloudiness.

Our model is similar to traditional mixed-layer models for stratocumulus-topped boundary layers, but we extended it to include a prognostic equation for cloud fraction. Cloud fraction in our model depends on the strength of boundary layer coupling as diagnosed by the decoupling parameter $\mathscr{D} = (\mathrm{LHF}/\rho\Delta R) \cdot ((z_i - z_b)/z_i)$. The decoupling idea is based on Bretherton and Wyant (1997) and Chung and Teixeira (2012). We included a simple representation of radiative transfer to explicitly link the cloud-top radiative cooling to concentrations of greenhouse gases (CO_2 and H_2O) in the overlying free-troposphere. We showed how our bulk model is sensitive to perturbations in various large-scale environmental conditions, CCFs and CO_2. We evaluated our bulk model by comparing predictions of cloud fraction to observations from the CALIPSO and CloudSat satellites across the North East Pacific stratocumulus-to-cumulus transition transect.

In some ways this model is overly simple, neglecting some important physical processes, and it should not be viewed as a parameterization. However, because this model is able to capture important features of the SCT, it is useful as a conceptual tool. In a companion paper, we elaborate further on the mechanisms governing SCTs in this model and use it to explore exotic climates with very high CO_2 concentration (Singer and Schneider, 2023).

Acknowledgements. CES acknowledges support from NSF Graduate Research Fellowship under Grant No. DGE-1745301. This research was additionally supported by the generosity of Eric and Wendy Schmidt by recommendation of the Schmidt Futures program and by Charles Trimble. We thank Zhaoyi Shen for many helpful discussions in early stages of this project.

Data availability statement. The bulk model, along with examples reproducing all figures in this paper and documentation, is available on Github (`https://github.com/claresinger/MixedLayerModel.jl`).

1.7 Appendix A: Subsetting daily reanalysis data

On long time scales, e.g., over monthly means, the North East Pacific (NEP) is a region of subsidence (see Fig. 1.4d). However, on daily timescales, there can be net upward motion in any location. The bulk model assumes there is subsidence, and from the equation of mass conservation (1.3a), the model will not reach steady state if D is negative. Therefore, when forcing the bulk model with boundary conditions from reanalysis observations, we only want to choose observations on days with subsidence.

There are two logical ways to subset the data to exclude observations of $D < 0$. They are both shown in Figure 1.9. 1) We can exclude only the locations of upward motion on certain days (black dotted). The downside to this approach is that it will result in unequal numbers of observations at different spatial locations. Or, 2) we can exclude all locations on days with any upward motion along the whole transect (red). The downside to this approach is that it more severely filters the data, and we are left with fewer total observations.

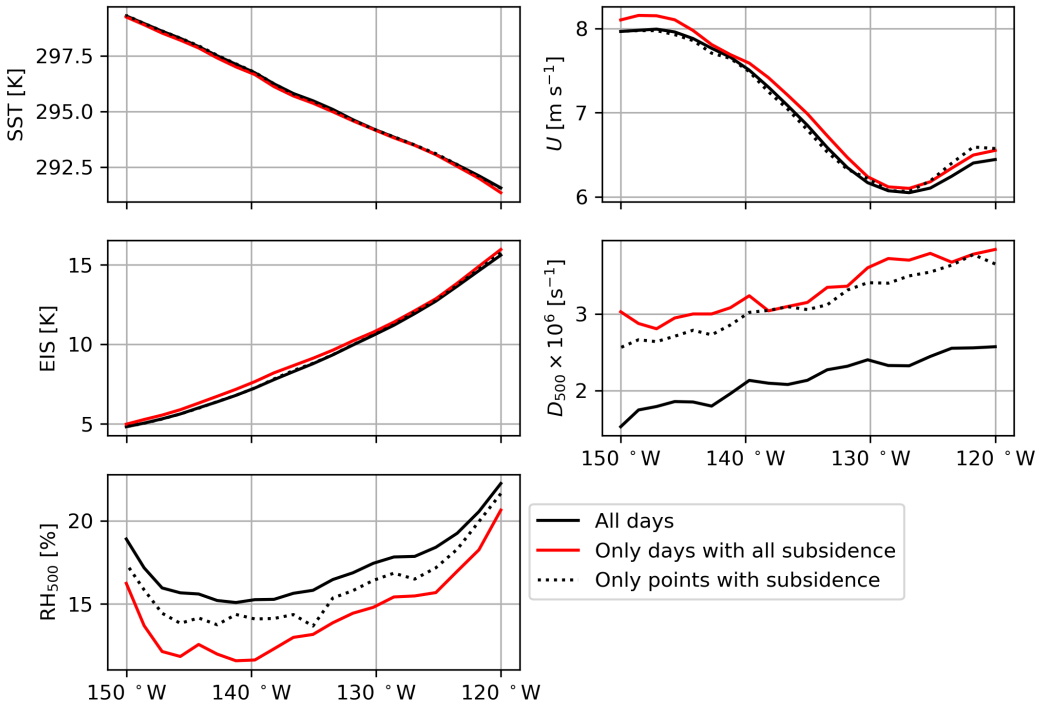

Figure 1.9: NEP transect of CCFs – sea surface temperature (SST), surface wind speed (U), estimated inversion strength (EIS), 500 hPa horizontal divergence (D_{500}), and 500 hPa relative humidity (RH_{500}) – showing all days in JJA 2007–2016 (black solid), only days with subsidence along the entire transect (red solid), and only points with local subsidence (black dotted).

However, we can see that both of these approaches have similar mean transect profiles. The transects for all quantities except horizontal divergence (D_{500}) are similar to the unfiltered data with all days (black solid). For simplicity, to keep the number of total observations at each spatial point equal, and because we retain enough data to reconstruct the climatological picture, we choose to keep only days where there is subsidence everywhere along the transect (red).

References

[1] C. E. Singer and T. Schneider. "CO_2-driven stratocumulus cloud breakup in a bulk boundary layer model". In: *J. Climate* (2023). In revision.

[2] R. Wood. "Stratocumulus Clouds". In: *Mon. Weather Rev.* 140.8 (2012), pp. 2373–2423. DOI: 10.1175/MWR-D-11-00121.1.

[3] G. Cesana et al. "The Cumulus And Stratocumulus CloudSat-CALIPSO Dataset (CASCCAD)". In: *Earth System Science Data* 11.4 (2019), pp. 1745–1764. DOI: 10.5194/essd-11-1745-2019.

[4] D. A. Randall et al. "Outlook for research on subtropical marine stratification clouds". In: *Bull. Amer. Meteor. Soc.* 65 (1984), pp. 1290–1301.

[5] T. Schneider et al. "Possible climate transitions from breakup of stratocumulus decks under greenhouse warming". In: *Nat. Geosci.* 12.3 (2019), pp. 163–167. DOI: 10.1038/s41561-019-0310-1.

[6] S. A. Klein, D. L. Hartmann, et al. "The Seasonal Cycle of Low Stratiform Clouds". In: *J. Climate* 6.8 (1993), pp. 1587–1606. DOI: 10.1175/1520-0442(1993)006<1587:TSCOLS>2.0.CO;2.

[7] Y. Zhang et al. "Low-Cloud Fraction, Lower-Tropospheric Stability, and Large-Scale Divergence". In: *J. Climate* 22.18 (2009), pp. 4827–4844. DOI: 10.1175/2009JCLI2891.1.

[8] R. Eastman et al. "Variations in Cloud Cover and Cloud Types over the Ocean from Surface Observations, 1954–2008". In: *J. Climate* 24 (2011), pp. 5914–5934. DOI: 10.1175/2011JCLI3972.1.

[9] D. Chung and J. Teixeira. "A Simple Model for Stratocumulus to Shallow Cumulus Cloud Transitions". In: *J. Climate* 25.7 (2012), pp. 2547–2554. DOI: 10.1175/JCLI-D-11-00105.1.

[10] T. A. Myers and J. R. Norris. "Observational Evidence That Enhanced Subsidence Reduces Subtropical Marine Boundary Layer Cloudiness". In: *J. Climate* 26.19 (2013), pp. 7507–7524. DOI: 10.1175/JCLI-D-12-00736.1.

[11] C. S. Bretherton and P. N. Blossey. "Low cloud reduction in a greenhouse-warmed climate: Results from Lagrangian LES of a subtropical marine

cloudiness transition". In: *J. Adv. Model. Earth Syst.* 6.1 (2014), pp. 91–114. DOI: 10.1002/2013MS000250.

[12] D. K. Lilly. "Models of cloud-topped mixed layers under a strong inversion". In: *Quart. J. Roy. Meteor. Soc.* 94 (1968), pp. 292–309. DOI: 10.1002/qj.49709440106.

[13] C. S. Bretherton and M. C. Wyant. "Moisture Transport, Lower-Tropospheric Stability, and Decoupling of Cloud-Topped Boundary Layers". In: *J. Atmos. Sci.* 54 (1997), pp. 148–167. DOI: 10.1175/1520-0469(1997)054<0148:MTLTSA>2.0.CO;2.

[14] B. Stevens. "Bulk boundary-layer concepts for simplified models of tropical dynamics". In: *Theor. Comput. Fluid Dyn.* 20.5-6 (2006), pp. 279–304. DOI: 10.1007/s00162-006-0032-z.

[15] G. Bellon and O. Geoffroy. "How finely do we need to represent the stratocumulus radiative effect?" In: *Quart. J. Roy. Meteor. Soc.* 142.699 (2016), pp. 2347–2358. DOI: 10.1002/qj.2828.

[16] B. Stevens and J.-l. Brenguier. "Cloud-controlling Factors: Low Clouds". In: *Clouds Perturbed Clim. Syst. Their Relatsh. to Energy Balanc. Atmos. Dyn. Precip.* 1802. 2009.

[17] A. P. Siebesma et al. "Cloud-controlling Factors". In: *Clouds Perturbed Climate Syst. Their Relatsh. to Energy Balance Atmos. Dyn. Precip.* MIT Press, 2009, pp. 269–290.

[18] C. S. Bretherton. "Insights into low-latitude cloud feedbacks from high-resolution models". In: *Philos. Trans. R. Soc. A Math. Phys. Eng. Sci.* 373.2054 (2015). DOI: 10.1098/rsta.2014.0415.

[19] X. Qu et al. "On the Spread of Changes in Marine Low Cloud Cover in Climate Model Simulations of the 21st Century". In: *Climate Dynamics* 42.9-10 (2014), pp. 2603–2626. DOI: 10.1007/s00382-013-1945-z.

[20] S. A. Klein, A. Hall, et al. "Low-Cloud Feedbacks from Cloud-Controlling Factors: A Review". In: *Surveys in Geophysics* 38 (2017), pp. 1307–1329. DOI: 10.1007/978-3-319-77273-8_7.

[21] M. C. Wyant et al. "Numerical Simulations and a Conceptual Model of the Stratocumulus to Trade Cumulus Transition". In: *J. Atmos. Sci.* 54.1 (1997), pp. 168–192. DOI: 10.1175/1520-0469(1997)054<0168:NSAACM>2.0.CO;2.

[22] S. R. de Roode et al. "Large-Eddy Simulations of EUCLIPSE–GASS Lagrangian Stratocumulus-to-Cumulus Transitions: Mean State, Turbulence, and Decoupling". In: *J. Atmos. Sci.* 73.6 (2016), pp. 2485–2508. DOI: 10.1175/JAS-D-15-0215.1.

[23] J. McGibbon and C. S. Bretherton. "Skill of ship-following large-eddy simulations in reproducing MAGIC observations across the northeast Pacific stratocumulus to cumulus transition region". In: *J. Adv. Model. Earth Syst.* 9.2 (2017), pp. 810–831. DOI: 10.1002/2017MS000924.

[24] T. Yamaguchi et al. "Stratocumulus to Cumulus Transition by Drizzle". In: *J. Adv. Model. Earth Syst.* 9.6 (2017), pp. 2333–2349. DOI: 10.1002/2017MS001104.

[25] R. A. J. Neggers et al. "Single-Column Model Simulations of Subtropical Marine Boundary-Layer Cloud Transitions Under Weakening Inversions". In: *J. Adv. Model. Earth Syst.* 9 (2017), pp. 2385–2412. DOI: 10.1002/2017MS001064.

[26] I. Sandu, B. Stevens, and R. Pincus. "On the transitions in marine boundary layer cloudiness". In: *Atmos. Chem. Phys.* 10 (2010), pp. 2377–2391. DOI: 10.5194/acp-10-2377-2010.

[27] B. A. Albrecht et al. "The Atlantic Stratocumulus Transition Experiment—ASTEX". In: *Bull. Amer. Meteor. Soc.* 76.6 (1995), pp. 889–904. DOI: 10.1175/1520-0477(1995)076<0889:TASTE>2.0.CO;2.

[28] J. Teixeira et al. "Tropical and Subtropical Cloud Transitions in Weather and Climate Prediction Models: The GCSS/WGNE Pacific Cross-Section Intercomparison (GPCI)". In: *J. Climate* 24.20 (2011), pp. 5223–5256. DOI: 10.1175/2011JCLI3672.1.

[29] P. Kalmus et al. "Observational Boundary Layer Energy and Water Budgets of the Stratocumulus-to-Cumulus Transition". In: *J. Climate* 27.24 (2014), pp. 9155–9170. DOI: 10.1175/JCLI-D-14-00242.1.

[30] C. S. Bretherton, I. L. McCoy, et al. "Cloud, Aerosol, and Boundary Layer Structure across the Northeast Pacific Stratocumulus–Cumulus Transition as Observed during CSET". In: *Mon. Weather Rev.* 147.6 (2019), pp. 2083–2103. DOI: 10.1175/MWR-D-18-0281.1.

[31] A. Lauer et al. "The Impact of Global Warming on Marine Boundary Layer Clouds over the Eastern Pacific—A Regional Model Study". In: *J. Climate* 23 (2010), pp. 5844–5863. DOI: 10.1175/2010JCLI3666.1.

[32] D. M. Romps. "The dry-entropy budget of a moist atmosphere". In: *J. Atmos. Sci.* 65 (2008), pp. 3779–3799.

[33] D. A. Randall. "Conditional Instability of the First Kind Upside-Down". In: *J. Atmos. Sci.* 37.1 (1980), pp. 125–130. DOI: 10.1175/1520-0469(1980)037<0125:CIOTFK>2.0.CO;2.

[34] Y. Zheng, Y. Zhu, et al. "Climatology of Cloud-Top Radiative Cooling in Marine Shallow Clouds". In: *Geophys. Res. Lett.* 48.19 (2021), e2021GL094676. DOI: 10.1029/2021GL094676.

[35] J. Uchida et al. “The Sensitivity of Stratocumulus-Capped Mixed Layers to Cloud Droplet Concentration: Do LES and Mixed-Layer Models Agree?” In: *Atmos. Chem. Phys.* 10 (2010), pp. 4097–4109. DOI: 10.5194/acp-10-4097-2010.

[36] B. Stevens, G. Vali, et al. “Pockets of Open Cells and Drizzle in Marine Stratocumulus”. In: *Bull. Amer. Meteor. Soc.* (2005), pp. 51–57. DOI: 10.1175/BAMS-86-1-51.

[37] O. Geoffroy et al. “Relationship between Drizzle Rate, Liquid Water Path and Droplet Concentration at the Scale of a Stratocumulus Cloud System”. In: *Atmos. Chem. Phys.* 8 (2008), pp. 4641–4654. DOI: 10.5194/acp-8-4641-2008.

[38] P. Prabhakaran et al. “Journal of the Atmospheric Sciences”. In: (Mar. 29, 2023). DOI: 10.1175/JAS-D-22-0207.1.

[39] J. L. Petters et al. “Radiative-Dynamical Feedbacks in Low Liquid Water Path Stratiform Clouds”. In: *J. Atmos. Sci.* 69.5 (2012), pp. 1498–1512. DOI: 10.1175/JAS-D-11-0169.1.

[40] Y. Zheng, D. Rosenfeld, et al. “Satellite-Based Estimation of Cloud Top Radiative Cooling Rate for Marine Stratocumulus”. In: *Geophys. Res. Lett.* 46.8 (2019), pp. 4485–4494. DOI: 10.1029/2019GL082094.

[41] H. Hersbach et al. “The ERA5 global reanalysis”. In: *Quart. J. of the Roy. Meteor. Soc.* 146.730 (2020), pp. 1999–2049. DOI: https://doi.org/10.1002/qj.3803.

[42] R. Wood and C. S. Bretherton. “On the Relationship between Stratiform Low Cloud Cover and Lower-Tropospheric Stability”. In: *J. Climate* 19.24 (2006), pp. 6425–6432. DOI: 10.1175/JCLI3988.1.

[43] Z. Tan et al. “Large-eddy simulation of subtropical cloud-topped boundary layers: 1. A forcing framework with closed surface energy balance”. In: *J. Adv. Model. Earth Syst.* 8.4 (2016), pp. 1565–1585. DOI: 10.1002/2016MS000655.

[44] C. S. Bretherton, J. Uchida, et al. “Slow Manifolds and Multiple Equilibria in Stratocumulus-Capped Boundary Layers”. In: *J. Adv. Model. Earth Syst.* 2 (2010), pp. 1–20. DOI: 10.3894/JAMES.2010.2.14.

[45] C. R. Jones et al. “Fast stratocumulus time scale in mixed layer model and large eddy simulation”. In: *J. Adv. Model. Earth Syst.* 6.1 (2014), pp. 206–222. DOI: 10.1002/2013MS000289.

[46] I. Sandu and B. Stevens. “On the factors modulating the stratocumulus to cumulus transitions”. In: *J. Atmos. Sci.* 68.9 (2011), pp. 1865–1881. DOI: 10.1175/2011JAS3614.1.

[47] P. N. Blossey et al. “Marine low cloud sensitivity to an idealized climate change: The CGILS LES intercomparison”. In: *J. Adv. Model. Earth Syst.* 5.2 (2013), pp. 234–258. DOI: 10.1002/jame.20025.

[48] J. Schalkwijk et al. “Simple Solutions to Steady-State Cumulus Regimes in the Convective Boundary Layer”. In: *J. Atmos. Sci.* 70.11 (2013), pp. 3656–3672. DOI: 10.1175/jas-d-12-0312.1.

[49] A. M. Salazar and E. Tziperman. “Exploring Subtropical Stratocumulus Multiple Equilibria Using a Mixed-Layer Model”. In: *J. Climate* (2023), pp. 1–38. DOI: 10.1175/JCLI-D-22-0528.1.

[50] R. C. Scott et al. “Observed Sensitivity of Low-Cloud Radiative Effects to Meteorological Perturbations over the Global Oceans”. In: *J. Climate* 33.18 (2020), pp. 7717–7734. DOI: 10.1175/JCLI-D-19-1028.1.

[51] G. L. Stephens. “Radiation Profiles in Extended Water Clouds. II: Parameterization Schemes”. In: *J. Atmos. Sci.* 35.11 (1978), pp. 2123–2132. DOI: 10.1175/1520-0469(1978)035<2123:RPIEWC>2.0.CO;2.

Chapter 2

CO_2-DRIVEN STRATOCUMULUS CLOUD BREAKUP IN A BULK BOUNDARY LAYER MODEL

[1] C. E. Singer and T. Schneider. "CO_2-driven stratocumulus cloud breakup in a bulk boundary layer model". In: *Journal of Climate* (2023). In revision.

Abstract. Stratocumulus clouds cover 20% of subtropical oceans and strongly cool the Earth by reflecting incoming shortwave radiation. Because of their small dynamical scales and their sensitivity to changing meteorological conditions, the response of stratocumulus clouds to climate change is one of the leading uncertainties in climate modeling. Recent work has made significant progress constraining this feedback using high-resolution large eddy simulations (LES) and satellite observations. Here we provide complementary constraints from a theoretical perspective, using a bulk boundary layer model to calculate the response of stratocumulus clouds to increasing CO_2. We extend the bulk model presented in Singer and Schneider, 2023 by coupling it to a slab ocean to allow for feedbacks between cloud cover and surface warming and use ensemble Kalman inversion to calibrate model parameters. We conduct climate change experiments, forcing the bulk model with increasing CO_2, and compare the cloud response to results from LES in Schneider, Kaul, et al., 2019. Past a critical CO_2 value, the cloud layer decouples from the surface, the clouds break up, and cloud fraction decreases to a shallow cumulus-like state. Cloud fraction shows hysteresis behavior, where the system remains in a low cloud fraction state even as CO_2 is decreased significantly past the breakup threshold. The hysteresis behavior is robust, but the critical CO_2 value is sensitive to parameters and assumptions of the bulk model. We show that surface warming and water vapor feedback are two important aspects of the breakup; without them, the critical CO_2 threshold for breakup is much larger.

Significance statement. The purpose of this study, and the companion paper Singer and Schneider, 2023, is to develop a simple model to explain mechanisms controlling stratocumulus-cumulus transitions. In this second paper, we describe the extended bulk model coupled to a slab ocean that is forced only with a prescribed

CO_2 concentration. We calibrate key parameters of this model based on high-resolution simulations. The simple model, like the high-resolution simulations, shows that stratocumulus clouds break up at very high CO_2 concentrations and that the boundary layer exhibits hysteresis, remaining in a cumulus-like state until CO_2 is reduced significantly past the breakup threshold. We conclude by showing a series of mechanism-denial experiments that highlight the importance of surface temperature and water vapor feedbacks on the stratocumulus breakup.

2.1 Introduction

The response of stratocumulus clouds to increasing CO_2 has been an outstanding question in the field for the past several decades; it remains one of the largest contributors to uncertainty in warming and equilibrium climate sensitivity (ECS) (Sherwood et al., 2020; Zelinka et al., 2022). Global climate models (GCMs) exhibit a large spread in predictions of changes in low clouds, which percolates into a large spread in ECS. GCMs struggle to model low clouds, in particular stratocumulus, because of the small dynamical scales relevant for cloud-scale turbulence ($\sim$ 10 m) compared to the coarse resolution of models ($\sim$ 100 km) (Schneider, Teixeira, et al., 2017). The result is inaccurate simulation of the present-day climate, with radiative biases on the order of 10 W m^{-2} and more in subtropical stratocumulus regions, and a large spread of model responses to CO_2 perturbations (Nam et al., 2012; Brient, Roehrig, et al., 2019). Increasing resolution of models, even into convection-permitting regimes, can only help improve predictions of stratocumulus clouds to a certain extent (Lee et al., 2022).

To get around this shortcoming of GCMs, some recent studies have taken the approach of using satellites to measure co-variability between clouds and meteorology to observationally constrain cloud feedbacks and ECS (e.g., Brient and Schneider, 2016; Cesana and Del Genio, 2021; Myers et al., 2021; Ceppi and Nowack, 2021). Other studies, such as the CGILS project (M. Zhang et al., 2012; Blossey et al., 2013; Bretherton, Blossey, et al., 2013) and Tan et al. (2017), have explored low-cloud responses to CO_2 in large-eddy simulations (LES), where the most energetic small-scale motions are directly resolved. Bretherton (2015) summarizes results from such LES studies.

However, given the shortcomings of GCMs in simulating clouds, and the difficulty of interpreting LES without a clear and quantitative conceptual framework, advances in theory are necessary for progress on the cloud problem. In this paper, we

present a bulk boundary layer model for stratocumulus-topped boundary layers that includes a very simple radiative transfer scheme and is coupled to a slab ocean surface. We build on previous work by Deardorff, 1980, Lilly (1968), Bretherton and Wyant (1997), Stevens (2006), Dal Gesso et al. (2014), and de Roode et al. (2014). Our purpose is to provide a conceptual bridge between LES and GCMs and a framework for understanding and interpreting both. Specifically, we build a conceptual model to interpret the LES of Schneider, Kaul, et al., 2019. This model is similar to, but developed independently from, Salazar and Tziperman, 2023, and comes to similar conclusions, which supports the robustness of both results. Schneider, Kaul, et al., 2019 simulated a stratocumulus-topped boundary layer under different CO_2 conditions. They concluded that eventually, at very high CO_2, the increased infrared opacity of the free troposphere will shut down the critical cloud-top longwave cooling that drives the sustaining overturning circulation in the boundary layer, leading to stratocumulus cloud breakup. The primary mechanism for the stratocumulus breakup is the "direct effect" of CO_2 on the cloud-top radiative cooling. CO_2 was only recently recognized as an important driver of this direct reduction in cloud-top longwave cooling (Bretherton, Blossey, et al., 2013; Tan et al., 2017; Schneider, Kaul, et al., 2019; Schneider, Kaul, et al., 2020), but other radiative drivers such as high clouds and water vapor, which both alter the downwelling longwave radiation at cloud-top have been noted previously (Christensen et al., 2013). The direct effect of CO_2 on cloudiness has also been recently noted as an important mechanism to explain the observed TOA energy imbalance in the historical satellite record (Raghuraman et al., 2021). Our bulk model provides a conceptual basis for quantitative analysis and interpretation of this direct effect, among other factors affecting cloud cover.

The paper is organized as follows: Section 2.2 describes the bulk boundary layer model coupled to a slab ocean. Section 2.3 discusses calibration of bulk model parameters. Section 2.4 discusses stratocumulus breakup mechanisms, presenting results from the bulk model and comparing them to LES from Schneider, Kaul, et al., 2019, and explores sensitivities of the results to the calibrated parameters. Section 2.5 summarizes the conclusions.

2.2 Bulk boundary layer model with interactive SSTs

Singer and Schneider, 2023 describe the derivation of the bulk boundary layer model with prescribed boundary conditions. The following section describes a further extension. First we couple the atmospheric boundary layer to a slab ocean

by adding a prognostic equation for sea surface temperature (SST), and we add an analytical radiative transfer formulation. Then we embed the stratocumulus "box" into a two-column framework (Pierrehumbert, 1995; Miller, 1997) and parameterize the coupling between the subtropics and tropics.

Specifying top and bottom thermodynamic boundary conditions

With a goal to study stratocumulus cloud feedbacks, we need to build a model where the boundary conditions are consistently solved for based on a prescribed value for CO_2. We couple the atmospheric boundary layer to a slab ocean through a surface energy balance to consistently represent surface warming due to increasing CO_2 and to include the positive feedback between cloud thinning and surface warming.

The bulk model is then defined by the following system of five coupled ordinary differential equations:

$$\frac{dz_i}{dt} = w_e - Dz_i + w_{\text{vent}}, \tag{2.1a}$$

$$\frac{ds}{dt} = \frac{1}{z_i}\left[V(s_0 - s) + w_e(s_+ - s) - \Delta R\right] + s_{\text{exp}}, \tag{2.1b}$$

$$\frac{dq_t}{dt} = \frac{1}{z_i}\left[V(q_{t,0} - q_t) + w_e(q_{t,+} - q_t)\right] + q_{\text{exp}}, \tag{2.1c}$$

$$\frac{d\text{CF}}{dt} = \frac{\text{CF}_d - \text{CF}}{\tau_{\text{CF}}}, \tag{2.1d}$$

$$C\frac{d\text{SST}}{dt} = \text{SW}_{\text{net}} - \text{LW}_{\text{net}} - \text{LHF} - \text{SHF} - \text{OHU}. \tag{2.1e}$$

Equations (2.1a) – (2.1d) are the same as Singer and Schneider, 2023. The cloud-top radiative cooling, ΔR, is a function of the CO_2 and H_2O above the cloud (Singer and Schneider (2023), their Eqs. 8 and 9). The cloud fraction is parameterized as a relaxation to the diagnosed state CF_d which depends on the decoupling parameter $\mathscr{D} = (\text{LHF}/\rho\Delta R) \cdot ((z_i - z_b)/z_i)$:

$$\text{CF}_d = \text{CF}_{\text{max}} - \frac{\text{CF}_{\text{max}} - \text{CF}_{\text{min}}}{1 + \frac{1}{9}\exp(-m(\mathscr{D} - \mathscr{D}_c))}.$$

For this application, to be consistent with the Schneider, Kaul, et al. (2019) LES, we set $\text{CF}_{\text{max}} = 100\%$ and $\text{CF}_{\text{min}} = 20\%$.

Equation (2.1e) is the standard surface energy budget equation for SST. On the left-hand side, $C = \rho_w c_w H_w$ is a heat capacity per unit area, where ρ_w and c_w are the density and specific heat capacity of water and H_w is the depth of the slab ocean. The value of H_w is arbitrary: it affects the equilibration time, but not the equilibrium

results, which are the object of interest here. We choose $H_w = 1$ m, which gives an equilibration timescale of $\tau_{\mathrm{SST}} \approx 50$ days. On the right-hand side are the source terms from shortwave and longwave radiation, latent and sensible heat fluxes, and ocean heat uptake (OHU), respectively.

Closed surface energy budget: parameterized surface radiation

The net surface shortwave radiation is simplified to be linear in cloud fraction,

$$\mathrm{SW}_{\mathrm{net}} = a_{\mathrm{SW}} + b_{\mathrm{SW}}(\mathrm{CF}_{\mathrm{max}} - \mathrm{CF}), \tag{2.2}$$

with coefficients $a_{\mathrm{SW}} = 120$ W m^{-2} and $b_{\mathrm{SW}} = 140$ W m^{-2}. The net longwave radiation is taken to be a constant $\mathrm{LW}_{\mathrm{net}} = -30$ W m^{-2}, consistent with LES results from (Schneider, Kaul, et al., 2019).

The ocean heat uptake (OHU) is determined as the residual from a steady-state simulation with 400 ppmv CO_2 in which the SST is fixed to 290 K. The OHU is kept fixed across the range of CO_2 concentrations considered (OHU = -12 W m^{-2}).

Large-scale circulations: parameterized above-cloud temperature

Reduction of subtropical cloud cover will increase TOA radiative imbalance locally and lead to energy export to the rest of the globe. Some of this energy will be exported to the tropics, warm the tropical free troposphere, and because of weak temperature gradients, feed back and warm the subtropical free-troposphere above the cloud layer (Figure 2.1). Simplifying the procedure of Schneider, Kaul, et al., 2019, we parameterize the effect of subtropical albedo changes on above-cloud temperatures by considering how both the direct warming from CO_2 as well as the additional warming from increased subtropical energy export change the strength of the temperature inversion in the subtropics. The inversion strength (IS) is modeled as

$$\Delta_+ T = a_T + b_T \log_2\left(\frac{\mathrm{CO}_2}{400}\right) - c_T(\mathrm{CF}_{\mathrm{max}} - \mathrm{CF}), \tag{2.3}$$

where $a_T = 8$ K is the IS in the base climate, $b_T = 1.5$ K describes the relative warming in the tropics versus subtropics per doubling of CO_2, and $c_T = 10$ K measures the strength of the energy export into the tropics from subtropical cloud thinning.

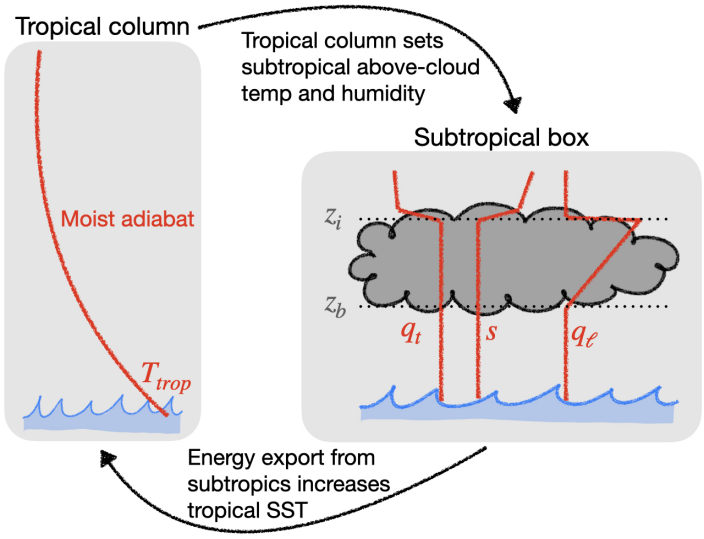

Figure 2.1: Schematic of coupling between subtropical domain and tropical domain. Energy is assumed to be exported from the tropics globally when cloud cover decreases; this warms the tropics, and in turn, warms the overlying free-troposphere above the subtropical clouds. This is parameterized by Equation 2.3.

2.3 Ensemble Kalman inversion for parameter calibration

The bulk model as described in Section 2.2 includes three principal free parameters: The surface exchange velocity $V \equiv C_d U$, the coefficient of ventilation mixing strength α_{vent} (Singer and Schneider (2023), their Eq. 7), and the surface SW cloud radiative feedback strength b_{SW}. Other free parameters, such as a_{SW} and a_T, are not included in the calibration, and are instead determined independently from the Schneider, Kaul, et al. (2019) LES results. We calibrate the parameters to minimize mismatch between the bulk model results and the LES from Schneider, Kaul, et al., 2019. The quantitative results of the model are sensitive to these exact parameter values; this is explored in detail in at the end of Section 2.4.

The values of these parameters have physical meaning and are constrained (by the assumed priors) to take on physically reasonable values based on external constraints (such as positivity or order-of-magnitude estimates for maximum ventilation velocities) or previous measurements/studies (order of magnitude for surface exchange velocity). Our parameter priors are Gaussian (Table 2.1).

We use Ensemble Kalman inversion (EKI), a flexible gradient-free optimization method (Schillings and Stuart, 2017), to calibrate these parameters. EKI is an adaptation for parameter estimation of the ensemble Kalman filter, which has been widely

Parameter [units]	**Prior**	**Optimal value**
V [m s^{-1}]	$\mathcal{N}(8,2)\times10^{-3}$	7.9×10^{-3}
α_{vent} [m s^{-1}]	$\mathcal{N}(1.2,0.3)\times10^{-3}$	1.69×10^{-3}
b_{SW} [W m^{-2}]	$\mathcal{N}(150,40)$	140

Table 2.1: Table of parameters calibrated, their assumed prior ranges, and the optimal value to which the Ensemble Kalman inversion converges.

used in the atmospheric sciences for state estimation (Houtekamer and F. Zhang, 2016). EKI is robust to noisy data or models with sharp or discontinuous gradients (Lopez-Gomez et al., 2022). We use the `EnsembleKalmanProcesses.jl` Julia implementation of EKI (Dunbar et al., 2022).

Our data in the loss function are domain-mean, time-mean SSTs and LHFs from LES in statistical steady states across a range of CO_2 concentrations both with increasing and decreasing CO_2 from (Schneider, Kaul, et al., 2019). The data covariance matrix is taken to be diagonal, assigning 10% error to each data point, with error reduced to 0.5% for the two endpoints of the up- and down-steps at 1600 ppmv and 200 ppmv, respectively, to put 20x greater weight and ensure the optimization converges on a solution that retains the hysteresis behavior, even at the expense of possible better quantitative accuracy at intermediate CO_2 concentrations. Our loss function is the L_2-norm of the SST and LHF mismatch, both normalized by the mean and standard deviation across the LES simulations.

To calibrate the three parameters, we choose an ensemble size of 90 particles and iterate 15 times until convergence (Figure 2.2). One evaluation of the forward model consists of evaluating the steady-state result in the bulk model at 17 CO_2 levels, increasing from 200 ppmv to 1600 ppmv and then back down to 200 ppmv. With each successive iteration, the collection of particles collapses toward the

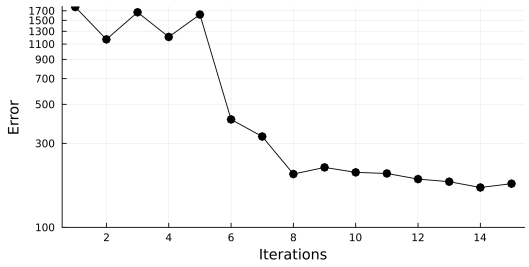

Figure 2.2: Error from EKI loss function for each iteration of the parameter optimization. As the particle ensemble collapses towards the optimal values the error decreases. Convergence happens after about 8 iterations.

optimal parameter values (Figure 2.3). The scatter plots show particles in each 2-dimensional space, and the histograms show the distribution of particles along each parameter dimension separately, with the initialized ensemble (sample from prior) in grey and the final ensemble in red.

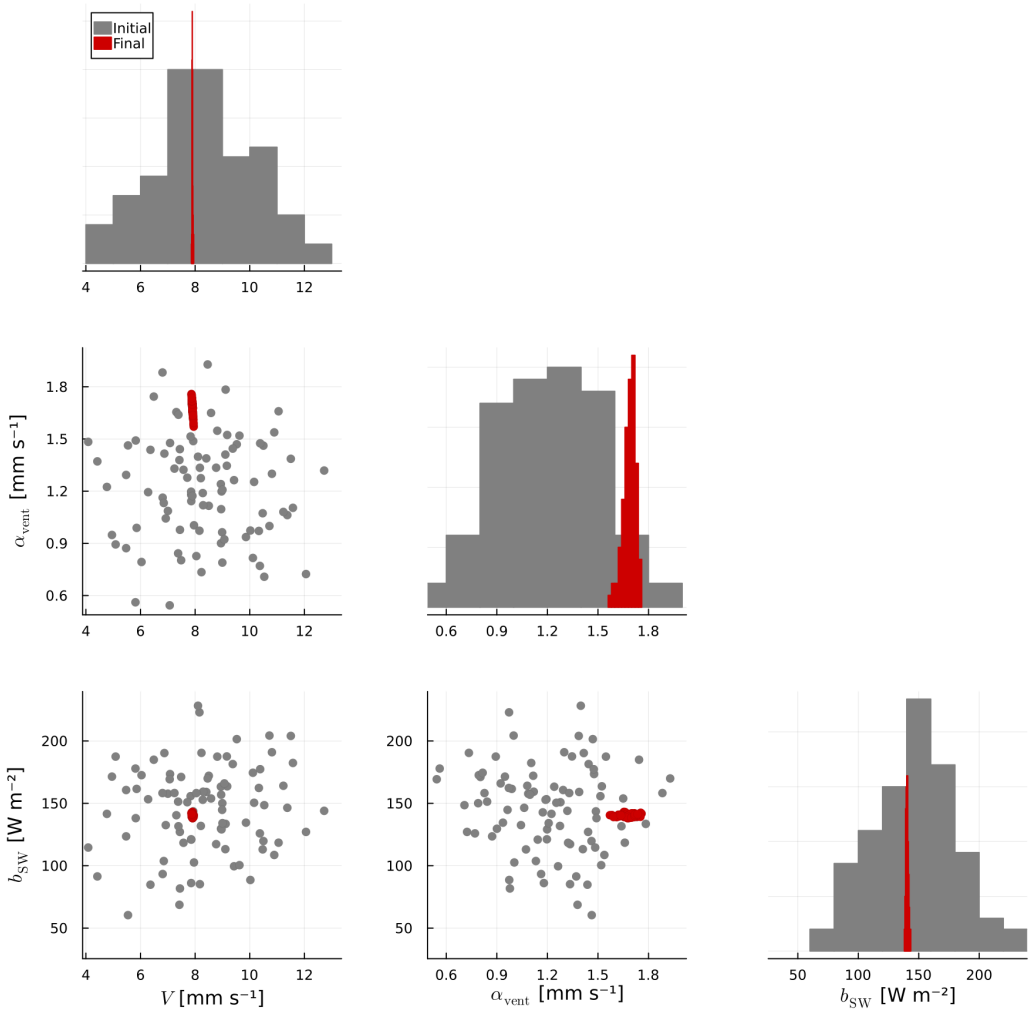

Figure 2.3: Plots of initialized (grey) and converged (red) particle ensembles. Scatter plots in the lower left of the figure show the distribution of particles in each 2-dimensional parameter space. Histograms on the diagonal show the distribution of particles in each parameter-dimension individually. Covariance between parameters is weak as indicated by the spread in red points mostly horizontal or vertical, not diagonal. The ventilation mixing strength parameter α_{vent} shows the largest variability in the final ensemble compared to the prior range.

The optimal parameter values (mean of all particles at final iteration) are given in Table 2.1. The predicted SSTs and LHFs from the bulk model using the optimal

calibrated parameters is shown compared to the LES results in Figure 2.4. Some particles in the final ensemble have clouds break up at values above or below 1300 ppmv (not shown). Similarly for the re-formation of stratocumulus at lower values of CO_2, some particles in the ensemble, despite having very similar parameter values, show clouds not reforming, while most show clouds reforming at 400 ppmv. This sensitivity to parameter choices is discussed further in Section 2.4.

2.4 Results

Stratocumulus breakup mechanisms

As was identified in the LES experiments from Schneider, Kaul, et al., 2019, at very high concentrations of CO_2, the stratocumulus clouds become unstable and break up into cumulus-like state with low cloud fraction. In our simplified bulk model, we reproduce this behavior (Figure 2.4).

We conduct the same experiment as presented in Schneider, Kaul, et al., 2019. The bulk model is sequentially run to equilibrium at various CO_2 concentrations, starting from 200 ppmv, increasing to 1800 ppmv, and then decreasing back to 200 ppmv. Each sequential simulation is initialized from the steady-state condition at the previous CO_2 level. In Figure 2.4, the red points indicate simulations where CO_2 was increased from the previous steady-state solution, and blue points indicate simulations where CO_2 was decreased. Following the red points, we see that the cloud deck remains stable up until 1200 ppmv CO_2, but when CO_2 is increased to 1300 ppmv, the stratocumulus deck dissipates (Figure 2.4d). Coincident is a rapid warming of sea surface temperatures (Figure 2.4b). As CO_2 is decreased from the maximum value simulated (1800 ppmv), the blue points indicate that the clouds remain in a cumulus-like state until CO_2 is lowered back to 400 ppmv. This strong hysteresis behavior is seen in both the LES and the bulk model.

To examine the cloud breakup and hysteresis further, we present two mechanism-denial experiments. First, shown in Figure 2.5, is a test for the influence of surface warming on cloud breakup. This experiment follows the same protocol of sequentially increasing and then decreasing CO_2 concentration, but this time with SST and IS fixed to their 400 ppmv baseline values of 290 K and 8 K, respectively. In this experiment, the clouds do not break up even at CO_2 concentrations of 8000 ppmv. The radiative cooling continues to decrease, but so does the LHF as the boundary layer shallows and warms. This keeps the clouds relatively stable, with $\mathscr{D}$ only increasing up to around 0.4 at these very high CO_2 concentrations.

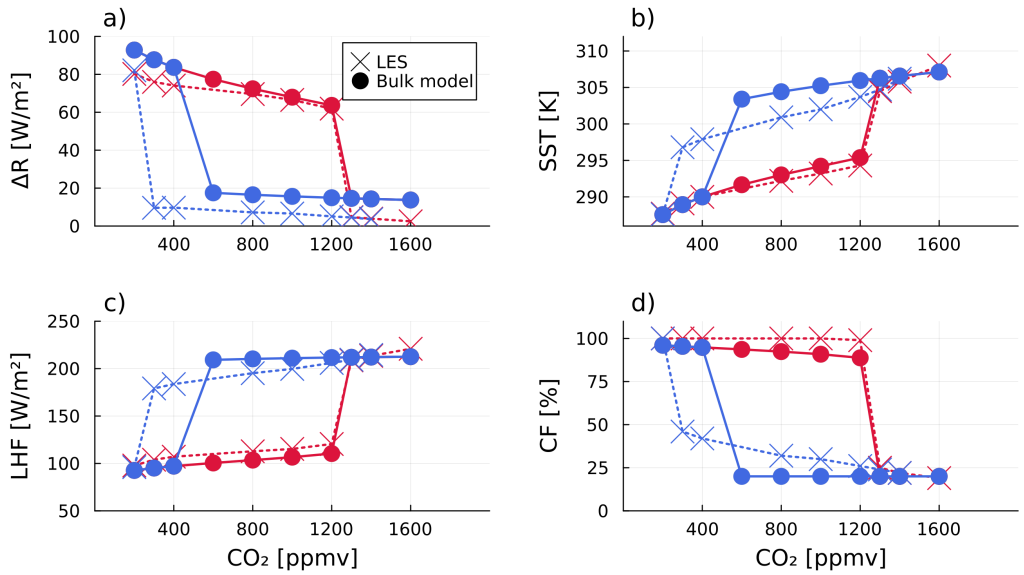

Figure 2.4: Steady-state solutions from the bulk model and LES for an experiment of sequentially increasing and then decreasing CO_2 concentrations. Simulations initialized from a lower CO_2 steady-state condition (increasing CO_2) are shown in red, and those initialized from a higher CO_2 state (decreasing) are shown in blue. Panels show (a) the cloud-top radiative cooling, ΔR, (b) sea surface temperature, SST, (c) surface latent heat flux, LHF, and (d) cloud fraction, CF. Results from the bulk model are shown in circles (solid lines) with results from the Schneider, Kaul, et al., 2019 LES shown in crosses (dotted lines).

The second experiment, shown in Figure 2.6, tests the impact of the water vapor feedback on cloud breakup. This experiment is the same as the original, but now with the above-cloud water vapor concentrations seen by the radiation fixed at 2 g kg^{-1}. The above-cloud water vapor entrained into the cloud is still interactive and increases with SST. Because water vapor is a greenhouse gas and absorbs outgoing longwave radiation from the cloud tops, keeping it fixed mutes the effect of increasing CO_2 and stabilizes the stratocumulus deck. Ultimately, the increasing CO_2 concentrations alone damp the cloud-top radiative cooling sufficiently to produce cloud breakup, but not until a concentration of 2800 ppmv is reached; this is nearly twice as much CO_2 as is required when the water vapor feedback is enabled. The hysteresis behavior is still seen, though the stratocumulus clouds do not reform until below 200 ppmv CO_2. The effect of radiative water vapor feedback thus is to shift the breakup threshold and broaden the hysteresis loop.

The mechanisms discussed are summarized in the schematic in Figure 2.7. In our setup, CO_2 is the external control on the system and all other changes in large-

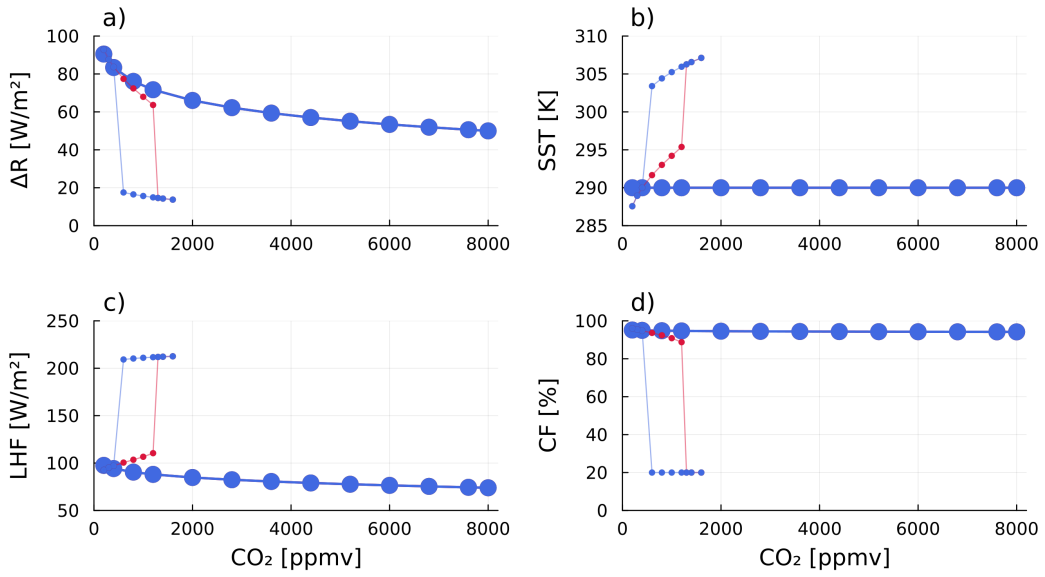

Figure 2.5: Same as Figure 2.4, but with SST and inversion strength (IS) fixed at the 400 ppmv baseline values of 290 K and 8 K. Results from the fixed SST/IS experiment shown in large circles, with results from the slab ocean setup (Figure 2.4) shown by the small circles and thin lines. In the fixed SST/IS case, the CO_2 is varied from 200 ppmv to 8000 ppmv. Due to the stabilizing effect of fixing the SST, despite the suppression of cloud-top radiative cooling via the direct effect of CO_2, the stratocumulus clouds remain stable up to the extreme value of 8000 ppmv.

scale conditions are parameterized. When CO_2 is increased, it directly reduces the cloud-top radiative cooling, ΔR. Smaller ΔR means the boundary layer is in a more decoupled state ($\mathscr{D}$ is around 3.5 after cloud breakup, or about 10x larger than at 400 ppmv). The cloud fraction is parameterized as a function of decoupling, so this decreases cloud cover. The first positive feedback, inherent to the system, is that cloud-top cooling is proportional to cloud cover, $\Delta R = \mathrm{CF} \cdot f(\mathrm{CO_2}, \mathrm{H_2O})$ (Singer and Schneider, 2023, their Eq. 8). This feedback is why the breakup is so rapid in CO_2-space, as demonstrated, for example, in Figure 2.4 and along the stratocumulus-cumulus transition transect discussed in Singer and Schneider, 2023.

The two mechanism-denial experiments above show the importance of the SST feedback and the radiative water vapor feedback. First, as cloud cover decreases, the ocean surface is exposed to more sunlight and warms up. This increases SSTs and increases latent heat fluxes, which also contributes to stronger decoupling of the boundary layer. Second, as SSTs increase, the amount of water vapor in the free troposphere above the clouds also increases (water vapor feedback). Since

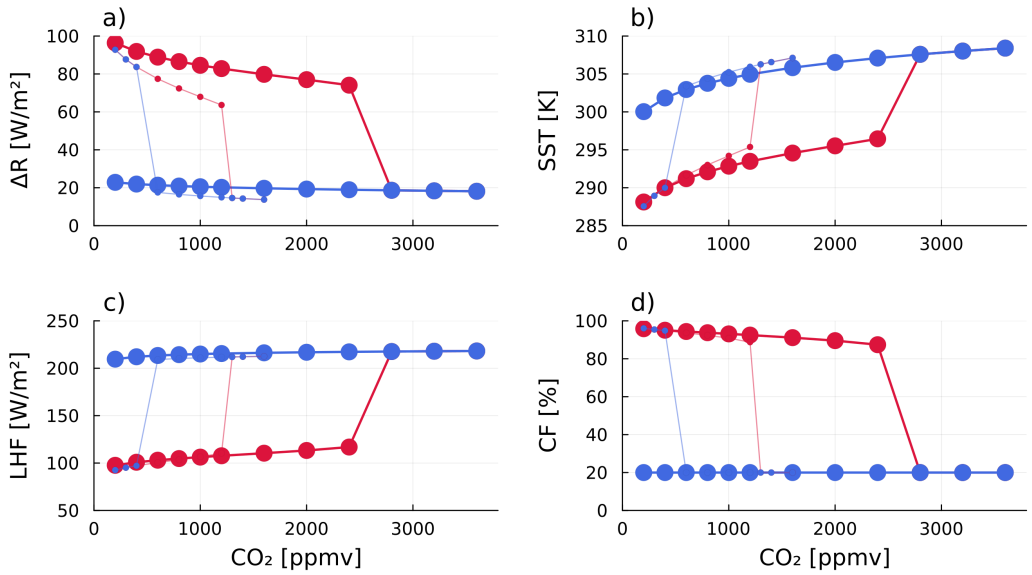

Figure 2.6: Same as Figure 2.4, but with above-cloud water vapor concentrations shown to the radiation fixed at 2 g kg^{-1}. Above-cloud water vapor seen in the entrainment mixing remains interactive and increases with warming. Results from the fixed water vapor experiment shown in large circles, with results from the interactive setup (Figure 2.4) shown by the small circles and thin lines. In the fixed water vapor case, the CO_2 is varied from 200 ppmv to 4000 ppmv. The critical CO_2 threshold for cloud breakup is at 2800 ppmv.

water vapor is a greenhouse gas, like CO_2, more water vapor inhibits cloud-top radiative cooling, which decreases cloud cover further. As we saw above, the SST coupling is crucial in this bulk model for exhibiting stratocumulus breakup at any CO_2 concentration below 8000 ppmv; the water vapor feedback also contributes strongly to the stratocumulus breakup, reducing the critical CO_2 threshold from 2800 ppmv to 1300 ppmv.

However, neither this bulk model nor the LES from Schneider, Kaul, et al., 2019 can give robust quantitative information about the exact value of this critical CO_2 breakup threshold. Both models are sensitive to various parameter values and choices about how to couple the single stratocumulus box with the rest of the globe—e.g., how large-scale circulations and atmospheric stability might change with CO_2—which is necessarily parameterized in these setups.

Sensitivity of CO_2 breakup threshold to model parameters

Figure 2.8 shows the critical CO_2 stratocumulus breakup threshold as a function of the three parameters calibrated with EKI. The critical CO_2 concentration is

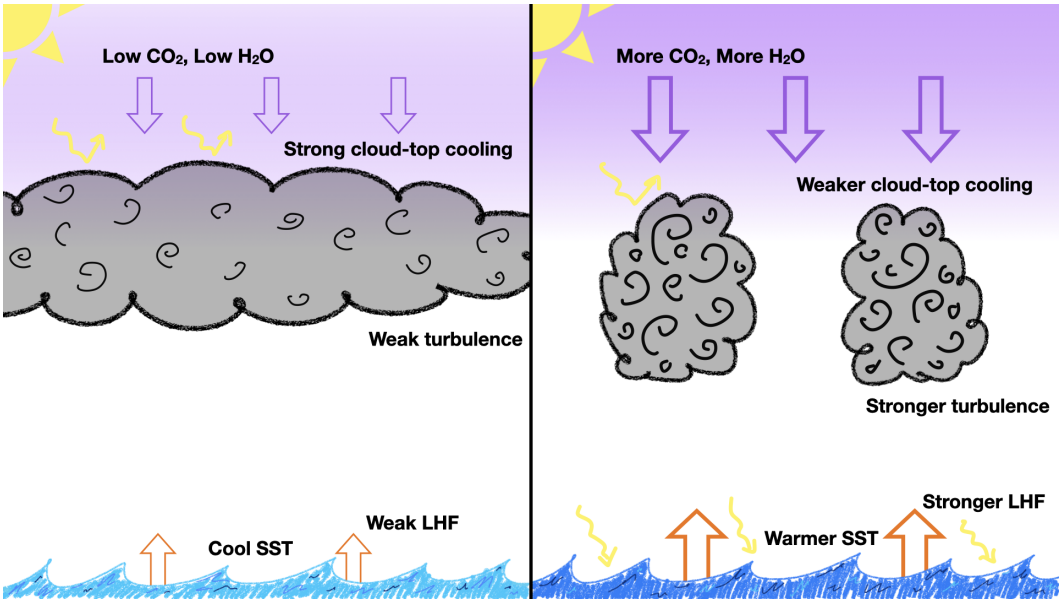

Figure 2.7: Sketch showing important physical processes and positive feedbacks that contribute to stratocumulus breakup mechanisms. (Left) Low CO_2 stratocumulus state. Low CO_2 results in less downwelling radiation at the cloud top and strong cloud-top cooling. SSTs are lower because the high cloud cover blocks incoming shortwave radiation from reaching the surface and results in weak LHF and weak in-cloud turbulence. The combination of strong cloud-top cooling and weak LHF both contribute to strong coupling ($\mathscr{D}$ small). (Right) High CO_2 cumulus state. More CO_2 creates more downwelling radiation at cloud-top and weaker cloud-top cooling. This results in stronger decoupling, which reduces cloud fraction. Less cloud cover means more sunlight can reach the surface and warm it. Higher SSTs mean stronger LHF, which results in stronger turbulence in the cloud layer and further enhances decoupling. Higher temperatures also result in more above-cloud moisture, which further increases downwelling longwave radiation at cloud-top and weakens cloud-top cooling. The SST and water vapor feedbacks both act as positive feedbacks on the system.

calculated as the lowest CO_2 concentration for which the steady-state cloud fraction is less than 50% in a simulation of increasing CO_2. With the optimal parameter configuration shown in earlier results, the critical CO_2 threshold is at 1350 ppmv. For all three calibrated parameters, increasing parameter values results in a smaller critical CO_2 concentration. The critical value for cloud breakup is most sensitive to the surface exchange velocity, V, changing from 1900 ppmv to 750 ppmv for an 7% increase in V. For a large surface exchange velocity, the surface fluxes are larger for a given SST, meaning LHF will become untenably large at a lower SST and lead to cloud breakup. The ventilation coefficient (α_{vent}) dictates how much extra

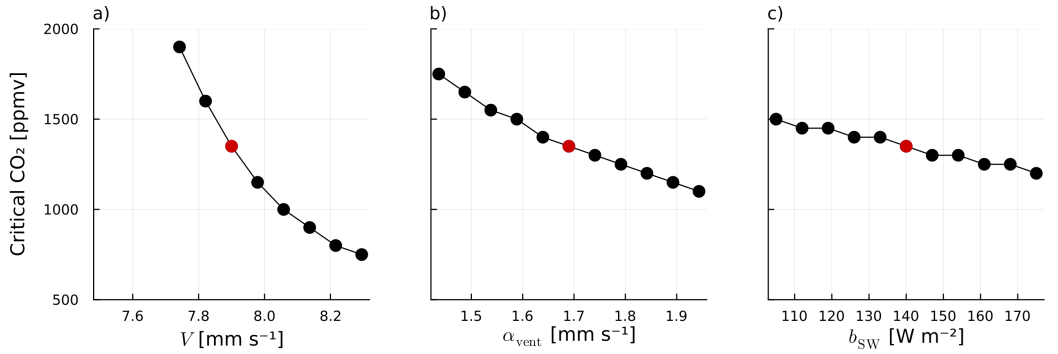

Figure 2.8: Critical CO_2 threshold for stratocumulus breakup given different values of calibrated parameters: (a) V surface exchange velocity, (b) α_{vent} entrainment ventilation mixing strength, and (c) b_{SW} shortwave cloud feedback strength. Optimal parameter values shown in red.

entrainment mixing results from cumulus updrafts in the decoupled state. As cloud fraction decreases and cumulus ventilation begins, stronger ventilation exacerbates decoupling by leading to clouds that occupy a smaller fraction of the boundary layer ($\mathscr{D} \propto (z_i - z_b)/z_i$). Therefore, stronger ventilation results in more rapid cloud breakup. Finally, the linearized surface shortwave cloud feedback is encoded in the b_{SW} term. When this radiation coefficient is larger, the surface heating resulting from cloud breakup is larger; hence, this also accelerates breakup and leads to a smaller critical CO_2 value.

Sensitivity of CO_2 breakup threshold to initial conditions

In addition to parameter sensitivity, the breakup threshold is also sensitive to the initial conditions. This sensitivity to initial conditions is manifest in the real world as spatial variability in the breakup threshold. Simply, some locations are closer to the decoupling threshold in the present climate state, and therefore will see stratocumulus cloud breakup at lower CO_2 concentrations than other regions.

Figure 2.9 shows the critical CO_2 concentration given different initial SST conditions at 400 ppmv CO_2 (only the SST initial condition is varied). The critical CO_2 concentration is calculated the same way as before. For this example, the initial condition SST ranges from 288 K to 294 K (the default is 290 K). For the coldest initial condition, where the boundary layer is in a more tightly coupled state at 400 ppmv, the critical CO_2 concentration is 2350 ppmv. While, for the warmest initial condition, the boundary layer is already decoupled at 400 ppmv.

We can extrapolate from Figure 2.9 to infer the cloud breakup behavior over an

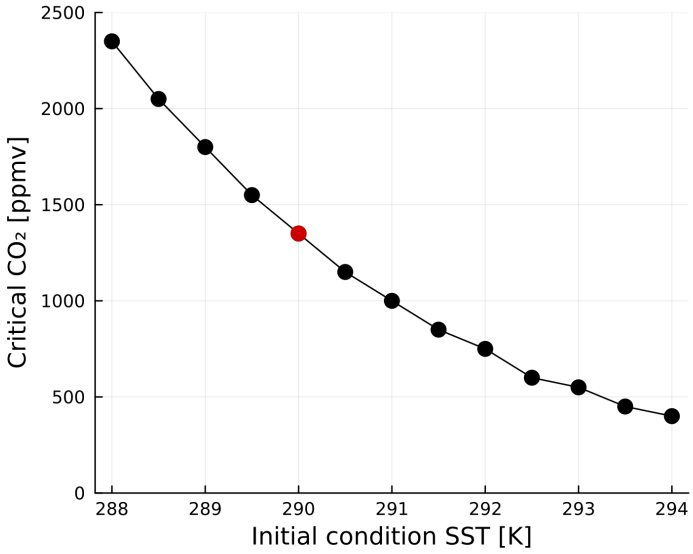

Figure 2.9: Critical CO_2 threshold for stratocumulus breakup given different initial conditions of SST (at 400 ppmv). The critical CO_2 concentration across the range of tested conditions varies from 400 ppmv to 2350 ppmv. Default initial condition SST (290 K) shown in red.

entire region with variable present-day SSTs. This is illustrated in Figure 2.10, which shows a map of contours of the critical CO_2 concentration in the North East Pacific stratocumulus region given observed values for the SST in the present climate as the 400 ppmv initial condition. The contours show the breakup threshold as a propagating front, where stratocumulus cloud decks retreat from their current spatial extent in eastern subtropical ocean basins to occupy smaller regions, more tightly confined to the coast where SSTs are coldest, until CO_2 concentrations are high enough to eliminate the clouds altogether. In a regional-mean sense, the breakup will be smooth, not sharp, because of the variability in initial conditions.

Figure 2.10 is a simplification of the full picture. Of course not just the SST varies spatially, also the climatological inversion strength, subsidence strength, surface wind speeds, and free-tropospheric relative humidity will factor into the critical CO_2 concentration. Furthermore, seasonal variability (and other timescales) will modulate and smooth this summer-time mean signal.

2.5 Conclusions

In this paper, we have highlighted the direct effect of CO_2 on stratocumulus clouds. These clouds, which are substantial contributors to the globally-averaged shortwave

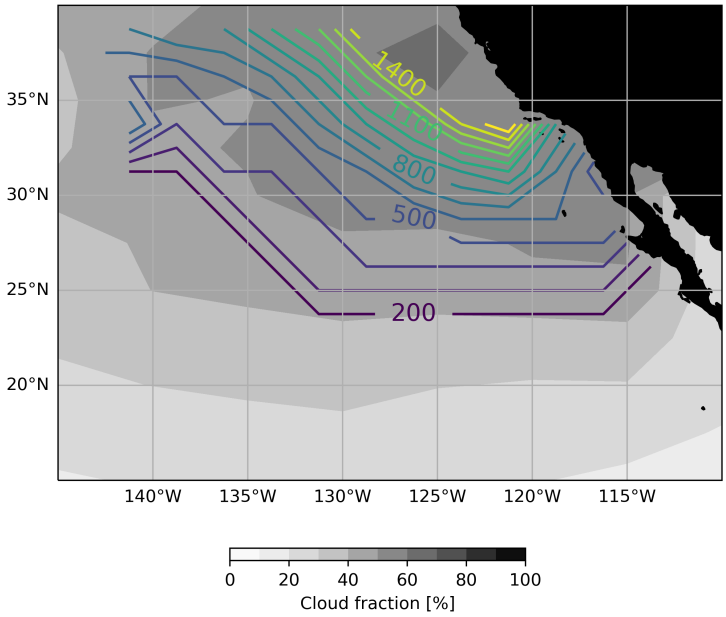

Figure 2.10: Colored contours of critical CO_2 threshold (in ppmv) for stratocumulus breakup over the North East Pacific stratocumulus region. Grey shading shows the climatological cloud fraction predicted by the bulk model (Figure 1.7b from Singer and Schneider, 2023).

reflectance, are dynamically driven by cloud-top longwave radiative cooling. The radiative cooling creates negatively buoyant air at the cloud top, which sinks towards the surface, generates a convective overturning circulation, and resupplies the cloud layer with moisture. CO_2 (or infrared absorbers more generally, including water vapor and higher-altitude clouds) above the boundary layer reduce this radiative cooling and, at high enough concentrations, can decouple this overturning circulation from the moisture supply at the surface. This ultimately leads to the breakup of the cloud layer.

We have explored this mechanism of stratocumulus breakup with a conceptual bulk boundary layer model. Our model is forced by an externally prescribed CO_2 concentration and parameterizes all feedbacks (local surface warming and remote warming of the free troposphere) to predict the boundary layer thermodynamic and cloud properties. We have calibrated unconstrained parameters of the model such that it realistically reproduces behavior seen in LES from Schneider, Kaul, et al., 2019. With the bulk model, we can easily explore the importance of the local surface warming feedback and the water vapor feedback, which is linked to the remote warming in the tropics that controls free-tropospheric temperatures

and water vapor concentrations. Because both local and remote surface warming, and hence water vapor concentrations in the free troposphere, increase with cloud cover reduction, there is strong hysteresis in the system: once the stratocumulus clouds break up, they will not reform again until CO_2 is lowered past the critical threshold at which they first broke up. The local surface warming will amplify the decoupling by increasing latent heat fluxes. And the remote surface warming and subsequent above-cloud water vapor increase will amplify decoupling by further reducing cloud-top cooling.

We have discussed the quantitative limitations of this model with regard to predicting the critical threshold of CO_2 for stratocumulus breakup. These limitations stem both from the simplicity of the representation of the subtropical cloud-topped boundary layer, as well as the simple representations of coupling between clouds and circulation. The threshold value is sensitive to parameter choices in our model, but the breakup and hysteresis behavior are robust and rooted in well understood physical principles.

The CO_2 direct effect, whereby cloud-top cooling is a mechanism for turbulence generation in the boundary layer, is included in some GCM parameterizations, but not in all (Qu et al., 2014). This neglect has implications for how GCMs respond to extreme CO_2 concentrations. These extreme concentrations are not relevant for 21st century climate change, but may be relevant for past climates; indeed, several studies suggest cloud feedbacks as a mechanism for enhanced warming in past climates (e.g., Zhu et al., 2019; Tierney et al., 2022). Furthermore, the direct effect of CO_2 on stratocumulus clouds introduces asymmetries and nonlinearities for deeper-time paleoclimate (Goldblatt et al., 2021) or future geoengineering scenarios (Schneider, Kaul, et al., 2020), where global cooling was, or could be, induced by solar dimming.

Acknowledgements. CES acknowledges support from NSF Graduate Research Fellowship under Grant No. DGE-1745301. This research was additionally supported by the generosity of Eric and Wendy Schmidt by recommendation of the Schmidt Futures program and by Charles Trimble. We thank Zhaoyi Shen for many helpful discussions in early stages of this project.

Data availability statement. The bulk model, along with examples reproducing all figures in this paper and documentation, is available on Github (`https://github.com/claresinger/MixedLayerModel.jl`).

References

[1] C. E. Singer and T. Schneider. "Stratocumulus-cumulus transition explained by bulk boundary layer theory". In: *J. Climate* (2023). In revision.

[2] T. Schneider, C. M. Kaul, et al. "Possible climate transitions from breakup of stratocumulus decks under greenhouse warming". In: *Nat. Geosci.* 12.3 (2019), pp. 163–167. DOI: 10.1038/s41561-019-0310-1.

[3] S. C. Sherwood et al. "An Assessment of Earth's Climate Sensitivity Using Multiple Lines of Evidence". In: *Rev. of Geophysics* 58.4 (2020), e2019RG000678. DOI: 10.1029/2019RG000678.

[4] M. D. Zelinka et al. "Evaluating Climate Models' Cloud Feedbacks Against Expert Judgment". In: *J. Geophys. Research: Atmospheres* 127.2 (2022), e2021JD035198. DOI: 10.1029/2021JD035198.

[5] T. Schneider, J. Teixeira, et al. "Climate goals and computing the future of clouds". In: *Nat. Climate Change opinion & comment* 7.1 (2017), pp. 3–5. DOI: 10.1038/nclimate3190.

[6] C. Nam et al. "The 'too few, too bright' tropical low-cloud problem in CMIP5 models". In: *Geophys. Res. Lett.* 39.21 (2012). DOI: 10.1029/2012GL053421.

[7] F. Brient, R. Roehrig, et al. "Evaluating Marine Stratocumulus Clouds in the CNRM-CM6-1 Model Using Short-Term Hindcasts". In: *J. Adv. Model. Earth Syst.* 11.1 (2019), pp. 127–148. DOI: 10.1029/2018MS001461.

[8] H.-H. Lee et al. "Resolving Away Stratocumulus Biases in Modern Global Climate Models". In: *Geophys. Res. Lett.* (2022). DOI: 10.1029/2022GL099422.

[9] F. Brient and T. Schneider. "Constraints on Climate Sensitivity from Space-Based Measurements of Low-Cloud Reflection". In: *J. Climate* 29.16 (2016), pp. 5821–5835. DOI: 10.1175/JCLI-D-15-0897.1.

[10] G. V. Cesana and A. D. Del Genio. "Observational constraint on cloud feedbacks suggests moderate climate sensitivity". In: *Nat. Climate Change* (2021). DOI: 10.1038/s41558-020-00970-y.

[11] T. A. Myers et al. "Observational constraints on low cloud feedback reduce uncertainty of climate sensitivity". In: *Nat. Climate Change* 11 (2021), pp. 501–507. DOI: 10.1038/s41558-021-01039-0.

[12] P. Ceppi and P. Nowack. "Observational evidence that cloud feedback amplifies global warming". In: *Proc. Natl. Acad. Sci.* 118.30 (2021), e2026290118. DOI: 10.1073/pnas.2026290118.

[13] M. Zhang et al. "The CGILS experimental design to investigate low cloud feedbacks in general circulation models by using single-column and large-eddy simulation models". In: *J. Adv. Model. Earth Syst.* 4 (2012), pp. 1–15. DOI: 10.1029/2012MS000182.

[14] P. N. Blossey et al. “Marine low cloud sensitivity to an idealized climate change: The CGILS LES intercomparison”. In: *J. Adv. Model. Earth Syst.* 5.2 (2013), pp. 234–258. DOI: 10.1002/jame.20025.

[15] C. S. Bretherton, P. N. Blossey, et al. “Mechanisms of marine low cloud sensitivity to idealized climate perturbations: A single-LES exploration extending the CGILS cases”. In: *J. Adv. Model. Earth Syst.* 5 (2013), pp. 316–337. DOI: 10.1002/jame.20019.

[16] Z. Tan et al. “Large-eddy simulation of subtropical cloud-topped boundary layers: 2. Cloud response to climate change”. In: *J. Adv. Model. Earth Sys.* 9 (2017), pp. 19–38.

[17] C. S. Bretherton. “Insights into low-latitude cloud feedbacks from high-resolution models”. In: *Philos. Trans. R. Soc. A Math. Phys. Eng. Sci.* 373.2054 (2015). DOI: 10.1098/rsta.2014.0415.

[18] J. W. Deardorff. “Stratocumulus-capped mixed layers derived from a three-dimensional model”. In: *Boundary-Layer Meteor.* 18 (1980), pp. 495–527.

[19] D. K. Lilly. “Models of cloud-topped mixed layers under a strong inversion”. In: *Quart. J. Roy. Meteor. Soc.* 94 (1968), pp. 292–309. DOI: 10.1002/qj.49709440106.

[20] C. S. Bretherton and M. C. Wyant. “Moisture Transport, Lower-Tropospheric Stability, and Decoupling of Cloud-Topped Boundary Layers”. In: *J. Atmos. Sci.* 54 (1997), pp. 148–167. DOI: 10.1175/1520-0469(1997)054<0148:MTLTSA>2.0.CO;2.

[21] B. Stevens. “Bulk boundary-layer concepts for simplified models of tropical dynamics”. In: *Theor. Comput. Fluid Dyn.* 20.5-6 (2006), pp. 279–304. DOI: 10.1007/s00162-006-0032-z.

[22] S. Dal Gesso et al. “A mixed-layer model perspective on stratocumulus steady states in a perturbed climate”. In: *Q. J. R. Meteorol. Soc.* 140.684 (2014), pp. 2119–2131. DOI: 10.1002/qj.2282.

[23] S. R. de Roode et al. “A mixed-layer model study of the stratocumulus response to changes in large-scale conditions”. In: *J. Adv. Model. Earth Syst.* 6.4 (2014), pp. 1256–1270. DOI: 10.1002/2014MS000347.

[24] A. M. Salazar and E. Tziperman. “Exploring Subtropical Stratocumulus Multiple Equilibria Using a Mixed-Layer Model”. In: *J. Climate* (2023), pp. 1–38. DOI: 10.1175/JCLI-D-22-0528.1.

[25] T. Schneider, C. M. Kaul, et al. “Solar geoengineering may not prevent strong warming from direct effects of CO_2 on stratocumulus cloud cover”. In: *Proc. Natl. Acad. Sci.* 117.48 (2020), pp. 30179–30185. DOI: 10.1073/pnas.2003730117.

[26] M. W. Christensen et al. “Radiative Impacts of Free-Tropospheric Clouds on the Properties of Marine Stratocumulus”. In: *J. Atmos. Sci.* 70.10 (2013), pp. 3102–3118. DOI: 10.1175/JAS-D-12-0287.1.

[27] S. P. Raghuraman et al. “Anthropogenic forcing and response yield observed positive trend in Earth’s energy imbalance”. In: *Nat. Comm.* 12.1 (2021), pp. 1–10. DOI: 10.1038/s41467-021-24544-4.

[28] R. T. Pierrehumbert. “Thermostats, Radiator Fins, and the Local Runaway Greenhouse”. In: *J. Atmos. Sci.* 52.10 (1995), pp. 1784–1806. DOI: 10.1175/1520-0469(1995)052<1784:TRFATL>2.0.CO;2.

[29] R. L. Miller. “Tropical Thermostats and Low Cloud Cover”. In: *J. Climate* 10 (1997), pp. 409–440.

[30] C. Schillings and A. M. Stuart. “Analysis of the ensemble Kalman filter for inverse problems”. In: *SIAM J. Numer. Anal.* 55 (2017), pp. 1264–1290.

[31] P. L. Houtekamer and F. Zhang. “Review of the Ensemble Kalman Filter for Atmospheric Data Assimilation”. In: *Mon. Wea. Rev.* 144 (2016), pp. 4489–4532.

[32] I. Lopez-Gomez et al. “Training Physics-Based Machine-Learning Parameterizations With Gradient-Free Ensemble Kalman Methods”. In: *J. Adv. Model. Earth Syst.* 14.8 (2022), e2022MS003105. DOI: 10.1029/2022MS003105.

[33] O. R. A. Dunbar et al. “EnsembleKalmanProcesses.jl: Derivative-free ensemble-based Model Calibration”. In: *J. Open Source Software* 7.80 (2022), p. 4869. DOI: 10.21105/joss.04869.

[34] X. Qu et al. “On the Spread of Changes in Marine Low Cloud Cover in Climate Model Simulations of the 21st Century”. In: *Climate Dynamics* 42.9-10 (2014), pp. 2603–2626. DOI: 10.1007/s00382-013-1945-z.

[35] J. Zhu et al. “Simulation of Eocene Extreme Warmth and High Climate Sensitivity through Cloud Feedbacks”. In: *Science Advances* 5.9 (2019), eaax1874. DOI: 10.1126/sciadv.aax1874.

[36] J. E. Tierney et al. “Spatial Patterns of Climate Change across the Paleocene–Eocene Thermal Maximum”. In: *Proc. Natl. Acad. Sci.* 119.42 (2022), e2205326119. DOI: 10.1073/pnas.2205326119.

[37] C. Goldblatt et al. “Earth’s long-term climate stabilized by clouds”. In: *Nat. Geosci.* (2021). DOI: 10.1038/s41561-021-00691-7.

Chapter 3

CO_2-INDUCED STRATOCUMULUS CLOUD BREAKUP IN A GLOBAL CLIMATE MODEL

Abstract. Recent work has shown that there is possible tipping-point behavior of stratocumulus cloud cover reduction under very high CO_2 conditions. In particular, these papers hypothesize that under very high CO_2 scenarios, the longwave cloud-top radiative cooling could be sufficiently reduced as to prevent the formation of stratocumulus clouds by decoupling the boundary layer. Once the clouds disappear, the positive feedbacks from surface warming (through enhanced surface shortwave absorption) and warming aloft with subsequent humidification, lead to hysteresis behavior, where the clouds will not reform until CO_2 is decreased to a much lower value than the breakup threshold. One limitation of these previous papers is their idealized representation of how the subtropical stratocumulus regions couple with the rest of the tropical atmosphere. In this work, we explore how realistic representations of the large-scale circulations and thermodynamic state impact the trajectory of stratocumulus breakup in a global model. Using CESM2 (The Community Earth System Model version 2), we replace the default cloud cover parameterization with a highly simplified cloud cover diagnosed from the state of boundary layer decoupling, as introduced in previous works. We conduct experiments with increasing concentrations of atmospheric CO_2 and show cloud adjustments and feedbacks to this forcing. We discuss the implications of these results for nonlinear cloud feedbacks and direct cloud adjustments.

3.1 Introduction

Stratocumulus clouds cover about 20% of tropical oceans in the annual-mean (Wood, 2012; Cesana et al., 2019). Their large areal coverage makes them an important regulator of Earth's radiative energy balance, cooling Earth by an estimated 8 K (Randall et al., 1984; Schneider et al., 2019). Stratocumulus cloud decks are especially common over eastern subtropical ocean basins, where sea surface temperatures (SSTs) are low, subsidence is strong, and there exists a strong temperature inversion (Klein et al., 1993; Myers and Norris, 2013; Bretherton, 2015). Uniquely among clouds, stratocumulus clouds are sustained by an upside-down convective circulation that is driven by cloud-top radiative cooling (CTRC), arising because stratocumulus clouds,

despite their geometric thinness, are relatively opaque to longwave radiation (Lilly, 1968; Bretherton and Wyant, 1997; Stevens, 2006). These clouds exist in a delicate balance between radiative cooling at the cloud tops and warming/drying by turbulent entrainment. Additionally, subsidence above the clouds works against the deepening of the cloud layer that otherwise results from entrainment of free-tropospheric air into the cloud layer.

Stratocumulus clouds are sensitive to climate changes like surface warming and circulation changes, but their dependence on CTRC also makes them directly respond to changes in CO_2 concentration, or other longwave absorbers like water vapor, high clouds, or aerosols (Bretherton, 2015; Christensen et al., 2013; Brient and Schneider, 2016; Petters et al., 2012). This direct CO_2 dependence constitutes a cloud "adjustment" rather than a "feedback," as it is not mediated by surface warming, though stratocumulus clouds are also sensitive to SST warming, and will respond indirectly to CO_2 increases as well.

Studying this direct effect of CO_2 in global climate models (GCMs), however, is challenging because many parameterizations of boundary layer clouds and turbulence do not directly account for the CTRC (J.-L. Lin et al., 2014; Qu et al., 2014). Furthermore, many studies of stratocumulus clouds in GCMs are complicated by the fact that the coarse resolution of GCMs and the imperfect parameterizations fails to faithfully represent these clouds in the current climate, which partly undermines our trust in their response to climate change (Lauer et al., 2010; Nam et al., 2012). However, Qu et al., 2014 found that models which do account for CTRC tend to have better representations of stratocumulus cloud cover in their base state.

Recent studies of the direct effect of CO_2 on stratocumulus clouds have concluded that in an idealized scenario, there exists a tipping point of CO_2 concentrations, past which the clouds are no longer stable (Schneider et al., 2019; Schneider et al., 2020; Singer and Schneider, 2023a; Salazar and Tziperman, 2023). These studies, using high-resolution large-eddy simulations (LES), and low resolution mixed-layer models (MLM), were idealized in their representations of spatial and temporal heterogeneity. Concretely, the experimental setup consisted of modeling one idealized patch of stratocumulus clouds and considered only the steady-state result of abrupt CO_2 increase and neglected variability (from diurnal to seasonal to interannual timescales). The LES and MLM both parameterized interactions of the subtropical stratocumulus region with the global atmosphere in an idealized way: assuming no changes in the circulation (dynamic) and coupling to an idealized

"tropical column" to represent global warming (thermodynamic), inspired by ideas from Pierrehumbert, 1995.

We know from the extensive literature on cloud controlling factors how important adjustments in the deep tropics are for stratocumulus clouds, both dynamically through changing subsidence rates (Myers and Norris, 2013), and thermodynamically through changing inversion strength (Klein et al., 1993; Wood and Bretherton, 2006). However, both of these important properties were necessarily parameterized by the previous studies that focused on running and explaining high-resolution models. In other previous work, which has explored stratocumulus feedbacks, important links have been found between low cloud regions and regions of deep convection, both thermodynamcially and dynamically, that further motivate exploring this question in a global model (Schiro et al., 2022).

Building from these previous works, in this paper we explore the idea of CO_2-induced stratocumulus breakup in a setting that better captures the large-scale interactions of the subtropical stratocumulus regions with the rest of the atmosphere. To do this, we take the ideas from Singer and Schneider, 2023b; Singer and Schneider, 2023a of boundary layer decoupling induced stratocumulus breakup, and write a new heuristic parameterization of low cloud cover. We implement this parameterization, overriding the default CLUBB scheme (Cloud Layers Unified by Binormals) in the Community Atmosphere Model version 6 (CAM6). Then we test the response of the clouds to abrupt increases in CO_2 concentration in a configuration of CESM (Community Earth System Model) that uses a slab ocean model with prescribed heat flux. This simple coupled configuration allows us to include important SST feedbacks to changing cloud cover without the need for centennial-scale simulations with a full dynamic ocean model (Tan et al., 2017; Schneider et al., 2019; Singer and Schneider, 2023a). Furthermore, by using a realistic AGCM, we can resolve questions of how spatiotemporal variability (seasonal, synoptic, and diurnal) imprint onto the idealized notion of "sudden" breakup of the stratocumulus deck.

In this paper, Section 3.2 reviews the ideas of boundary layer decoupling, discusses the implementation of our idealized decoupling-based parameterization into CAM6, and describes the model configuration and experiments run. The main results are in Section 3.3, where we show changes in decoupling, cloud cover, and climate feedbacks in increasing CO_2 experiments.

3.2 Methodology

Theory of decoupling-induced stratocumulus breakup

To review, the overturning circulations in stratocumulus cloud decks are driven by cloud-top cooling, rather than surface heating. This makes these clouds directly sensitive to changes in longwave absorbers (CO_2 or water vapor) in the free-atmosphere above the cloud decks. Recent work has found that this direct effect of CO_2 has the potential to induce a tipping point in the stratocumulus clouds, forcing the boundary layer into a low cloud cover, high SST state (Schneider et al., 2019; Singer and Schneider, 2023a). Due to the strong positive feedback between surface temperature and cloud cover, there is bistability in the system which drives strong hysteresis behavior. This means that once the stratocumulus clouds are lost, and surface temperatures are warmed, the clouds will not reform immediately when CO_2 is decreased back to the pre-tipping point concentration.

The decoupling-driven transition from stratocumulus to cumulus regime was parameterized in Singer and Schneider, 2023b; Singer and Schneider, 2023a as a function of the decoupling parameter, first introduced in Bretherton and Wyant, 1997:

$$\mathscr{D} = \left(\frac{\mathrm{LHF}}{\Delta R}\right)\left(\frac{z_i - z_b}{z_i}\right). \tag{3.1}$$

The decoupling parameter $\mathscr{D}$ describes the competition between the circulation driven by longwave radiative cooling ΔR and the inhibition of mixing from stratification which is related to the surface latent heat flux LHF; this ratio is multiplied by the fraction of the boundary layer occupied by clouds (where z_i is the cloud top altitude and z_b is the cloud base altitude).

The diagnostic cloud fraction (CF_d) was given by the following expression, describing a smooth transition between some maximum value $\mathrm{CF}_{\mathrm{max}}$ and minimum value $\mathrm{CF}_{\mathrm{min}}$ over a scale m,

$$\mathrm{CF}_d = \mathrm{CF}_{\mathrm{max}} - \frac{\mathrm{CF}_{\mathrm{max}} - \mathrm{CF}_{\mathrm{min}}}{1 + \frac{1}{9}\exp(-m(\mathscr{D} - \mathscr{D}_c)}. \tag{3.2}$$

The cloud fraction parameterization is constructed such that CF is 90% depleted at the critical value of the decoupling parameter $\mathscr{D}_c = 1$. In Singer and Schneider, 2023b, the maximum/minimum cloud fraction values ($\mathrm{CF}_{\mathrm{max}} = 0.8$ and $\mathrm{CF}_{\mathrm{max}} = 0.1$) and scale parameter $m = 8$ are chosen based on monthly-mean satellite observations; these values are necessarily resolution dependent, as the maximum cloud fraction will never reach 1 when averaged over a large enough area and/or time period. We use these same values in this work.

Implementation in CESM2

The CESM2 model uses the CLUBB scheme (Cloud Layers Unified by Binormals) to parameterize boundary layer turbulence and shallow convection (Bogenschutz, Gettelman, Morrison, Larson, Schanen, et al., 2012; Bogenschutz, Gettelman, Morrison, Larson, Craig, et al., 2013; Guo et al., 2015; Thayer-Calder et al., 2015). We take a simple and heavy-handed approach, inspired by the cloud-locking literature to introduce our decoupling-based cloud fraction parameterization (Voigt et al., 2020). We let CLUBB run as normal, but introduce a second synonymous cloud fraction variable that is passed to the radiation code instead of the default output from CLUBB. This means that the thermodynamics, microphysics, etc. all see the unaltered cloud properties, but the heating/cooling rates calculated by the radiation code are altered based on the modified cloud properties.

We use a simplified decoupling criteria with the fractional cloud thickness term assumed constant $(z_i - z_b)/z_i = 0.4$. We only override the CLUBB cloud fraction at low levels, between cloud base and cloud top pressure levels:

$$\mathrm{CBP} \quad = 900 \text{ hPa} \tag{3.3}$$

$$\mathrm{CTP} \quad = 700 + 100 \left(\frac{\mathrm{CF}_d - \mathrm{CF}_{\min}}{\mathrm{CF}_{\max} - \mathrm{CF}_{\min}} \right) \text{ hPa}. \tag{3.4}$$

The cloud base pressure is taken to be constant for simplicity and due to the very coarse vertical resolution. Cloud top pressure varies between 700 and 800 hPa based on cloud fraction with lower cloud top in high cloud fraction stratocumulus regimes, and deeper clouds in lower cloud fraction, more convective regimes. Stated pressure levels are interpreted as the nearest level, without interpolation. It is worth noting that CAM6 uses a Lagrangian coordinate in the vertical (S.-J. Lin, 2004), so the pressure levels are not exactly uniform, though the variations are not significant.

Additionally, we only apply the cloud fraction modification under the following conditions:

1. Over ocean regions,
2. When there is subsidence at 500 hPa,
3. And at low latitudes.

These criteria are specified in terms of a weighting function (γ) of latitude (φ) and longtidue (λ),

$$\gamma(\varphi,\lambda) = \begin{cases} 0 & \text{LANDFRAC}(\varphi,\lambda) > 0.1 \\ 0 & \omega_{500}(\varphi,\lambda) \leq 0 \\ \frac{1}{2}\left(\tanh\left(5\left(\varphi+\frac{\pi}{6}\right)\right) - \tanh\left(5\left(\varphi-\frac{\pi}{6}\right)\right)\right) & \text{else} \end{cases} . \tag{3.5}$$

The modified cloud fraction (CF_m) is the weighted sum of the default CLUBB cloud fraction (CF_{CLUBB}) and the decoupling cloud fraction (CF_d):

$$\text{CF}_m = (1-\gamma)\cdot\text{CF}_{\text{CLUBB}} + \gamma\cdot\text{CF}_d. \tag{3.6}$$

The default CLUBB cloud fraction is retained in all circumstances where $\gamma = 0$ and outside of the specified pressure levels for the modification (Figure 3.1).

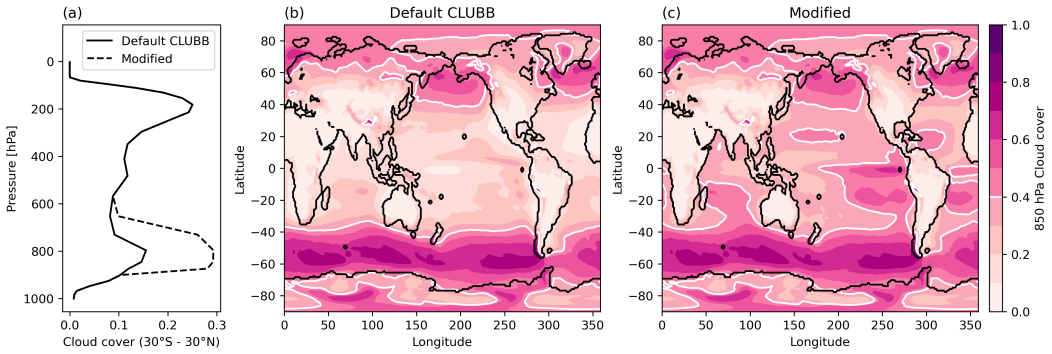

Figure 3.1: 1xCO2 climatological cloud cover (a) vertical profiles of tropical-mean (30°S – 30°N) default and modified cloud cover. (b) Cloud cover at 850 hPa predicted by the default CLUBB scheme compared to (c) the modified cloud cover that is shown to the radiation scheme. Climatologies are calculated as the mean over 10 years after spin-up. White contour shows 40% low cloud cover.

Figure 3.1 shows the low cloud climatology in the 1xCO2 experiment, both with the default CLUBB scheme and with the modification based on the boundary layer decoupling parameter. The decoupling modification generally about doubles the low cloud cover in the tropics from 15% to 30%, predominantly in the low cloud regions in eastern subtropical ocean basins. The cloud cover modification is only seen in regions where $\gamma > 0$, over ocean, in regions of climatological subsidence in the tropics, and at low levels.

The modification of low cloud cover has a small effect on global climate (Figure 3.2). The increase shortwave reflectance creates an initial top-of-model (TOM) negative

net energy flux of $N_{\mathrm{TOM}} = -1.5$ W m^{-2} (Fig. 3.2b), which is compensated for by global cooling of about 0.6 K (Fig. 3.2a). The 1xCO2 experiment is run for 20 years in total and the last 10 years, once the model has equilibrated, are used as the 1xCO2 climatology.

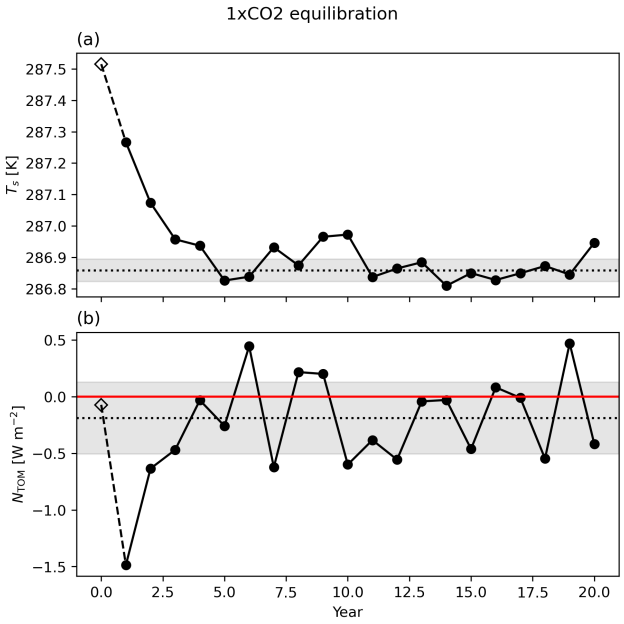

Figure 3.2: Annual-mean time series of (a) global-mean surface temperature and (b) top-of-model net energy imbalance (N_{TOM}) in the 1xCO2 experiment. Open diamond marker and dashed lines show the initial condition in year zero, from a simulation without modified cloud cover. The dotted lines (and grey shading) show the mean (and 1σ standard deviation) over the last 10 years of the simulation.

Experiment configuration

Experiments are run with CESM version 2.1.3, using a customized configuration ("compset" in CESM parlance). We use the full atmosphere model (CAM60), with described cloud cover modification. The atmosphere is coupled to a diagnostic slab ocean (DOCN%SOM), with q-fluxes prescribed from the default CESM2 pre-industrial control run. The land model is run in prognostic mode with satellite phenology (CLM50%SP). The sea ice (CICE) and river components (MOSART) are also run in prognostic mode. The glacier and wave components are in stub mode (SGLC and SWAV).

We used the `f09_g17` grid in CESM2 with displaced pole over Greenland. The atmospheric component uses a nominal 1° (1.25° in longitude and 0.9° in latitude) horizontal resolution with 32 vertical levels. The land component shares the hor-

izontal resolution of the atmosphere. The slab ocean component has horizontal resolution in the zonal direction of uniform 1.125° and in the meridional direction it varies with the finest resolution of 0.27° at the equator. The sea ice component uses the same horizontal grid as the ocean, with 8 levels in the vertical. The prescribed q-fluxes for the slab ocean model come from a previous fully coupled experiment with CESM that has spatially and seasonally varying mixed layer depth and heat flux.

Simulations with CO_2 concentrations of 285 ppm and other pre-industrial forcing ("1xCO2") serve as the baseline climate (Figs. 3.1 and 3.2). Figure 3.3 shows the 1xCO2 climatology of surface temperature, 500 hPa vertical velocity, and shortwave radiative fluxes at the surface and top-of-atmosphere (TOA).

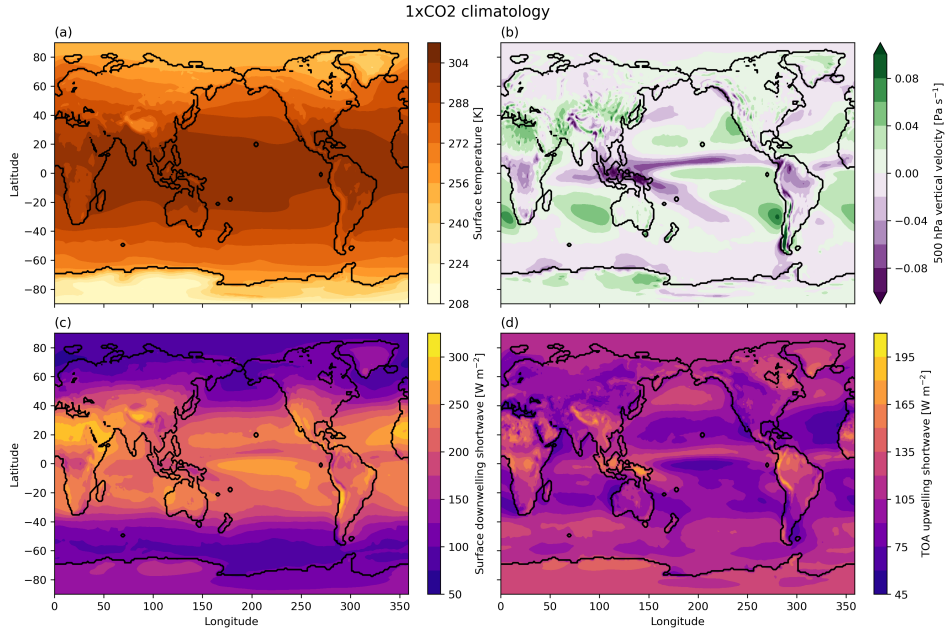

Figure 3.3: 1xCO2 climatologies of (a) surface temperature (TS), (b) 500 hPa vertical velocity (OMEGA500), (c) surface shortwave radiation (FSDS), and (d) TOA shortwave radiation (FSUTOA). Climatologies are calculated as the mean over 10 years after spin-up.

Increased CO_2 experiments are run with abrupt CO_2 forcing (in the radiation, but not seen by the land component, e.g. only `co2vmr_rad` is modified), but all other forcing agents are kept at pre-industrial levels. Simulations are run to equilibrium and then for 10 more years to accumulate statistics. Equilibrium is diagnosed based on the top-of-model energy imbalance (N_{TOM} = FSNT − FLNT) reaching zero (as in Bacmeister et al., 2020). Figure 3.4 shows N_{TOM} scattered against global mean

surface temperature change after CO_2 quadrupling. Initially, the energy imbalance is 7 W m^{-2}, and the equilibrium warming is ~11 K. This is quite similar to the default CESM2 response to 4xCO2, where the energy imbalance is around 8 W m^{-2} and equilibrium warming is around 12 K (Bacmeister et al., 2020 their Figures 1 and 14).

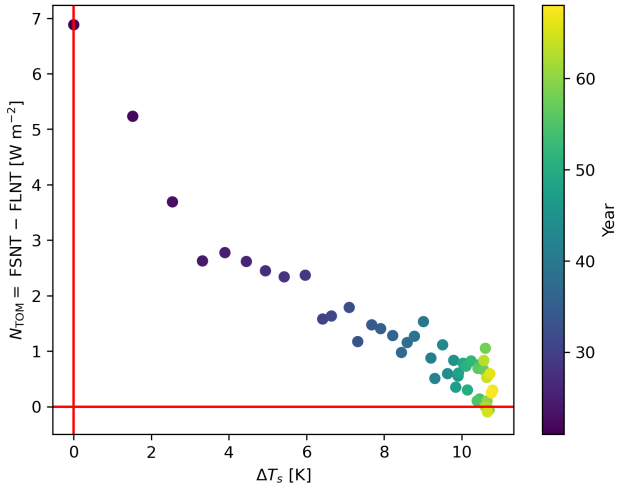

Figure 3.4: Gregory regression plot of N_{TOM} scattered against global mean surface temperature change ΔT_s in the abrupt 4xCO2 experiment. Marker colors show the year. The last 10 years of the simulation are used to compute the equilibrium climatology.

3.3 Preliminary results: Response to CO_2 quadrupling

Figure 3.5 shows the modified low cloud cover and decoupling parameter changes between the 4xCO2 and 1xCO2 experiments. The decoupling parameter $\mathscr{D}$ climatology is calculated as a weighted mean of the decoupling parameter, where the weights are the frequency the decoupling cloud fraction is applied at each grid point. The left column shows the climatology in the 1xCO2 control experiment, the center column shows the 4xCO2 climatology, and the right column shows the change with quadrupling CO_2.

As expected, the decoupling parameter is less than the critical value ($\mathscr{D} < 1$, white contour) in the subtropical stratocumulus regions (Fig. 3.5d). Under 4xCO2, the areas that are well-coupled, shrink further east towards the continents (Fig. 3.5e) and the magnitude of the decoupling parameter increases throughout the entire well-coupled region (Fig. 3.5f).

The cloud cover shows similar patterns, decreasing almost everywhere equatorward

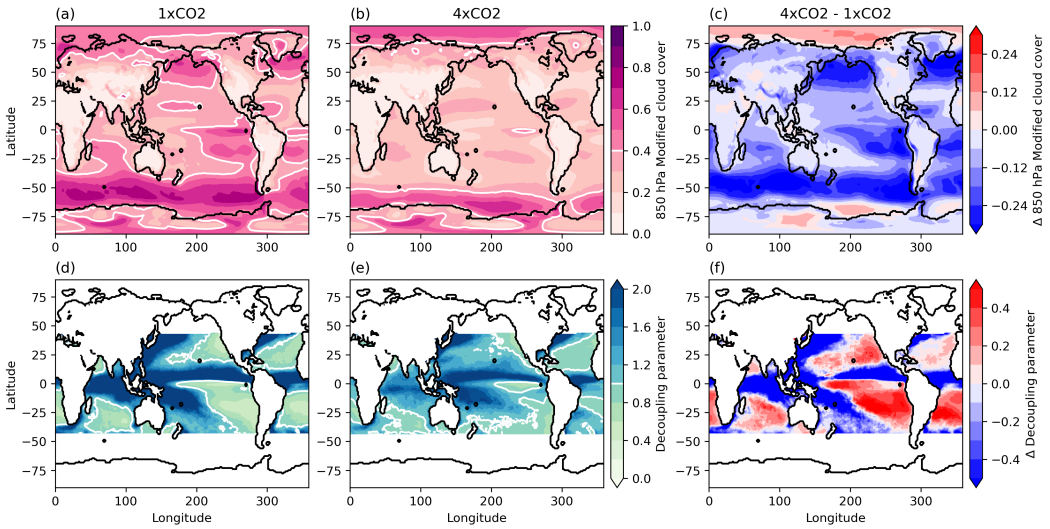

Figure 3.5: Top row: 850 hPa modified cloud cover climatology in (a) 1xCO2, (b) 4xCO2, and (c) the difference 4xCO2-1xCO2. Bottom row: Decoupling parameter climatology in (d) 1xCO2, (e) 4xCO2, and (f) the difference 4xCO2-1xCO2. White contours enclose the 40% cloud cover and $\mathscr{D} = 1$ regions, respectively, to highlight the shrinkage of the well-coupled low cloud regions with increased CO_2. Climatologies are calculated as the mean over the last 10 years of the simulations.

of 50°, though also with decreases in the storm track regions that are independent of the decoupling parameter. For the most part, the weighted decoupling parameter is very large in regions of deep convection because the weighting is very small, indicating that the modified cloud cover is almost never used in place of the default CLUBB or deep convection schemes of CAM6. And the decoupling parameter is not shown over land or poleward of about 40° because the weighting there is negligible $\gamma \approx 0$.

Figure 3.6 shows differences in surface temperature, 500 hPa vertical velocity, and shortwave radiative fluxes between the 4xCO2 and 1xCO2 experiments. The changes in low cloud cover also imprint clearly on the shortwave radiative fluxes (Fig. 3.6c,d). Under 4xCO2, the downwelling shortwave flux at the surface is larger by about 30 W m^{-2} and the upwelling shortwave flux at the top-of-model is smaller by a similar amount over the stratocumulus regions that also stand out in Figure 3.5.

Figure 3.6a shows the global-mean temperature increase, which is due in part to the reduction of outgoing longwave radiation (the Planck feedback), but also from cloud adjustments and feedbacks which reduce the global albedo. Figure 3.7 shows the transient behavior as the climate requilibrates after the abrupt 4xCO2 forcing. As

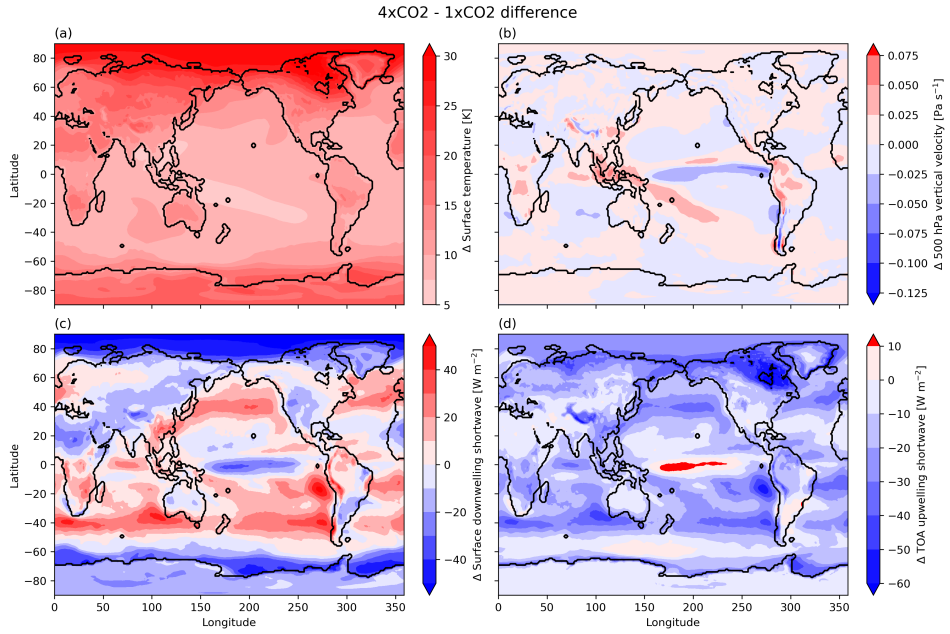

Figure 3.6: Difference of 4xCO2-1xCO2 climatologies of (a) surface temperature (TS), (b) 500 hPa vertical velocity (OMEGA500), (c) surface shortwave radiation (FSDS), and (d) TOA shortwave radiation (FSUT). Climatologies are calculated as the mean over 10 years after spin-up.

the model slowly returns towards $N_{\mathrm{TOM}} = SW_{\mathrm{net,TOM}} - LW_{\mathrm{net,TOM}} = 0$, this new state is achieved through adjustments in both the shortwave and longwave components (Fig. 3.7b,c). Surface temperatures rise to increase outgoing longwave radiation (Fig. 3.7c,e), while cloud cover decreases in response to CO_2 and surface warming, which also increases the net shortwave (Fig. 3.7b,d).

Also of interest is the fast adjustment in the first year after abrupt CO_2 quadrupling. In the initial year, the low cloud cover decreases by nearly 2.3%, compared to a rate of decrease of $< 1\%$ per year in the next two years (Fig. 3.7d). The net shortwave flux $SW_{\mathrm{net,TOM}}$, similarly has twice as large an increase in the first year compared to subsequent years (Fig. 3.7c). However, surface temperature does not show an initial increase in the same way, with ΔT_s in the first year being the same as in the second, because it is moderated by the timescale of the slab ocean adjustment ($\tau \approx 4$ years for an median ocean mixed-layer depth of 30 m) (Fig. 3.7e). The fast adjustment of low cloud cover is largest in regions that are climatologically well-coupled: the initial decrease in cloud cover for the global mean is 2.3% (as above), for a tropical mean (30°S – 30°N) it is 2.6%, and for a conditional mean over regions with $\mathscr{D} < 1$ in the 1xCO2 climatology the initial decrease is 3.9%.

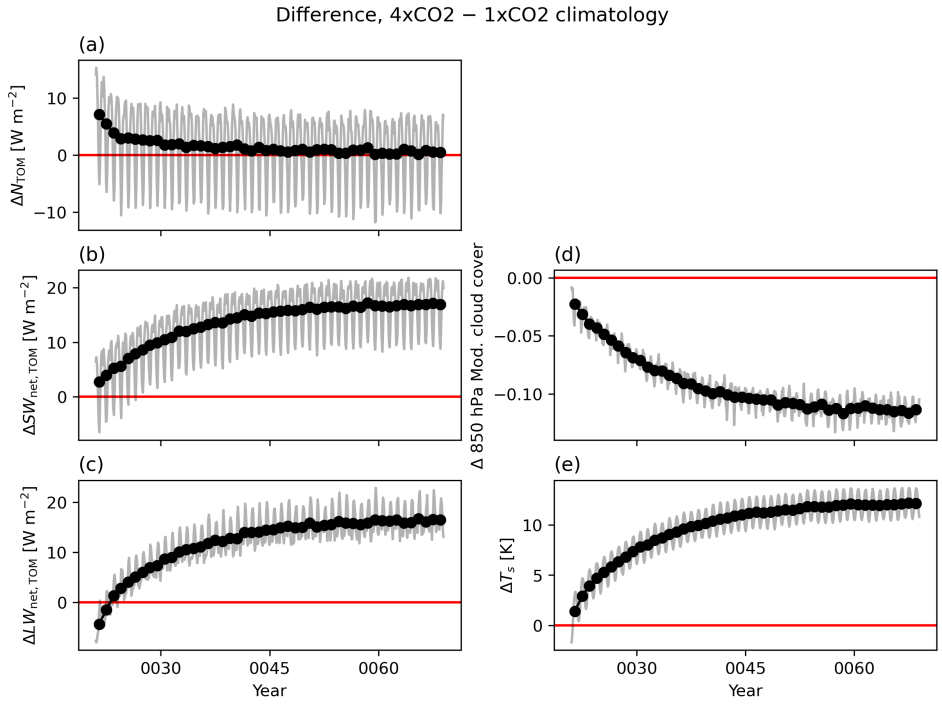

Figure 3.7: Transient behavior of 4xCO2 experiment as it approaches equilibrium, shown relative to 1xCO2 climatology. Global mean (a) Net top-of-model radiative fluxes (N_{TOM}), (b) Shortwave net fluxes (FSNT), (c) 850 hPa modified cloud cover, (d) Longwave net fluxes (FLNT), and (e) Surface temperature (TS). Grey lines show monthly mean and black points show annual-mean.

Looking in more detail at specific locations, Figure 3.8 shows local changes in 850 hPa modified cloud cover at various points along the stratocumulus-cumulus transect in the Southeast Pacific. We see the same trend of large decreases in low cloud cover in the initial year after CO_2 quadrupling. The diamonds indicate the 1xCO2 climatology of low cloud cover at the six locations, and dotted lines show the initial decrease during the first year.

Overall, there a 15–20% decrease in cloud cover at all locations along the transect in the equilibrium state. Locations with higher cloud cover under 1xCO2 show larger decreases, and thus the range of cloud cover values across this spatial transect narrows under the 4xCO2 forcing. There is also substantial interannual variability, especially for sites 3–5, located equatorward of 20°S. This may be due to interannual variations in ITCZ position and climate modes such as the El Niño Southern Oscillation (ENSO). In particular, years 25, 33, and 52 show large spatially coherent positive deviations in low cloud cover (Fig. 3.8a).

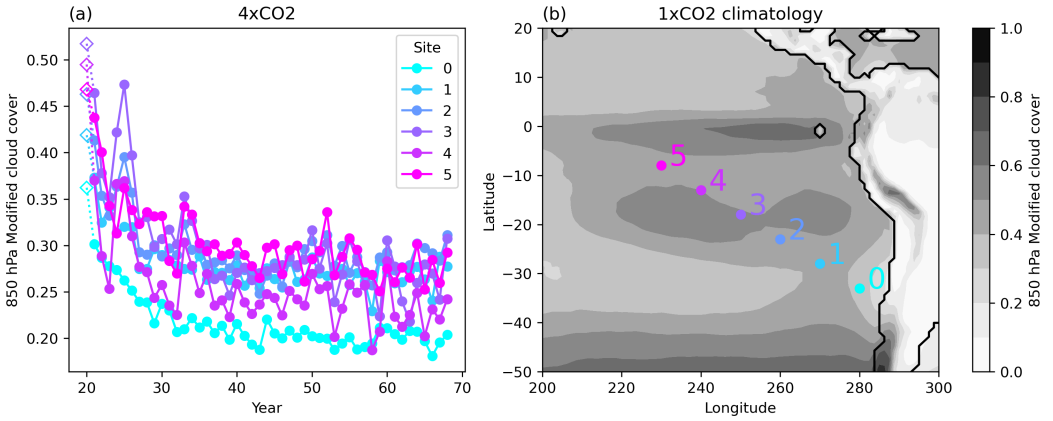

Figure 3.8: Time series of low cloud cover at 850 hPa in 4xCO2 experiment from various sites along the Southeast Pacific stratocumulus-cumulus transect (a), with locations shown on the 1xCO2 climatological 850 hPa low cloud cover (b). Open diamond symbols show the mean cloud cover values from the 1xCO2 experiment, and dotted lines indicate the decrease in cloud cover in the first year after CO_2 quadrupling.

3.4 Future work

Further analysis of the existing 1xCO2 and 4xCO2 experiments may include the following. First, an examination of changes to the seasonal cycle of low cloud cover. Additionally, we hope to conduct an analysis similar to the cloud controlling factor study in Lauer et al., 2010. There they showed that correlations between low cloud cover and various meteorological variables in a present-day climate were different in magnitude, and sometimes in sign, from the correlations under climate change. In particular, they found that between El Niño and neutral ENSO years, cloud cover and lower tropospheric stability (LTS) were positively correlated, but between global warming and present-day years, cloud cover and LTS were negatively correlated.

Next steps on this project also include evaluating cloud changes under different forcing scenarios. We will run a series of experiments testing different magnitudes of abrupt CO_2 increase, including 2xCO2 and 8xCO2. With these additional simulations we will be able to test whether or not the cloud response is linear per doubling of CO_2. We also plan to run simulations with abrupt decreases of CO_2 concentration. By starting in the equilibrated state of NxCO2 and abruptly decreasing concentrations back to 1xCO2, we will test for any hysteresis in the system. Finally, it may be interesting to run experiments with fixed SST under different CO_2 forcing scenarios.

Acknowledgements. I would like to acknowledge high-performance computing support from Cheyenne (CISL, 2019) provided by NCAR's Computational and Information Systems Laboratory, sponsored by the National Science Foundation.

References

[1] R. Wood. "Stratocumulus Clouds". In: *Mon. Weather Rev.* 140.8 (2012), pp. 2373–2423. DOI: 10.1175/MWR-D-11-00121.1.

[2] G. Cesana et al. "The Cumulus And Stratocumulus CloudSat-CALIPSO Dataset (CASCCAD)". In: *Earth System Science Data* 11.4 (2019), pp. 1745–1764. DOI: 10.5194/essd-11-1745-2019.

[3] D. A. Randall et al. "Outlook for research on subtropical marine stratification clouds". In: *Bull. Amer. Meteor. Soc.* 65 (1984), pp. 1290–1301.

[4] T. Schneider et al. "Possible climate transitions from breakup of stratocumulus decks under greenhouse warming". In: *Nat. Geosci.* 12.3 (2019), pp. 163–167. DOI: 10.1038/s41561-019-0310-1.

[5] S. A. Klein et al. "The Seasonal Cycle of Low Stratiform Clouds". In: *J. Climate* 6.8 (1993), pp. 1587–1606. DOI: 10.1175/1520-0442(1993)006<1587:TSCOLS>2.0.CO;2.

[6] T. A. Myers and J. R. Norris. "Observational Evidence That Enhanced Subsidence Reduces Subtropical Marine Boundary Layer Cloudiness". In: *J. Climate* 26.19 (2013), pp. 7507–7524. DOI: 10.1175/JCLI-D-12-00736.1.

[7] C. S. Bretherton. "Insights into low-latitude cloud feedbacks from high-resolution models". In: *Philos. Trans. R. Soc. A Math. Phys. Eng. Sci.* 373.2054 (2015). DOI: 10.1098/rsta.2014.0415.

[8] D. K. Lilly. "Models of cloud-topped mixed layers under a strong inversion". In: *Quart. J. Roy. Meteor. Soc.* 94 (1968), pp. 292–309. DOI: 10.1002/qj.49709440106.

[9] C. S. Bretherton and M. C. Wyant. "Moisture Transport, Lower-Tropospheric Stability, and Decoupling of Cloud-Topped Boundary Layers". In: *J. Atmos. Sci.* 54 (1997), pp. 148–167. DOI: 10.1175/1520-0469(1997)054<0148:MTLTSA>2.0.CO;2.

[10] B. Stevens. "Bulk boundary-layer concepts for simplified models of tropical dynamics". In: *Theor. Comput. Fluid Dyn.* 20.5-6 (2006), pp. 279–304. DOI: 10.1007/s00162-006-0032-z.

[11] M. W. Christensen et al. "Radiative Impacts of Free-Tropospheric Clouds on the Properties of Marine Stratocumulus". In: *J. Atmos. Sci.* 70.10 (2013), pp. 3102–3118. DOI: 10.1175/JAS-D-12-0287.1.

[12] F. Brient and T. Schneider. "Constraints on Climate Sensitivity from Space-Based Measurements of Low-Cloud Reflection". In: *J. Climate* 29.16 (2016), pp. 5821–5835. DOI: 10.1175/JCLI-D-15-0897.1.

[13] J. L. Petters et al. "Radiative-Dynamical Feedbacks in Low Liquid Water Path Stratiform Clouds". In: *J. Atmos. Sci.* 69.5 (2012), pp. 1498–1512. DOI: 10.1175/JAS-D-11-0169.1.

[14] J.-L. Lin et al. "Stratocumulus Clouds in Southeastern Pacific Simulated by Eight CMIP5–CFMIP Global Climate Models". In: *Journal of Climate* 27.8 (2014), pp. 3000–3022. DOI: 10.1175/JCLI-D-13-00376.1.

[15] X. Qu et al. "On the Spread of Changes in Marine Low Cloud Cover in Climate Model Simulations of the 21st Century". In: *Climate Dynamics* 42.9-10 (2014), pp. 2603–2626. DOI: 10.1007/s00382-013-1945-z.

[16] A. Lauer et al. "The Impact of Global Warming on Marine Boundary Layer Clouds over the Eastern Pacific—A Regional Model Study". In: *J. Climate* 23 (2010), pp. 5844–5863. DOI: 10.1175/2010JCLI3666.1.

[17] C. Nam et al. "The 'too few, too bright' tropical low-cloud problem in CMIP5 models". In: *Geophys. Res. Lett.* 39.21 (2012). DOI: 10.1029/2012GL053421.

[18] T. Schneider et al. "Solar geoengineering may not prevent strong warming from direct effects of CO_2 on stratocumulus cloud cover". In: *Proc. Natl. Acad. Sci.* 117.48 (2020), pp. 30179–30185. DOI: 10.1073/pnas.2003730117.

[19] C. E. Singer and T. Schneider. "CO_2-driven stratocumulus cloud breakup in a bulk boundary layer model". In: *J. Climate* (2023). In revision.

[20] A. M. Salazar and E. Tziperman. "Exploring Subtropical Stratocumulus Multiple Equilibria Using a Mixed-Layer Model". In: *J. Climate* (2023), pp. 1–38. DOI: 10.1175/JCLI-D-22-0528.1.

[21] R. T. Pierrehumbert. "Thermostats, Radiator Fins, and the Local Runaway Greenhouse". In: *J. Atmos. Sci.* 52.10 (1995), pp. 1784–1806. DOI: 10.1175/1520-0469(1995)052<1784:TRFATL>2.0.CO;2.

[22] R. Wood and C. S. Bretherton. "On the Relationship between Stratiform Low Cloud Cover and Lower-Tropospheric Stability". In: *J. Climate* 19.24 (2006), pp. 6425–6432. DOI: 10.1175/JCLI3988.1.

[23] K. A. Schiro et al. "Model Spread in Tropical Low Cloud Feedback Tied to Overturning Circulation Response to Warming". In: *Nature Communications* 13.1 (2022), p. 7119. DOI: 10.1038/s41467-022-34787-4.

[24] C. E. Singer and T. Schneider. "Stratocumulus-cumulus transition explained by bulk boundary layer theory". In: *J. Climate* (2023). In revision.

[25] Z. Tan et al. “Large-eddy simulation of subtropical cloud-topped boundary layers: 2. Cloud response to climate change”. In: *J. Adv. Model. Earth Sys.* 9 (2017), pp. 19–38.

[26] P. A. Bogenschutz, A. Gettelman, H. Morrison, V. E. Larson, D. P. Schanen, et al. “Unified Parameterization of the Planetary Boundary Layer and Shallow Convection with a Higher-Order Turbulence Closure in the Community Atmosphere Model: Single-Column Experiments”. In: *Geoscientific Model Development* 5.6 (2012), pp. 1407–1423. DOI: 10.5194/gmd-5-1407-2012.

[27] P. A. Bogenschutz, A. Gettelman, H. Morrison, V. E. Larson, C. Craig, et al. “Higher-Order Turbulence Closure and Its Impact on Climate Simulations in the Community Atmosphere Model”. In: *Journal of Climate* 26.23 (2013), pp. 9655–9676. DOI: 10.1175/JCLI-D-13-00075.1.

[28] Z. Guo et al. “Parametric Behaviors of CLUBB in Simulations of Low Clouds in the C Ommunity A Tmosphere M Odel (CAM)”. In: *Journal of Advances in Modeling Earth Systems* 7.3 (2015), pp. 1005–1025. DOI: 10.1002/2014MS000405.

[29] K. Thayer-Calder et al. “A Unified Parameterization of Clouds and Turbulence Using CLUBB and Subcolumns in the Community Atmosphere Model”. In: *Geoscientific Model Development* 8.12 (2015), pp. 3801–3821. DOI: 10.5194/gmd-8-3801-2015.

[30] A. Voigt et al. “Clouds, Radiation, and Atmospheric Circulation in the Present-day Climate and under Climate Change”. In: *WIREs Climate Change* 12.2 (2020). DOI: 10.1002/wcc.694.

[31] S.-J. Lin. “A “Vertically Lagrangian” Finite-Volume Dynamical Core for Global Models”. In: *Monthly Weather Review* 132.10 (2004), pp. 2293–2307. DOI: 10.1175/1520-0493(2004)132<2293:AVLFDC>2.0.CO;2.

[32] J. T. Bacmeister et al. “CO $_2$ Increase Experiments Using the CESM: Relationship to Climate Sensitivity and Comparison of CESM1 to CESM2”. In: *Journal of Advances in Modeling Earth Systems* 12.11 (2020). DOI: 10.1029/2020MS002120.

[33] CISL. *Cheyenne: HPE/SGI ICE XA System (University Community Computing)*. Boulder, CO, 2019. DOI: 10.5065/D6RX99HX.

Chapter 4

STRATOCUMULUS CLOUD SENSITIVITY TO AEROSOL HYGROSCOPICITY

Abstract. The role of aerosols acting as cloud condensation nuclei in warm clouds remains one of the largest sources of uncertainty in climate projections. This uncertainty stems, in large part, from a problem of scales: the microphysical processes of cloud droplet activation cannot be directly resolved in global models or even high-resolution large-eddy simulations (LES). Moment-based microphysics schemes used in models assume the shape of the cloud droplet size distribution and ignore the details about the underlying aerosol populations upon which these droplets form. In this study we use the University of Warsaw Lagrangian Cloud Model with particle-based microphysics scheme which explicitly represents a statistical sample of the aerosols, cloud droplets, and rain particles. This scheme can resolve changes to the shapes of the cloud droplet size distribution due to condensation/evaporation and collisions. We simulate stratocumulus clouds with a broad range of initial aerosol populations, covering the full parameter space of size, number concentration, and hygroscopicity. We find that the stratocumulus clouds are sensitive to the aerosol radius and number concentration, as well as to the aerosol hygroscopicity. Under conditions with small aerosol sizes, the liquid water path or cloud droplet number concentration can vary up to 25% or 40%, respectively, just from changes in aerosol hygroscopicity. Comparing the results from the particle-based scheme to a classic two-moment bulk scheme shows that the bulk scheme is sometimes able to capture the hygroscopicity susceptibility of cloud liquid water path, but in cases of small aerosol sizes is significantly oversensitive.

4.1 Introduction

In Earth's atmosphere, aerosols act as cloud condensation nuclei (CCN), forming the nucleation site for every cloud droplet and ice crystal, and limiting supersaturations from ever exceeding more than a few percent. Aerosol activation controls cloud droplet number concentrations, which affects the radiative properties of clouds as well as precipitation. In climate projections the aerosol indirect effect (the radiative forcing from aerosol-cloud interactions) remains one of the largest sources of uncertainty (e.g. Myhre et al., 2013; Seinfeld et al., 2016; Rosenfeld et al., 2019;

Sato and Suzuki, 2019; Toll et al., 2019).

In the atmosphere, number of cloud droplets is primarily controlled by the number of aerosols. However, the efficacy of an aerosol as a CCN depends on its size and chemical composition. This is described by κ-Köhler theory, which can be conveniently written in terms of the critical supersaturation at which a given aerosol particle will activate into a cloud droplet:

$$S_c(r) = \left(\frac{r^3 - r_d^3}{r^3 - (1-\kappa) r_d^3} \right) \exp\left(\frac{2\sigma M_w}{RT\rho_w r} \right). \tag{4.1}$$

In this equation, r is the radius of the droplet, r_d is the radius of the dry aerosol particle, κ is the hygroscopicity parameter, σ is the surface tension of the droplet, M_w and ρ_w are the molecular weight and density of water, R is the universal gas constant, and T is the temperature. The first term in this equation represents the solute effect and is sometimes replaced by a_w, the water activity, and describes the effect of the aerosol chemical composition on the droplet growth. The second term, in the exponential, represents the Kelvin, or curvature, effect and describes the effect of droplet size on droplet growth.

Due to the scale separation, the microphysical processes including cloud droplet activation have to be parameterized in global models (GCMs) and even high-resolution large-eddy simulation (LES). In global models, due to computational limitations, aerosol and cloud distributions are represented by a fixed number of moments (usually one or two). In these schemes, usually called moment or bulk schemes, assumptions are made about the shape of the size distributions and many processes including cloud droplet activation. Additionally, aerosols are categorized into a finite number of types representing their composition (e.g., sulfate, dust, black carbon), which ignores the complexity of mixing state, liquid-liquid phase partitioning, and more. However, even in more complex spectral or bin schemes which discretize the aerosol and droplet size distributions into a finite number of bins, assumptions are made about process rates. These schemes also can suffer from numerical diffusion (e.g., Grabowski, Morrison, et al., 2019; Bulatovic et al., 2019). Moreover, both bulk and bin microphysics schemes are traditionally limited computationally by problems of dimensionality to representing only finite classes of particles, either in terms of aerosol chemical composition, or ice crystal shape.

A newer class of Lagrangian particle-based microphysics schemes avoids these assumptions about size distributions, artificial process rates that convert between

aerosol, cloud, and rain categories, simplifications to finite classes of aerosol chemical composition, and numerical diffusion (Shima et al., 2009; Andrejczuk et al., 2010; Hoffmann, Raasch, et al., 2015; Grabowski, Dziekan, et al., 2018; Hill et al., 2023). These schemes get around all these problems by tracking a statistical sample of aerosol, cloud, and rain particles. These Lagrangian schemes are sometimes referred to colloquially as "superdroplet" schemes due to a common method of numerically dealing with collisions between particles (Shima et al., 2009). By tracking individual tracers, which can have an arbitrary number of attributes, it becomes trivial, and computationally tractable, to include more details about the particle composition. However, even these Lagrangian particle-based microphysics schemes tend to dramatically simplify the aerosol representation compared to e.g., Zaveri et al., 2008; Riemer et al., 2009; Tian et al., 2014; Zuend, Marcolli, Luo, et al., 2008; Zuend, Marcolli, Booth, et al., 2011; they track only a few aerosol attributes beyond size, sometimes the hygroscopicity (as in this work), surface tension (Jong et al., 2023), or concentration of a few ion species (Jaruga and Pawlowska, 2018).

In this study, we consider the effects of aerosols size, number concentration, and chemical composition on marine stratocumulus clouds. Stratocumulus clouds are low-level marine boundary layer clouds that occur primarily in eastern subtropical ocean basins due to climatological subsidence and cold sea surface temperatures due to ocean upwelling (Wood, 2012). Where they occur, they have high cloud fraction, near 100%, therefore they reflect much of the incoming shortwave radiation, leading to a large net cooling effect. Furthermore, because of their high prevalence, covering up to 20% of tropical oceans in the annual mean, they have an overall large effect on global climate, estimated to cool the planet by approximately 8 K (Randall et al., 1984; Schneider et al., 2019).

When in the non-precipitating regime, stratocumulus clouds are brightened by aerosols because liquid water is partitioned amongst more aerosols into smaller cloud droplets which more efficiently scatter sunlight (Twomey, 1974; Twomey, 1977). And when they are near a precipitating transition, often characterized by a change in morphology from closed- to open-cells, the clouds have the potential to be brightened by aerosols via precipitation suppression or liquid water path adjustments (Wood, Bretherton, et al., 2011; Wood, Leon, et al., 2012; Kazil et al., 2017; Glassmeier and Feingold, 2017; Glassmeier, Hoffmann, et al., 2019). Background aerosols in the marine environment are multimodal, coming from natural and an-

thropogenic sources. Sulfate is prevalent, usually in the size range of $10 - 100$ µm radius particles (Ackerman, VanZanten, et al., 2009, and Figure 4.2). There is some evidence of the importance of giant CCN sea spray aerosol in these conditions, too (Dziekan, Jensen, et al., 2021; Kuba and Murakami, 2010; Houghton, 1938; Jensen and Nugent, 2017). Highly localized anthropogenic sources of sulfate particles from shipping emissions have been studied for many years and form the basis of much of what we understand about marine stratocumulus susceptibility (Ackerman, Toon, et al., 2000; Y.-C. Chen et al., 2012; Gryspeerdt et al., 2020; Christensen and Stephens, 2011; Blossey et al., 2018), as well as serving as much of the motivation for climate intervention strategies like marine cloud brightening (MCB) (Latham et al., 2012; Hoffmann and Feingold, 2021; Diamond et al., 2022; Prabhakaran et al., 2023).

In this study, we use the University of Warsaw Lagrangian Cloud Model (UWLCM) with *libcloudph++* microphysics library (Dziekan, Waruszewski, et al., 2019; Arabas et al., 2015; Jaruga and Pawlowska, 2018) to examine the sensitivity of stratocumulus clouds to aerosol size, number concentration, and chemical composition. We run large-eddy simulations with UWLCM to simulate marine stratocumulus (DYCOMS-II RF02) (Ackerman, VanZanten, et al., 2009). We parameterize aerosol composition using κ-Köhler theory, where κ is the hygroscopicity parameter (Petters and Kreidenweis, 2007). Aerosol hygroscopicity effects have been investigated before in parcel models (Feingold, 2003; Reutter et al., 2009; Kuba and Murakami, 2010; J. Chen et al., 2016; Pöhlker et al., 2021), but not rigorously quantified in an LES framework. In this work, where we use Lagrangian particle-based microphysics coupled to an LES, we are able to explore the feedback from the aerosol activation on the dynamics and downstream microphysical processes like collision-coalescence. Finally, we compare results from simulations using superdroplets to those from a two-moment bulk scheme to understand to what extent a bulk scheme can capture the pattern and magnitude of cloud sensitivity to the underlying aerosol distribution.

We report results from simulations covering a wide range of aerosol property parameter space. We find that the stratocumulus clouds are highly sensitive to κ in the regime of small aerosol sizes. For instance, the liquid water path, cloud cover, and cumulative precipitation can vary up to 50% just from changes in κ. The maximum supersaturation inside the cloud is highest for the least hygroscopic aerosol because they are less likely to activate and take water out of the vapor phase. Higher supersat-

urations mean that activated droplets grow larger faster through condensation which leads to more precipitation and ultimately less liquid water in the cloud. Comparisons show that the 2-moment bulk scheme is able to capture the relative influence of aerosol number, size, and composition only in certain cases, while in other cases the sensitivities of the two schemes are quite different, and often the magnitude of response varies substantially between the superdroplets and bulk schemes.

4.2 Methods

We use the University of Warsaw Lagrangian Cloud Model (UWLCM) (Dziekan, Waruszewski, et al., 2019; Dziekan and Zmijewski, 2022). UWLCM relies on the *libcloudph++* and *libmpdata++* libraries for microphysical processes and advection. In this study, we use both the Lagrangian particle microphysics ("lgrngn") based on the superdroplet method (Shima et al., 2009) and the double-moment bulk method ("blk2m") based on (Morrison and Grabowski, 2007). The *libcloudph++* software is described in Arabas et al., 2015.

For the double-moment scheme, the droplet size distribution is represented by two moments, the number concentration N_x and the water mixing ratio q_x. The size distribution is divided arbitrarily into two categories, for cloud and rain, so four prognostic variables are advected in the Eulerian coordinate system: N_c, q_ℓ, N_r, and q_r. The scheme assumes the shape of the size distributions as lognormal, gamma, and exponential, for interstitial aerosol, cloud droplets, and rain, respectively. Cloud droplets are created by activation of aerosol, as predicted by κ-Köhler theory, with an assumed initial size of 1 μm. Rain formation by autoconversion and accretion is parameterized according to Khairoutdinov and Kogan, 2000, with drizzle drops formed by autoconversion given an initial size of 25 μm. Unlike the superdroplet scheme, only rain water, not cloud water sedimentation, is included in the two-moment scheme, which leads to much smaller estimates of the precipitation flux (see Figure 4.1f). The inclusion of cloud water sedimentation has been discussed numerous times in the literature previously (Feingold et al., 1998; Bretherton et al., 2007; Ackerman, VanZanten, et al., 2009), but was neglected in the Morrison and Grabowski, 2007 scheme development upon which this model is based. Future work to include a parameterization of cloud water sedimentation, for example following Morrison, Curry, et al., 2005, would be interesting to explore. This double-moment scheme is described in Morrison and Grabowski, 2007 (c.f. Section 2) and the implementation is described in Arabas et al., 2015 (c.f. Section 4).

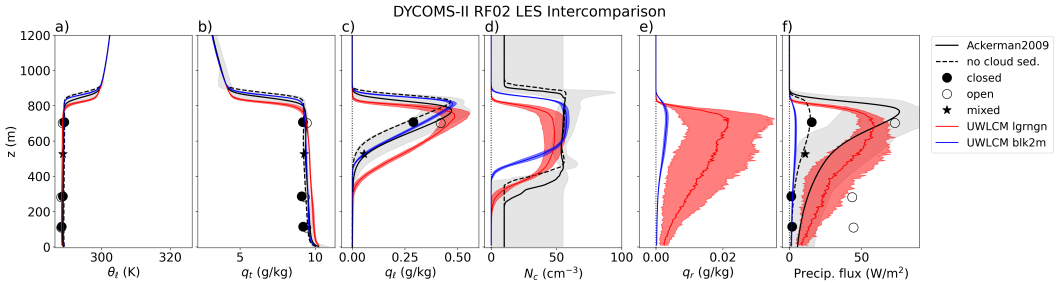

Figure 4.1: Profiles (from left to right) of liquid-water potential temperature θ_ℓ, total water mixing ratio q_t, liquid water mixing ratio q_ℓ, cloud droplet number concentration N_c, rain water mixing ratio q_r, and precipitation flux comparing LES from the Ackerman, VanZanten, et al., 2009 intercomparison paper (black) and in-situ observations (markers) to UWLCM run with Lagrangian particle (red) and double-moment bulk (blue) microphysics schemes. Solid lines and shading for UWLCM experiments indicate the mean and standard deviation across an ensemble of ten members each. Solid black lines show the LES models from Ackerman, VanZanten, et al., 2009 that included cloud water sedimentation, dashed lines show models that did not. In-situ observations from closed-cell stratocumulus, open-cell, and mixed are shown by filled circles, open circles, and star markers, respectively. Profiles are averaged over the last two hours of the six hour simulations.

For the superdroplet simulations, potential temperature (θ) and water vapor mixing ratio (q_v) are advected in the Eulerian coordinate system, while the Lagrangian component tracks the computational superdroplets. Because it is too burdensome to simulate each individual particle, particles with similar properties are grouped together into a single "superdroplet" and the multiplicity stands for the number of real particles each superdroplet represents. In addition to the multiplicity, each computational superdroplet has attributes of the particle location (x, y, z), dry radius cubed (r_d^3), wet radius cubed (r_w^3), and aerosol hygroscopicity (κ). The explicit droplet size distribution is represented, without artificial separation between interstitial aerosol, cloud droplets, and drizzle droplets. Details about the implementation are described in (Arabas et al., 2015).

UWLCM is run for the DYCOMS-II RF02 case study (Ackerman, VanZanten, et al., 2009) in the two-dimensional large-eddy simulation (LES) configuration in the x-z plane, to save on computational expense. Dziekan, Waruszewski, et al., 2019 showed that this approach is valid for the DYCOMS case when averaged over multiple realizations; we use ensembles of 5 simulations with random initial conditions. We use the standard DYCOMS-II RF02 dynamical setup (according to Ackerman, Toon, et al., 2000) with perturbed initial aerosol conditions. The initial liquid-water

potential temperature and total water mixing ratio profiles are prescribed as constant up to the inversion height, which is initialized at z_i = 795 m, and then increasing linearly and decaying exponentially, respectively. Large-scale forcings from horizontal divergence (subsidence) and radiation are prescribed. Surface sensible and latent heat fluxes are prescribed as constant, 16 and 93 Wm^{-2}, respectively, and horizontal winds are prescribed. Simulations are run for the prescribed 6 hours, with one hour of spinup during which precipitation formation is disabled. All plots of domain-averaged profiles shown throughout the manuscript are averaged over the last two hours of the simulation unless otherwise stated.

Figure 4.1 shows profiles of environmental, cloud, and precipitation variables from a standard DYCOMS-II RF02 simulation. Results from the UWLCM simulations with Lagrangian particle-based microphysics (red) and 2-moment bulk microphysics (blue) are shown compared to simulations from the Ackerman, VanZanten, et al., 2009 LES intercomparison paper (black) and aircraft observations from the flight campaign (symbols). In general, both microphysics schemes produce realistic results, in agreement with the few observations and with what other LES models produce. Differences between the two schemes are most notable in the rain statistics: the rain water mixing ratio, q_r is about 7x larger in the Lagrangian scheme than the bulk scheme; and the precipitation flux is about 13x larger. It is expected that the precipitation flux is larger, because the 2-moment bulk scheme does not include sedimentation of cloud water, whereas the Lagrangian scheme does. This difference between models was also noted in the Ackerman, VanZanten, et al., 2009 paper, and they divided the set of LES models into those which include cloud water sedimentation (solid lines) and those which do not (dashed lines). As seen in Figure 4.1f, amongst the other LES, the inclusion of cloud water sedimentation tended to increase the precipitation flux by about 5x. Although, the UWLCM 2-moment bulk scheme still is on the low end of the range for models that do not include cloud water sedimentation.

In the Ackerman, VanZanten, et al., 2009 LES description, the initial aerosol distribution is prescribed based on measurements made during the flights, as a bimodal distribution composed of ammonium sulfate with modes centered at r_a = 11 and 60 nm, with concentrations of N_a = 125 and 65 cm^{-3}, respectively (see black curve in Figure 4.2). In this study, we use an idealized single-mode aerosol initial distribution. This is done in part as an idealization, but also because by ignoring complications like multiple modes, giant CCN, size-dependent hygroscopicity, and

more, this situation is the most likely for a bulk scheme to be able to replicate. The prescribed aerosol distribution is varied between simulations by changing the number concentration, mean aerosol radius, and hygroscopicity. For each simulation, a single mode with fixed width (geometric standard deviation $\sigma = 1.2$) is used. This setup is quite idealized with a single narrow mode, which precludes any microphysical buffering (Feingold, 2003; McFiggans et al., 2006; Stevens and Feingold, 2009), and likely affects the results at least quantitatively; further studies are necessary to determine the extent to which this buffering may mute the hygroscopicity susceptibility.

In total, 54 experiments were performed, 27 with superdroplets and 27 with 2-moment bulk microphysics. The 27 experiments cover the parameter space of aerosol number concentration (N_a), mean aerosol radius (r_a), and aerosol hygroscopicity (κ). Number concentrations range from $N_a = 50, 100, 200$ cm^{-3}; mean radii range from $r_a = 10, 50, 100$ nm; hygroscopicities range from $\kappa = 0.1, 0.7, 1.3$.

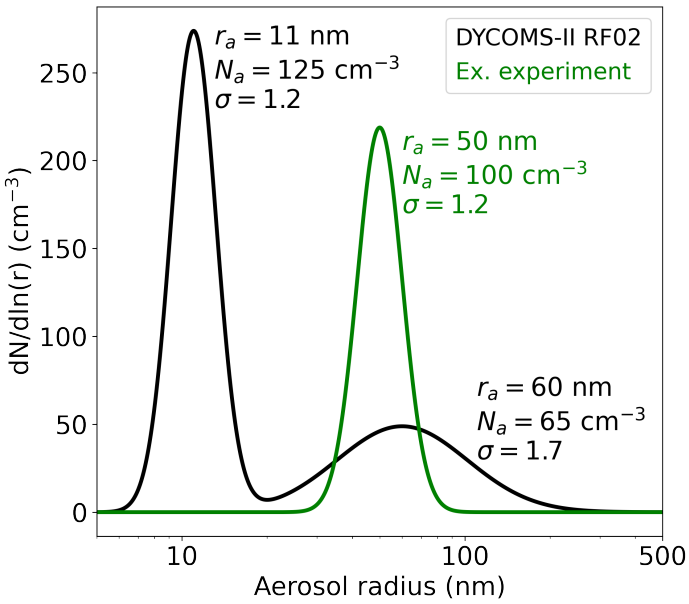

Figure 4.2: Aerosol distributions from DYCOMS-II RF02 measurements (black) and an example from experiment 11x in green. The measured aerosol is bimodal, while the prescribed idealized experimental aerosol is unimodal. Across the experiments, the mean radius, number concentration, and hygroscopicity of the single mode are varied, but the width of the aerosol distribution is fixed at $\sigma = 1.2$.

These idealized aerosol configurations were chosen to probe the full space of possibilities from very clean, to more polluted marine environments. However, they

are not necessarily very realistic. Of course, in the real atmosphere, one expects composition to be correlated with size in many cases due to the emissions sources of these particles: for instance, primary emission of sea salt aerosols from sea spray are both large in size and very hygroscopic. And very polluted marine conditions, with large N_a, might be preferential due to e.g. anthropogenic shipping emissions, which will then be predominantly sulfate aerosols with moderate hygroscopicity. However, these idealized experiments are still useful and interesting by allowing us to untangle these three factors: concentration, size, and composition, and explore the dynamics of the idealized aerosol-cloud system.

4.3 Results from simulations with particle-based microphysics

An illustrative example

To begin with an expected result, we first present an illustrative example of how cloud properties and precipitation vary as aerosol number concentration (N_a) is increased. Figure 4.3 shows profiles of cloud and precipitation metrics from experiments with N_a = 50, 100, and 200 cm^{-3} and mean aerosol radius and hygroscopicity of intermediate values r_a = 50 nm and κ = 0.7.

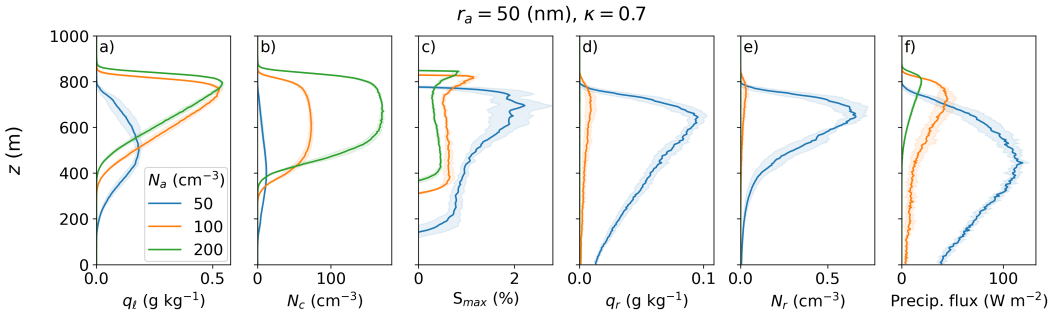

Figure 4.3: Profiles averaged over the last two hours of a six hour simulation from three experiments with the same aerosol mean radius (r_a = 50 nm) and same aerosol composition (κ = 0.7), but varying aerosol number concentration (N_a = 50, 100, 200 cm^{-3}). Subplots show a) liquid water mixing ratio q_ℓ, b) cloud droplet number concentration (N_c), c) maximum supersaturation S_{max}, d) rain water mixing ratio q_r, e) rain droplet number concentration (N_r), and f) precipitation flux. Solid lines and shading indicate the mean and standard deviation from ensembles of five members each.

Across these three experiments, the cloud droplet number concentration (N_c) increases with N_a (Figure 4.3b), indicating that these cases fall into an aerosol-limited regime (Reutter et al., 2009). The cloud liquid water mixing ratio q_ℓ increases with N_a, but saturates due to thermodynamic constraints for N_a = 200 cm^{-3} (Figure 4.3a).

Especially in the case of $N_a = 50$ cm^{-3}, the paucity of aerosols is not sufficient to drive down supersaturations, which can be up to 2% in the cloud (Figure 4.3c). Furthermore, fewer total aerosols means there are especially fewer large aerosols in the tail of the distribution; but since large aerosols have a dominant effect on reducing supersaturations by forming drizzle embryos, this can further emphasize the difference in experiments with varying N_a. This causes rapid droplet growth and rain formation, leading to more precipitation in the experiments with fewer aerosols (Figure 4.3d).

Overview of the parameter space

Liquid water path, LWP

We now present an overview of the 27 experiments spanning a large range of parameter space for aerosol number concentration, size, and chemical composition.

Figure 4.4 shows time series plots of liquid water path (LWP) for all 27 experiments. The experiments are arranged in a 3x3 table with N_a sorted by rows, r_a sorted by columns, and κ shown by the different colored lines. From these figures, we can see that all but the experiments h and i have reached a quasi steady-state after 4 hours. Experiments h and i with relatively large, but few aerosols, which very efficiently precipitate and lose liquid water without reaching an equilibrium. We see that experiments with very small and relatively fewer aerosols (d, g) also have larger precipitation loss of liquid water, but do reach a new equilibrium in a state with a thinner cloud.

From all the experiments, we can tell that there is more variability between experiments with different N_a and r_a than hygroscopicity (note that the y-axes vary between subplots). In general, the LWP is largest for experiments with large r_a and moderate N_a (e, f), compared to experiments with large r_a and N_a (b, c).

The LWP dependence on aerosol parameter values is summarized in Figure 4.5. Each subplot shows steady-state LWP for fixed hygroscopicity across the range of aerosol size and number concentration. First, we can notice that the shapes of the LWP contour surfaces are very similar for aerosols of varying composition. Similarly, we see that the liquid water path range is about the same, from 50 gm^{-2} to 160 gm^{-2}, with the minima occurring for the smallest, fewest aerosols, and the maximum occurring for moderately sized and moderate concentrations. In all cases, the liquid water path stays very constant when mean aerosol radius is varied between 50 to 100 nm (horizontal contours in Figure 4.5abc).

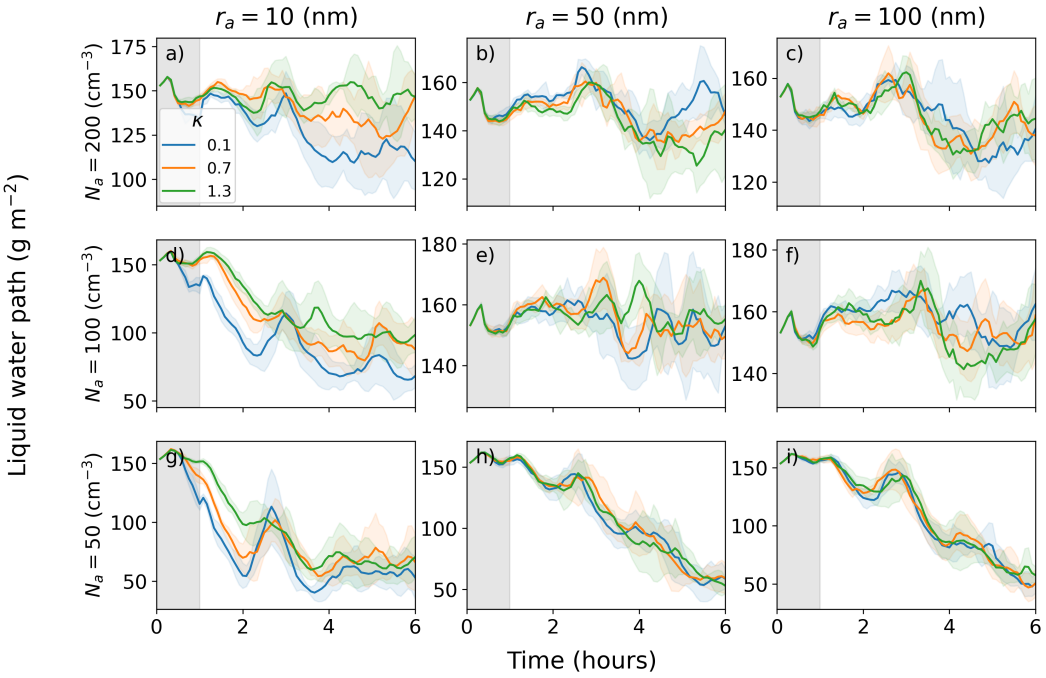

Figure 4.4: Time series of liquid water path from all 27 experiments with Lagrangian microphysics. Columns show experiments with fixed aerosol mean radius (left: $r_a = 10$ nm, center: $r_a = 50$ nm, right: $r_a = 100$ nm). Rows show experiments with fixed aerosol number concentration (top: $N_a = 200$ cm^{-3}, middle: $N_a = 100$ cm^{-3}, bottom: $N_a = 50$ cm^{-3}). Colored lines indicate experiments with different aerosol composition (blue: $\kappa = 0.1$, orange: $\kappa = 0.7$, green: $\kappa = 1.3$). Solid lines and shading indicate the mean and standard deviation from ensembles of five members each. Grey shaded region shows spinup period during the first hour of the simulation where precipitation is disabled.

The subtle differences however between aerosol compositions are also interesting. For one, the most hygroscopic aerosols, $\kappa = 1.3$, show the most pronounced maximum in LWP, peaked sharply at moderate r_a and N_a, while the least hygroscopic aerosols, $\kappa = 0.1$, show a broader maximum, with equivalent LWP for moderate to large r_a. Another interesting point is to look at the gradient of LWP for small aerosol sizes. We see that for $\kappa = 0.1$ the contours are nearly vertical, indicating that for very small aerosols $r_a = 10$ nm the LWP hardly depends on the number concentration. But for more hygroscopic aerosol, $\kappa = 0.7$ and 1.3, the contours are less vertical, indicating that there is some sensitivity to number concentration in these regimes.

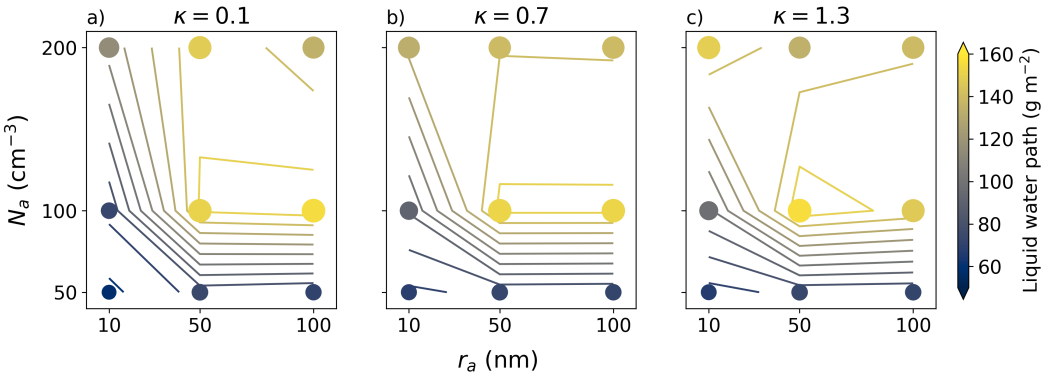

Figure 4.5: Liquid water path for each aerosol mean radius and aerosol number concentration. Scatter points are colored and sized according to the liquid water path. Contours are added for additional interpretability. Experiments with different hygroscopicity are shown in each subplot: a) $\kappa = 0.1$, b) $\kappa = 0.7$, c) $\kappa = 1.3$. Liquid water path is time-averaged over the last 2 (of 6) hours of each simulation.

Cloud droplet number concentration, N_c

Figure 4.6 shows time-averaged profiles of N_c for all 27 simulations. The x-axes are scaled to be the same for each row of experiments with constant N_a; this highlights cases where $N_c \approx N_a$ (aerosol-limited regime) compared to cases where $N_c \ll N_a$ (updraft-limited regime). In all experiments, $N_{c,\max}$ increases with κ, within the noise (indicated by variation between ensemble members as 1σ shading). All experiments except f, h, and i show visible differences in N_c between $\kappa = 0.1$ and larger κ.

In experiments with moderate to large aerosols and moderate to high number concentrations (b,c,e,f), the maximum droplet concentrations N_c, indicating a very high activated fraction, or aerosol-limited regime. But for smaller aerosols ($r_a < 50$ nm), and for $N_a = 50$ cm^{-3}, N_c is significantly less than N_a. For the case of the smallest aerosol loading, this can be attributed to precipitation. But for experiments a and d, this is simply due to these clouds being in an updraft-limited regime, where the vertical velocity is not strong enough to produce supersaturations necessary to activate these smaller aerosols. In the canonical framework of aerosol- vs. updraft-limited regimes introduced by Reutter et al., 2009, this space is characterized by only two-dimensions, not explicitly considering the aerosol size or composition. But here, we see that both of these additional properties can matter, and shift the transition zone between regimes. For example, in experiments b and e, the reduction of κ to 0.1 also shifts the cloud out of the aerosol-limited regime, into the updraft-limited

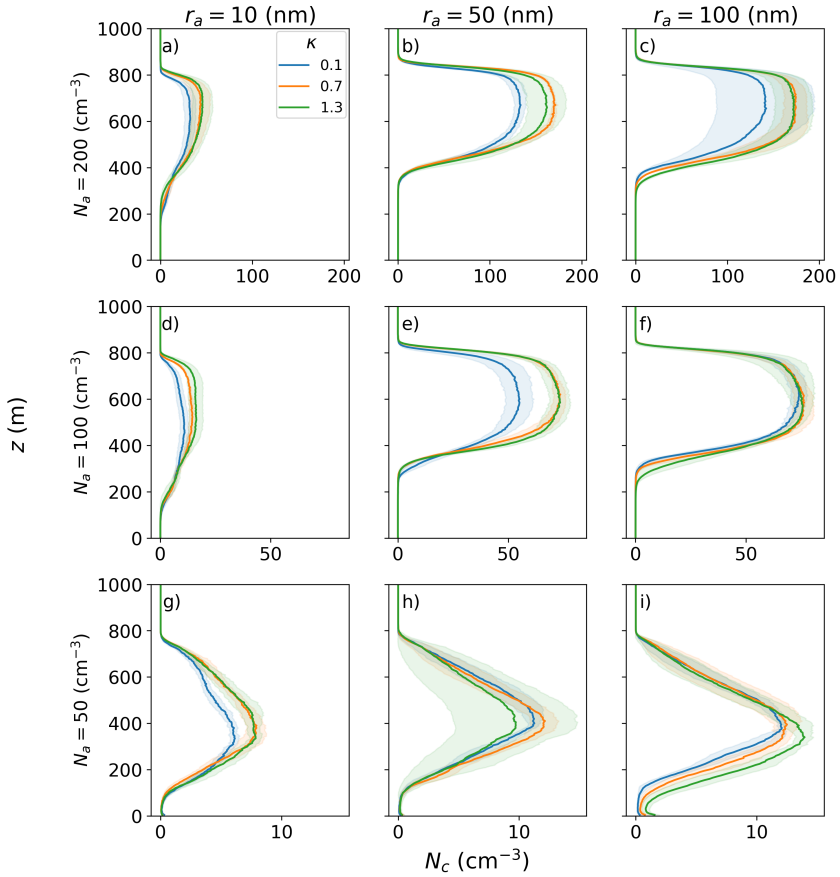

Figure 4.6: Profiles of cloud droplet number concentration (N_c) from all 27 simulations. Like Figure 4.4, columns show experiments with fixed aerosol mean radius (left: r_a = 10 nm, center: r_a = 50 nm, right: r_a = 100 nm). Rows show experiments with fixed aerosol number concentration (top: N_a = 200 cm^{-3}, middle: N_a = 100 cm^{-3}, bottom: N_a = 50 cm^{-3}). Note that the x-axis scale is consistent for each row, but varied between rows, to highlight difference is N_c due to r_a, but allow for expected differences between experiments of varying N_a (as N_c cannot be larger than N_a). Colored lines indicate experiments with different aerosol composition (blue: κ = 0.1, orange: κ = 0.7, green: κ = 1.3). Profiles are averaged over the last 2 (of 6) hours of the simulation. Solid lines and shading indicate the mean and standard deviation from ensembles of five members each.

regime.

Experiments with N_a = 50 cm^{-3} (g, h, i) show vertical profiles with more gradual transitions in N_c and very low cloud base, indicative of the broken stratocumulus clouds. In these experiments, the clouds are precipitating and significantly depleted of liquid water. Additionally, as shown in Figure 4.4, experiments h and i are not in steady-state, with the LWP continually declining in the last two hours of the

simulation. The shape of the N_c profiles changes from having a well-defined cloud base and "U" shape, to a "V" shape due to precipitation.

Figure 4.7 summarizes these results, showing the vertically mass-weighted mean droplet number concentration (mean N_c) for different r_a and N_a. Like Figure 4.5, the three subplots showing the N_c surface for different κ values look very similar. Droplet concentrations range from 0 cm^{-3} for very few, small aerosols, to almost 150 cm^{-3} for many, larger aerosols. For $\kappa = 0.1$ (Figure 4.7a), the maximum N_c is lower, only around 110 cm^{-3}.

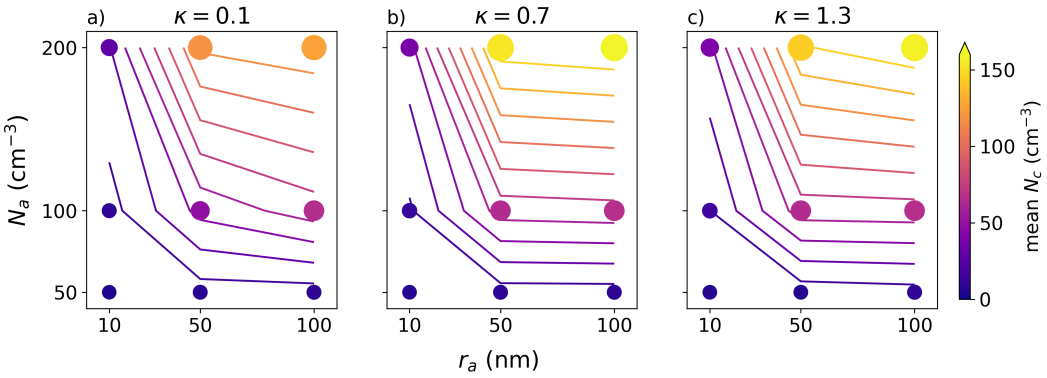

Figure 4.7: Like Figure 4.5, but for cloud droplet number concentration (N_c). Mean N_c is mass-weighted in the vertical.

Across the range of κ values, N_c is hardly sensitive to increases of r_a past 50 nm, shown by the nearly horizontal contours on the right side of each subplot. But for smaller aerosols, the droplet number concentration will increase (by up to 325% for a 5x increase in r_a) for fixed N_a. The sloped contours on these plots further demonstrate how aerosol radius can act as another dimension in the aerosol- vs. updraft-limited regime space, whereby an aerosol-limited regime can become more updraft-limited if the aerosols are smaller, and vice versa.

Hygroscopicity susceptibility

Both LWP and N_c are most sensitive to aerosol hygroscopicity in the regime of small aerosols, especially at moderate number concentrations (Figure 4.8). The LWP can increase up to 25% per unit change in κ in this regime, and the N_c can increase up to 45%. We define a hygroscopicity susceptibility,

$$S_x = \partial \ln x / \partial \kappa, \tag{4.2}$$

defined as the percentage change in x for unit change in κ (here x is either LWP or N_c). This susceptibility is mostly positive for N_c across the parameter space, excluding

a small regime of very few, larger aerosols (Figure 4.8b, bottom center). However, LWP exhibits negative susceptibility for all experiments when $r_a > 50$ nm. A positive susceptibility indicates that increases in aerosol hygroscopicity will increase the LWP or N_c, which is expected, because more hygroscopic aerosols are more easily activated. A negative susceptibility means that more easily activated aerosols counter-intuitively lead to few droplets or less cloud water.

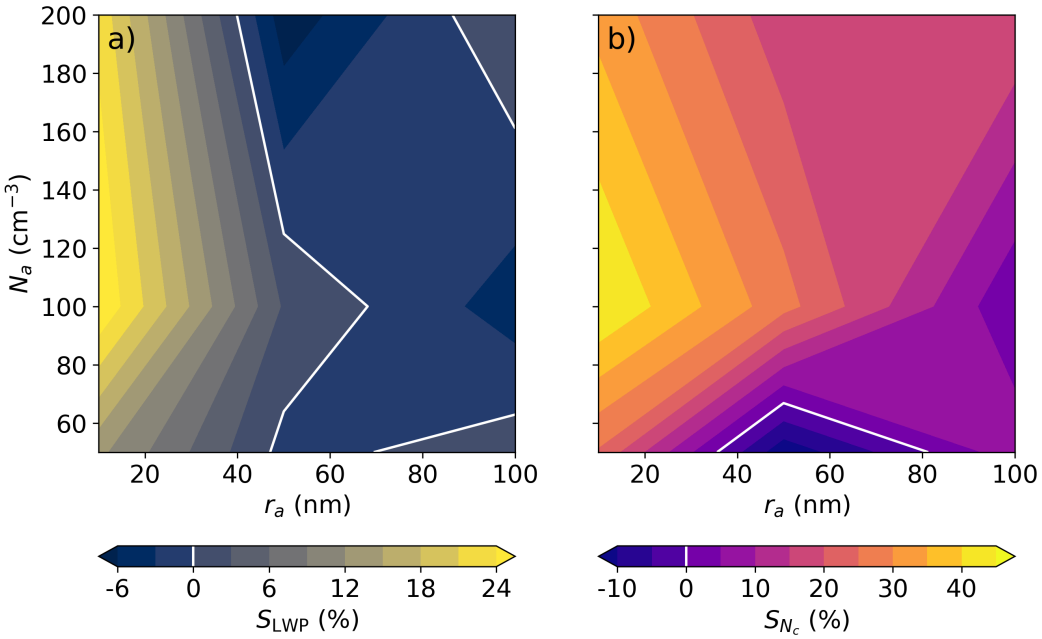

Figure 4.8: Contours of a) LWP susceptibility (S_{LWP}, the percentage change in LWP for unit change in κ) and b) N_c susceptibility (S_{N_c}) for each aerosol mean radius and aerosol number concentration. White contour lines indicate the zero line to highlight regimes of negative susceptibility.

Negative susceptibilities arise here because the more hygroscopic aerosols lead to cloud droplets that grow faster from condensation and collisions which results in enhanced precipitation efficiency, and ultimately less cloud liquid and fewer cloud droplets. S_{LWP} is positive for small r_a because these small particles are difficult to activate, and increasing their hygroscopicity will help them activate and form thicker clouds; S_{LWP} becomes negative for larger r_a because these sized aerosols are already easily activatable, and increasing their hygroscopicity helps them grow "too quickly" one might say, because then the clouds rain out.

4.4 Comparison with 2-moment bulk scheme

Figure 4.9 shows timeseries of the difference in liquid water path between the 2-moment bulk simulations and the Lagrangian particle simulations. For all equilibrated experiments (all but h and i), the LWP is smaller in the bulk simulation compared to the Lagrangian.

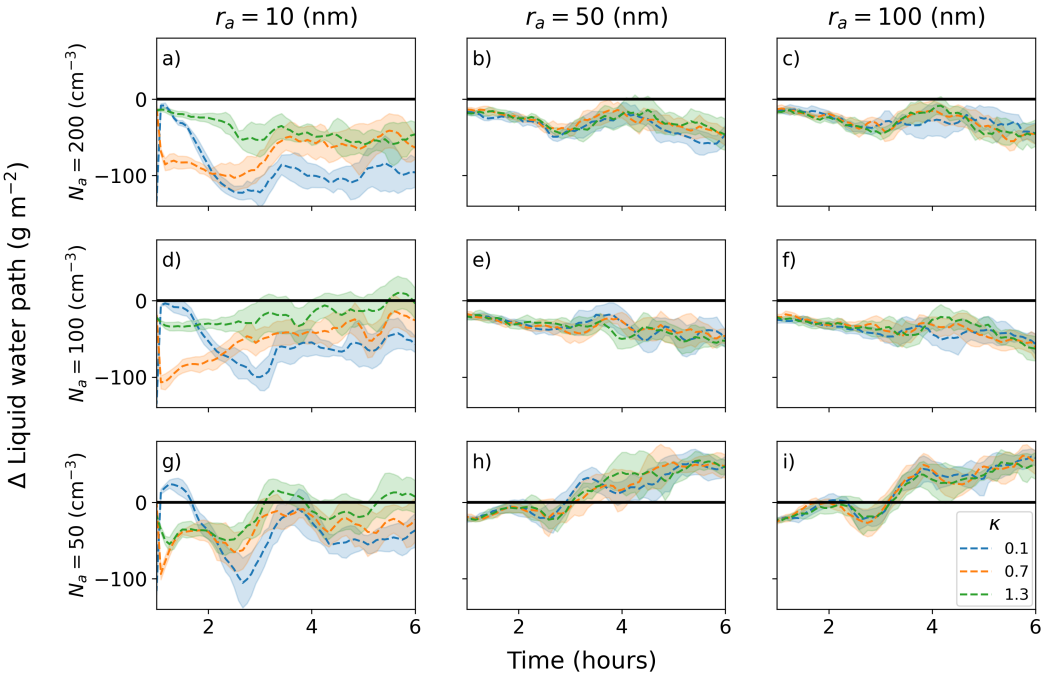

Figure 4.9: Like Figure 4.4, but showing difference in liquid water path between 2-moment bulk simulations and Lagrangian particle simulations. Dashed lines and shading indicate the mean and combined standard deviation from ensembles of five members each. Spinup period (first hour) is not shown for brevity.

For all experiments with $r_a \geq 50$ nm, the bulk simulations do not reach equilibrium, but evolve relatively slowly, with LWP declining from around 150 to 100 gm^{-2} over the 6 hours (see Figure 4.12). In experiments h and i, where the Lagrangian simulations do not reach steady-state and have continually declining LWPs over the 6 hour simulation, the bulk LWP is declining more slowly, and thus the difference shifts from negative to positive around hour 3. In general, for this regime of moderate to large r_a, the LWP between the two schemes is similar, and the sensitivity to aerosol properties is consistent.

For experiments with $r_a = 10$ nm, the differences between the two schemes are much larger, and most notable for experiment a with many, small aerosols. The time evolution of LWP between the schemes is quite different: the Lagrangian simulations

evolve slowly reaching steady-state around hour 4, while the bulk simulations evolve quickly and reach a steady-state by hour 2 (also seen in Figure 4.12). For these experiments, with the Lagrangian scheme, the LWP tends to be very similar for all values of κ, but depends strongly on the aerosol number concentration N_a. While for the 2-moment bulk scheme, the opposite is true, where the LWP depends more strongly on κ than it does on N_a. However, despite these large differences, the sign of sensitivity (to N_a, r_a, and κ) is the same between the two schemes (see Figure 4.13 for a summary).

Figure 4.10 shows profiles of cloud droplet number concentration N_c from the 2-moment bulk simulations, overlaid on the Lagrangian simulations. For better comparison between the two schemes, the profiles are plotted in a normalized height coordinate, z/z_t, where the cloud tops are aligned (cloud top is defined as the maximum altitude with $N_c \geq N_{c,\max}/2$); the two schemes show slightly offset cloud top altitudes, which is likely due again to the difference in that they do or do not include cloud water sedimentation. Unlike Figure 4.6, the scale on the x-axes are all different, to highlight differences between experiments with different κ and between the two schemes.

First, we can compare the experiments where the two schemes perform similarly: b, c, e, and f. These experiments, with moderate to large aerosols ($r_a \geq 50$ nm) and moderate to high number concentrations ($N_a \geq 100$ cm^{-3}), show very similar values of cloud droplet number concentration in both magnitude and sensitivity to κ. Specifically, experiments c and f with $r_a = 100$ nm show very little sensitivity to κ, and $N_c \approx N_a$, indicating they are in the aerosol-limited regime. Experiments b and e with $r_a = 50$ nm show smaller N_c for $\kappa = 0.1$, but no sensitivity between $\kappa = 0.7$ and 1.3; this demonstrates again how hygroscopicity changes have the ability to shift a cloud between the aerosol- and updraft-limited regimes.

For the experiments where the two schemes disagree substantially, we can focus first on h and i, where the Lagrangian scheme has significant precipitation, while the bulk scheme does not (see also Figures 4.9 and 4.12). In the bulk results, the N_c response for $N_a = 50$ cm^{-3} is very similar to the response for larger N_a (h is similar to b and e, and i is similar to c and f); but in the Lagrangian results, N_c is very depleted ($\ll N_a$) in both experiments and there is no sensitivity to κ.

The experiments with $r_a = 10$ nm (a, d, g) are also very different between the two schemes, specifically in the sensitivity of the N_c to κ. However, both schemes show that these experiments with very small aerosols are always in an updraft-limited

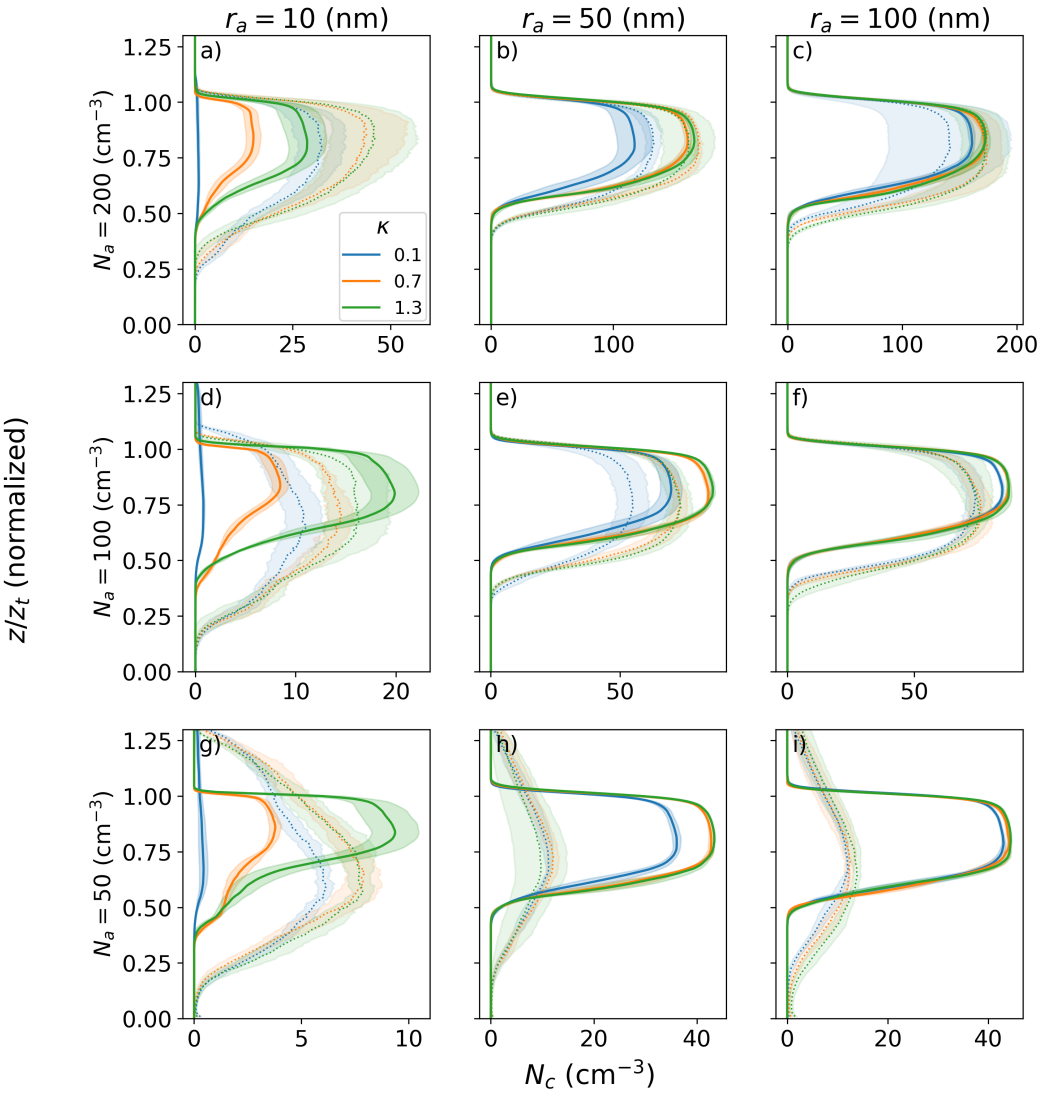

Figure 4.10: Like Figure 4.6, but showing 2-moment bulk simulations (solid) overlaid on Lagrangian particle simulations (dotted). Note that the x-axis varies for each subplot to best showcase differences between the schemes and for varying κ. All profiles are averaged over the last 2 (of 6) hours of the simulation. Lines and shading indicate the mean and standard deviation from ensembles of five members each.

regime ($N_c \ll N_a$), regardless of N_a or κ. For the Lagrangian simulations, we see that there is sensitivity to $\kappa = 0.1$, but little difference between $\kappa = 0.7$ and 1.3, for all N_a. For the bulk simulations however, we see very strong sensitivity to κ for all values of κ and for all N_a. And for $r_a = 10$ nm and $\kappa = 0.1$ in the 2-moment bulk simulations, $N_c \approx 1$ cm^{-3}. See Figure 4.14 for a summary of N_c response to N_a and r_a in the 2-moment bulk scheme.

Comparison: Hygroscopicity susceptibility

The patterns of hygroscopicity susceptibilities shown in Figure 4.8 are very interesting, particularly the region of negative LWP susceptibility, where LWP decreases with increasing κ. In this section, we will explore how the 2-moment bulk scheme can resolve these hygroscopicity susceptibilities. As we have seen already in Figures 4.9 and 4.10, the absolute value of LWP or N_c between the schemes can be quite different, or the magnitude of response to changing aerosol properties can be quite different, which makes these comparisons sometimes challenging. To overcome this challenge, in addition to comparisons of the response magnitudes, we will focus on the patterns of response, which is a more fair comparison between schemes.

Figure 4.11 shows the same hygroscopicity susceptibilities S_{LWP} and S_{N_c} as Figure 4.8, but for the 2-moment bulk scheme. The first very notable difference is the magnitude of S_x, indicated by the colorbar scales, which is substantially larger than for the Lagrangian simulations. The huge values here are seen in the experiments with $r_a = 10$ nm, where the cloud is nearly depleted and LWP and N_c are both near 0.

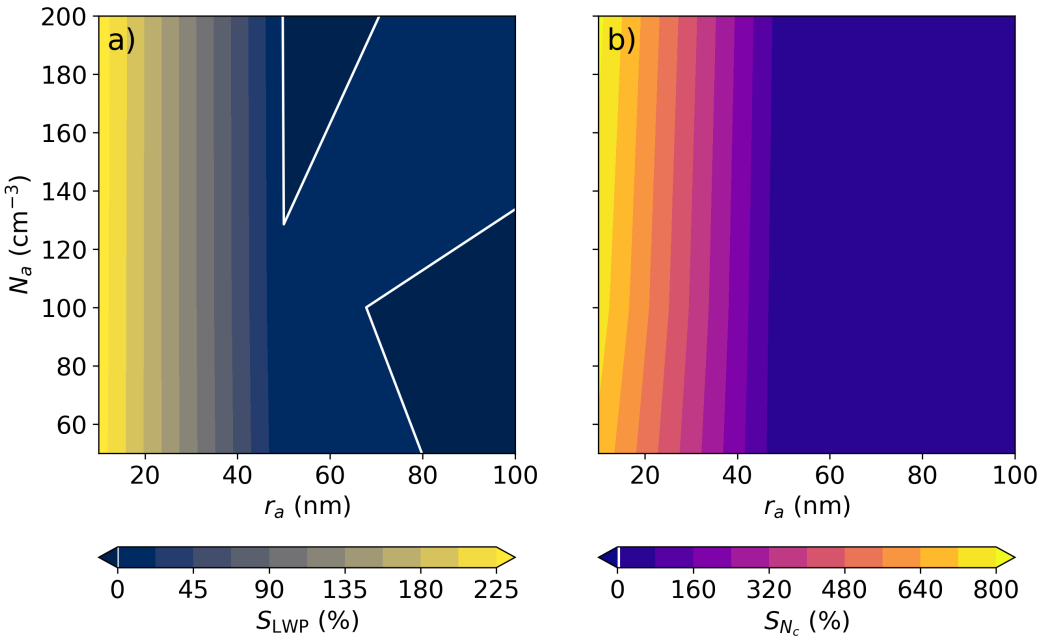

Figure 4.11: Like Figure 4.8, but for 2-moment bulk scheme.

The second notable difference is that the contours here are almost entirely vertical (S_x does not depend on N_a), compared to Figure 4.8, where there was variation of S_{LWP} and S_{N_c} in experiments with the same r_a but different N_a.

However, one key similarity is that the region of negative (or very small) S_{LWP} for $r_a \geq 50$ nm seen in the Lagrangian experiments is retained in the 2-moment bulk experiments. This very interesting feature came about from experiments where changing κ had a notable effect on hygroscopic growth, leading to enhanced precipitation and depleted cloud water. That this feature is seen by both schemes is reassuring and indicative that the physical mechanism is robust to varied resolution of the size spectrum and microphysical processes.

4.5 Conclusions

Stratocumulus cloud brightness, which exerts strong control on global climate through the clouds' shortwave radiative effects, is modulated by aerosol properties. It has been noted for over 50 years that the number concentration of aerosol particles is a key element in determining cloud albedo through its control on cloud droplet size and precipitation. In this study, we highlight the importance also of aerosol size and chemical composition on the macrophysical cloud properties.

We first presented results from the University of Warsaw Lagrangian Cloud Model (UWLCM) using a Lagrangian particle-based representation of the microphysics. With the Lagrangian scheme, we saw that variations hygroscopicity have the ability to change liquid water path (LWP) and cloud droplet number concentration (N_c) by up to 25% and 40%, respectively, with the largest changes occurring in the regime of very small aerosols. Furthermore, even when changes were smaller magnitude, variations in aerosol hygroscopicity still contributed to shifts of the cloud from an aerosol- to updraft-limited regime.

Our comparison between the particle-based microphysics scheme and a classic two-moment bulk scheme revealed distinct differences in their ability to capture the effects of aerosol hygroscopicity. Overall, the Lagrangian and bulk schemes had many differences in the magnitude of LWP or precipitation predicted for various aerosol conditions. Some of these discrepancies may be from structural differences in the models (their representation of the size distributions, inclusion of sedimentation of cloud droplets, and more), while other differences surely stem from differences in assumed rates (e.g., accretion rates in the bulk scheme are not tuned to match the collision kernel assumed in the Lagrangian scheme). But in terms of relative sensitivity to variations in aerosol properties, the bulk scheme was often in agreement with the Lagrangian scheme. In particular, it was able to capture the region of negative LWP susceptibility to hygroscopicity found for larger aerosol

sizes. However, it proved to be significantly oversensitive in cases involving small aerosol sizes. This disparity underscores the limitations of traditional schemes in accurately representing the intricate interplay between aerosols and cloud dynamics.

Code and data availability. The UWLCM, libmpdata++, and libcloudph++ source codes are available at `https://github.com/igfuw`.

Acknowledgements. Thank you to Piotr Dziekan for help with the UWLCM code. Thank you to Anna Jaruga, Emily K. de Jong, and Raymond A. Shaw for helpful discussions and feedback. The computations presented here were conducted in the Resnick High Performance Center, a facility supported by Resnick Sustainability Institute at the California Institute of Technology.

4.6 Appendix A: Supplemental figures

References

[1] G. Myhre et al. "Anthropogenic and Natural Radiative Forcing". In: *Climate Change 2013: The Physical Science Basis. Contribution of Working Group I to the Fifth Assessment Report of the Intergovernmental Panel on Climate Change*. Ed. by T. Stocker et al. Cambridge, United Kingdom and New York, NY, USA: Cambridge University Press, 2013. Chap. 8, pp. 659–740.

[2] J. H. Seinfeld et al. "Improving our fundamental understanding of the role of aerosol-cloud interactions in the climate system". In: *Proceedings of the National Academy of Sciences* 113.21 (2016), pp. 5781–5790. DOI: 10.1073/pnas.1514043113.

[3] D. Rosenfeld et al. "Aerosol-driven droplet concentrations dominate coverage and water of oceanic low-level clouds". In: *Science* 363.6427 (2019), eaav0566. DOI: 10.1126/science.aav0566.

[4] Y. Sato and K. Suzuki. "How do aerosols affect cloudiness?" In: *Science* 363.6427 (2019), pp. 580–581. DOI: 10.1016/B978-0-12-374347-3.X0001-7.

[5] V. Toll et al. "Weak average liquid-cloud-water response to anthropogenic aerosols". In: *Nature* 572.7767 (2019), pp. 51–55. DOI: 10.1038/s41586-019-1423-9.

[6] W. W. Grabowski, H. Morrison, et al. "Modeling of Cloud Microphysics: Can We Do Better?" In: *Bulletin of the American Meteorological Society* 100.4 (2019), pp. 655–672. DOI: 10.1175/BAMS-D-18-0005.1.

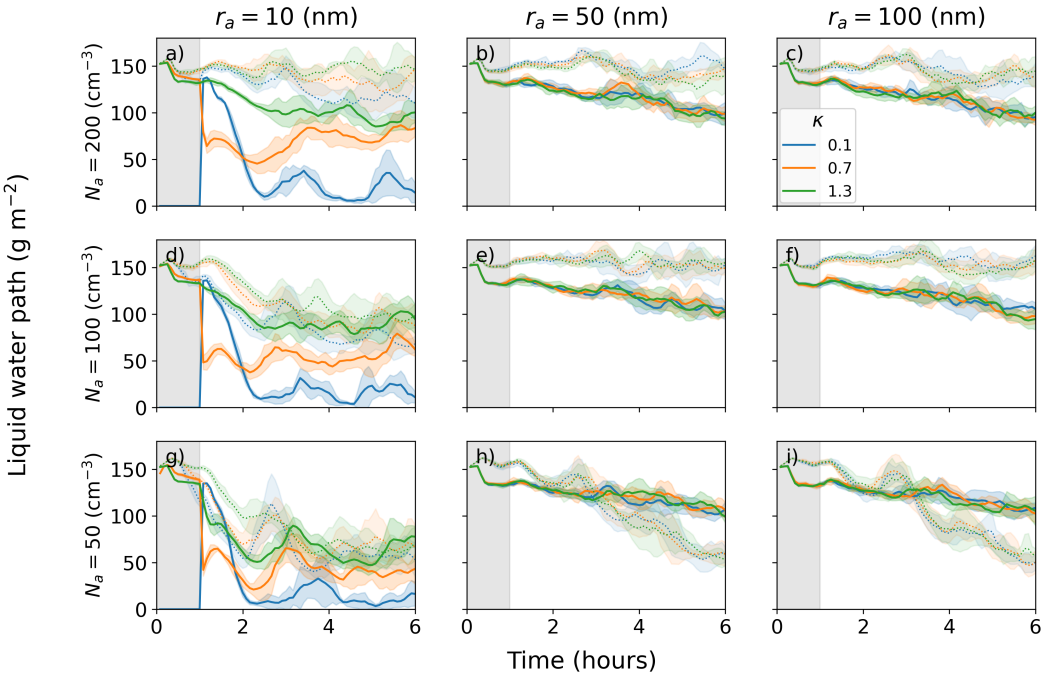

Figure 4.12: Time series of liquid water path from all 54 experiments. Solid lines show results from the 2-moment bulk scheme and dotted lines from the Lagrangian scheme. Columns show experiments with fixed aerosol mean radius (left: r_a = 10 nm, center: r_a = 50 nm, right: r_a = 100 nm). Rows show experiments with fixed aerosol number concentration (top: N_a = 200 cm^{-3}, middle: N_a = 100 cm^{-3}, bottom: N_a = 50 cm^{-3}). Colored lines indicate experiments with different aerosol composition (blue: κ = 0.1, orange: κ = 0.7, green: κ = 1.3). Shading indicate and standard deviation from ensembles of five members each. Grey shaded region shows spinup period during the first hour of the simulation where precipitation is disabled. Unlike Figure 4.4, the y-axis scale on all subplots is the same.

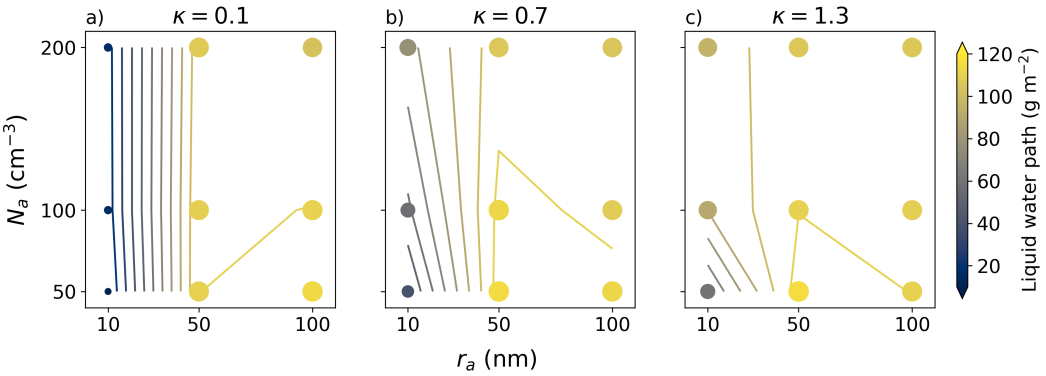

Figure 4.13: Like Figure 4.5, but for the 2-moment bulk scheme.

[7] I. Bulatovic et al. “Aerosol Indirect Effects in Marine Stratocumulus: The Importance of Explicitly Predicting Cloud Droplet Activation”. In: *Geo-*

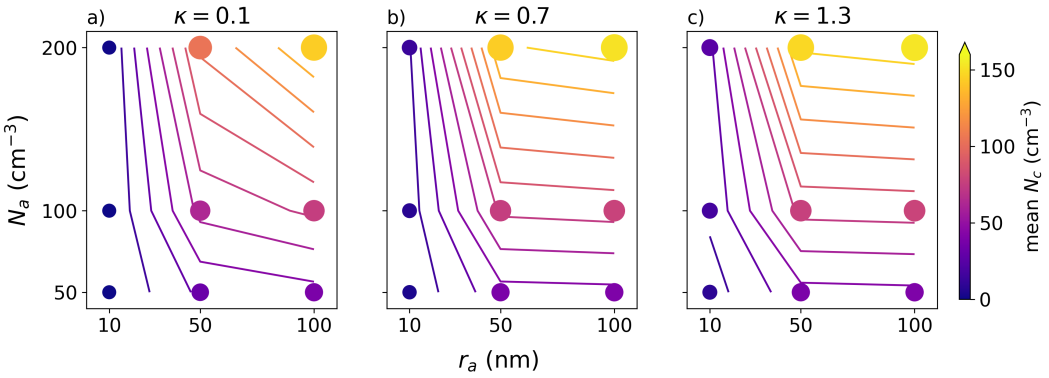

Figure 4.14: Like Figure 4.7 but for the 2-moment bulk scheme.

physical Research Letters 46.6 (2019), pp. 3473–3481. DOI: 10.1029/2018GL081746.

[8] S.-I. Shima et al. "The super-droplet method for the numerical simulation of clouds and precipitation: a particle-based and probabilistic microphysics model coupled with a non-hydrostatic model". In: *Q. J. R. Meteorol. Soc.* 135.642 (2009), pp. 1307–1320. DOI: 10.1002/qj.441.

[9] M. Andrejczuk et al. "Cloud-Aerosol Interactions for Boundary Layer Stratocumulus in the Lagrangian Cloud Model". In: *Journal of Geophysical Research* 115.D22 (2010), p. D22214. DOI: 10.1029/2010JD014248.

[10] F. Hoffmann, S. Raasch, et al. "Entrainment of Aerosols and Their Activation in a Shallow Cumulus Cloud Studied with a Coupled LCM–LES Approach". In: *Atmospheric Research* 156 (2015), pp. 43–57. DOI: 10.1016/j.atmosres.2014.12.008.

[11] W. W. Grabowski, P. Dziekan, et al. "Lagrangian Condensation Microphysics with Twomey CCN Activation". In: *Geoscientific Model Development* 11 (2018), pp. 103–120. DOI: 10.5194/gmd-11-103-2018.

[12] A. A. Hill et al. "Toward a Numerical Benchmark for Warm Rain Processes". In: *Journal of the Atmospheric Sciences* 80.5 (2023), pp. 1329–1359. DOI: 10.1175/JAS-D-21-0275.1.

[13] R. A. Zaveri et al. "Model for Simulating Aerosol Interactions and Chemistry (MOSAIC)". In: *Journal of Geophysical Research* 113.D13 (2008), p. D13204. DOI: 10.1029/2007JD008782.

[14] N. Riemer et al. "Simulating the Evolution of Soot Mixing State with a Particle-resolved Aerosol Model". In: *Journal of Geophysical Research* 114.D9 (2009), p. D09202. DOI: 10.1029/2008JD011073.

[15] J. Tian et al. "Modeling the Evolution of Aerosol Particles in a Ship Plume Using PartMC-MOSAIC". In: *Atmospheric Chemistry and Physics* 14.11 (2014), pp. 5327–5347. DOI: 10.5194/acp-14-5327-2014.

[16] A. Zuend, C. Marcolli, B. P. Luo, et al. “A Thermodynamic Model of Mixed Organic-Inorganic Aerosols to Predict Activity Coefficients”. In: *Atmospheric Chemistry and Physics* 8.16 (2008), pp. 4559–4593. DOI: 10.5194/acp-8-4559-2008.

[17] A. Zuend, C. Marcolli, A. M. Booth, et al. “New and Extended Parameterization of the Thermodynamic Model AIOMFAC: Calculation of Activity Coefficients for Organic-Inorganic Mixtures Containing Carboxyl, Hydroxyl, Carbonyl, Ether, Ester, Alkenyl, Alkyl, and Aromatic Functional Groups”. In: *Atmospheric Chemistry and Physics* 11.17 (2011), pp. 9155–9206. DOI: 10.5194/acp-11-9155-2011.

[18] E. K. de Jong et al. “New Developments in PySDM and PySDM-examples v2: Collisional Breakup, Immersion Freezing, Dry Aerosol Initialization, and Adaptive Time-Stepping”. In: *Journal of Open Source Software* 8.84 (2023), p. 4968. DOI: 10.21105/joss.04968.

[19] A. Jaruga and H. Pawlowska. “Libcloudph++ 2.0: Aqueous-Phase Chemistry Extension of the Particle-Based Cloud Microphysics Scheme”. In: *Geoscientific Model Development* 11 (2018), pp. 3623–3645. DOI: 10.5194/gmd-11-3623-2018.

[20] R. Wood. “Stratocumulus Clouds”. In: *Monthly Weather Review* 140.8 (2012), pp. 2373–2423. DOI: 10.1175/MWR-D-11-00121.1.

[21] D. A. Randall et al. “Outlook for research on subtropical marine stratification clouds”. In: *Bull. Amer. Meteor. Soc.* 65 (1984), pp. 1290–1301.

[22] T. Schneider et al. “Possible Climate Transitions from Breakup of Stratocumulus Decks under Greenhouse Warming”. In: *Nature Geoscience* 12.3 (2019), pp. 163–167. DOI: 10.1038/s41561-019-0310-1.

[23] S. Twomey. “Pollution and the Planetary Albedo”. In: *Atmospheric Environment (1967)* 8.12 (1974), pp. 1251–1256. DOI: 10.1016/0004-6981(74)90004-3.

[24] S. Twomey. “The Influence of Pollution on the Shortwave Albedo of Clouds”. In: *Journal of the Atmospheric Sciences* 34.7 (1977), pp. 1149–1152. DOI: 10.1175/1520-0469(1977)034<1149:TIOPOT>2.0.CO;2.

[25] R. Wood, C. S. Bretherton, et al. “An Aircraft Case Study of the Spatial Transition from Closed to Open Mesoscale Cellular Convection over the Southeast Pacific”. In: *Atmospheric Chemistry and Physics* 11 (2011), pp. 2341–2370. DOI: 10.5194/acp-11-2341-2011.

[26] R. Wood, D. Leon, et al. “Precipitation driving of droplet concentration variability in marine low clouds”. In: *J. Geophys. Res* 117 (2012), p. 19210. DOI: 10.1029/2012JD018305.

[27] J. Kazil et al. “Mesoscale Organization, Entrainment, and the Properties of a Closed-Cell Stratocumulus Cloud”. In: *Journal of Advances in Modeling Earth Systems* 9.5 (2017), pp. 2214–2229. DOI: 10.1002/2017MS001072.

[28] F. Glassmeier and G. Feingold. “Network Approach to Patterns in Stratocumulus Clouds”. In: *Proceedings of the National Academy of Sciences* 114.40 (2017), pp. 10578–10583. DOI: 10.1073/pnas.1706495114.

[29] F. Glassmeier, F. Hoffmann, et al. “An Emulator Approach to Stratocumulus Susceptibility”. In: *Atmospheric Chemistry and Physics* 19.15 (2019), pp. 10191–10203. DOI: 10.5194/acp-19-10191-2019.

[30] A. S. Ackerman, M. C. VanZanten, et al. “Large-Eddy Simulations of a Drizzling, Stratocumulus-Topped Marine Boundary Layer”. In: *Monthly Weather Review* 137.3 (2009), pp. 1083–1110. DOI: 10.1175/2008MWR2582.1.

[31] P. Dziekan, J. B. Jensen, et al. “Impact of Giant Sea Salt Aerosol Particles on Precipitation in Marine Cumuli and Stratocumuli: Lagrangian Cloud Model Simulations”. In: *Journal of the Atmospheric Sciences* 78.12 (2021), pp. 4127–4142. DOI: 10.1175/JAS-D-21-0041.1.

[32] N. Kuba and M. Murakami. “Effect of hygroscopic seeding on warm rain clouds-numerical study using a hybrid cloud microphysical model”. In: *Atmospheric Chemistry and Physics* 10 (2010), pp. 3335–3351.

[33] H. G. Houghton. “Problems connected with the condensation and precipitation processes in the atmosphere”. In: *Bulletin of the American Meteorological Society* 19.4 (1938), pp. 152–159.

[34] J. B. Jensen and A. D. Nugent. “Condensational Growth of Drops Formed on Giant Sea-Salt Aerosol Particles”. In: *Journal of the Atmospheric Sciences* 74.3 (2017), pp. 679–697. DOI: 10.1175/JAS-D-15-0370.1.

[35] A. S. Ackerman, O. B. Toon, et al. “Effects of Aerosols on Cloud Albedo: Evaluation of Twomey’s Parameterization of Cloud Susceptibility Using Measurements of Ship Tracks”. In: *Journal of the Atmospheric Sciences* 57 (2000).

[36] Y.-C. Chen et al. “Occurrence of Lower Cloud Albedo in Ship Tracks”. In: *Atmospheric Chemistry and Physics* 12.17 (2012), pp. 8223–8235. DOI: 10.5194/acp-12-8223-2012.

[37] E. Gryspeerdt et al. “Observing the Timescales of Aerosol-Cloud Interactions in Snapshot Satellite Images”. In: *Atmospheric Chemistry and Physics Discussions* (October 2020), pp. 1–30. DOI: 10.5194/acp-2020-1030.

[38] M. W. Christensen and G. L. Stephens. “Microphysical and Macrophysical Responses of Marine Stratocumulus Polluted by Underlying Ships: Evidence of Cloud Deepening”. In: *Journal of Geophysical Research* 116 (2011). DOI: 10.1029/2010JD014638.

[39] P. N. Blossey et al. “Locally Enhanced Aerosols Over a Shipping Lane Produce Convective Invigoration but Weak Overall Indirect Effects in Cloud-Resolving Simulations”. In: *Geophysical Research Letters* 45.17 (2018), pp. 9305–9313. DOI: 10.1029/2018GL078682.

[40] J. Latham et al. “Marine Cloud Brightening”. In: *Philosophical Transactions of the Royal Society A: Mathematical, Physical and Engineering Sciences* 370.1974 (2012), pp. 4217–4262. DOI: 10.1098/rsta.2012.0086.

[41] F. Hoffmann and G. Feingold. “Cloud Microphysical Implications for Marine Cloud Brightening: The Importance of the Seeded Particle Size Distribution”. In: *Journal of the Atmospheric Sciences* 78.10 (2021), pp. 3247–3262. DOI: 10.1175/JAS-D-21-0077.1.

[42] M. S. Diamond et al. “To Assess Marine Cloud Brightening’s Technical Feasibility, We Need to Know What to Study—and When to Stop”. In: *Proceedings of the National Academy of Sciences* 119.4 (2022), e2118379119. DOI: 10.1073/pnas.2118379119.

[43] P. Prabhakaran et al. “Journal of the Atmospheric Sciences”. In: (Mar. 29, 2023). DOI: 10.1175/JAS-D-22-0207.1.

[44] P. Dziekan, M. Waruszewski, et al. “University of Warsaw Lagrangian Cloud Model (UWLCM) 1.0: a modern large-eddy simulation tool for warm cloud modeling with Lagrangian microphysics”. In: *Geosci. Model Dev.* 12 (2019), pp. 2587–2606. DOI: 10.5194/gmd-12-2587-2019.

[45] S. Arabas et al. “libcloudph++ 1.0: a single-moment bulk, double-moment bulk, and particle-based warm-rain microphysics library in C++”. In: *Geosci. Model Dev.* 8 (2015), pp. 1677–1707. DOI: 10.5194/gmd-8-1677-2015.

[46] M. D. Petters and S. M. Kreidenweis. “A single parameter representation of hygroscopic growth and cloud condensation nucleus activity”. In: *Atmos. Chem. Phys.* 7.8 (2007), pp. 1961–1971. DOI: 10.5194/acp-7-1961-2007.

[47] G. Feingold. “Modeling of the First Indirect Effect: Analysis of Measurement Requirements”. In: *Geophysical Research Letters* 30.19 (2003), p. 1997. DOI: 10.1029/2003GL017967.

[48] P. Reutter et al. “Aerosol-and updraft-limited regimes of cloud droplet formation: influence of particle number, size and hygroscopicity on the activation of cloud condensation nuclei (CCN)”. In: *Atmos. Chem. Phys.* 9 (2009), pp. 7067–7080. DOI: 10.5194/acp-9-7067-2009.

[49] J. Chen et al. “New understanding and quantification of the regime dependence of aerosol-cloud interaction for studying aerosol indirect effects”. In: *Geophys. Res. Lett.* 43.4 (2016), pp. 1780–1787. DOI: 10.1002/2016GL067683.

[50] M. L. Pöhlker et al. “Aitken mode particles as CCN in aerosol- and updraft-sensitive regimes of cloud droplet formation”. In: *Atmos. Chem. Phys.* 21.15 (2021), pp. 11723–11740. DOI: 10.5194/acp-21-11723-2021.

[51] P. Dziekan and P. Zmijewski. “University of Warsaw Lagrangian Cloud Model (UWLCM) 2.0: Adaptation of a Mixed Eulerian–Lagrangian Numerical Model for Heterogeneous Computing Clusters”. In: *Geoscientific Model Development* 15.11 (2022), pp. 4489–4501. DOI: 10.5194/gmd-15-4489-2022.

[52] H. Morrison and W. W. Grabowski. “Comparison of Bulk and Bin Warm-Rain Microphysics Models Using a Kinematic Framework”. In: *Journal of the Atmospheric Sciences* 64.8 (2007), pp. 2839–2861. DOI: 10.1175/JAS3980.

[53] M. Khairoutdinov and Y. Kogan. “A New Cloud Physics Parameterization in a Large-Eddy Simulation Model of Marine Stratocumulus”. In: *Monthly Weather Review* 128.1 (2000), pp. 229–243. DOI: 10.1175/1520-0493(2000)128<0229:ANCPPI>2.0.CO;2.

[54] G. Feingold et al. “Simulations of Marine Stratocumulus Using a New Microphysical Parameterization Scheme”. In: *Atmospheric Research* 47–48 (June 1998), pp. 505–528. DOI: 10.1016/S0169-8095(98)00058-1.

[55] C. S. Bretherton et al. “Cloud Droplet Sedimentation, Entrainment Efficiency, and Subtropical Stratocumulus Albedo”. In: *Geophysical Research Letters* 34.3 (Feb. 9, 2007), p. L03813. DOI: 10.1029/2006GL027648.

[56] H. Morrison, J. A. Curry, et al. “A New Double-Moment Microphysics Parameterization for Application in Cloud and Climate Models. Part I: Description”. In: *Journal of the Atmospheric Sciences* 62.6 (2005), pp. 1665–1677. DOI: 10.1175/JAS3446.1.

[57] G. McFiggans et al. “The Effect of Physical and Chemical Aerosol Properties on Warm Cloud Droplet Activation”. In: *Atmospheric Chemistry and Physics* 6.9 (July 5, 2006), pp. 2593–2649. DOI: 10.5194/acp-6-2593-2006.

[58] B. Stevens and G. Feingold. “Untangling Aerosol Effects on Clouds and Precipitation in a Buffered System”. In: *Nature* 461.7264 (2009), pp. 607–613. DOI: 10.1038/nature08281.

Chapter 5

TOP-OF-ATMOSPHERE ALBEDO BIAS FROM NEGLECTING THREE-DIMENSIONAL CLOUD RADIATIVE EFFECTS

[1] C. E. Singer et al. "Top-of-Atmosphere Albedo Bias from Neglecting Three-Dimensional Cloud Radiative Effects". In: *Journal of the Atmospheric Sciences* 78.12 (2021), pp. 4053–4069. DOI: 10.1175/JAS-D-21-0032.1.

Abstract. Clouds cover on average nearly 70% of Earth's surface and regulate the global albedo. The magnitude of the shortwave reflection by clouds depends on their location, optical properties, and three-dimensional (3D) structure. Due to computational limitations, Earth system models are unable to perform 3D radiative transfer calculations. Instead they make assumptions, including the independent column approximation (ICA), that neglect effects of 3D cloud morphology on albedo. We show how the resulting radiative flux bias (ICA-3D) depends on cloud morphology and solar zenith angle. We use high-resolution (20–100 m horizontal resolution) large-eddy simulations to produce realistic 3D cloud fields covering three dominant regimes of low-latitude clouds: shallow cumulus, marine stratocumulus, and deep convective cumulonimbus. A Monte Carlo code is used to run 3D and ICA broadband radiative transfer calculations; we calculate the top-of-atmosphere (TOA) reflected flux and surface irradiance biases as functions of solar zenith angle for these three cloud regimes. Finally, we use satellite observations of cloud water path (CWP) climatology, and the robust correlation between CWP and TOA flux bias in our LES sample, to roughly estimate the impact of neglecting 3D cloud radiative effects on a global scale. We find that the flux bias is largest at small zenith angles and for deeper clouds, while the albedo bias is most prominent for large zenith angles. In the tropics, the annual-mean shortwave radiative flux bias is estimated to be 3.1 ± 1.6 W m^{-2}, reaching as much as 6.5 W m^{-2} locally.

Significance Statement. Clouds cool the Earth by reflecting sunlight back to space. The amount of reflection is determined by their location, details of their 3D structure, and the droplets or ice crystals they are composed of. Global models

cannot simulate the 3D structure of clouds because computational power is limited, so they approximate that clouds only scatter sunlight in a 1D vertical column. In this study, we use local models to directly simulate how clouds scatter sunlight in 3D and compare with a 1D approximation. We find the largest bias for overhead sun and for deeper clouds. Using satellite observations of bulk cloud properties, we estimate the tropical annual-mean bias introduced by the 1D approximation to be 3.1 ± 1.6 W m^{-2}.

5.1 Introduction

Earth's average albedo is roughly 29%, with clouds accounting for about half of the solar radiative energy fluxes reflected back to space (Stephens et al., 2015). Accurately simulating clouds is crucial for modeling Earth's albedo. However, Earth system models (ESMs) struggle to accurately represent the albedo's magnitude, spatial patterns, and seasonal variability (Bender et al., 2006; Voigt et al., 2013; Engström et al., 2015). Simulating clouds is difficult for several reasons, but one major factor is their wide range of spatial scales. Clouds have complex three-dimensional (3D) morphologies created by turbulent motions at length scales down to tens of meters or smaller. However, the typical resolution of an ESM is around only 10–100 km in the horizontal and 100–200 m in the vertical in the lower troposphere (Schneider et al., 2017). This discrepancy means that clouds are not explicitly resolved in ESMs. Instead, they are represented by parameterizations and, for purposes of radiative transfer (RT) calculations, are approximated as broken plane-parallel structures within grid cells (Marshak and Davis, 2005).

The plane-parallel approximation (PPA) leads to important biases in RT calculations (R. Cahalan and Wiscombe, 1992). Over the past 20 years, RT solvers have made significant progress in reducing some of these biases, either by making use of semi-empirical deterministic parameterizations of cloud heterogeneity (J. K. Shonk and Hogan, 2008) or through stochastic sampling of plane-parallel cloudy columns based on assumed distributions and characteristics of cloud structural properties (Pincus et al., 2003). These approximate solvers are likely to become even more accurate in the future, as dynamical parameterizations provide increasingly detailed cloud statistics (e.g., Cohen et al., 2020). Moreover, the PPA bias may be reduced in ESMs by using embedded cloud-resolving models (Cole, Barker, Randall, et al., 2005; Kooperman et al., 2016), albeit at great additional computational expense, in an approach known as cloud superparameterization (Khairoutdinov and Randall, 2001).

This progress has led to a renewed interest in another source of bias that was, until recently, overshadowed by biases due to the PPA: the treatment of horizontal radiative fluxes in ESMs (R. F. Cahalan et al., 1994; Schäfer et al., 2016; Hogan, Fielding, et al., 2019). ESMs make the independent column approximation (ICA) when performing RT calculations. This approximation neglects horizontal radiative fluxes, decoupling the RT calculation between atmospheric columns to make the problem computationally tractable. 3D radiative transfer will remain too expensive to run in ESMs in the foreseeable future, making the ICA a necessary simplification (Hogan and Bozzo, 2018). For this reason, it is important to quantify and document biases due to the ICA.

In this context, the effect of cloud structure on horizontal radiative transfer has gained attention, enabled by advances in computation that make 3D RT feasible at high spectral resolution (Mayer and Kylling, 2005; Emde et al., 2016; Villefranque et al., 2019; Gristey et al., 2019; Veerman et al., 2020). The structural differences between ICA and a full 3D RT calculation have been documented before (Marshak, Davis, Wiscombe, and Titov, 1995; O'Hirok and Gautier, 1998; O'Hirok and Gautier, 2005; Barker, Stephens, et al., 2003; Barker, Kato, et al., 2012), and many alternatives to ICA have been proposed to minimize their mismatch (e.g., Marshak, Davis, Wiscombe, and R. Cahalan, 1995; Várnai and Davies, 1999; Frame et al., 2009; Hogan and J. K. P. Shonk, 2013; Wissmeier et al., 2013; Okata et al., 2017; Oreopoulos and Barker, 1999; Klinger and Mayer, 2016; Klinger and Mayer, 2020; Hogan, Fielding, et al., 2019).

Nevertheless, most studies have been focused on theoretical cases, small spatial and temporal domains, or improving satellite retrieval algorithms. Some notable exceptions are Cole, Barker, O'Hirok, et al. (2005), who calculate the ICA bias from two-dimensional (2D) RT in a superparameterized cloud resolving model at 4 km horizontal resolution; and Barker, Cole, Li, Yi, et al. (2015) and Barker, Cole, Li, and Salzen (2016), who calculate the ICA bias using 2D cloud fields retrieved from CloudSat and CALIPSO.

Here we discuss the magnitude of the bias that results from neglecting the 3D cloud radiative effects by making the ICA. We use large-eddy simulations (LES) to generate 3D cloud fields representing three canonical cloud regimes: shallow cumulus convection, stratocumulus, and deep convection. These cloud regimes are representative of the clouds typically found in the tropics. Previous studies that quantify 3D cloud radiative effects globally have used 2D cloud fields retrieved from

satellites or superparameterized models, or inferred 3D fields using some stochastic generator (O'Hirok and Gautier, 1998; O'Hirok and Gautier, 2005; Barker, Cole, Li, Yi, et al., 2015; Barker, Cole, Li, and Salzen, 2016). These approaches can better represent the spatial distribution of cloud types but are restricted to the coarse resolution of satellite footprints or rely on assumptions to generate 3D fields. We instead use high-fidelity models to generate realistic 3D cloud fields at very high resolution, sacrificing some ability to generalize beyond the tropics from our limited number of LES cases. All of these methods present different challenges, either in generalizing to global scales, or in representing the details of small scales, but the simplifications are necessary because 3D cloud retrievals from satellite are not yet available. However, recent progress in stereoscopic observations is bringing us closer to having global high-resolution observations of 3D cloud structure (e.g., Romps and Öktem, 2018; Castro et al., 2020).

We calculate the bias between the true reflected flux and the flux approximated by ICA using a Monte Carlo RT code. The shortwave radiative flux bias is shown to vary with solar zenith angle and cloud type. Because the solar zenith angle varies with the diurnal and seasonal cycle, we quantify the effect of the 3D bias on these timescales. Finally, using global satellite observations of cloud climatology, we estimate the spatiotemporal bias that would result in global models that resolve clouds but still make the ICA. As stated earlier, most ESMs make the ICA and use some cloud heterogeneity parameterization to reduce the PPA bias, so the bias associated with only the ICA is an underestimate of the total bias. Because of the diversity of assumptions made by global models to account for phenomena such as cloud overlap, and the fundamental resolution dependence of cloud heterogeneity emulators, in this study we focus on the bias resulting from RT using only the ICA on fully resolved 3D cloud structures from LES.

5.2 Methods

Large-eddy simulations of clouds

We generate three-dimensional cloud fields from high-resolution LES using the anelastic solver PyCLES (Pressel, Kaul, et al., 2015; Pressel, Mishra, et al., 2017). The LES are run in three dynamical regimes to simulate shallow cumulus (ShCu), stratocumulus (Sc), and deep-convective cumulonimbus clouds (Cb). Figure 5.1 shows volume renderings of each cloud regime alongside profiles of cloud fraction; key properties of the different cloud regime simulations can be found in Table 5.1 with more details in appendix A. In general, LES are capable of reproduc-

ing observed cloud characteristics (e.g., cloud cover, liquid water path, cloud depth) including aspects of 3D structures (Griewank et al., 2020).

ShCu clouds are convective clouds with typical cloud cover of 10–20% and cloud top height (CTH) around 2 km. They occur frequently over tropical oceans, on average covering 20% but up to 40% of their surface (Cesana et al., 2019). In this study, ShCu are represented by two LES case studies, BOMEX and RICO, which represent non-precipitating and precipitating shallow convection over tropical oceans, respectively (Siebesma et al., 2003; vanZanten et al., 2011). Sc clouds are shallower, with CTH only around 1 km. They have near 100% cloud cover and typically blanket subtropical oceans off the west coast of continents (Cesana et al., 2019). Sc are represented by the DYCOMS-II RF01 LES case of a Sc deck off the coast of California (Stevens et al., 2005). Cb clouds are deep convective thunderstorm clouds that occur frequently over mid-latitude continents in summer and in the tropics, e.g., in the intertropical convergence zone (ITCZ). Their CTH can reach up to 15 km or higher, they often contain ice, and anvils at the top contribute to a cloud cover around 30%. Cb clouds are represented in this paper by the TRMM-LBA LES case, based on measurements of convection over land in the Amazon (Grabowski et al., 2006).

An ensemble of snapshots is used to estimate the mean and variance of the bias for each cloud type. The snapshots are chosen to be at least one convective turnover time apart (1 hour for BOMEX and RICO, 30 minutes for DYCOMS-II RF01, and 90 minutes for TRMM-LBA). For ShCu and Sc, we take snapshots evenly spaced in time starting once the simulation has reached a statistically quasi-steady state, after an initial spin-up period. For the Cb case we take snapshots from an initial-condition ensemble at several time points representative of transient and fully-developed deep convection at 4, 5.5, and 7 hours into the simulation (10:00, 11:30, and 13:00 local time). We also analyze the effect of convective aggregation in Cb (Jeevanjee and Romps, 2013; Wing et al., 2017; Patrizio and Randall, 2019) by analyzing snapshots from an initial-condition ensemble run over a larger domain $((40\ \mathrm{km})^2$, compared to the original $(20\ \mathrm{km})^2$). In both cases, we use only the snapshots at 13:00 local time of fully-developed deep convection, characterized by stable liquid and ice water paths, for the cloud-type specific calculations. The rest of the snapshots are used in our estimate of the tropical shortwave flux bias. We choose ensemble sizes that capture the natural variability of morphology in each LES case: 20 for ShCu (10 each of BOMEX and RICO) and 5 for Sc; for Cb we take 15 snapshots from each time

LES Case Name	Cloud Type	Domain Size (km^3)	Resolution (m^3)	Cloud cover	CWP ($g\ m^{-2}$)	CTH (km)	Cloud Phase
BOMEX	ShCu	$6.4 \times 6.4 \times 3$	$20 \times 20 \times 20$	0.22 ± 0.03	44.6 ± 7.8	1.72 ± 0.08	Liquid
RICO	ShCu	$12.8 \times 12.8 \times 6$	$40 \times 40 \times 40$	0.25 ± 0.01	90 ± 20	2.28 ± 0.18	Liquid
DYCOMS II RF01	Sc	$3.36 \times 3.36 \times 1.5$	$35 \times 35 \times 5$	0.996 ± 0.002	53.8 ± 0.7	0.911 ± 0.004	Liquid
TRMM-LBA, t = 4 hr	Cb	$20 \times 20 \times 22$	$100 \times 100 \times 50$	0.35 ± 0.01	280 ± 20	6.4 ± 0.5	Liquid/Ice
TRMM-LBA, t = 5.5 hr	Cb	$20 \times 20 \times 22$	$100 \times 100 \times 50$	0.33 ± 0.02	380 ± 60	9.4 ± 1.5	Liquid/Ice
TRMM-LBA, t = 7 hr	Cb	$20 \times 20 \times 22$	$100 \times 100 \times 50$	0.32 ± 0.06	290 ± 80	10 ± 2	Liquid/Ice
TRMM-LBA agg.	Cb	$40 \times 40 \times 22$	$100 \times 100 \times 50$	0.30 ± 0.02	360 ± 80	12.2 ± 0.6	Liquid/Ice

Table 5.1: LES case properties: name, type of cloud (shallow cumulus, ShCu; stratocumulus, Sc; deep convective cumulonimbus, Cb), domain size, resolution, cloud cover, in-cloud cloud water path (CWP), cloud top height (CTH), and thermodynamic phase. Shown are ensemble means and standard deviations not accounting for spatial variance within a single ensemble member.

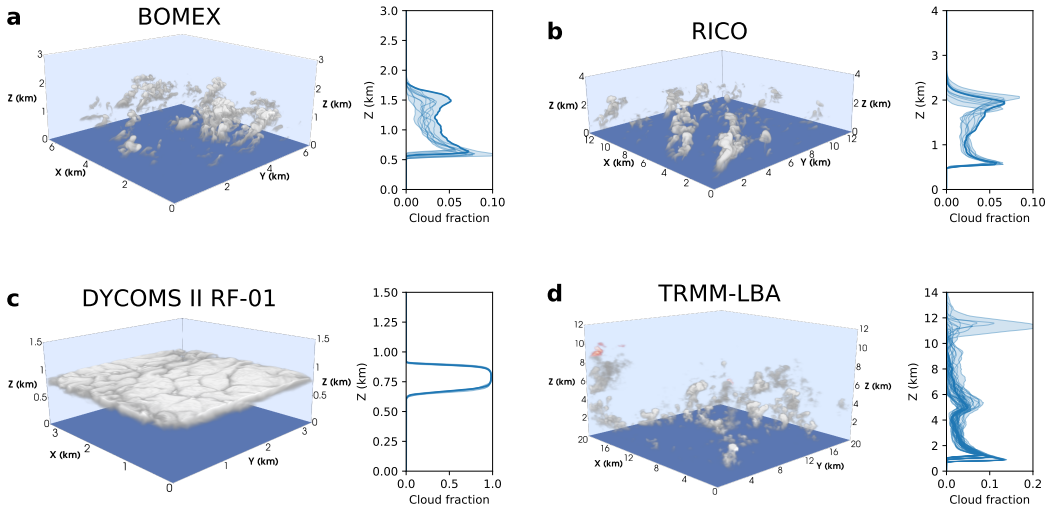

Figure 5.1: Snapshots of LES clouds, showing liquid water specific humidity (gray to white, low to high) and ice water specific humidity (red to white, low to high). Subplots to the right show vertical profiles of cloud fraction for each case. The thick line shows the profile for the specific snapshot in the 3D rendering, the thin lines show all other snapshots, and the shading shows the range. (a) and (b) Shallow convective clouds. (c) Stratocumulus clouds. (d) Deep convective clouds. Note that the domain sizes vary between the cases.

point (45 in total) from the (20 km)^2 TRMM-LBA simulations and 5 snapshots of fully-developed, more aggregated deep convection from the (40 km)^2 TRMM-LBA aggregated (agg.) simulations. The smaller ensemble is determined to sufficiently capture the dynamical variability for the larger domain.

The increase in convective aggregation for the larger domain Cb simulations can be seen in typical measures such as the variance of the column relative humidity or total precipitable water (Wing et al., 2017) (see appendix A, Fig. A1). The domain-mean cloud cover, cloud top height, and cloud water path from the two sets of Cb simulations are similar, indicating that the difference in radiative flux bias is being driven by a change in the aggregation or domain size. Larger domains may lead to even more aggregation (Patrizio and Randall, 2019); however, synoptic noise may become important and disrupt the self-aggregation of convection on large scales in reality (Bretherton, 2015). The Sc and ShCu results are unchanged for larger domain sizes (not shown), but we do see an expected reduction in variance across the ShCu ensemble ($N_{\mathrm{LES}} = 10$) due to the larger dynamical variability captured in each snapshot of the larger domain.

Radiative transfer computations

The RT calculations were done using the libRadtran software package with the MYSTIC Monte Carlo solver (Mayer and Kylling, 2005; Mayer, 2009; Emde et al., 2016). Details of the set-up can be found in appendix B. The MYSTIC solver requires 3D fields of liquid and ice water content and particle effective radius as input. We use MYSTIC to do the full 3D RT and ICA calculations. The LES uses simple microphysics schemes that do not explicitly compute the effective radius. To compute the effective radius, we follow the parameterization from Ackerman et al. (2009) and Blossey et al. (2013) for liquid and Wyser (1998) for ice (appendix B). For the RT calculation, MYSTIC finds the scattering phase function from pre-computed lookup tables. In the case of liquid droplets, which are assumed spherical, the full Mie phase function is used. For the case of ice clouds, a parameterization of the habit-dependent scattering must be used. We use the `hey` parameterization with "general habit mixture" (Yang et al., 2013; Emde et al., 2016). The results are insensitive to the choice of ice parameterization (Fig. B1) because the reflected flux signal is dominated by the liquid droplets for the clouds we simulated.

Observations of cloud climatology

The LES cloud fields allow for precise calculation of the 3D cloud radiative effect on small domains. To estimate the global impact of the 3D cloud radiative effect, we use the results from LES along with satellite observations of cloud climatology and surface albedo to scale up from these few cases to a global picture. We find that in-cloud cloud water path (CWP), defined as the domain-mean cloud water path divided by cloud cover, is a simple but robust predictor of the flux bias (will be shown in Section 5). We use the International Satellite Cloud Climatology Project (ISCCP) D2 dataset of CWP (W. B. Rossow et al., 1999; W. Rossow and Duenas, 2004; Marchand et al., 2010; C. Stubenrauch et al., 2012; C. J. Stubenrauch et al., 2013). The ISCCP D2 cloud product is a monthly climatological mean with spatial resolution of $1^\circ \times 1^\circ$ constructed from measurements during the period 1984–2007. These data are collected by a suite of weather satellites that are combined into a 3-hourly global gridded product at the D1 level and are averaged, including a mean diurnal cycle, into the D2 product we use.

We also account for the observed surface albedo that varies seasonally and spatially and affects the flux bias. We use observations of surface albedo from the Global Energy and Water Exchanges Project's surface radiation budget product version 3.0, which is aggregated to a monthly mean climatology for the period 1984–2007 and

gridded to $1^\circ \times 1^\circ$.

5.3 Radiative flux bias dependence on zenith angle

Top-of-atmosphere

The top-of-atmosphere (TOA) radiative flux bias is measured (in W m^{-2}) as the difference in reflected irradiance between the ICA and 3D RT calculations averaged over the full domain. A positive bias means that, under the ICA, clouds reflect more energy back to space than in reality (i.e., 3D), implying that the Earth's surface is artificially dimmed (cooled) in a model that uses the ICA. The albedo bias ($\Delta\alpha$) is computed as the flux bias ($\Delta F = F_{\mathrm{ICA}} - F_{\mathrm{3D}}$) divided by the total incoming solar flux (F_{in}),

$$\Delta\alpha = \frac{\Delta F}{F_{\mathrm{in}}} \times 100\%. \tag{5.1}$$

Fig. 5.2 shows the flux and albedo biases (ICA−3D) for the five cases of ShCu, Sc, and Cb clouds. The solid lines show the ensemble mean bias, and the shading denotes one standard deviation (σ). The combined variance (σ^2) is computed as,

$$\sigma^2 = \frac{1}{N_{LES}} \sum_{i=1}^{N_{\mathrm{LES}}} \left[\left(\sigma_{i,\mathrm{ICA}}^2 + \sigma_{i,\mathrm{3D}}^2 \right) + \left(\Delta F_i - \langle \Delta F \rangle \right)^2 \right] \tag{5.2}$$

where N_{LES} is the number of ensemble members, $\sigma_{i,\mathrm{ICA}}$ and $\sigma_{i,\mathrm{3D}}$ are the standard deviations from the MYSTIC solver photon tracing, ΔF_i is the TOA flux bias of each ensemble member, and $\langle \cdot \rangle$ denotes a mean over the LES ensemble. This variance includes both the statistical noise from the Monte Carlo RT and the dynamical variability of the cloud field (which are assumed to be uncorrelated). The Monte Carlo noise is proportional to $1/\sqrt{n}$ where $n = 10^4$ is the number of photons used for the RT simulation, and is in fact $\sim 0.7\%$ for these calculations. The variance between cloud scenes is much larger than the Monte Carlo error, by more than an order of magnitude.

Sc show negligible deviation between ICA and 3D reflected fluxes. For convective clouds (ShCu and Cb), the bias from the ICA is positive, except for ShCu at very large solar zenith angles. At large zenith angles, ShCu show a large negative flux and albedo bias for ICA. ShCu scatter far fewer photons than Cb due to the low cloud cover and their smaller optical thickness, corresponding to small vertical extent. Cb exhibit the largest reflected irradiance and also the largest bias between the ICA and 3D RT calculations. While the mean flux bias is similar, the structure of the bias with zenith angle is markedly different for the two domain sizes (Fig. 5.2). For the small-domain simulations with a lesser degree of aggregation, the bias is

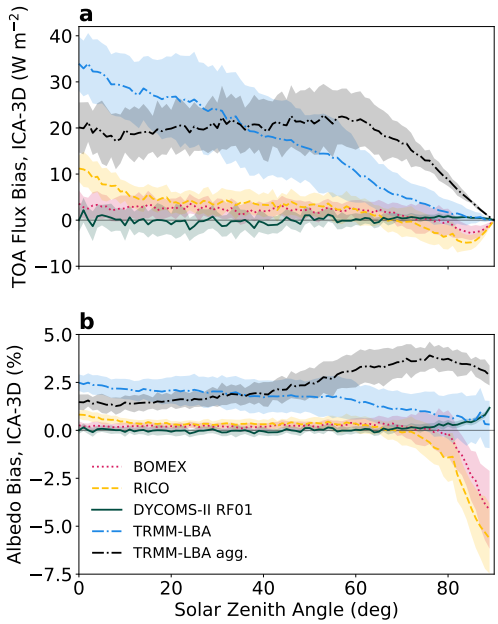

Figure 5.2: Bias (ICA-3D) in (a) TOA reflected flux and (b) albedo as a function of zenith angle for ShCu (BOMEX and RICO), Sc (DYCOMS-II RF01), and Cb (TRMM-LBA and TRMM-LBA agg.). For each cloud type, average fluxes (with shaded 1σ error bars) are computed over the individual snapshots. Positive bias means the ICA approximation is reflecting more incoming flux than in the 3D RT calculation.

approximately linear with zenith angle (as seen by Barker, Cole, Li, Yi, et al. (2015) and Barker, Cole, Li, and Salzen (2016)). For the more aggregated case, the flux bias is nearly uniform up until a solar zenith angle of 60° and then decreases rapidly towards zero; this translates to an albedo bias that peaks at large zenith angles (around 70°).

The convective clouds show much more variation than the stratiform clouds between snapshots due to the variability in cloud cover even in a statistically steady state. The less aggregated Cb clouds have the largest variability, which is expected since the domain size is small relative to the scale of the clouds, i.e., in each snapshot we capture only approximately one deep convective cloud, compared to many small cumulus clouds; therefore, we are effectively averaging over fewer realizations even though we take our ensemble size to be larger. Similarly, for the more aggregated Cb clouds, since we use a four times larger domain, a smaller ensemble ($N_{\text{LES}} = 5$ compared to 15) is large enough to capture the variability.

In the ICA, the horizontal photon fluxes between neighboring columns are ignored.

For the Sc clouds that uniformly cover the whole domain (Fig. 5.1c), this assumption has little effect: the flux bias is near zero for all zenith angles. However, for cumulus clouds, making the ICA has two effects that are described in detail by Hogan, Fielding, et al. (2019).

1. The long-recognized "cloud-side illumination" effect in 3D radiative transfer. This describes how horizontally propagating photons can encounter the side of a cloud and can be scattered by it, rather than being restricted to hit the top of a cloud in the ICA. Side-illumination happens when photons travel across columns at slant angles, brightening the cloud sides and enhancing cloud reflectance; it also creates larger shadows, or larger effective cloud cover. This effect acts to enhance reflectance in 3D, and thus would appear as a negative ICA flux bias in our terminology.

2. The newer "entrapment" effect that Hogan, Fielding, et al. (2019) presented. This mechanism is similar to the "upward trapping" mechanism discussed by Várnai and Davies (1999). It describes how in 3D a scattered photon may be intercepted by another cloud, or the same cloud, in a different column higher in the domain and scattered back down to the surface. In the ICA by contrast, when a photon travels through clear-sky and is scattered by a cloud, it will necessarily travel back through the same column of clear-sky to the TOA. The entrapment mechanism acts to decrease cloud reflectance in 3D, i.e., it creates a positive flux bias.

The calculated 3D effects we show in Fig. 5.2 are a combination of these competing mechanisms. At large solar zenith angles, cloud shadowing, by which clouds can shade each other, clear-sky regions, and the surface when photons are coming in at slant angles, can be important for surface irradiance and surface fluxes (Frame et al., 2009; Veerman et al., 2020).

For small zenith angles, when the sun is overhead, the convective clouds (ShCu and Cb) produce a positive flux bias because entrapment is dominant over cloud-side illumination. For large zenith angles, the flux and albedo bias from ShCu is negative because cloud-side illumination becomes the dominant effect. In the mean, the solar zenith angle at which the flux bias becomes negative is around 70°, but for the individual ensemble members this ranges from around 45° to 75°. This has been seen before for ShCu by Barker, Cole, Li, Yi, et al. (2015) and Barker, Cole, Li, and Salzen (2016) and Hogan, Fielding, et al. (2019). For Cb clouds,

however, even at large zenith angles, the flux and albedo biases remain positive, indicating that the entrapment mechanism continues to dominate over cloud-side illumination. This is not the case for every scene in the Cb ensemble, but it is true in the mean, in agreement with the results from Hogan, Fielding, et al. (2019). This difference between ShCu and Cb is related to the aspect ratio of the clouds; the cloud-side illumination mechanism can only become dominant if the aspect ratio is small (clouds are not too deep). Furthermore, in the case of the more aggregated Cb clouds, a greater degree of aggregation decreases the surface area to volume ratio of the clouds, or what Schäfer et al. (2016) call the length of cloud edge, or cloud perimeter. A smaller cloud perimeter will decrease the cloud side illumination as well as the entrapment efficiency of the cloud (Hogan, Fielding, et al., 2019). The uncertainty in flux bias due to the degree of aggregation of deep convection is much larger than the spread across the LES ensemble and represents a structural uncertainty, which is more challenging to quantify.

These 3D cloud effects can be understood from Fig. 5.1, which shows illustrations of the clouds from the four LES cases. The scattered cumulus in the BOMEX and RICO cases are shallow and spaced apart, which allows for cloud-side illumination at large zenith angles to dominate over the entrapment mechanism. The DYCOMS-II RF01 stratocumulus clouds are quite horizontally homogeneous over this small domain, therefore, ICA biases are small. As discussed in Hogan, Fielding, et al. (2019), when in-cloud heterogeneity is larger, e.g., for open-celled marine stratocumulus, the entrapment effect is larger. Finally, for the deep TRMM-LBA clouds, the entrapment mechanism remains dominant even for large zenith angles because the clouds at higher levels can intercept and trap outgoing photons that are able to escape to TOA in the ICA.

In addition to the LES ensembles described previously, we run one additional set of tests to quantify the dependence of the flux bias calculations on the LES resolution (Fig. 5.3). We take the original LES simulations and systematically coarse-grain the 3D fields to lower resolution. Doing so ensures that we do not change the dynamics of the clouds so that we can test the effect of resolution on only the radiative transfer. We are not able to bridge the gap all the way to ESM scales (10–100 km horizontal resolutions) due to computational limits on running the LES, but we show results across a range of horizontal scales. When coarse-graining, we keep the vertical resolution fixed to better represent the very large aspect ratio grid boxes found in ESMs compared to the relatively isotropic grid boxes in LES. The

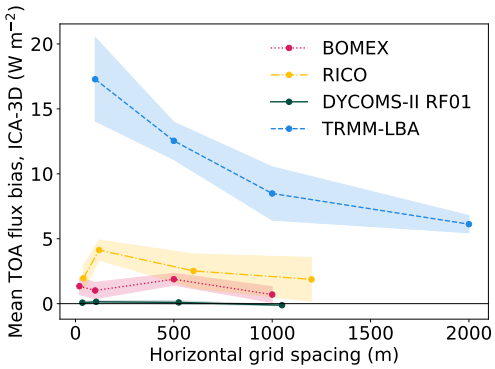

Figure 5.3: Mean TOA reflected flux bias across all solar zenith angles computed for different resolutions of the same cloud fields. The horizontal axis shows the horizontal resolution; the vertical resolution is kept fixed. The four cases of ShCu, Sc, and Cb are shown in the same colors as Fig. 5.2. For each case, three snapshots from the original ensemble are used and the spread is shown by the shading.

mean TOA flux bias is nearly constant across resolutions for the shallow clouds (Sc and ShCu). For Cb, the mean TOA flux bias decreases with larger grid spacing, as expected, from around 17 W m^{-2} at the original resolution and down to 6 W m^{-2} for 2 km horizontal resolution. Since the bias does not asymptote as we move towards smaller horizontal grid spacing, we expect that if the LES were run at even higher resolutions, we would find an even larger larger bias between the ICA and 3D. We conclude that our estimated bias is a lower bound in this regard.

Surface

Using the same radiative transfer calculations, we also quantify the bias in downwelling surface irradiance. This bias as a function of solar zenith angle is shown for each cloud type in Fig. 5.4. The total bias (Fig. 5.4a) is the sum of a direct component and diffuse component, shown in Fig. 5.4b and c, respectively. These components largely offset each other, as has been found in previous studies (Gristey et al., 2019). The direct surface irradiance bias is always positive and the diffuse always negative, resulting from side-illumination (shadowing) and entrapment, respectively. Note that these two mechanisms have opposite effects in the surface irradiance bias and the TOA reflected flux bias.

For the total surface irradiance bias (Fig. 5.4), we observe a similar pattern to the TOA bias (Fig. 5.2), except with the opposite sign. This has been noted before (Barker, Cole, Li, Yi, et al., 2015), and is to be expected given that when the ICA

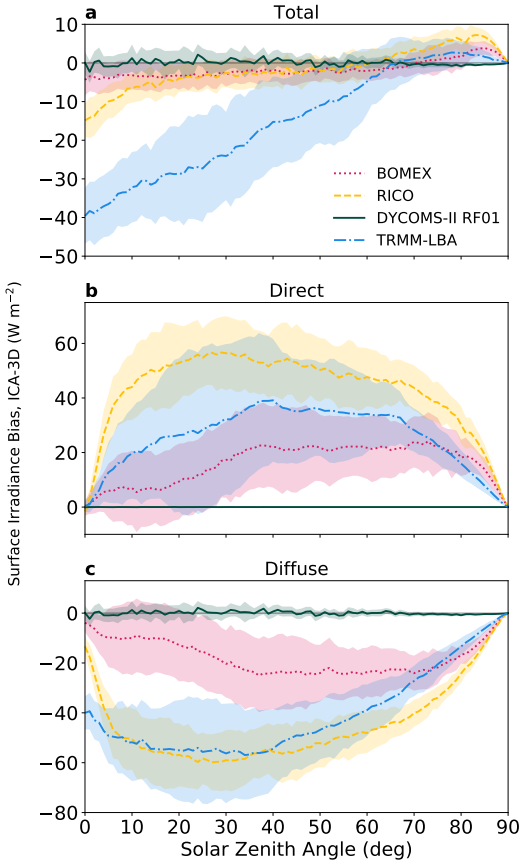

Figure 5.4: Surface irradiance bias (ICA-3D) as function of zenith angle for ShCu (BOMEX and RICO), Sc (DYCOMS-II RF01), and Cb (TRMM-LBA). The total surface irradiance bias (a) is split into the direct (b) and diffuse (c) components, which largely compensate each other, especially at larger zenith angles. For each cloud type, average fluxes (with shaded 1σ error bars) are computed over the individual snapshots. Positive bias means the ICA approximation has more downwelling radiation at the surface than the 3D calculation.

produces anomalous extra TOA reflectance, it simultaneously decreases the surface irradiance with respect to the 3D calculation. We can quantify this by considering in a simple way how the TOA reflected flux and surface irradiance depend on the incoming flux, surface albedo (α_s), cloud albedo (α_c), and cloud cover (f_c). The total scene albedo stems from scattering by the clouds and scattering by the surface. Considering up to two scattering events, we can write

$$\alpha = f_c\alpha_c + (1 - f_c)\alpha_s + 2f_c(1 - f_c)(1 - \alpha_c)\alpha_s.$$

The first term comes from reflection directly from the clouds, the second from reflection directly from the surface, and the third from reflection of diffuse radiation

from the surface. The albedo bias is therefore

$$\Delta\alpha = f_c \Delta\alpha_c (1 - 2\alpha_s (1 - f_c)), \tag{5.3}$$

where $\Delta\alpha = \alpha_{\mathrm{ICA}} - \alpha_{\mathrm{3D}}$. From Eq. 5.3 we see that the albedo bias will decrease with surface albedo because when the surface accounts for a larger fraction of the total albedo the cloud bias is less pronounced. For the downwelling surface irradiance (I), we can do the same and consider up to two scattering events,

$$I = \left[(1 - f_c) + f_c(1 - \alpha_c) + f_c(1 - f_c)\alpha_c\alpha_s\right] F_{\mathrm{in}},$$

where the first term comes from direct irradiance, the second from forward scattering through the cloud, and the third from multiple scattering first off the surface and then back down off the cloud. To first order the surface irradiance does not depend on the surface albedo, but including higher order terms we see that the surface irradiance increases with surface albedo. The surface irradiance bias ($\Delta I = I_{\mathrm{ICA}} - I_{\mathrm{3D}}$) can be written as

$$\Delta I = -f_c \Delta\alpha_c (1 - \alpha_s (1 - f_c)) F_{\mathrm{in}}. \tag{5.4}$$

Finally, with these approximations, and noting that $\Delta F = \Delta\alpha F_{\mathrm{in}}$, we can relate the surface irradiance bias to the TOA reflected flux bias by

$$\Delta I = -\Delta F \left(\frac{1 - \alpha_s (1 - f_c)}{1 - 2\alpha_s (1 - f_c)} \right). \tag{5.5}$$

Fig. 5.5 shows the calculated surface irradiance bias compared to the predicted bias calculated from the TOA bias via Eq. 5.5. The relation between surface irradiance bias and TOA reflected flux bias is robust and predictable, with an $r^2 = 0.92$. Eq. 5.5 considers up to two-scattering events, but considering only one scattering event, which simplifies the equation to $\Delta I = -\Delta F$, does not significantly change the quality of the prediction ($r^2 = 0.91$ in this case).

While the surface irradiance bias is critically important for surface fluxes, which may have dynamical feedbacks on the clouds, or for impacts on vegetation and carbon uptake (Veerman et al., 2020), the relevant quantity for the overall climate system energetics is the TOA energy balance. The remainder of this paper is devoted to analyzing the TOA reflected flux bias and the relevance of 3D cloud radiative effects for climate.

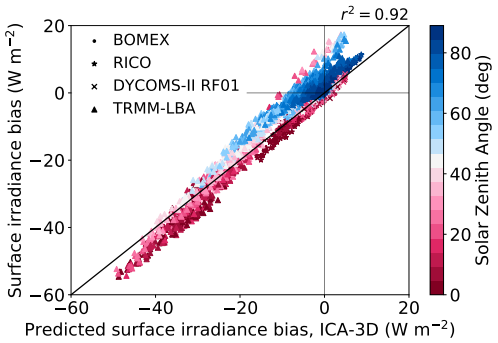

Figure 5.5: Bias (ICA-3D) in surface irradiance as predicted by bias in TOA reflected flux via Eq. 5.5 compared to the computed surface irradiance bias. Cloud type and zenith angle are indicated by marker shape and color, respectively. The 1:1 line is shown for reference.

5.4 Seasonal cycle of radiative flux bias

The solar zenith angle varies over the course of the day from sunrise to sunset, and therefore the dependence of the bias on zenith angle manifests itself as a diurnally varying bias. But the zenith angle also varies on seasonal timescales for different latitudes.

To assess the climate impact of the ICA bias, we consider the flux and albedo bias for each cloud type as a function of day of year and latitude. This calculation is done by assuming that the LES-generated cloud field is present at any given latitude circle on any given day of the year. This exercise is done without a claim to be realistic, but to demonstrate the impact each cloud type might have on Earth given the spatiotemporal variations of solar zenith angle. For any location and time, including a diurnal cycle, the solar zenith angle is calculated and the flux bias is estimated based on the results presented in Fig. 5.2. The flux and albedo biases are computed hourly and averaged to show the daily-mean bias.

Fig. 5.6 shows the annual mean and seasonal cycle of TOA flux and albedo biases for each cloud type. To estimate the uncertainties of the annual-mean bias, we calculate the LES ensemble spread as follows. For each hour in the year and each latitude, the solar zenith angle is calculated, and we interpolate between integer zenith angles in the flux bias calculations to find the mean flux bias. This is done individually for each LES cloud scene in the ensemble. The ensemble mean for each latitude and day of the year is shown (colored contour plots in Fig. 5.6), as well as the annual mean of the ensemble (black lines on Fig. 5.6). The spread across the ensemble in

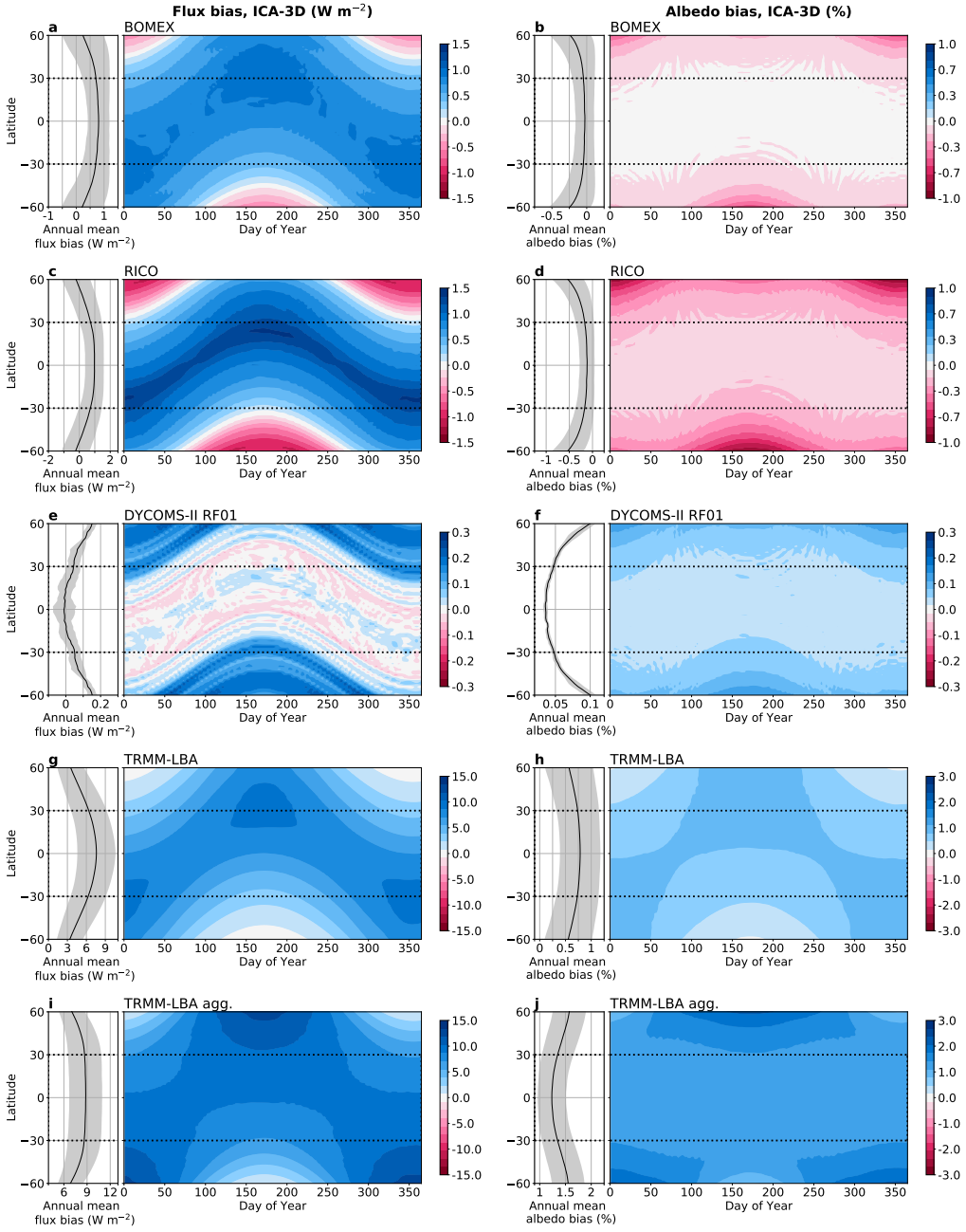

Figure 5.6: Daily mean bias (ICA-3D) as a function of latitude and day of year assuming the globe is covered by (a-d) ShCu (BOMEX and RICO), (e-f) Sc (DYCOMS-II RF01), (g-h) Cb (TRMM-LBA), and (i-j) more aggregated Cb (TRMM-LBA agg.). Left column shows flux bias, and right columns shows albedo bias. Note the color scales vary between LES cases. Inset panels on the left show annual average biases with shaded error bars that denote the spread across the LES ensembles as described in the text. Only latitudes from 60°S to 60°N are shown because the simulated clouds are not representative of the high-latitude regions.

the annual mean is shown as one standard deviation (gray shading on Fig. 5.6).

Both ShCu cases show similar patterns of flux bias with latitude and time (Fig. 5.6a and c). As seen in Fig. 5.2, these cases both have a small positive bias for small solar zenith angles, transitioning to a small negative bias for larger zenith angles, which is manifest here as a positive bias at low latitudes, transitioning to a negative bias only in mid-latitude winters. The albedo bias for both ShCu cases is near zero in the tropics and becomes more negative at higher latitudes. Sc show a very small flux (and albedo) bias for all solar zenith angles due to their high cloud cover and horizontal homogeneity, but they do exhibit a small positive flux bias ($\sim$ 0.2 W m^{-2}) during winter in mid-latitudes (Fig. 5.6e). For Cb, the flux bias is comparatively large and always positive (Fig. 5.2). In the less aggregated state, the flux bias is nearly linear in zenith angle, which gives rise to a bias pattern that roughly mimics the insolation pattern with latitude and day of year (Fig. 5.6g). In the more aggregated state, the flux bias is roughly constant in the tropics and overall larger than in the less aggregated case (Fig. 5.6i). The albedo bias for Cb is largest and positive during summer, though seasonal variations are less pronounced for aggregated convection (Fig. 5.6h and j). In particular, deep convective clouds are frequently found in the ITCZ, which migrates with the insolation maxima and therefore results in a tropical TOA reflected flux bias that peaks in each hemisphere during their respective summers and is smallest during the shoulder seasons (Fig. 5.6g and i).

5.5 Implications for Climate Models

To make an assessment of the effect that the 3D radiative transfer through cloud fields has on climate simulated with ESMs, we must account for the climatological occurrence of different cloud types in space and time. A simple parameter that can account for much of the flux bias variability in our calculations is in-cloud cloud water path (CWP), defined as domain-mean cloud water path divided by cloud cover. By regressing the flux bias against CWP for integer solar zenith angles between 0° and 90°, constraining the regression lines to pass through the origin because there is no flux bias in clear-sky conditions (CWP = 0), we observe a robust positive correlation between CWP and flux bias (Fig. 5.7). The best fit line and confidence intervals are estimated with Gaussian process regression; we use a dot product kernel, with the intercept constrained to zero. We apply regularization by specifying the "nugget" (the values added to the diagonal of the correlation matrix) as the empirically calculated variance scaled by a constant factor. The variance is calculated as the sample variance in a 100 g m^{-2} CWP interval around each point.

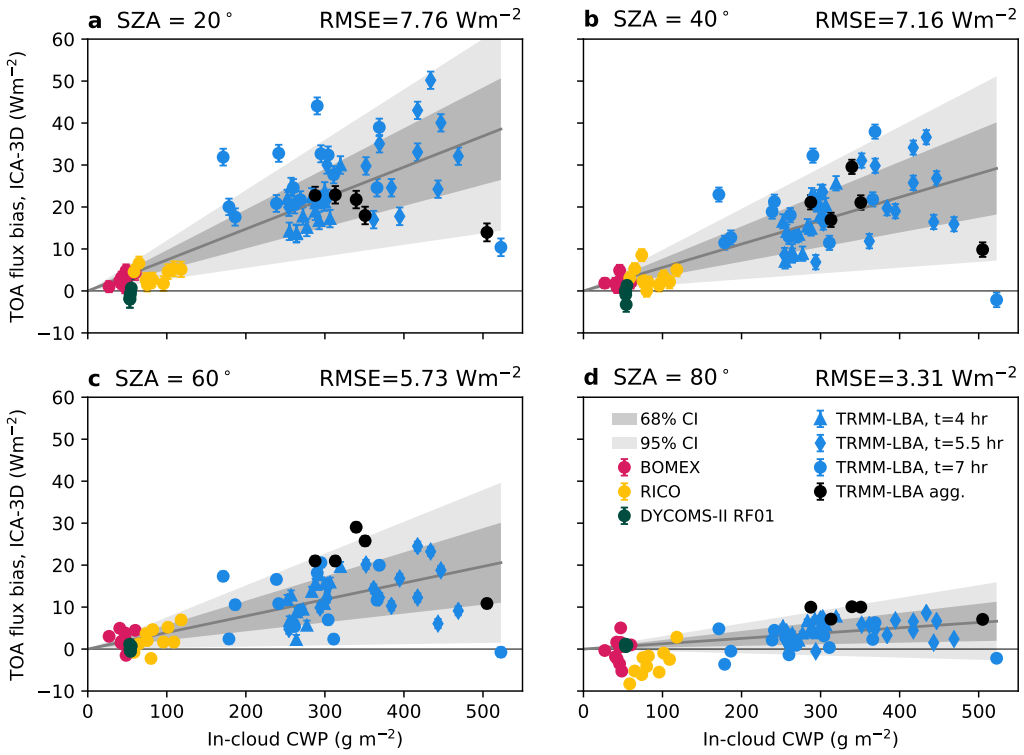

Figure 5.7: Scatter plot of in-cloud cloud water path (CWP) from LES domain against flux bias at zenith angles (a) 20°, (b) 40°, (c) 60°, and (d) 80°. LES ensemble members are plotted with the same color convention as in Fig. 5.2. The grey lines show the regression fit constrained to go through the origin. The gray shaded areas show the 68% and 95% confidence intervals. The rms error of the regression is indicated at the top.

The positive correlation between CWP and flux bias, though not perfect, allows us to approximate TOA flux biases using CWP on the global scale. We choose CWP as our proxy for flux bias because it is robustly observed by satellite and, among the other cloud properties we explored (e.g., cloud top height), the best predictor for flux bias (Fig. C1). Despite the fact that the radiative flux bias certainly depends on more than just CWP, we use it here as a first approximation to model the flux bias.

Using this relationship between CWP and flux bias for a series of zenith angles, we can use the observed climatological CWPs from ISCCP to infer the resulting flux bias that would be associated with using the ICA for RT calculations in place of 3D RT. The monthly temporal resolution is not inherently an issue for this analysis given that we use a linear relationship between CWP and flux bias.

Additionally, we may account for the variations in surface albedo. In the RT

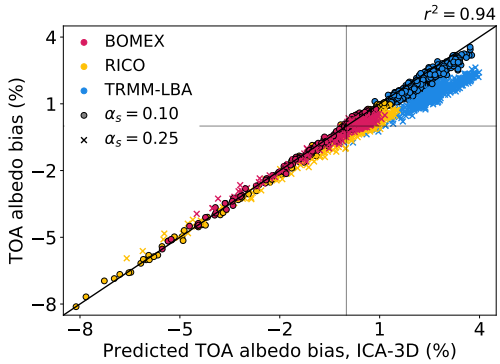

Figure 5.8: Predicted albedo bias from Eq. 5.6 compared to the computed albedo bias for convective cloud scenes (BOMEX, RICO, and TRMM-LBA) with different surface albedos. The predicted surface albedo is calculated from the simulations using a surface albedo of $\alpha_O = 0.06$ corresponding to an ocean surface. Each point represents the albedo bias at integer solar zenith angle from 0° to 90° for 5 ensemble members of each LES case. The colors denote the different cases and the symbol shapes denote the surface albedo. The 1:1 line is shown for reference.

calculations previously shown, we assume a constant surface albedo of $\alpha_O = 0.06$, corresponding to an ocean surface. The surface albedo affects the computed TOA and surface flux biases as shown in Eqs. 5.3 and 5.4. The albedo bias, written in Eq. 5.3, scales with the factor $(1 - 2\alpha_s(1 - f_c))$. We can therefore correct for the effect of the surface albedo by multiplying our computed flux or albedo bias by the ratio of the surface absorptions:

$$\Delta\alpha|_{\alpha_s} = \left(\frac{1 - 2\alpha_s(1 - f_c)}{1 - 2\alpha_O(1 - f_c)}\right) \Delta\alpha|_{\alpha_O} \,. \tag{5.6}$$

We run additional RT calculations for the convective cloud cases (BOMEX, RICO, and TRMM-LBA) and vary the specified surface albedo from $\alpha_s = 0.1$ to 0.25 (spanning the range for sub-polar land surfaces). Fig. 5.8 shows the correlation between the predicted TOA albedo bias using Eq. 5.6 and the explicitly calculated TOA albedo bias. The prediction based on Eq. 5.6 is robust with an r^2 value of 0.94. For stratocumulus clouds, since the cloud cover is nearly 1, the albedo bias depends very little on the surface albedo and is not shown. We use Eq. 5.6 globally to account for variations in the observed surface albedo without the need to run additional RT calculations and interpolate between discrete values.

To construct the annual-mean flux bias map shown in Fig. 5.9, we first calculated the solar zenith angle for each location on Earth and each hour of the year. Then,

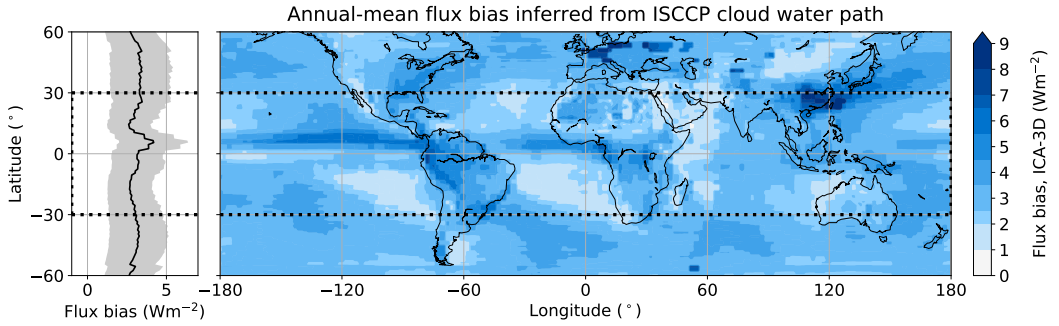

Figure 5.9: Map of annual-mean flux bias inferred from ISCCP in-cloud CWP. Left panel shows the zonally averaged flux bias in the black line and 1σ error bars in the grey shading that are derived from the linear regression in Fig. 5.7. Like in Fig. 5.6, we show only 60°S to 60°N because the clouds we have modeled are not representative of high-latitudes.

we obtained the flux bias given the observed CWP from the linear regression at the given zenith angle (Fig. 5.7). Finally, we made a correction using Eq. 5.6, based on the ratio of the observed surface absorption to the assumed ocean surface absorption used in the MYSTIC RT calculations. The resulting flux bias is an estimate of the bias that would be present in an ESM that is able to resolve the relevant dynamical scales of clouds, but makes the ICA during radiative transfer. This bias is smaller than the bias present in current ESMs, which also contains the biases due to PPA and cloud parameterizations, given their very coarse horizontal resolution (Cole, Barker, Randall, et al., 2005).

We focus on the tropics (30°S to 30°N, dotted box on Fig. 5.9), where our estimation of flux bias based on the LES cases is most robust and relevant; for higher-latitudes, we do not capture all the relevant cloud regimes with our sample of LES clouds, and so our flux bias estimate needs to be interpreted with caution. Shown in the left inset plot is the zonal-mean flux bias. The shading represents 1σ error from the regression of flux bias on CWP shown in Fig. 5.7 (as opposed to spatial or temporal variability).

The largest bias occurs in the ITCZ region and the storm track regions, especially over eastern Asia where the climatological CWP is maximal (Fig. 5.9). It corresponds to locations where the tallest clouds on Earth exist and where the mean zenith angle is smallest. The region of maximum bias migrates seasonally following the location of the ITCZ (and maximum insolation). Seasonal variations in cloud cover and cloud type are also manifest in the seasonal cycle of the 3D flux bias. In the annual

mean, the zonal-mean tropical flux bias is estimated to be 3.1 ± 1.6 W m^{-2}, and the maximum local flux bias in the annual mean is around 6.5 W m^{-2} (99th percentile). The annual-mean, zonal-mean tropical albedo bias is $0.7 \pm 0.4\%$ and is locally as large as 1.5% (99th percentile).

Our results are of the same order as those reported in Cole, Barker, O'Hirok, et al. (2005) and Barker, Cole, Li, Yi, et al. (2015) and Barker, Cole, Li, and Salzen (2016). Cole, Barker, O'Hirok, et al. (2005) also found the largest flux bias occurring over the ITCZ region, with a maximum bias of 5 W m^{-2} and tropical zonal-average bias of 1.5 W m^{-2} during the boreal winter. The larger value reported here is likely due to the fact that Fig. 5.9 averages over the shoulder seasons and the regression is based on higher-resolution cloud scenes, as quantified in Figures 5.3 and 5.6.

5.6 Summary and conclusions

In this paper we estimated the TOA flux and albedo biases that result from neglecting 3D radiative transfer through cloudy atmospheres. Although TOA shortwave radiative flux biases in current ESMs are predominantly due to deficiencies of subgrid-scale dynamical parameterizations that generate cloud cover biases, as convection parameterizations improve and model resolution increases, the relative contribution of 3D radiative effects to the total model error will increase. We have quantified the radiative flux and albedo bias that results from making the ICA by using a 3D Monte Carlo radiative transfer scheme applied to LES-generated 3D cloud fields. The flux and albedo biases were assessed across different cloud regimes and solar zenith angles. We took our findings from four canonical LES cases and applied them to observed climatological cloud occurrence to infer the spatially- and temporally-resolved flux and albedo biases.

We find that the largest flux bias comes from deep convective clouds at small solar zenith angles. The albedo bias is large and negative for shallow cumulus clouds at large solar zenith angles. These results quantitatively agree with previous studies using LES clouds to assess 3D effects (Hogan, Fielding, et al., 2019). There is room for future work considering a larger ensemble of cloud morphologies, which could be generated again by LES or alternatively could be retrieved from satellite observations. Our inferred global flux bias is based on only four tropical/subtropical LES cases and therefore does not represent the full diversity of extratropical cloud morphologies. This methodology cannot fully capture the effects of mid-latitude storms, for instance, which is why we do not emphasize our results outside of the

tropics.

We use the observed positive correlation between CWP and TOA flux bias from our LES ensemble to estimate the global spatiotemporal bias from neglecting 3D radiative transfer in a high-resolution ESM. We choose a simple linear model to map from satellite observations of climatological CWP to TOA flux bias. The deviations in our regression fit suggest that there is potential for a more robust mapping from cloud properties to radiative flux bias. Future work is necessary to explore this path towards a parameterization of 3D radiative effects in ESMs.

The large flux bias for Cb clouds at small solar zenith angles translates into a seasonal bias that peaks just off the equator in the summer hemisphere, tracking the position of the ITCZ. We estimate the annual-mean tropical-mean flux bias to be 3.1 ± 1.6 W m^{-2}. The flux bias computed here is small compared to the TOA shortwave flux errors typical for CMIP5 and CMIP6 models, which are on the order of 10 W m^{-2} in the mean (Zhao et al., 2018; Hourdin et al., 2020) and can reach 50 W m^{-2} in stratocumulus regions (Brient et al., 2019). However, the 3D bias is still comparable to the signal of anthropogenic greenhouse gas emissions for the coming decades, which is on the order of 2.5–3.1 W m^{-2} (Myhre et al., 2013). These results highlight the importance of considering the 3D radiative fluxes through clouds for Earth's radiation budget and Earth system modeling.

Acknowledgements. C.E.S. acknowledges support from NSF Graduate Research Fellowship under Grant No. DGE-1745301. I.L. is supported by a fellowship from the Resnick Sustainability Institute at Caltech. This research was additionally supported by the generosity of Eric and Wendy Schmidt by recommendation of the Schmidt Futures program. Part of this research was carried out at the Jet Propulsion Laboratory, California Institute of Technology, under a contract with the National Aeronautics and Space Administration. We thank three anonymous reviewers for helpful comments on an earlier version of this paper.

Data avaialability statement. All code or data used in this paper are freely available online. The LES were run using the PyCLES code (`https://climate-dynamics.org/software/#pycles`). The radiative transfer computations were done using the libRadtran code (`http://www.libradtran.org`). Post-processed LES 3D fields used as input files for libRadtran computations are available in Singer et al. (2021). The ISCCP data were downloaded from `https://climserv.ipsl.`

polytechnique.fr/gewexca/ and the GEWEX albedo measurements were downloaded from https://eosweb.larc.nasa.gov.

5.7 Appendix A: LES model setup

LES are performed using the anelastic fluid solver PyCLES (Pressel, Kaul, et al., 2015). Subgrid-scale fluxes are treated implicitly by the WENO scheme used in the numerical discretization of the equations (Pressel, Mishra, et al., 2017).

For each case, the characteristic timescale of convection is evaluated and taken to be representative of the dynamical decorrelation time τ. Snapshots are taken at least one dynamical decorrelation time apart, so that the cloud samples can be treated as independent in a statistical analysis of the flux biases. The decorrelation timescale is calculated as

$$\tau = \frac{z_{bl}}{w^*} + \frac{d_c}{\bar{w}_u}, \tag{5.7}$$

where z_{bl} is the mixed-layer height, $w^* = \left(z_{bl} \, \overline{w'b'}\Big|_s \right)^{1/3}$ is the Deardoff convective velocity, d_c is the cloud depth, and $\bar{w}_u$ is the mean updraft velocity within the cloud.

Shallow cumulus (ShCu) convection, BOMEX

The BOMEX LES case study is described in Siebesma et al. (2003). Surface boundary conditions, $\overline{w'q_t'}|_s$ and $\overline{w'\theta_l'}|_s$ are prescribed, resulting in sensible and latent heat fluxes of about 10 and 130 W m^{-2}, respectively. The atmospheric column is forced by clear-sky longwave radiative cooling, neglecting radiative cloud effects. A prescribed subsidence profile induces mean vertical advection of all fields, and specific humidity is further forced by large-scale horizontal advective drying in the lower 500 m. The liquid-water specific humidity is diagnosed through a saturation adjustment procedure. For BOMEX, the characteristic timescale of convection is $\tau \approx 40$ min, where $z_{bl} = 500$ m, $w^* = 0.66$ m s^{-1}, $d_c = 1300$ m, and $\bar{w}_u = 0.85$ m s^{-1}, and snapshots are taken every 1 hour. The domain size is set to 6.4 km in the horizontal and 3 km in the vertical. Results are reported for an isotropic resolution of $\Delta x_i = 20$ m.

Shallow cumulus (ShCu) convection, RICO

The RICO LES case study is described in vanZanten et al. (2011). The surface sensible and latent heat fluxes are modeled using bulk aerodynamic formulae with drag coefficients as specified in vanZanten et al. (2011), resulting in fluxes of around 6 and 145 W m^{-2}, respectively. The atmospheric column is forced by

prescribed profiles for subsidence and large-scale heat and moisture forcings that are a combination of radiative and advective forcings. The two-moment cloud microphysics scheme from Seifert and Beheng (2006) is used with cloud droplet concentration set to $N_d = 70$ cm^{-3}. For RICO, the characteristic timescale of convection is $\tau \approx 50$ min, where $z_{bl} \approx 500$ m, $w^* \approx 0.62$ m s^{-1}, $d_c = 2500$ m, and $\bar{w}_u \approx 1.2$ m s^{-1}, and snapshots are taken every 1 hour. The domain size is set to 12.8 km in the horizontal and 6 km in the vertical. Results are reported for an isotropic resolution of $\Delta x_i = 40$ m.

Stratocumulus-topped marine boundary layer (Sc), DYCOMS-II RF01

The simulation setup for DYCOMS-II RF01 follows the configuration of Stevens et al. (2005). The initial state consists of a well-mixed layer topped by a strong inversion in temperature and specific humidity, with $\Delta\theta_l = 8.5$ K and $\Delta q_t = -7.5$ g kg^{-1}. Surface latent and sensible heat fluxes are prescribed as 115 and 15 W m^{-2}, respectively. In addition, the humidity profile induces radiative cooling above cloud-top and warming at cloud-base. As in BOMEX, the liquid-water specific humidity is diagnosed through a saturation adjustment procedure. For the stratocumulus clouds, without strong updrafts and a thin cloud layer, the characteristic convective timescale is taken to be just the first term of Eq. (5.7), which evaluates to $\tau \approx 20$ min, with $z_{bl} = 850$ m and $w^* = 0.8$ m s^{-1}. Snapshots taken every 30 minutes are used in the analysis. The domain size is set to 3.36 km in the horizontal and 1.5 km in the vertical. Results are reported for a resolution of $\Delta z = 5$ m in the vertical and $\Delta x = \Delta y = 35$ m in the horizontal.

Deep convection (Cb), TRMM-LBA

Deep convective clouds are generated using the TRMM-LBA configuration detailed in Grabowski et al. (2006), based on observations of the diurnal cycle of convection in the Amazon during the rainy season. The diurnal cycle is forced by the surface fluxes, which are prescribed as a function of time. The magnitude of the fluxes maximizes 5.25 hours after dawn, with a peak latent and sensible heat fluxes of 554 and 270 W m^{-2}, respectively. The radiative cooling profile is also prescribed as a function of time. We use the one-moment microphysics scheme based on Kaul et al. (2015) with modifications described in Shen et al. (2020). Since this case study is not configured to reach a steady state, the simulation is run up to $t = 7$ hours. Deep convection is considered to be fully developed after 5 hours, when the liquid-water and ice-water paths stabilize (Grabowski et al., 2006). The ensemble

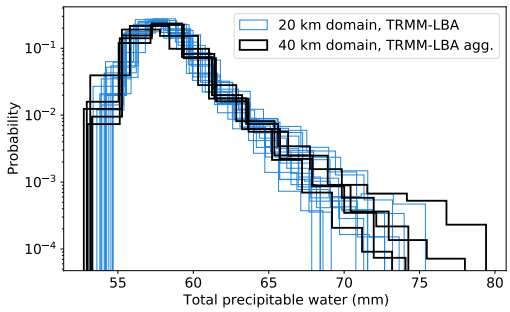

Figure 5.10: Normalized histogram of total precipitable water from the TRMM-LBA simulations in a 20 km domain vs. 40 km domain, which we use as a less and more-aggregated case of deep convection. The variance across the ensemble, shown by the width of the histogram, is representative of the degree of convective aggregation.

of cloud snapshots is formed by sampling after $t = 4$, 5.5, and 7 hours from a set of simulations with different initial conditions. For the idealized case (Figs. 5.2 and 5.6) only the 15 snapshots from $t = 7$ hours are used. The characteristic convective timescale is given by just the second term of Eq. (5.7), $\tau = \int_0^{z_{ct}} w_u^{-1} dz \approx 80$ min, where z_{ct} and w_u are the cloud-top height and updraft vertical velocity averaged over the last two hours, respectively. The random perturbations used in the initialization ensure that all cloud snapshots in the ensemble are uncorrelated. The domain size is set to 20 km in the horizontal and 22 km in the vertical. Results are reported for a resolution of $\Delta z = 50$ m in the vertical and $\Delta x = \Delta y = 100$ m in the horizontal.

For the large-domain simulations, we double the domain size to 40 km in the horizontal and run a smaller ensemble of $N_{\mathrm{LES}} = 5$ simulations. The mean cloud cover, cloud top heights, and cloud water path in the large and small domain ensembles are comparable at 0.30 and 0.32, 12.2 and 10.0 km, and 360 and 290 g m^{-2}, respectively. The large-domain simulations show a higher degree of aggregation as measured by the variance in total precipitable water, 4.3 mm^2, compared to 3.7 mm^2 in the original 20 km domain. Fig. A1 shows histograms of the total precipitable water for each of the TRMM-LBA simulations at 7 hours ($N_{\mathrm{LES}} = 15$ for the 20 km domain, and $N_{\mathrm{LES}} = 5$ for the 40 km domain). The wider histograms for the large-domain simulations illustrate the larger variance in this field, which is indicative of a higher degree of convective aggregation.

5.8 Appendix B: Radiative transfer details

We use the libRadtran MYSTIC Monte Carlo solver for the 3D and ICA radiative transfer calculations with no variation reduction techniques applied. The ICA is done using the `mc_ipa` setting which horizontally averages the fluxes from the full 3D calculation. The RT is done using $n = 10^4$ photons using the `atlas_plus_modtran` solar spectrum. The atmospheric molecular absorption is done using the `kato2` correlated-k parameterization (Kato et al., 1999; Mayer and Kylling, 2005). The atmospheric profile (pressure, temperature, density, and specific humidity) defined for the radiative transfer comes from the LES output and aerosols are neglected in these calculations. Because we only consider the flux bias and not absolute values, the LES are not embedded in a clear-sky atmosphere with a profile extension to a fixed height, although this is typical for radiative transfer calculations. The surface is treated as a Lambertian scatterer and the albedo was set to $\alpha_s = 0.06$ for all RT calculations. The observed surface albedo is accounted for through the approximation described in Section 5. Both the LES and RT assume doubly-periodic horizontal boundary conditions and the spatial resolution, which can be found in Table 5.1 for each case, is the same.

The MYSTIC solver from libRadtran requires 3D fields of liquid and ice water content and particle effective radius as input. The LES uses bulk microphysics schemes and does not explicitly compute the effective radius. For liquid-only clouds, the parameterization from Ackerman et al. (2009) and Blossey et al. (2013) with assumed droplet number of $N_d = 10^8$ m^{-3} is used. The full Mie scattering phase function is taken from the libRadtran lookup tables. Because the lookup tables are only valid for droplets with radius greater than 1 μm, smaller calculated effective radii were rounded to this minimum value.

For ice clouds, the parameterization from Wyser (1998) is used. The `hey` parameterization from Yang et al. (2013) and Emde et al. (2016) with habit type set to `ghm` (general habit mixture) is used. The `hey` parameterization uses the complete scattering phase function as calculated from single scattering models for ice crystals in (Yang et al., 2013), rather than employing an approximation like Henyey-Greenstein phase function, which has been shown to be another source of error in RT (Barker, Cole, Li, Yi, et al., 2015). The results are not dependent on the exact choice for ice crystal shape or roughness (Fig. B1). Note that the `hey` ice parameterization is only valid for radii less than 90 μm, and larger calculated effective radii were rounded to this maximum value.

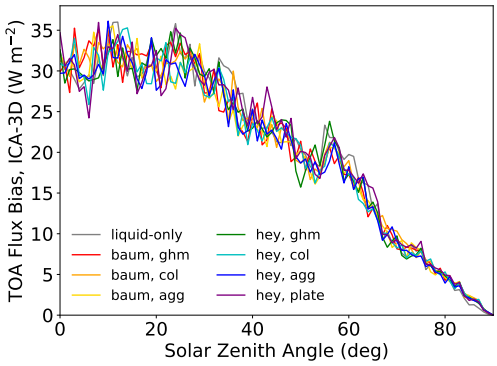

Figure 5.11: TOA reflected bias across zenith angles for different ice parameterizations in one TRMM-LBA cloud snapshot.

Deep convective clouds, reaching upwards of 10 km, nearly always contain ice crystals in addition to liquid water. Optical properties of ice crystals depend on their size, shape (or habit), and surface smoothness. Two different parameterizations, with three and four habit choices, respectively, were tested. The differences between these parameterization variants are negligible; they are much smaller than the variability stemming from the cloud dynamics (statistical spread between snapshots) and also much smaller than the magnitude of the 3D effects (Fig. B1).

The `hey` parameterization with general habit mixture (`ghm`) is used in the main text (Yang et al., 2013; Emde et al., 2016). This parameterization is valid for a spectral range from $0.2 - 5\mu$m, and for ice effective radii from $5 - 90\mu$m. `hey` assumes smooth crystals and allows for four choices of habit: `ghm`, solid column (`col`), rough aggregate (`agg`), and `plate`.

The other parameterization tested was `baum_v36` (Heymsfield et al., 2013; Yang et al., 2013; Baum et al., 2014). This parameterization is valid over a wider spectral range ($0.2 - 99\mu$m), but a narrower effective radius range ($5 - 60\mu$m). Particles with effective radius outside of the accepted range were rounded to the maximum allowed value. The `baum_v36` parameterization assumes severely roughened particles. It allows for three choices of habit: `ghm`, solid column (`col`), and rough-aggregate (`agg`).

These seven variants are compared in Fig. B1 for one cloud snapshot from the TRMM-LBA case and they show very similar results. Also shown in Fig. B1 is a RT calculation done on the same cloud field, but only including the liquid droplets and ignoring the ice particles. We use the full Mie scattering phase function without

any parameterization for the liquid portion of the cloud in all cases. The difference between the liquid-only and liquid and ice simulated absolute fluxes can be up to 20% depending on the parameterization used (not shown), but the flux bias (ICA - 3D) is very similar for the liquid-only and all ice parameterizations.

5.9 Appendix C: Cloud property proxy for flux bias

We explored several different cloud properties to use as a proxy for the flux bias. Our limited study concluded that the in-cloud cloud water path (CWP) was the best proxy because it shows a strong positive, linear correlation with flux bias. Other cloud scene properties we examined included cloud top height (CTH), cloud cover (cc), and the geometric mean of covered area and uncovered area, $\sqrt{\text{cc}(1-\text{cc})}$. The linear regression fits are shown in Fig. C1. The rms error for CWP is the smallest. Although CTH (or cloud depth) are also reasonable proxies, they are more difficult to measure from satellite, and therefore we use CWP in this study. An important extension to this work would be to allow for multiple cloud properties and a more complex model than a linear fit to describe the flux bias. However, with our limited data from only four LES cases in this present study, we do not feel justified to use a more complex model.

References

[1] G. L. Stephens et al. “The albedo of Earth”. In: *Reviews of Geophysics* 53.1 (2015), pp. 141–163. DOI: 10.1002/2014RG000449.

[2] F. A.-M. Bender et al. “22 views of the global albedo—comparison between 20 GCMs and two satellites”. In: *Tellus A: Dynamic Meteorology and Oceanography* 58.3 (2006), pp. 320–330. DOI: 10.1111/j.1600-0870.2006.00181.x.

[3] A. Voigt et al. “The observed hemispheric symmetry in reflected shortwave irradiance”. In: *J. Climate* 26 (2013), pp. 468–477. DOI: https://doi.org/10.1175/JCLI-D-12-00132.1.

[4] A. Engström et al. “The nonlinear relationship between albedo and cloud fraction on near-global, monthly mean scale in observations and in the CMIP5 model ensemble”. In: *Geophysical Research Letters* 42.21 (2015), pp. 9571–9578. DOI: https://doi.org/10.1002/2015GL066275.

[5] T. Schneider et al. “Climate goals and computing the future of clouds”. In: *Nat. Climate Change opinion & comment* 7.1 (2017), pp. 3–5. DOI: 10.1038/nclimate3190.

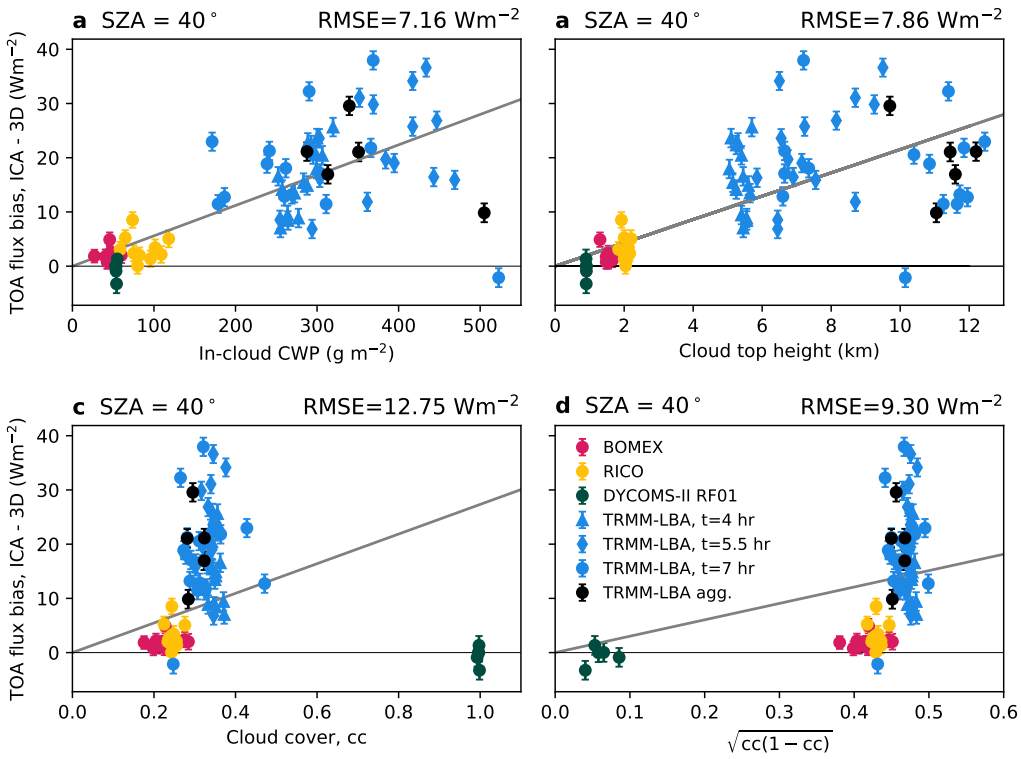

Figure 5.12: Regression of flux bias on several different cloud properties (a) in-cloud cloud water path (CWP), (b) cloud top height, (c) cloud cover, and (d) $\sqrt{cc(1-cc)}$. All panels show the flux bias for a zenith angle of 40°. (a) is the same as Fig. 5.7b. The rms error is shown for each panel and is smallest for the in-cloud CWP case (a).

[6] A. Marshak and A. Davis, eds. *3D radiative transfer in cloudy atmospheres*. Physics of Earth and Space Environments. Berlin/Heidelberg: Springer-Verlag, 2005. DOI: 10.1007/3-540-28519-9.

[7] R. Cahalan and W. Wiscombe. "Proceedings of the Second Atmospheric Radiation Measurement (ARM) Science Team Meeting". In: *Plane-Parallel Albedo Bias*. December. Denver, Colorado, 1992, p. 35.

[8] J. K. Shonk and R. J. Hogan. "Tripleclouds: An efficient method for representing horizontal cloud inhomogeneity in 1D Radiation schemes by using three regions at each height". In: *Journal of Climate* 21.11 (2008), pp. 2352–2370. DOI: 10.1175/2007JCLI1940.1.

[9] R. Pincus et al. "A fast, flexible, approximate technique for computing radiative transfer in inhomogeneous cloud fields". In: *Journal of Geophysical Research: Atmospheres* 108.13 (2003), pp. 1–5. DOI: 10.1029/2002jd003322.

[10] Y. Cohen et al. "Unified Entrainment and Detrainment Closures for Extended Eddy-Diffusivity Mass-Flux Schemes". In: *Journal of Advances in*

Modeling Earth Systems 12.9 (2020), e2020MS002162. DOI: 10.1029/2020MS002162.

[11] J. N. S. Cole, H. W. Barker, D. A. Randall, et al. "Global consequences of interactions between clouds and radiation at scales unresolved by global climate models". In: *Geophysical Research Letters* 32.6 (2005). DOI: 10.1029/2004GL020945.

[12] G. J. Kooperman et al. "Robust effects of cloud superparameterization on simulated daily rainfall intensity statistics across multiple versions of the Community Earth System Model". In: *Journal of Advances in Modeling Earth Systems* 8.1 (2016), pp. 140–165. DOI: 10.1002/2015MS000574.

[13] M. F. Khairoutdinov and D. A. Randall. "A cloud resolving model as a cloud parameterization in the NCAR Community Climate System Model: Preliminary results". In: *Geophysical Research Letters* 28.18 (2001), pp. 3617–3620. DOI: 10.1029/2001GL013552.

[14] R. F. Cahalan et al. "Independent Pixel and Monte Carlo Estimates of Stratocumulus Albedo". In: *Journal of the Atmospheric Sciences* 51.24 (1994), pp. 3776–3790. DOI: 10.1175/1520-0469(1994)051<3776:IPAMCE>2.0.CO;2.

[15] S. A. K. Schäfer et al. "Representing 3-D cloud radiation effects in two-stream schemes: 1. Longwave considerations and effective cloud edge length". In: *Journal of Geophysical Research: Atmospheres* 121.14 (2016), pp. 8567–8582. DOI: 10.1002/2016JD024876.

[16] R. J. Hogan, M. D. Fielding, et al. "Entrapment: An Important Mechanism to Explain the Shortwave 3D Radiative Effect of Clouds". In: *Journal of the Atmospheric Sciences* 2019 (1 2019), pp. 48–66. DOI: 10.1175/JAS-D-18-0366.1.

[17] R. J. Hogan and A. Bozzo. "A Flexible and Efficient Radiation Scheme for the ECMWF Model". In: *Journal of Advances in Modeling Earth Systems* 10 (8 2018). https://doi.org/10.1029/2018MS001364, pp. 1990–2008. DOI: https://doi.org/10.1029/2018MS001364.

[18] B. Mayer and A. Kylling. "Technical note: The libRadtran software package for radiative transfer calculations - description and examples of use". In: *Atmospheric Chemistry and Physics* 5.7 (2005), pp. 1855–1877. DOI: 10.5194/acp-5-1855-2005.

[19] C. Emde et al. "The libRadtran software package for radiative transfer calculations (version 2.0.1)". In: *Geoscientific Model Development* 9.5 (2016), pp. 1647–1672. DOI: 10.5194/gmd-9-1647-2016.

[20] N. Villefranque et al. "A Path-Tracing Monte Carlo Library for 3-D Radiative Transfer in Highly Resolved Cloudy Atmospheres". In: *Journal of Advances in Modeling Earth Systems* 11.8 (2019), pp. 2449–2473. DOI: 10.1029/2018MS001602.

[21] J. J. Gristey et al. “Surface solar irradiance in continental shallow cumulus fields: Observations and large eddy simulation”. In: *Journal of the Atmospheric Sciences* (2019), pp. 19–0261. DOI: 10.1175/JAS-D-19-0261.1.

[22] M. A. Veerman et al. “Three-Dimensional Radiative Effects By Shallow Cumulus Clouds on Dynamic Heterogeneities Over a Vegetated Surface”. In: *Journal of Advances in Modeling Earth Systems* 12.7 (2020). DOI: 10.1029/2019MS001990.

[23] A. Marshak, A. Davis, W. Wiscombe, and G. Titov. “The verisimilitude of the independent pixel approximation used in cloud remote sensing”. In: *Remote Sensing of Environment* 52 (1995), pp. 71–78. DOI: 10.1016/0034-4257(95)00016-T.

[24] W. O’Hirok and C. Gautier. “A Three-Dimensional Radiative Transfer Model to Investigate the Solar Radiation within a Cloudy Atmosphere. Part I: Spatial Effects”. In: *Journal of the Atmospheric Sciences* 55.12 (1998), pp. 2162–2179. DOI: 10.1175/1520-0469(1998)055<2162:ATDRTM>2.0.CO;2.

[25] W. O’Hirok and C. Gautier. “The impact of model resolution on differences between independent column approximation and Monte Carlo estimates of shortwave surface irradiance and atmospheric heating rate”. In: *Journal of the Atmospheric Sciences* 62.8 (2005), pp. 2939–2951. DOI: 10.1175/JAS3519.1.

[26] H. W. Barker, G. L. Stephens, et al. “Assessing 1D Atmospheric Solar Radiative Transfer Models: Interpretation and Handling of Unresolved Clouds”. In: *Journal of Climate* 16.16 (2003), pp. 2676–2699. DOI: 10.1175/1520-0442(2003)016<2676:ADASRT>2.0.CO;2.

[27] H. W. Barker, S. Kato, et al. “Computation of Solar Radiative Fluxes by 1D and 3D Methods Using Cloudy Atmospheres Inferred from A-train Satellite Data”. In: *Surveys in Geophysics* 33.3-4 (2012), pp. 657–676. DOI: 10.1007/s10712-011-9164-9.

[28] A. Marshak, A. Davis, W. Wiscombe, and R. Cahalan. “Radiative smoothing in fractal clouds”. In: *Journal of Geophysical Research* 100.D12 (1995), p. 26247. DOI: 10.1029/95JD02895.

[29] T. Várnai and R. Davies. “Effects of cloud heterogeneities on shortwave radiation: Comparison of cloud-top variability and internal heterogeneity”. In: *Journal of the Atmospheric Sciences* 56.24 (1999), pp. 4206–4224. DOI: 10.1175/1520-0469(1999)056<4206:EOCHOS>2.0.CO;2.

[30] J. W. Frame et al. “An application of the tilted independent pixel approximation to cumulonimbus environments”. In: *Atmospheric Research* 91 (2009), pp. 127–136. DOI: 10.1016/j.atmosres.2008.05.005.

[31] R. J. Hogan and J. K. P. Shonk. "Incorporating the Effects of 3D Radiative Transfer in the Presence of Clouds into Two-Stream Multilayer Radiation Schemes". In: *Journal of the Atmospheric Sciences* 70.2 (2013), pp. 708–724. DOI: 10.1175/JAS-D-12-041.1.

[32] U. Wissmeier et al. "paNTICA: A fast 3D radiative transfer scheme to calculate surface solar irradiance for NWP and LES models". In: *Journal of Applied Meteorology and Climatology* 52.8 (2013), pp. 1698–1715. DOI: 10.1175/JAMC-D-12-0227.1.

[33] M. Okata et al. "A study on radiative transfer effects in 3-D cloudy atmosphere using satellite data". In: *Journal of Geophysical Research: Atmospheres* 122.1 (2017), pp. 443–468. DOI: 10.1002/2016JD025441.

[34] L. Oreopoulos and H. W. Barker. "Accounting for subgrid-scale cloud variability in a multi-layer 1d solar radiative transfer algorithm". In: *Quarterly Journal of the Royal Meteorological Society* 125.553 (1999), pp. 301–330. DOI: 10.1002/qj.49712555316.

[35] C. Klinger and B. Mayer. "The Neighboring Column Approximation (NCA) – A fast approach for the calculation of 3D thermal heating rates in cloud resolving models". In: *J. Quant. Spectrosc. Radiat. Transf.* 168 (2016), pp. 17–28. DOI: 10.1016/j.jqsrt.2015.08.020.

[36] C. Klinger and B. Mayer. "Neighboring Column Approximation—An Improved 3D Thermal Radiative Transfer Approximation for Non-Rectangular Grids". In: *J. Adv. Model. Earth Syst.* 12.1 (2020). DOI: 10.1029/2019MS001843.

[37] J. N. S. Cole, H. W. Barker, W. O'Hirok, et al. "Atmospheric radiative transfer through global arrays of 2D clouds". In: *Geophysical Research Letters* 32.19 (2005). DOI: 10.1029/2005GL023329.

[38] H. W. Barker, J. N. S. Cole, J. Li, B. Yi, et al. "Estimation of Errors in Two-Stream Approximations of the Solar Radiative Transfer Equation for Cloudy-Sky Conditions". In: *Journal of the Atmospheric Sciences* 72.11 (2015), pp. 4053–4074. DOI: 10.1175/JAS-D-15-0033.1.

[39] H. W. Barker, J. N. S. Cole, J. Li, and K. von Salzen. "A parametrization of 3-D subgrid-scale clouds for conventional GCMs: Assessment using A-Train satellite data and solar radiative transfer characteristics". In: *Journal of Advances in Modeling Earth Systems* 8.2 (2016), pp. 566–597. DOI: 10.1002/2015MS000601.

[40] D. M. Romps and R. Öktem. "Observing clouds in 4d with multiview stereophotogrammetry". In: *Bulletin of the American Meteorological Society* 99.12 (2018), pp. 2575–2586. DOI: 10.1175/BAMS-D-18-0029.1.

[41] E. Castro et al. "Determination of Cloud-top Height through Three-dimensional Cloud Reconstruction using DIWATA-1 Data". In: *Scientific Reports* 10.1 (2020), pp. 1–13. DOI: 10.1038/s41598-020-64274-z.

[42] K. G. Pressel, C. M. Kaul, et al. “Large-eddy simulation in an anelastic framework with closed water and entropy balances”. In: *J. Adv. Model. Earth Syst.* 7.3 (2015), pp. 1425–1456. DOI: 10.1002/2015MS000496.

[43] K. G. Pressel, S. Mishra, et al. “Numerics and subgrid-scale modeling in large eddy simulations of stratocumulus clouds”. In: *Journal of Advances in Modeling Earth Systems* 9.2 (2017), pp. 1342–1365. DOI: 10.1002/2016MS000778.

[44] P. J. Griewank et al. “Size dependence in chord characteristics from simulated and observed continental shallow cumulus”. In: *Atmospheric Chemistry and Physics* 20.17 (2020), pp. 10211–10230. DOI: 10.5194/acp-20-10211-2020.

[45] G. Cesana et al. “The Cumulus And Stratocumulus CloudSat-CALIPSO Dataset (CASCCAD)”. In: *Earth System Science Data* 11.4 (2019), pp. 1745–1764. DOI: 10.5194/essd-11-1745-2019.

[46] A. P. Siebesma et al. “A large eddy simulation intercomparison study of shallow cumulus convection”. In: *Journal of the Atmospheric Sciences* 60.10 (2003), pp. 1201–1219. DOI: 10.1175/1520-0469(2003)60<1201:ALESIS>2.0.CO;2.

[47] M. C. vanZanten et al. “Controls on precipitation and cloudiness in simulations of trade-wind cumulus as observed during RICO”. In: *Journal of Advances in Modeling Earth Systems* 3.2 (2011). DOI: 10.1029/2011MS000056.

[48] B. Stevens et al. “Evaluation of large-eddy simulations via observations of nocturnal marine stratocumulus”. In: *Monthly Weather Review* 133.6 (2005), pp. 1443–1462. DOI: 10.1175/MWR2930.1.

[49] W. W. Grabowski et al. “Daytime convective development over land: A model intercomparison based on LBA observations”. In: *Quarterly Journal of the Royal Meteorological Society* 132.615 (2006), pp. 317–344. DOI: 10.1256/qj.04.147.

[50] N. Jeevanjee and D. M. Romps. “Convective self-aggregation, cold pools, and domain size”. In: *Geophysical Research Letters* 40.5 (2013), pp. 994–998. DOI: 10.1002/grl.50204.

[51] A. A. Wing et al. “Convective Self-Aggregation in Numerical Simulations: A Review”. In: *Surveys in Geophysics* 38.6 (2017), pp. 1173–1197. DOI: 10.1007/s10712-017-9408-4.

[52] C. R. Patrizio and D. A. Randall. “Sensitivity of Convective Self-Aggregation to Domain Size”. In: *Journal of Advances in Modeling Earth Systems* 11.7 (2019), pp. 1995–2019. DOI: 10.1029/2019MS001672.

[53] C. S. Bretherton. “Insights into low-latitude cloud feedbacks from high-resolution models”. In: *Philos. Trans. R. Soc. A Math. Phys. Eng. Sci.* 373.2054 (2015). DOI: 10.1098/rsta.2014.0415.

[54] B. Mayer. "Radiative transfer in the cloudy atmosphere". In: *EPJ Web of Conferences* 1 (2009), pp. 75–99. DOI: 10.1140/epjconf/e2009-00912-1.

[55] A. S. Ackerman et al. "Large-Eddy Simulations of a Drizzling, Stratocumulus-Topped Marine Boundary Layer". In: *Monthly Weather Review* 137.3 (2009), pp. 1083–1110. DOI: 10.1175/2008MWR2582.1.

[56] P. N. Blossey et al. "Marine low cloud sensitivity to an idealized climate change: The CGILS LES intercomparison". In: *J. Adv. Model. Earth Syst.* 5.2 (2013), pp. 234–258. DOI: 10.1002/jame.20025.

[57] K. Wyser. "The effective radius in ice clouds". In: *Journal of Climate* 11.7 (1998), pp. 1793–1802. DOI: 10.1175/1520-0442(1998)011<1793:TERIIC>2.0.CO;2.

[58] P. Yang et al. "Spectrally consistent scattering, absorption, and polarization properties of atmospheric ice crystals at wavelengths from 0.2 to 100 um". In: *Journal of the Atmospheric Sciences* 70.1 (2013), pp. 330–347. DOI: 10.1175/JAS-D-12-039.1.

[59] W. B. Rossow et al. "Advances in understanding clouds from ISCCP". In: *Bulletin of the American Meteorological Society* 80.11 (1999), pp. 2261–2287. DOI: 10.1175/1520-0477(1999)080<2261:AIUCFI>2.0.CO;2.

[60] W. Rossow and E. Duenas. "The International Satellite Cloud Climatology Project (ISCCP) web site: An online resource for research". In: *Bulletin of the American Meteorological Society* 85.2 (2004), pp. 167–176. DOI: 10.1175/BAMS-85-2-167.

[61] R. Marchand et al. "A review of cloud top height and optical depth histograms from MISR, ISCCP, and MODIS". In: *Journal of Geophysical Research* 115.D16 (2010). DOI: 10.1029/2009JD013422.

[62] C. Stubenrauch et al. *Assessment of global cloud data sets from satellites: A project of the world climate research programme Global Energy and Water Cycle Experiment (GEWEX) Radiation Panel*. Tech. rep. 23. World Climate Research Programme, 2012.

[63] C. J. Stubenrauch et al. "Assessment of clobal cloud datasets from satellites: Project and database initiated by the GEWEX radiation panel". In: *Bulletin of the American Meteorological Society* 94.7 (2013), pp. 1031–1049. DOI: 10.1175/BAMS-D-12-00117.1.

[64] M. Zhao et al. "The GFDL Global Atmosphere and Land Model AM4.0/LM4.0: 2. Model Description, Sensitivity Studies, and Tuning Strategies". In: *Journal of Advances in Modeling Earth Systems* 10.3 (2018), pp. 735–769. DOI: 10.1002/2017MS001209.

[65] F. Hourdin et al. “LMDZ6A: the atmospheric component of the IPSL climate model with improved and better tuned physics”. In: *Journal of Advances in Modeling Earth Systems* (2020). DOI: 10.1029/2019MS001892.

[66] F. Brient et al. “Evaluating Marine Stratocumulus Clouds in the CNRM-CM6-1 Model Using Short-Term Hindcasts”. In: *J. Adv. Model. Earth Syst.* 11.1 (2019), pp. 127–148. DOI: 10.1029/2018MS001461.

[67] G. Myhre et al. “Anthropogenic and Natural Radiative Forcing”. In: *Climate Change 2013: The Physical Science Basis. Contribution of Working Group I to the Fifth Assessment Report of the Intergovernmental Panel on Climate Change*. Ed. by T. Stocker et al. Cambridge, United Kingdom and New York, NY, USA: Cambridge University Press, 2013. Chap. 8, pp. 659–740.

[68] C. Singer et al. *Data for “Top-of-atmosphere albedo bias from neglecting three-dimensional radiative transfer through clouds”*. 2021. DOI: 10.22002/D1.1637.

[69] A. Seifert and K. D. Beheng. “A two-moment cloud microphysics parameterization for mixed-phase clouds. Part 1: Model description”. In: *Meteorology and Atmospheric Physics* 92.1-2 (2006), pp. 45–66. DOI: 10.1007/s00703-005-0112-4.

[70] C. M. Kaul et al. “Sensitivities in Large-Eddy Simulations of Mixed-Phase Arctic Stratocumulus Clouds Using a Simple Microphysics Approach”. In: *Monthly Weather Review* 143.11 (2015), pp. 4393–4421. DOI: 10.1175/MWR-D-14-00319.1.

[71] Z. Shen et al. “Statistically Steady State Large-Eddy Simulations Forced by an Idealized GCM: 1. Forcing Framework and Simulation Characteristics”. In: *Journal of Advances in Modeling Earth Systems* 12.2 (2020). DOI: 10.1029/2019MS001814.

[72] S. Kato et al. “The k-distribution method and correlated-k approximation for a shortwave radiative transfer model”. In: *Journal of Quantitative Spectroscopy and Radiative Transfer* 62.1 (1999), pp. 109–121. DOI: https://doi.org/10.1016/S0022-4073(98)00075-2.

[73] A. J. Heymsfield et al. “Ice cloud particle size distributions and pressure-dependent terminal velocities from in situ observations at temperatures from 0° to -86°C”. In: *Journal of the Atmospheric Sciences* 70.12 (2013), pp. 4123–4154. DOI: 10.1175/JAS-D-12-0124.1.

[74] B. A. Baum et al. “Ice cloud single-scattering property models with the full phase matrix at wavelengths from 0.2 to 100um”. In: *Journal of Quantitative Spectroscopy and Radiative Transfer* 146 (2014), pp. 123–139. DOI: 10.1016/j.jqsrt.2014.02.029.

Appendix A

GENDER DISPARITIES IN GPS QUALIFYING EXAM OUTCOMES

A.1 Remarks from the author

The following chapter details information on outcomes of the Caltech GPS qualifying exam that have been collected by myself and a collection of graduate student colleagues. The chapter is broken into two sections:

1. The first section is based on a report I wrote for Heather Knutson's Ge/Ay 117 course in Winter 2020. The analysis was updated in Spring 2021. Data collection has been transferred to the GPS Division.

2. The survey, presented later in this chapter, originated as a response to the statistical analysis of Part 1. The survey targeted the same cohort of students (and recent alumni) who made up the years of analysis in the original report.

Myself and my collaborators on this work are indebted to the generation of graduate students who came before us, who preserved these ideas through a whisper network, and motivated the initial statistical study.

The following is the first ever compilation of GPS qualifying exam data. The results are not surprising to those engaged with the issue, but are deeply troubling nonetheless. I hope that this report inspires a recognition of the importance of collecting meta-data about the exams. Without this multi-year dataset it is impossible to discern any trends from small annual samples with lots of variability. However, the numbers do add up over time and with only six (and now seven, or more) years, these data are able to demonstrate stark discrepancies in exam outcomes. It is necessary for the Division to keep a thorough record of exams and use that data to help inform changes to the Qualifying Exams themselves, mentoring of graduate students, and even admissions criteria.

This chapter is presented as a record of the efforts made by myself and my colleagues during our time as Ph.D. students at Caltech with the hopes that it will preserve our knowledge gained and the progress we have made through tireless advocacy.

A.2 Part 1: Are there robust statistical differences in exam outcome between men and women?

Summary

This project uses a statistical model to understand GPS qualifying exam outcomes. I use a data set of exam outcomes from the past six years to inform my model. I test the hypothesis that demographic information about the students can be used to predict the outcome of the qualifying exam.

The previous literature addressing topics of bias in exam scores and outcomes is very rich. A through review has not been conducted, but there are so many more extensions and additions to this analysis that can, and should, be inspired by previous work.

What is the exam?

In the Caltech Geological and Planetary Science Division (GPS), all graduate students take a qualifying exam in September at the end of their first year of study. The exam format consists of a written report (10 pages) and an oral defense (3 hours) of the two proposition projects to a committee of historically five, and now four, faculty members, including the two proposition advisors.

Data

These data have been compiled through interviews with individuals, scraped from online CVs, and corroborated by friends and colleagues. These data only extend back to 2014 due to limited time and resources for collecting them. Data for additional individuals exists dating back 10 years, but only data from "complete" years (where every individual in a cohort has been accounted for) has been included in this analysis to limit sampling bias.

The anonymized dataset consists of information for each of the 119 students who have taken the GPS qualifying exam since 2014. The information collected includes: (1) year exam was taken, (2) option within GPS, (3) (binary) gender of student, (4) are they a native or non-native English speaker, (5) did they have a masters before coming to Caltech, and (6) the outcome of the exam.

Figure A.1 shows the number of students who passed and failed the qualifying exam in each of the six years. Figure A.2 shows the total number of students who passed and failed the exam by option, gender, or English language status.

Additional information about whether a student who failed retook the exam and the

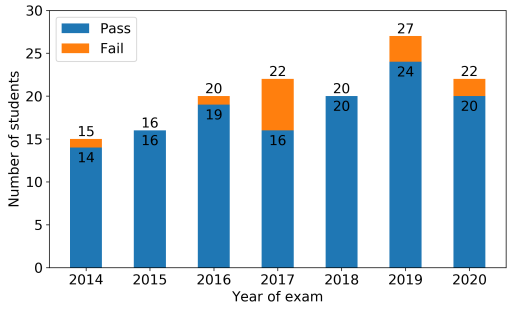

Figure A.1: Number of students per year who passed or failed the exam. Labels are total number of students and number who passed for each year.

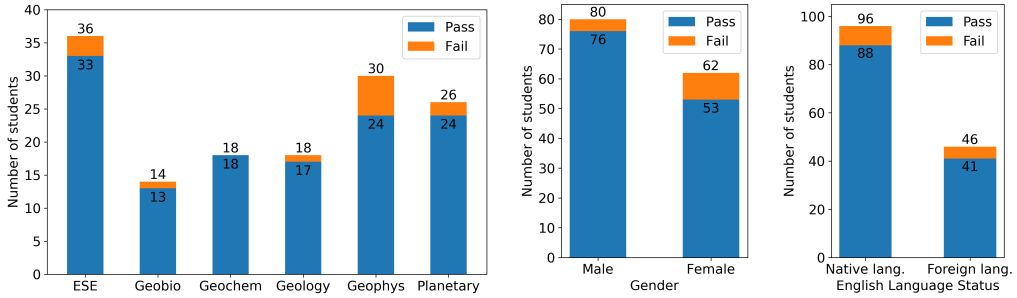

Figure A.2: Number of students per option (left), gender (center), or English language status (right) who passed or failed the exam. Labels are total number of students and number who passed for each category.

outcome of that retake has also been tracked, but is not included in the analysis. For some individuals, there is data on whether they left the PhD program after passing their exam but before completing the degree. Additional variables that are of interest to the author based in previous literature include the student's status as a underrepresented minority or first-generation college student, bachelor's GPA, GRE score, and the faculty on the examining committee. These data have yet to be collected.

For each additional variable included in the model, more individuals are needed to constrain the uncertainties on the power of that predictor, which poses a challenge to this analysis. For the present study only the students' option, gender, and English language status are included as predictors. These factors were determined as being potentially predictive via a preliminary analysis of these data. Figure A.3 shows the fraction of students per category who passed or failed the exam. It is very obvious that being in the Geophysics option is a relevant predictor for exam success. Given

that women and foreign speakers of English fail at higher rates than men and native speakers (respectively), it is possible that these are also important predictors. While having a masters degree appears to be less important (and also possibly correlated with English language status given that a large number of international students come with prior masters degrees).

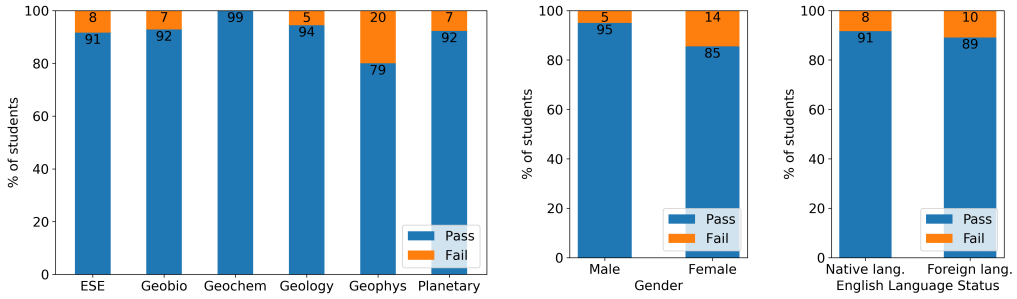

Figure A.3: Percentage of students per option (left), gender (center), or English language status (right) who passed or failed the exam. Labels are percentage of students who passed or failed for each category.

The goal of this study is to determine whether these patterns observed in the data are statistically significant, and if so, how much being in one of these groups statistically helps or hurts your probability of passing your qualifying exam.

Statistical Methods

Based on the preliminary analysis shown above, I consider the dependence of exam outcome on three variables for my model: (1) option, (2) gender, and (3) English language status. The statistical analysis is done in the following steps.

1. Because these variables are categorical, I first create dummy variables to use in the model. For each variable, there must be $n-1$ binary dummy variables where n is the number of possible categories. This is to avoid the "dummy variable trap." So the total number of variables will be $N = 1 + \sum_{i=1}^{3}(n_i - 1)$. When one variable for each category is thrown away I am implicitly creating a "base state" against which all perturbations are compared against.

2. The exam outcome is a binary variable (pass or fail). For this reason I am using a logistic model

$$\sigma(t) = \frac{1}{1+e^{-t}}. \tag{A.1}$$

Here, t is known as a "latent variable" because it is not observed. In this case, I propose using

$$t = \beta_0 + \beta_1 x_1 + \beta_2 x_2 + ... + \beta_N x_N + \beta_{N+1} x_1 x_2 + \beta_{N+2} x_1 x_3 + ..., \quad (A.2)$$

a linear combination of the explanatory variables ($\vec{x} = \{x_1 ... x_N\}$), including interaction terms. These interaction terms quantify the importance of intersectional identities. These can be included in extensions of the present analysis, but were omitted due to time and data constraints.

For simplicity, I reduce this model to

$$t = \beta_0 + \beta_1 x_1 + \beta_2 x_2 + \beta_3 x_3 + \beta_4 x_4 + \beta_5 x_5, \quad (A.3)$$

where β_0 is the constant term representing the base case, β_1 represents the effects of gender, β_2 represents the effects of English language status, and $\beta_3 - \beta_5$ represent the effect of option. It is possible/likely that some of these β_i terms are zero within uncertainty.

3. I use a Bayesian approach to calculate these coefficients β_i using these data. I model the process of the qualifying exams as a Bernoulli process, where the demographic factors will predict a certain probability of passing ($p_k = \sigma(f(\vec{x}_k))$). The result, if a person actually passes or not, follows a binomial distribution. Therefore, the likelihood can be calculated as

$$\mathcal{L} = \prod_{k=1}^{M} p_k^{y_k} (1 - p_k)^{1 - y_k}. \quad (A.4)$$

4. Finally, I use a standard Metropolis-Hastings Markov Chain Monte Carlo (MCMC) to fit β_i. With the results of the MCMC, I calculate the probability of passing $p = \sigma(\vec{x})$ and the odds $e^{f(\vec{x})}$. Furthermore, I calculate the odds ratio. For example, the odds ratio for exam outcome for men vs. women, given that the base state of $x_1 = 0$ is woman,

$$OR = \frac{e^{f(\vec{x}|x_1=1)}}{e^{f(\vec{x}|x_1=0)}} = e^{\beta_1} \quad (A.5)$$

quantifies how many times more likely it is to pass given that you are a man vs. woman.

Results

The MCMC was initialized by first doing optimal estimation of the parameters. This led to very rapid convergence and the burn-in period was negligible. The MCMC was run for 50,000 steps. The initial parameter values were

$$\vec{\beta}_{guess} = [2.55, 1.14, -0.14, -0.57, -1.96, -0.01]$$

and the parameters converged to

$$\vec{\beta}_{final} = [2.70, 1.23, -0.13, -0.37, -2.11, 0.22].$$

Figure A.4 shows a corner plot of the six coefficients fit in the model $\beta_0 - \beta_5$. The probability of passing for the base state is

$$p_{base} = \frac{1}{1 + e^{-\beta_0}} = \frac{1}{1 + e^{-2.70}} = 0.937.$$

The β_i coefficients that are statistically different from zero (at the 1σ level) are β_1 and β_4 which correspond to the gender effect ($x_1 = 0$ for women and $x_1 = 1$ for men) and geophysics effect. Because β_1 is positive, this means that it is more likely for men to pass the exam compared to women, and β_4 being negative means it is more likely for someone in geophysics to fail the exam compared to someone in ESE (the base state).

Given that women and students who speak English as a foreign language were both failing the exam at twice the rate of their peers (Figure A.3), why is gender but not English language status a statistically significant predictor? This must be because English language status is correlated with some other variable. This becomes evident when looking at Figure A.5: gender is not highly correlated with option, but English language status is.

While students who speak English as a foreign language fail at higher rates, it turns out this is because most of these students are in the Geophysics or ESE options, while very few of these students are in Geobiology, Geochemistry, or Geology. But, Geophysics has by far the highest failure rate (20%) and Geochemistry and Geology have a 0% failure rate (in the past six years).

On the other hand, for gender, there is no strong correlation between options. All options except Geophysics have nearly equal proportions of male and female students. But by looking at this breakdown by gender and option it is clear that

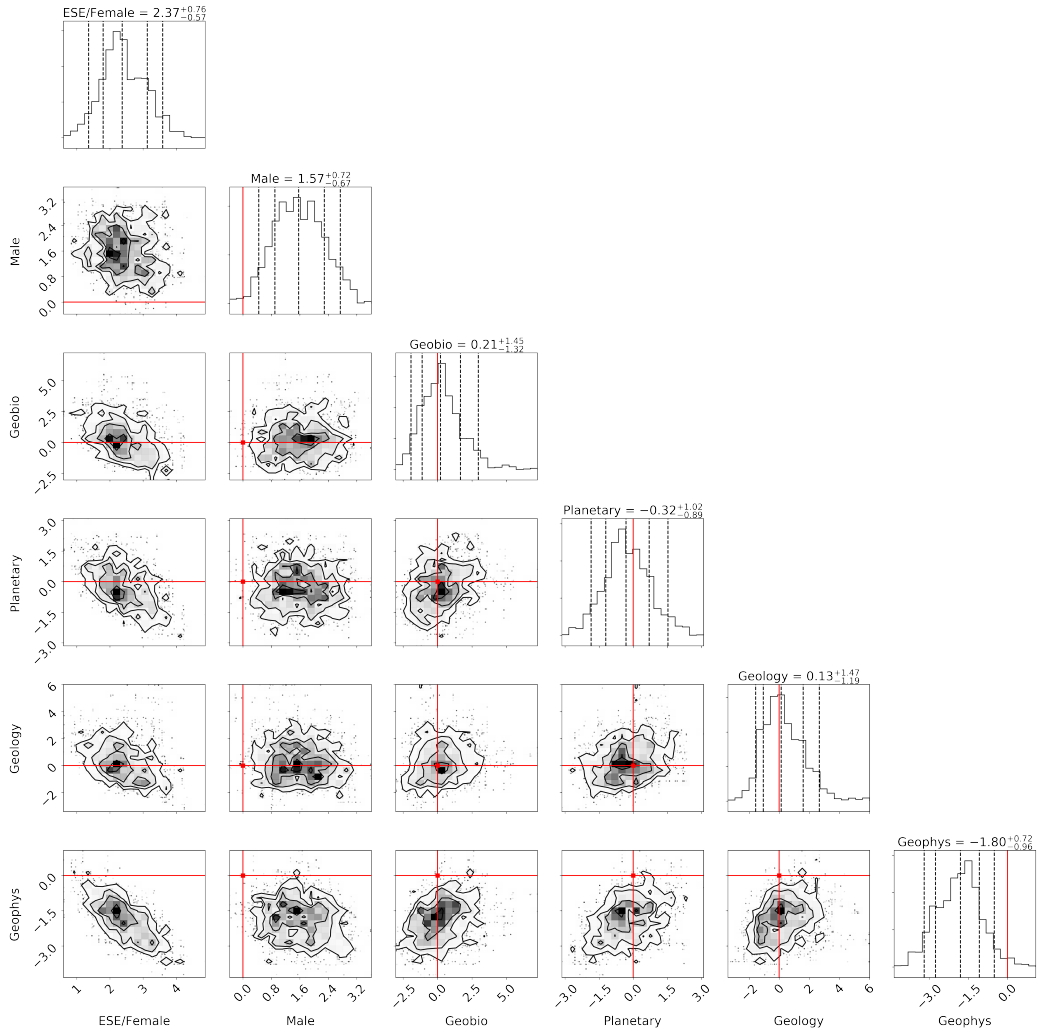

Figure A.4: Corner plot of β_i values from MCMC analysis. The solid lines show $\beta_i = 0$ and the dashed lines show the mean and $\pm 1\sigma$ error bars for each β_i. (Note: The null hypothesis does not correspond to $\beta_0 = 0$, so this is not plotted.)

women in Geophysics are failing at a significantly higher rate than a) women in other options and b) men in Geophysics.

To further study this effect, we can examine an abbreviated model with predictor variables that are not statistically different from zero excluded. The new model is

$$\sigma(\vec{x}) = \frac{1}{1 + e^{-(\beta_0 + \beta_1 x_1 + \beta_4 x_4)}}. \tag{A.6}$$

The parameter best fit results with the new model are shown in Figure A.6 using MCMC with only 10,000 steps.

The shorter MCMC run can be justified by calculating the autocorrelation length for

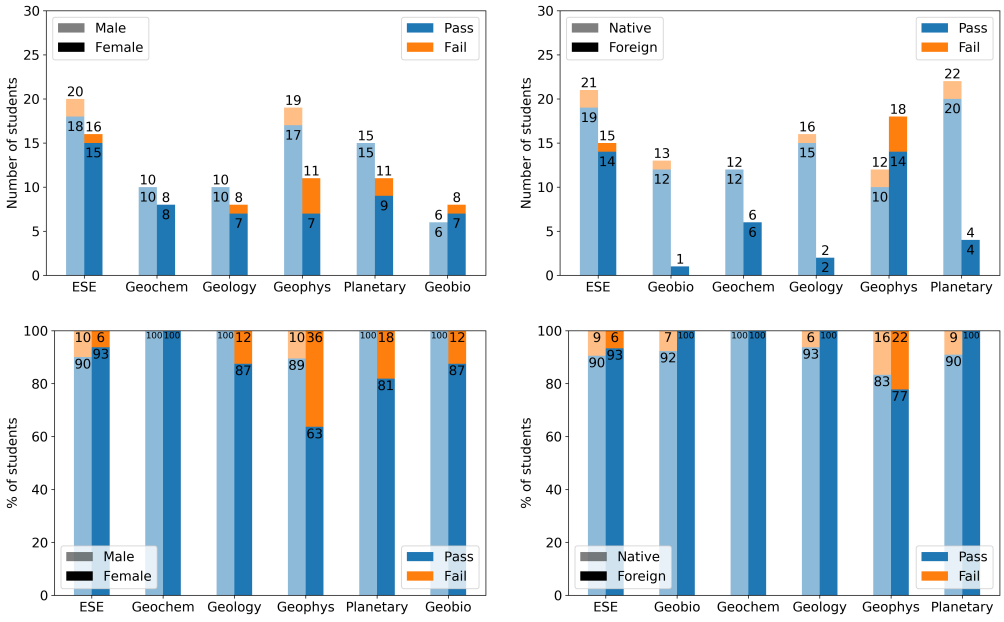

Figure A.5: Number of students per option per gender (top left) or English language status (top right) who passed or failed the exam. Labels are total number of students and number who passed for each category. Bottom panels show percentage of students who passed or failed the exam in each category (left for gender and right for English language status).

the chain. The autocorrelation length was found to be $ACL \sim 300$, so, $N = 10000$ steps obeys the rule-of-thumb that $ACL/N \geq 10$. I obtain slightly different β_i values from this abbreviated model, but they agree well within the 1σ error bars. This is shown in Table A.1.

	full model	abbreviated model
β_0	$2.37^{+0.76}_{-0.57}$	$2.19^{+0.41}_{-0.37}$
β_1	$1.57^{+0.72}_{-0.67}$	$1.39^{+0.68}_{-0.59}$
β_5	$-1.80^{+0.72}_{-0.96}$	$-1.49^{+0.54}_{-0.60}$

Table A.1: Table showing β_i values calculated via MCMC using the full model with all 5 predictors versus the abbreviated model with only two predictors. The results agree.

Based on this model and the β_i parameters fit with MCMC, I can calculate the predicted probability of passing the GPS qualifying exam for the different demographic groups. In particular I am interested in the difference between male and female and the difference between Geophysics and ESE (the base case). These mean

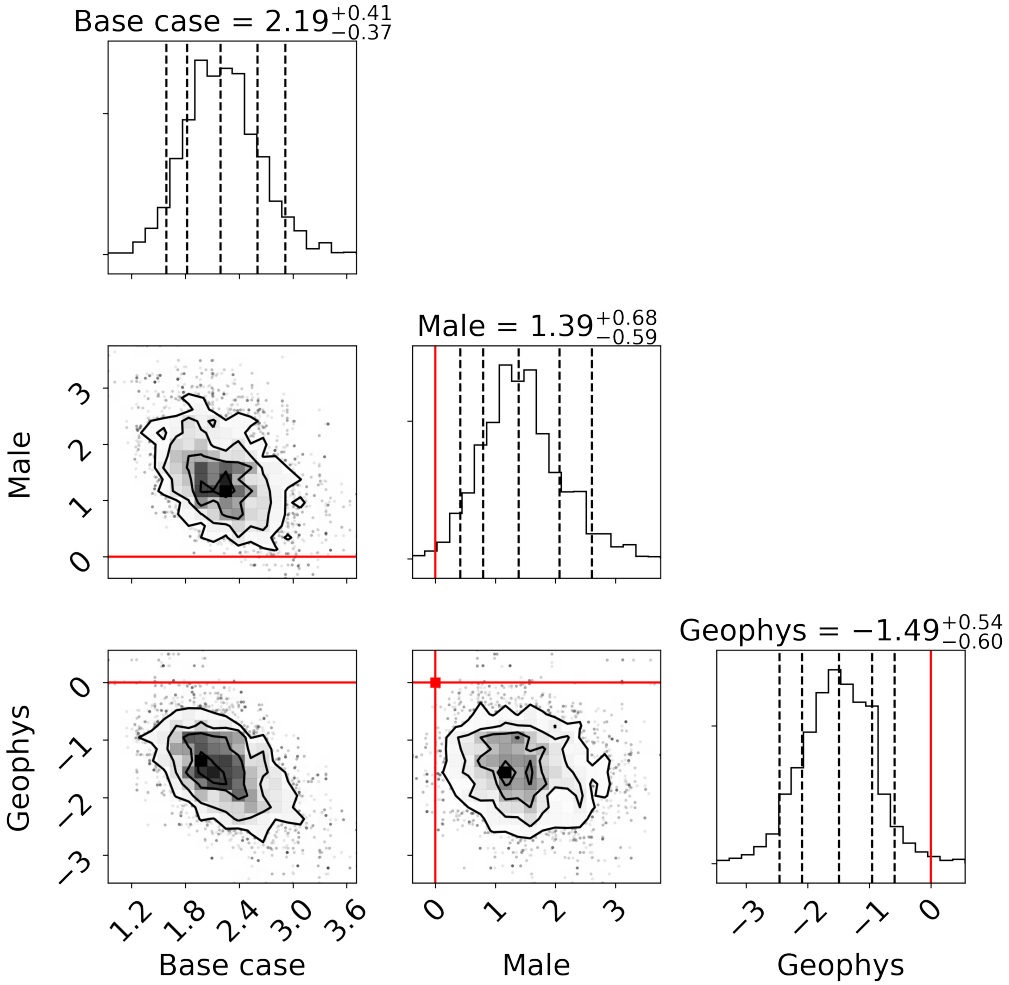

Figure A.6: Corner plot of β_i values from MCMC analysis. The solid lines show $\beta_i = 0$ and the dashed lines show the mean and $\pm 1\sigma$ error bars for each β_i.

predicted values and one standard deviation are show in Table A.2. These values were calculated as

$$\delta\sigma = \sqrt{\left(\frac{\partial\sigma}{\partial\beta_0}\delta\beta_0\right)^2 + \left(\frac{\partial\sigma}{\partial\beta_1}\delta\beta_1 x_1\right)^2 \left(\frac{\partial\sigma}{\partial\beta_4}\delta\beta_4 x_4\right)^2} \tag{A.7}$$

The error bars on these passing probabilities are large, but the trends still clearly stand out. To more confidently demonstrate these discrepancies across gender and option categories, more years of data must be added to this analysis to increase the sample size beyond $N = 119$ students.

	Women	Men
ESE	90 ± 4%	97 ± 2%
Geophysics	67 ± 15%	89 ± 9%

Table A.2: Probability of passing the GPS Qualifying Exam based on the logistic model with MCMC fit best parameters.

Preliminary conclusions

These preliminary findings indicated that more years of data are needed, but also more data on the student experience, beyond pass/fail rates, is needed to gain understanding of why students are failing, why the failure rates are so disproportionate across options and across genders, and what changes could be implemented to remedy these problems. To follow up, myself along with two other students, staff from the Title IX office, and in coordination with the GPS Core Committee (the group of faculty responsible for administering the exams) designed and conducted a survey of current students and recent alumni about their experiences surrounding the qualifying exams. The details of the survey are discussed in the following sections.

A.3 Part 2: Why are there differences in exam outcome between men and women?

Co-authors, listed alphabetically: Lilian A. Dove, Sara E. Murphy, Clare E. Singer

The survey

The survey was conducted in Summer 2021. The survey was written by Lily Dove, Sara Murphy, and Clare Singer, with help from Allie McIntosh (Equity & Title IX Office), and after approval from Mike Brown, Ed Stolper, and Paul Wennberg (GPS/ESE Core Committee[1] members). The survey was administered to all current students who had taken the qualifying exam and to as many recent alumni as we could contact. The survey results were collected and anonymized by the Caltech Title IX office. The authors only ever had access to anonymized, aggregated, or redacted results from the survey.

[1] The Core Committee is the faculty committee responsible for administering the qualifying exams each year. Every examining committee consists of at least one member of the Core Committee, often two. The administration of the ESE exams is done by a separate ESE Core Committee, which operates in parallel to the GPS Core Committee. Typically faculty on the Core Committee change every year. One result of this analysis and the survey was to expand the scope of the Core Committee slightly. They now claim some responsibility for the design of the exam, not just the implementation. Furthermore, the chair of the Core Committee now has a three year, rather than one year, term so that they may provide continuity and oversee changes on slightly longer timescales.

Survey questions

1. Before quals:
    a) How supported did you feel while preparing for your exam? (1-5)
    b) How confident were you leading up to your exam? (1-5)
    c) How informed were you about the format of the exam? (1-5)
    d) How prepared did you feel for your exam? (1-5)
    e) When did you start your first (second) proposition? (Mult. choice)
    f) How often did you meet with your first (second) advisor about your proposition during your first year? (Mult. choice)
    g) Was this frequent enough to meet your advising needs? (Yes/No)
    h) What was your experience leading up to quals? (Open-ended)
    E.g. Who gave you the most support? What was the messaging you received from your advisor about the exam? Did you have adequate information about what to expect and from whom did you get that information?

2. During the exam:
    a) Was the format of the exam as it was described to you? (1-5)
    b) Do you feel that the qualifying exam allowed you to show your achievements and growth as a researcher over the course of the first year? (1-5)
    c) Were the questions asked during your exam relevant to your research? (Yes/No)
    d) Were the questions asked in a respectful manner? (Yes/No)
    e) What was your experience on the day of quals? (Open-ended)
    E.g. What did you feel the exam was testing? Were your committee members attentive, engaged, respectful during the exam? Did the exam challenge you in a positive way? – Please be as specific as you would like. Your answers to all questions will be anonymized and/or aggregated before shown to the faculty.

3. After the exam:
    a) Did the qualifying exam make you aware of your weaknesses as a researcher in a constructive way? (1-5)

b) How helpful was the feedback from your committee members? (1-5)

c) What 2-3 words best describe your feelings immediately after finishing the exam?

d) What 2-3 words best describe your feelings 1 week after finishing the exam?

e) Did you talk to your committee members after the exam? (Yes/No)

f) When did you talk to your committee members? (Mult. choice)

g) If you didn't talk with your committee members after the exam, why not? (Open-ended)

h) What was your experience after quals? (Open-ended)
E.g. From whom did you get feedback? How useful was that feedback? Did you feel confident in your abilities as a scientist after the exam? Do you feel like you know why you passed/failed? Did the feedback you received help you identify your strengths and weaknesses? Did it help you figure out how to improve on those weaknesses?

4. General questions:

a) In an ideal world, how would you restructure or change quals? (Open-ended)

b) Are there events or activities during the first year, prior to the qualifying exam, that would improve exam preparation? (Open-ended)

5. Demographic questions:

a) When did you take quals? (Mult. choice)

b) What was the outcome of your exam? (Pass/Fail/Other)

c) Racial identity (Mult. choice)

d) Gender identity (Mult. choice)

e) Do you identify as LGBTQIA+? (Yes/No)

f) Do you identify as a first generation student? (Yes/No)

g) Do you identify as someone with a disability? (Yes/No)

h) Are you a native English speaker? (Yes/No)

Email sent to students about survey

"Dear G2+ GPS students,

Consistent feedback from students across the GPS Division demonstrates that the Qualifying Exam is an area that requires further reflection and discussion within the division. With the assistance of the GPS/ESE Qualifying Exam Core Committees and the Equity and Title IX Office, we have constructed a survey to assess the current state of the qualifying exam. The goal of this form is to collect student experiences from before, during, and after their qualifying exam, to help develop a clear picture of where students feel supported, where there can be improvement, and where the exam is meeting and/or falling short of its intended goals. Please take the survey (link) before June 15.

While we have a number of 1-5 questions on the form, we would like to emphasize the long-answer questions. Please take the time to fill them out, if you feel comfortable. The purpose of this form is to collect stories and details, and this is the information that will be most helpful. Below, you can see the long-form questions so you can think about them ahead of time.

All questions on this survey are optional, and your responses will never be shared in a way that may be identifying. The responses to this form will only be directly accessible to Deputy Equity and Title IX Coordinator Allie McIntosh (allie@caltech.edu) and Julie Lee who will further anonymize the stories/information before sharing them with the faculty.

As an incentive, 4 survey respondents will receive $25 gift cards to their choice of Urban Plates or Vroman's Bookstore. You must enter your email in the secondary google form after you complete the survey to be entered into the lottery.

If you have any questions or concerns, please reach out to us.

Best,
Sara Murphy, Clare Singer, Lily Dove (ESE G3s)
GPS Qualifying Exam Core Committee (Chair: Mike Brown)
ESE Qualifying Exam Core Committee (Chair: Paul Wennberg)"

Overview of survey results

Who took the survey?

The survey was completed by 71 current and former Caltech GPS students, which represented approximately an 65% completion rate (compared to an average of 110 total students in the Division). The demographics of students taking the survey was commensurate with the demographics of the overall student body. Figure A.7 shows histograms of survey-taker demographics including English language status, ability status, first-generation student status, year of exam, racial identity, and exam outcome. For all questions, demographic and otherwise, survey participants were allowed to opt out or not answer; these responses are labeled as "NoResponse" throughout the results.

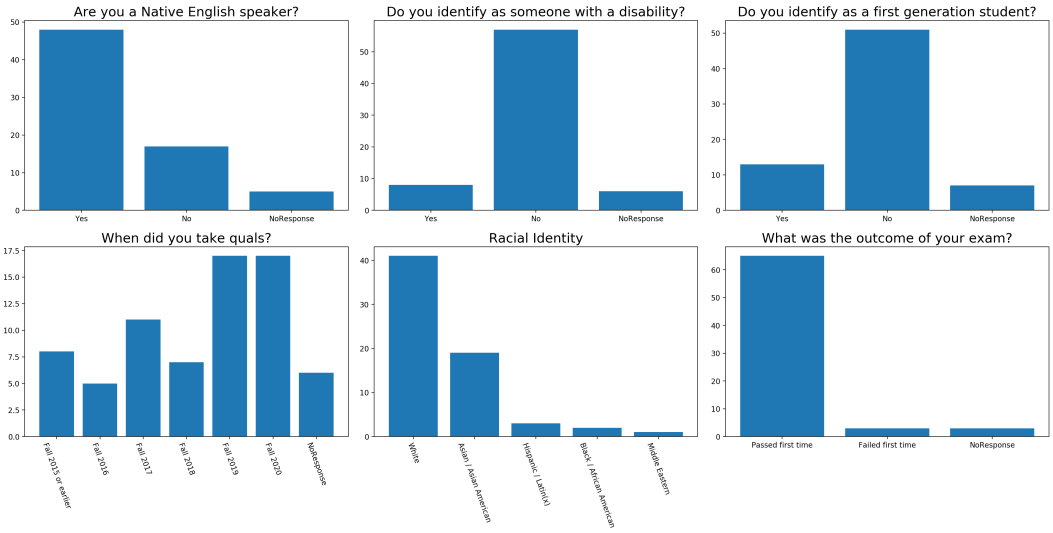

Figure A.7: Demographic information on survey participants for categories that could not be dis-aggregated due to concerns of anonymity: a) Native English speaker, b) ability status, c) first-generation student status, d) year of exam, e) racial identity, and f) exam outcome.

General impressions

First, we can investigate the aggregated results from the survey to understand overall student impressions of the exam. Figure A.8 shows responses to the eight numerical survey questions asking about student experience *before*, *during*, and *after* the exam. Overall, students felt most positively about their knowledge of the exam format and most negatively about their experience receiving feedback on the exam.

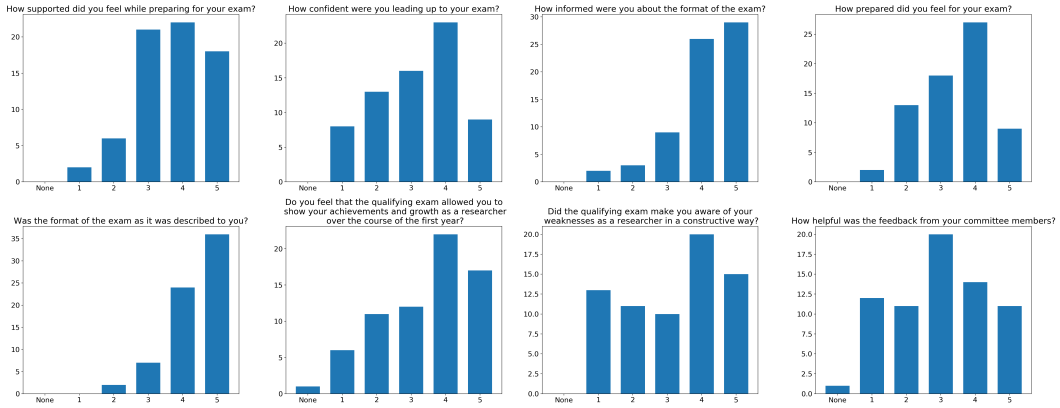

Figure A.8: Histograms of responses to questions with numerical answers (1–5) asking students how a) supported, b) confident, c) informed, d) prepared they felt before the exam, e) if the exam format was in fact as expected, f) whether the exam format allowed them to demonstrate their achievements, g) if the exam provided constructive criticisms, and h) how helpful the feedback was overall from the committee. Students felt most negatively about the feedback that was provided (g,h).

To gather more qualitative data on student experience during the 3 hour exam, we asked students to describe in 2-3 words how they felt when they finished. The word cloud in Figure A.9 shows these responses. Words are sized by the number of times they were written by students in answer to the survey. The most common feelings were relieved, exhausted, disappointed, tired, happy, confused, relaxed, excited, depressed, overwhelmed, demoralized, and so on.

The survey also asked open-ended questions to which students could respond with long-format answers. Students were asked about their experience during each phase of the first year (before, during, or after the exam). To summarize some of these responses, the answers were coded as "overall positive," "neutral/mixed," or "overall negative." These results are shown in Figure A.10. Overall, the majority of students felt mixed or neutral before the exam, equally split during the exam, and majority negative after the exam. The time period when the most students felt overall positive was on the day of the exam itself, and the least students felt this way after the exam.

From the long-format responses, a theme emerged of disrespect by the committee towards the students. Students described situations of "hostile" questions, arguments between committee members, and being laughed at during the exam. Overall, an astounding number of students mentioned disrespectful behavior in their responses, including:

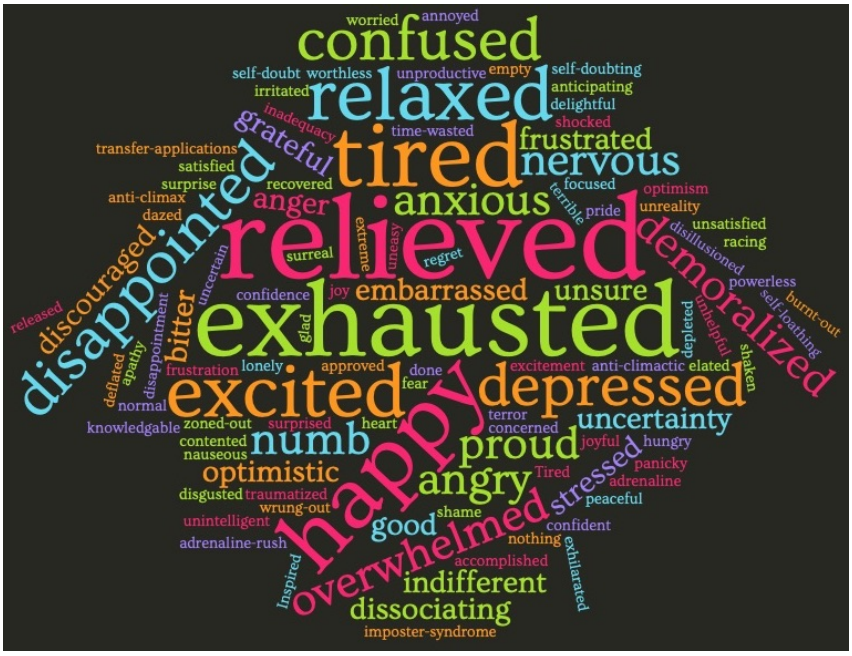

Figure A.9: Word cloud of responses to the following survey question: *What 2-3 words best describe your feelings immediately after finishing the exam?*

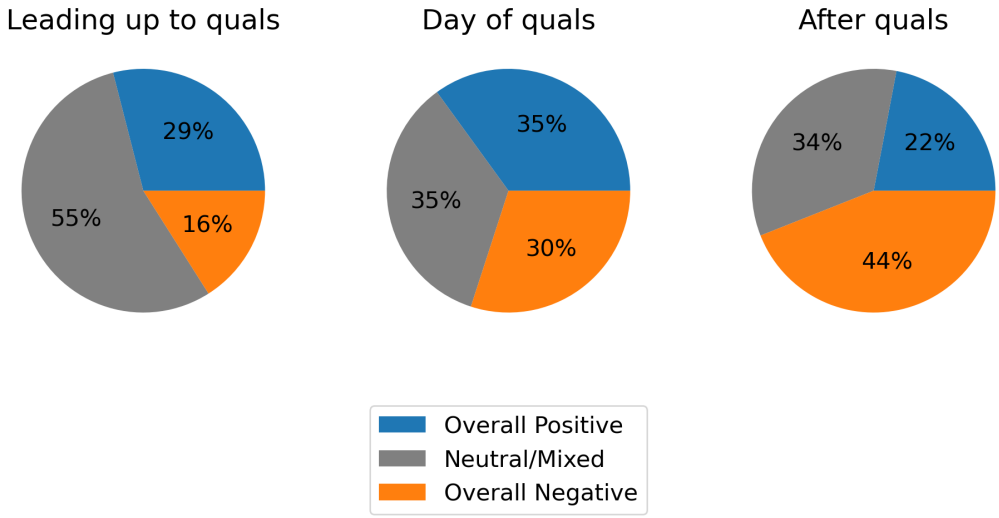

Figure A.10: Pie charts summarizing students' feelings leading up the exam (left), on the day of the exam (center), and after the exam (right). Long form responses were coded into categories of "overall positive" (blue), "neutral or mixed" (grey), and "overall negative" (orange). Students felt most positive during the exam itself, and most negative after the exam. Before the exam the majority of students had neutral or mixed feelings.

- 12% of respondents mentioned committee members falling asleep during the exam,
- 12% of respondents said they were asked questions in a rude/disrespectful manner, and
- 7% of respondents mentioned committee members arriving late or leaving early.

Finally, long-format answers were coded with respect to how students described their interactions with different groups of people. Figure A.11 shows how students characterized their interactions with their faculty "advisors" compared to other student or postdoc "peers" in their experience leading up to the exam. When responses mentioned interactions with either of these groups, the response was ranked as either positive or negative. Overall, many more students wrote about interactions with their faculty advisors compared to interactions with peers. About 20% more interactions with faculty were ranked as negative than positive, compared to about 50% more of cited interactions with students or postdocs being ranked positive than negative. Additionally, many responses described the power imbalance between students and faculty and how difficulties with communication or other interactions often arose from this inherent, but often ignored, power imbalance.

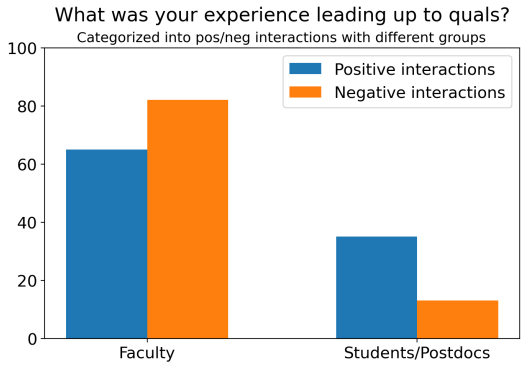

Figure A.11: Percentage of responses that described positive or negative interactions with faculty or with other students and postdocs. Responses could indicate both positive and negative interactions with either or both groups, so the total does not sum to 100%. Overall, students described interacting more often with faculty than other students/postdocs and these interactions were described as both positive and negative at fairly comparable rates, but with more negative interactions described. Fewer descriptions of interactions with students/postdocs existed, but these were mostly described as positive.

Gender discrepancies

For all of the questions asked, we can disaggregate the responses by the students' gender identity. For other identity characteristics this was not always possible while still retaining anonymity due to the small sample size. Similarly for gender only a gender binary (men and women) is presented in these results because the number of nonbinary respondents was too small to present anonymously. Therefore, this analysis only focuses on gender discrepancies in exam experience. However, the same questions asked here can and should be asked pertaining to other identity characteristics like race, first-generation status, and more.

We focus here on the numerical questions about exam experience shown in Figure A.8. Figure A.12 shows the same results, but split by gender. The results here are striking and show that across the whole timeline — before, during, and after the exam — women are feeling less supported, less prepared, and receiving worse feedback than their male peers.

1. For all questions except b (confidence) and d (preparedness), the mode answer from women was less than the mode answer from men.

2. For all questions more women responded with numerical values 1 or 2 than men, and fewer responded with 4 and 5.

3. For questions c to e (information, preparedness, format knowledge), only women responded with the lowest value.

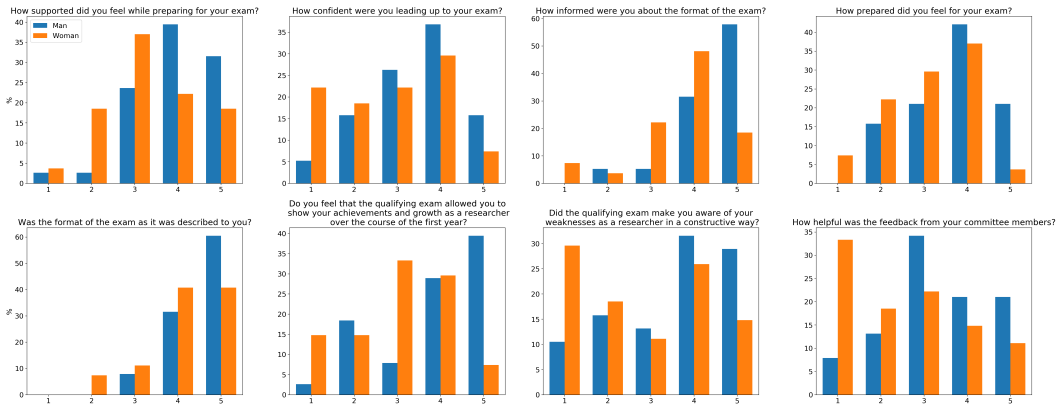

Figure A.12: Histogram of scores for each of the eight questions with numerical 1–5 answers broken down by gender of respondent, normalized by total number of respondents from each category.

To help summarize these results, Figure A.13 shows the average score on each of the eight questions separately for men and women, with 0.5σ error bars. For all eight questions, the average score from women was less than from men, though of course with considerable spread (as evident from the full histograms in Figure A.12).

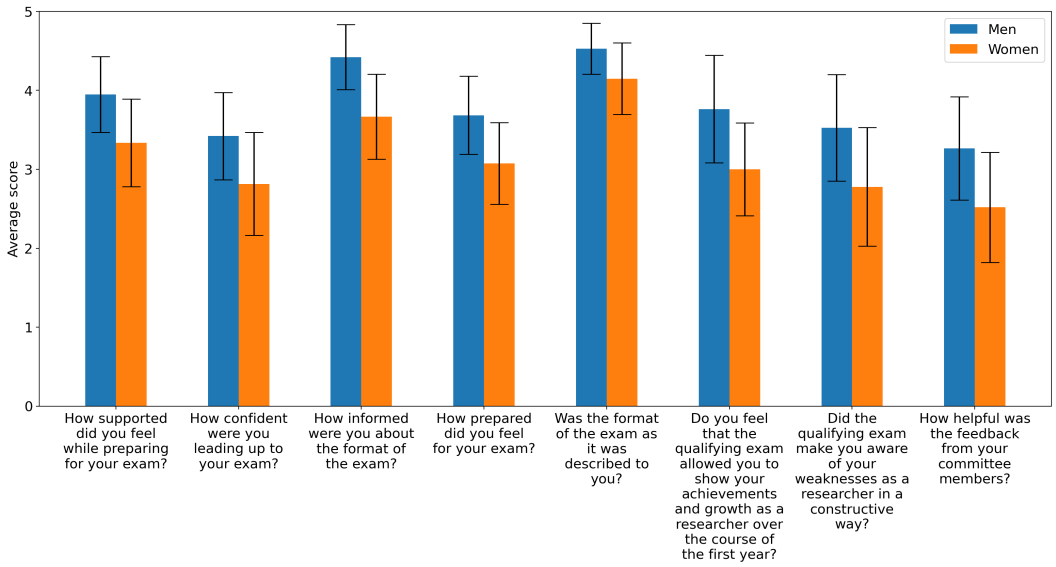

Figure A.13: Average score for each of the eight questions with numerical 1–5 answers aggregated by gender of respondent. The first four questions ask about experiences before the exam, the second three about the experience during the exam, and the last question about the feedback received after the exam. For all eight questions the average response from women was lower than from men. The error bars show 0.5σ to represent the spread in answers amongst respondents.

Recommendations to the Division

Based on the survey results, we recommended a number of improvements the Division could make to the examination itself and the process surrounding first year advising. These recommendations were discussed with the Core Committee in Summer 2022.

1. Have committee members write down 3 exam successes and 3 areas for improvement immediately after the exam in order to provide more actionable and specific feedback.

2. Empower committee chairs to call out un-attentive, distracted, or sleeping members during the exam.

3. Advertise Caltech Accessibility Student Services and consider making the exam shorter or splitting into two sessions in order to provide students with disabilities an equitable exam-taking experience.

4. Openly discuss the possibility of failing and what happens with regard to financial support, visa status, and academics in order to reduce undue stress on first year students.

5. Write and publish a statement describing the faculty goals for the qualifying exam and what it is testing and how success is measured.

6. Require mandatory yearly faculty mentorship training and scheduled check-ins between advisors and first years.

7. Create a universal course for first years that covers presentation skills, writing an abstract, and building mentorship circles.

8. Organize communication between G1s and G2+s to learn about quals organized by option representatives.

9. Offer oral finals instead of written finals in most GPS graduate classes.

10. Offer spring term sessions or a class where students can practice talking about their research in a low-stakes environment.

11. Change the required paper to a poster that can be engaged with by the full division and give student practice speaking about their work.

12. Consider more flexible scheduling (spread exams over a semester).

13. Maintain a database of the qualifying exam results by gender identity, race, and other protected characteristics.

Recent progress

Continued conversations with the qualifying exam committee have extended until the writing of this thesis. Some changes already implemented in the exam process are documented here. The authors recognize the efforts of Professor Mike Brown in working to improve the qualifying exam since 2022, some of which is documented here: `https://www.gps.caltech.edu/documents/4829/Core_report_2022.pdf`

1. 1-credit lunchtime seminar course for first year students that covers aspects ranging from how to find an advisor, to how to conduct fieldwork safely and ethically, to how to get involved in outreach, to where on campus to find resources from scientific writing to gender harassment support.

2. Mandatory acknowledgement from students that their proposition advisors have signed-off on their project abstracts when they are first submitted in May.

3. Mid-summer (July) progress report to ensure that students and advisors are communicating appropriately about expectations.

4. Annotated rubric provided to students before the exam that clearly explains what each requirement means.

5. Examining committee meets one week prior to exam to decide upon a list of topics to cover based on the submitted abstracts.

6. A record of the past topic/abstract pairs will be made publicly available for students to read while preparing for their own exam.

7. Reduction of committee size from five to four members to reduce faculty burn out during exam season and increase attentiveness from each faculty during the examinations.

8. Detailed written feedback letter sent to students after the exam.[2]

[2]This does not yet apply to the ESE option.